APR1400
DESIGN CONTROL DOCUMENT TIER 2

CHAPTER 4
REACTOR

APR1400-K-X-FS-13002
REVISION 0
SEPTEMBER 2013

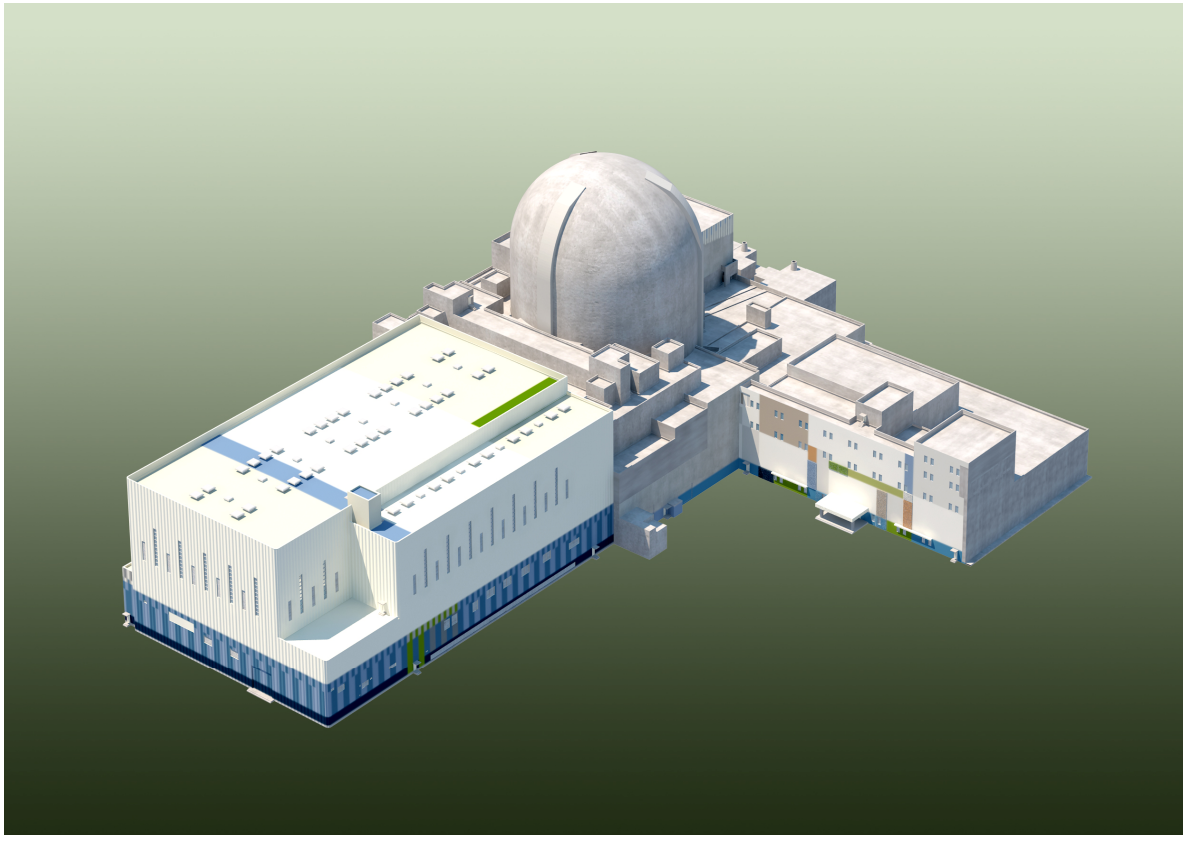

KOREA ELECTRIC POWER CORPORATION
KOREA HYDRO & NUCLEAR POWER CO., LTD

CHAPTER 4 – REACTOR

TABLE OF CONTENTS

LIST OF TABLES

LIST OF FIGURES

ACRONYM AND ABBREVIATION LIST

AMS	Aerospace Material Specification
AOO	Anticipated Operational Occurrence
APR	Advanced Power Reactor
ARO	All Rod Out
ASME	American Society of Mechanical Engineers
ASTM	American Society for Testing and Materials
ATWS	Anticipated Transient Without Scram
BOC	Beginning Of Cycle
BOL	Beginning Of Life
CEA	Control Element Assembly
CEDM	Control Element Drive Mechanism
CET	Core Exit Thermocouple
CHF	Critical Heat Flux
COL	Combined License
COLSS	Core Operating Limit Supervisory System
CPC	Core Protection Calculator
CPCS	Core Protection Calculator System
CRDS	Control Rod Drive System
CRX	Canadian Research Reactor
CVCS	Chemical and Volume Control System
DIT	Discrete Integral Transport
DNB	Departure from Nucleate Boiling
DNBR	Departure from Nucleate Boiling Ratio
DRCS	Digital Rod Control System
ECCS	Emergency Core Cooling System
ENFMS	Ex-core Neutron Flux Monitoring System
EOC	End Of Cycle
EOL	End Of Life
EPRI	Electric Power Research Institute

FMEA	Failure Modes and Effects Analysis
GDC	General Design Criteria (of 10 CFR 50, Appendix A)
HFP	Hot Full Power
HJTC	Heated Junction Thermocouple
I&C	Instrumentation And Control
ICCMS	Inadequate Core Cooling Monitoring System
ICI	In-Core Instrumentation
ID	Inner Diameter
ITC	Isothermal Temperature Coefficient
KAERI	Korea Atomic Energy Research Institute
KEPCO NF	KEPCO Nuclear Fuel Co., Ltd.
KWU	Kraftwerk Union AG
LCO	Limiting Conditions for Operation
LHGR	Linear Heat Generation Rate
LHR	Linear Heat Rate
LMFBR	Liquid Metal Fast Breeder Reactor
LOCA	Loss Of Coolant Accident
LPMS	Loose Parts Monitoring System
LSSS	Limiting Safety System Setting
NEM	Nodal Expansion Method
NPSH	Net Positive Suction Head
NSA	Neutron Source Assembly
OD	Outside Diameter
OECD	Organization for Economic Cooperation and Development
ORNL	Oak Ridge National Laboratory
PDIL	Power Dependent Insertion Limit
PSCEA	Part-Strength Control Element Assembly
PWR	Pressurized Water Reactor
PWSCC	Primary Water Stress Corrosion Cracking
RCPB	Reactor Coolant Pressure Boundary
RCS	Reactor Coolant System

RPS	Reactor Protection System
RRS	Reactor Regulating System
RTSG	Reactor Trip Switchgear
SAFDL	Specified Acceptable Fuel Design Limit
SCU	Statistical Combination of Uncertainties
SIS	Safety Injection System
SLB	Steam Line Break
SRP	Standard Review Plan

CHAPTER 4– REACTOR

4.1 Summary Description

The APR1400 reactor is a pressurized water reactor (PWR) with two reactor coolant loops. A vertical cross section of the reactor is shown in Figure 4.1-1. Table 4.1-1 contains a summary of the core configuration.

The reactor core is composed of 241 fuel assemblies and 93 control element assemblies (CEAs). The fuel assemblies are arranged to approximate a right circular cylinder with an equivalent diameter of 3,647 mm (143.6 in) and an active length of 3,810 mm (150 in). The fuel assembly, which provides for 236 fuel rod positions (16 × 16 array), includes four guide thimbles and one instrument tube welded to grids. The fuel assembly is closed at the top and bottom by nozzles. Each guide thimble displaces four fuel rod positions and provides channels that guide the CEAs over their entire length of travel. In-core instrumentation (ICI) is installed in the instrument tube of selected fuel assemblies. The ICI is routed into the bottom of the fuel assemblies through the bottom head of the reactor vessel. Figure 4.1-2 shows the reactor core cross section and dimensional relations between fuel assemblies, fuel rods, and CEA guide thimbles.

The reactor coolant enters the inlet nozzles of the reactor vessel, flows downward between the reactor vessel wall and the core support barrel, and passes through the flow skirt section where the flow distribution is equalized, and into the lower plenum. The coolant then flows upward through the core, removing heat from the fuel rods. The heated coolant enters the core outlet region, where it flows around the outside of the CEA guide tubes to the reactor vessel outlet nozzles. The CEA guide tubes protect the individual neutron absorber elements of the CEAs from the effects of coolant crossflow above the core.

The reactor internals support and orient the fuel assemblies, CEAs, and ICI and guide the reactor coolant through the reactor vessel. The reactor internals also absorb static and dynamic loads and transmit the loads to the reactor vessel flange. They safely perform their functions during normal operation, anticipated operational occurrences (AOOs), and postulated accidents. The internals are designed to safely withstand forces due to deadweight, handling, temperature and pressure differentials, flow impingement, vibration, and seismic acceleration. All reactor internal components are considered Category I for the seismic design. The stress values of all structural members under normal operating and

expected transient conditions are not greater than those established by the American Society of Mechanical Engineers (ASME) Section III. The effect of neutron irradiation on reactor internal materials is included in the design evaluation. The effect of accident loadings on the internals is included in the design analysis.

Reactivity control is provided by two independent systems: the control element drive mechanism (CEDM) and the chemical and volume control system (CVCS). The CEDM controls short-term reactivity changes and is used for rapid shutdown. The CVCS is used to compensate for long-term reactivity changes and can make the reactor subcritical without the benefit of the CEDM. The design of the core and the reactor protection system (RPS) prevents fuel damage limits from being exceeded for any single malfunction in either of the reactivity control systems.

4.1.1 Initial Core Design Description and Permissible Changes

The fuel system design, nuclear design, and thermal-hydraulic design are described in Sections 4.2, 4.3, and 4.4, respectively, with respect to typical core characteristics. The design features are provided in Table 4.1-2, and the evaluated design parameters and associated acceptance criteria are provided in Table 4.1-3.

4.1.2 Analytical Techniques

Table 4.1-4 contains a summary of the primary techniques and codes used in the analyses that are described in Chapter 4. Table 4.1-4 provides cross references to the subsections in Chapter 4 with more information about the primary techniques and codes.

4.1.3 Combined License Information

No COL information is required with regard to Section 4.1.

Table 4.1-1

Core Configuration

Item	Value
Number of fuel assemblies in core, total	241
Number of CEAs	93
Number of fuel rod locations	56,876
Spacing between fuel assemblies, fuel rod surface to surface, cm (in)	0.549 (0.216)
Spacing, outer fuel rod surface to core shroud, cm (in)	0.554 (0.218)
Hydraulic diameter, nominal channel, cm (ft)	1.264 (0.04147)
Total flow area (excluding guide thimble tubes), m^2 (ft^2)	5.825 (62.7)
Total core area, m^2 (ft^2)	10.433 (112.3)
Core equivalent diameter, m (in)	3.647 (143.6)
Core circumscribed diameter, m (in)	3.873 (152.5)
Total fuel loading, kg U (lb U) (assuming all rod locations are fuel rods)	103.82×10^3 (228.9×10^3)
Total fuel weight, kg UO_2 (lb UO_2) (assuming all rod locations are fuel rods)	117.8×10^3 (259.7×10^3)
Total weight of zirconium alloy, kg (lb)	29,510.6 (65,059)
Fuel volume (including dishes), m^3 (ft^3)	11.42 (403.3)

Table 4.1-2

Design Features for Initial Core Design

Design Feature	Nominal Values
Fuel rod U-235 enrichment	3.64, 3.14, 2.64, 1.71 w/o
Burnable absorber concentration (Gd_2O_3)	8.0 w/o
Number of burnable absorber rods per fuel assembly (Gd_2O_3)	12, 16
Burnable absorber rod cutback length (top and bottom)	304.8 mm (12.0 in)
Core power level	3,983 MWt
Cycle length	17,571 MWD/MTU
Critical boron concentration (HFP, BOC, ARO, E_q. Xenon)	817 ppm

Table 4.1-3

Evaluated Design Parameters and
Associated Acceptance Criteria for Initial Core Design

Evaluated Design Parameter	Acceptance Criteria
Maximum unrodded three-dimensional peaking factor (F_q)	2.43
Minimum departure from nucleate boiling ratio (DNBR)	1.29
Minimum net CEA shutdown worth hot full power (HFP)	8.0 % $\Delta\rho$
Least negative moderator temperature coefficient (HFP, ARO)	0.0×10^{-4} $\Delta\rho$/°C
Most negative moderator temperature coefficient (HFP, ARO)	-5.4×10^{-4} $\Delta\rho$/°C
Least negative power	< 0.0 $\Delta\rho$/(W/cm)
Maximum fuel rod average burnup	*[60,000 MWD/MTU]**

Table 4.1-4

Analytical Techniques Summary

Design Category	Analysis Techniques/Approach	Primary Code	Subsection in Chapter 4
Key parameters such as fuel rod internal pressure, fuel temperatures, and cladding stress and strain	Fuel performance analysis using thermal and fission gas release models based on extensive empirical data	FATES	4.2.3 4.4.1.2
Few-group microscopic and macroscopic cross sections	Spectral calculations using discrete integral transport (DIT) theory and few-group spatial calculations in exact assembly geometry	DIT	4.3.3.1
Three-dimensional power distributions, peaking factors, fuel depletion, boron concentrations, reactivity coefficients, control rod worth, and transient fission product behavior (Xe, Sm)	Two-group diffusion theory applied with a nodal expansion method (NEM)	ROCS	4.3.2 4.3.3.1
Fast neutron flux	Discrete ordinates Sn transport methodology	DORT	4.3.2.8 4.3.3.3
Three-dimensional steady-state thermal-hydraulic parameters and departure from nucleate boiling ratio (DNBR) inside core	Subchannel analysis of the local fluid condition in the core by solving conservation equations of mass, momentum, and energy	TORC	4.4.4.5

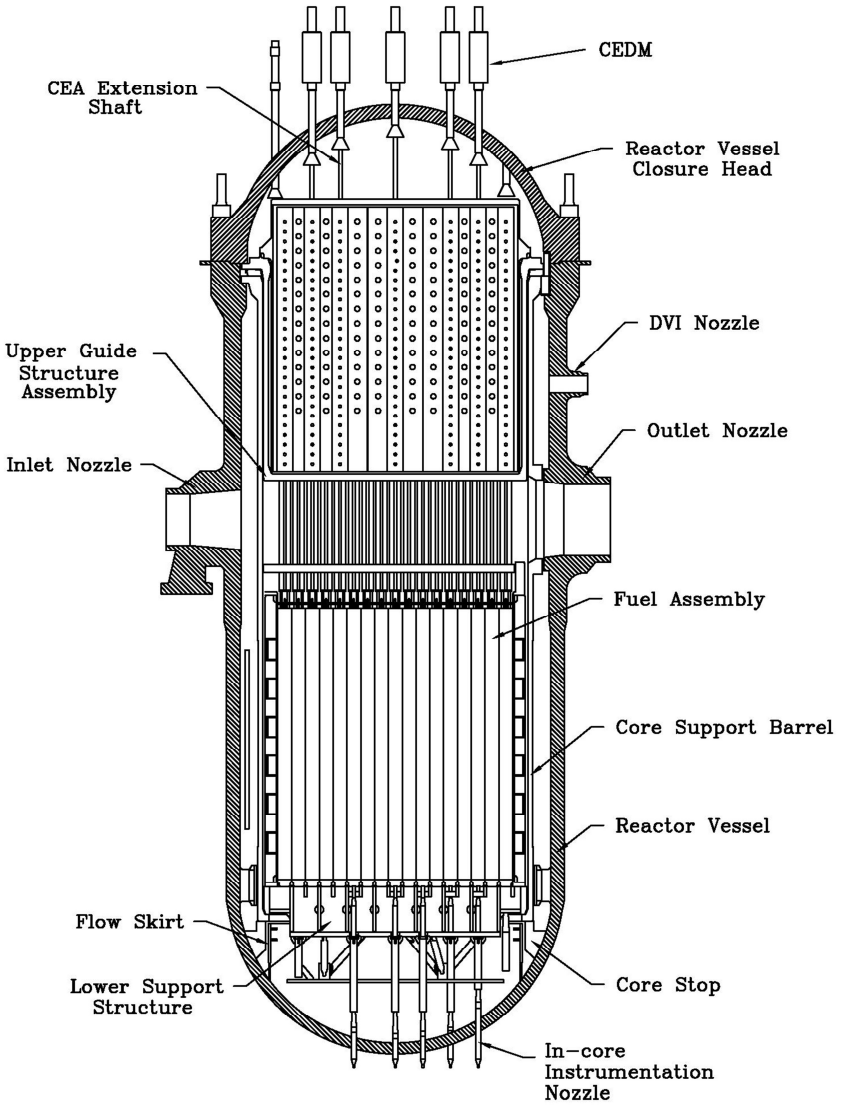

Figure 4.1-1 Reactor General Assembly

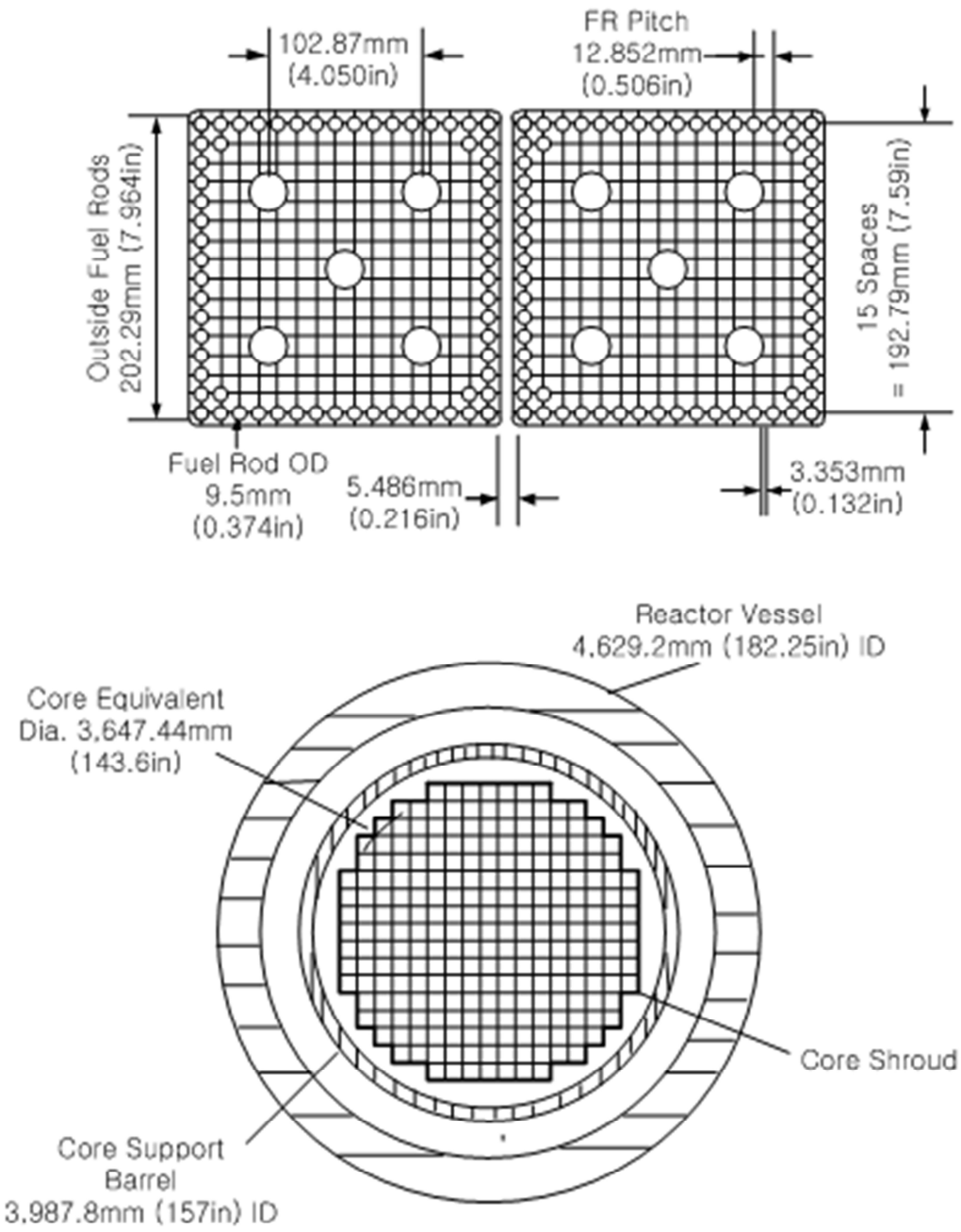

Figure 4.1-2 Reactor Core Cross Section and Fuel Assemblies

4.2 Fuel System Design

The fuel assembly (Figure 4.2-1) consists of 236 fuel rods and burnable absorber rods, 4 guide thimbles, 1 instrument tube, 12 grids, 1 top nozzle, and 1 bottom nozzle (Table 4.2-1).

The fuel system is designed to satisfy the General Design Criteria (GDC) specified in GDC 10, 27, and 35 of 10 CFR 50 Appendix A. Coolability requirements for the loss-of-coolant accident (LOCA) are given in 10 CFR 50.46.

The objectives of the fuel system safety are to provide assurance that (a) the fuel system is not damaged as a result of normal operation and anticipated operational occurrences (AOOs), (b) fuel system damage is never so severe as to prevent control rod insertion when it is required, (c) the number of fuel rod failures is not underestimated for postulated accidents, and (d) coolability is always maintained.

4.2.1 Design Bases

The design bases and criteria for the APR1400 fuel rod and fuel assembly design are described in *[Reference 1]** based on the requirements identified in the Standard Review Plan (SRP) 4.2.

Design bases for APR1400 fuel rod are established to prevent fuel rod failure and fuel system damage in terms of the fuel rod design criteria. The influences of irradiation and temperature are considered in fuel rod design bases. Design bases and criteria have been established for application up to rod average burnup of *[60,000 MWD/MTU]** for the APR1400.

The design bases for the fuel assembly to provide structural integrity for non-operational, normal operational, AOO, and postulated accident loads are described.

The design bases and associated design criteria for the control element assemblies (CEAs) are established in terms of thermal-physical properties of absorber material, compatibility of absorber and cladding materials, cladding stress-strain limits, and irradiation behavior of absorber materials.

4.2.1.1 Cladding

The cladding material for the APR1400 fuel design is ZIRLO, which was manufactured using a zirconium alloy that was developed by Westinghouse Electric Company, LLC, for improved corrosion resistance.

4.2.1.1.1 Mechanical Properties

The mechanical properties of ZIRLO cladding (i.e., modulus of elasticity, Poisson's Ratio, thermal expansion, yield strength, ultimate strength, and uniform tensile strain) are specified in References 2 and 3.

4.2.1.1.2 Stress-Strain Limits

The fuel cladding is designed to sustain the effects of steady-state and expected transient operating conditions without exceeding the acceptable levels of stress and strain. Except where noted, the design bases presented in this subsection are consistent with those described in *[Reference 1]**. The fuel rod design accounts for cladding irradiation growth, external pressure, differential expansion of fuel and clad, fuel swelling, densification, clad creep, fission and other gas releases, initial internal helium pressure, thermal stress, pressure and temperature cycling, and flow-induced vibrations.

The structural criteria and bases described below address the normal and AOO loading combinations.

a. The maximum primary tensile stress in the clad shall not exceed two-thirds of the minimum unirradiated yield strength of the material at the applicable temperature. The corresponding limit for compressive stress is the material yield strength. The use of the unirradiated material yield strength as the basis for allowable stress is conservative because the yield strength of ZIRLO increases with irradiation.

b. At any time during the fuel rod lifetime, the net unrecoverable circumferential tensile cladding strain shall not exceed 1 percent based on beginning of life (BOL) cladding dimensions. This criterion is applicable to normal operation conditions and following a single AOO. The total (elastic plus plastic) circumferential

cladding strain increment produced as a result of a single AOO, shall not exceed 1 percent. The acceptability of a 1 percent unrecoverable circumferential strain limit is demonstrated by data from irradiated ZIRLO clad fuel rods (References 2 and 3, Table 4.2-2).

4.2.1.1.3 Vibration and Fatigue

Fretting wear by flow-induced vibration can cause fuel rod damage during normal operation. To preclude fuel rod damage, the maximum fretting wear depth is limited.

Cumulative strain cycling usage, which is defined as the sum of the ratios of the number of cycles in a given effective strain range ($\Delta\varepsilon$) to the permitted number (N) at that range, shall not exceed 0.8.

The cycling usage factor based on the Langer-O'Donnell model (Reference 4 and Figure 4.2-2) is conservatively calculated considering a safety factor of 2 on the stress amplitude or a safety factor of 20 on the number of cycles.

4.2.1.1.4 Chemical Properties

The corrosion resistance of ZIRLO cladding is higher than that of Zircaloy-4 cladding. The external oxide thickness and absorbed hydrogen content of ZIRLO cladding are below the limits specified in *[Reference 1]**.

Internal hydriding is precluded from acting as a cladding failure mechanism because the level of hydrogen impurities in the fuel during fabrication is controlled.

4.2.1.2 Fuel Material

4.2.1.2.1 Thermal-Physical Properties of UO_2 Fuel Pellet

a. The thermal expansion of UO_2 is described in References 8 and 9.

b. A value of 0.85 is used for the thermal emissivity of UO_2 pellets over the temperature range of 800 to 2,600 °K (References 10, 11, and 12).

c. Variations in the melting point and thermal conductivity with burnup are addressed in References 5, 6, and 7.

d. The specific heat of UO_2 is addressed in Reference 13.

e. The static modulus of elasticity of unirradiated fuel of 97 percent theoretical density and deformed under a strain rate of 0.097 hr^{-1} is given in Reference 14.

f. Poisson's Ratio of polycrystalline UO_2 gas has a value of 0.32 at 25 °C based on Reference 15. Reference 15 also indicates a 10 percent decrease in value over the range of 25 to 1,800 °C. A constant value of 0.29 is used for Poisson's Ratio at temperatures above 1,800 °C.

4.2.1.2.2 Thermal-Physical Properties of Burnable Absorber Fuel Pellet

This subsection references evaluations of gadolinia-urania properties and thermal conductivity and melting temperature correlations appropriate for the gadolinia-urania compositions of interest in the PWR application of Gd_2O_3-UO_2 burnable absorbers.

The material properties that influence the thermal performance of gadolinia-urania fuel have been reviewed to ascertain how UO_2 properties are influenced by the addition of gadolinia. The material properties include thermal conductivity, solidus temperature, specific heat, and the coefficient of thermal expansion. The effects of gadolinia additions on these properties are described in Reference 16.

4.2.1.2.3 Fuel Densification and Fission Product Swelling

Manufactured fuel pellets are assumed to consist of a two-phase mixture of homogeneous solid material interspaced with pores. The pellet-circumscribed volume changes with irradiation as a result of fuel densification and solid fission product swelling. The effects of irradiation on the density of sintered UO_2 pellets are treated in compliance with the intent of NRC RG 1.126, through use of the NRC-approved model.

Fuel densification and fission product swelling behaviors are described in References 5 and 6.

4.2.1.2.4 Chemical Properties of Fuel

The moisture and hydrogen impurities in the fuel pellets are tightly controlled to minimize pellet interactions with the cladding. The moisture and hydrogen in the fuel pellets are controlled through a rigorous testing and inspection program to demonstrate that each lot of pellets conforms to design requirements and criteria (Subsection 4.2.3.1.4).

4.2.1.3 Fuel Rod Performance

4.2.1.3.1 Analytical Models

Steady-state fuel temperatures are determined by the FATES computer program. The calculation procedure considers the effect of linear heat generation rate (LHGR), fuel relocation, fuel swelling, densification, thermal expansion, fission gas release, and clad deformation. The model for predicting fuel thermal performance, including the specific effects of fuel densification on increased LHGR and stored energy, is described in References 5, 6, and 7. Discussion of uncertainties associated with the performance model, and of comparative analytical and experimental results, is included in References 5, 6, and 7.

Parameters such as cold pellet and clad diameters, gas pressure and composition, burnup, and void volumes are calculated and used as the initial conditions subsequent calculations of stored energy during the operation of the emergency core cooling system (ECCS) analyses. The coupling mechanism between the FATES and ECCS calculations is described in Reference 17.

4.2.1.3.2 Mechanical Design Limits

4.2.1.3.2.1 Cladding Collapse

The time required for the radial buckling of the cladding in any fuel rod must exceed the reactor operating time for the appropriate batch to accumulate its design average discharge burnup. This criterion must be satisfied for the continuous reactor operation at any reasonable power level and during normal operation and AOOs. It will be considered satisfied if it can be demonstrated that axial gaps longer than 0.125 inch will not occur

between fuel pellets and the plenum spring radial support capacity is sufficient to prevent clad collapse under all design conditions.

4.2.1.3.2.2 Rod Internal Pressure

The fuel rod internal pressure is limited by the following three rod internal pressure design limits:

a. The fuel rod internal hot gas pressure shall not exceed the critical maximum pressure determined to cause an outward clad creep rate that is in excess of the fuel radial growth rate anywhere locally along the entire active length of the fuel rod.

b. Fuel rod internal pressure shall not exceed the pressure to cause the reorientation of the hydride in the radial direction in the cladding

c. The radiological dose consequences of DNB failure shall remain within the specified limits.

4.2.1.4 Grid

4.2.1.4.1 Material Properties

The function of the grids is to provide lateral support to fuel and burnable absorber rods in a manner that the axial forces are not sufficient to bow the rods and the wear at the grid-to-clad contact points is limited to acceptable amounts. The grids maintain their structural integrity under the loads imposed during shipping and handling and postulated seismic and LOCA events.

The top, bottom, and protective grids are made of nickel-chromium-iron alloy 718 (Inconel 718), and the mid-grids are made of ZIRLO. Inconel 718 is a strong material with good ductility, corrosion resistance, and stability under irradiation at high temperatures. ZIRLO has a low neutron absorption cross section and high corrosion resistance to the reactor water environment.

4.2.1.4.2 Vibration and Fatigue

The grids support fuel rods to minimize fuel rod fretting wear from flow-induced vibration during normal operation. The fuel rod fretting wear limit is described in Subsection 4.2.1.1.3.

4.2.1.4.3 Chemical Compatibility with Other Core Components, including Coolant

ZIRLO is used in the mid-grid and also in the fuel rods and guide thimble tubes with which the mid-grid is in contact, thereby preventing chemical incompatibility of these components.

The Inconel 718 that is used in the top, bottom, and protective grids is in contact with the Type 304 stainless steel bottom nozzle, ZIRLO fuel and burnable absorber rods, and ZIRLO guide thimble tubes. The chemical compatibility of these materials in a reactor environment has been verified by operating experience.

In addition, the compatibility of ZIRLO and Inconel 718 with the reactor coolant has been verified by operating experience.

4.2.1.5 Fuel Assembly

The fuel assemblies meet the design criteria for non-operational, normal operational, AOO, and postulated accident loads. The thermal-hydraulic design is described in Section 4.4.

4.2.1.5.1 Non-operational Load

Loads correspond to the maximum possible axial and lateral loads and accelerations imposed on the fuel assembly during shipping and handling, assuming there is no abnormal contact between the fuel assembly and any surface or any equipment malfunction. Additional information on shipping and handling loads is provided in Subsection 4.2.3.5.1. The stresses in the fuel assembly components are less than the acceptance stress limits under non-operational loads. The stress limits and strength theory presented in ASME Section III are used as a guide.

4.2.1.5.2 Normal Operational and Anticipated Operational Occurrence Loads

Normal operation and AOO stress limits for fuel assembly structural components are listed below. Stress nomenclature follows ASME Section III.

a. General primary membrane stress intensity limit: S_m

b. Primary membrane plus bending stress intensity: 1.5 S_m

Where:

S_m = design stress intensity values

Fuel assembly structural components use austenitic steels and zirconium alloys.

The design stress intensity (S_m) for austenitic steel is defined as the lowest of the following unirradiated values:

a. One-third of the specified minimum tensile strength (S_u) at room temperature

b. One-third of the tensile strength at temperature

c. Two-thirds of the specified minimum yield strength (S_y) at room temperature

d. Ninety percent of the yield strength at temperature

For the zirconium alloy, the design stress intensity on the unirradiated yield strength is conservative.

The design stress intensity of zirconium alloy is defined as follows:

a. Two-thirds of the minimum yield strength at temperature

4.2.1.5.3 Postulated Accident Loads

Worst-case abnormal loads during postulated accidents are represented by seismic and LOCA loads. For these conditions, the reactor is able to be brought to a safe shutdown condition, and the core is kept subcritical with the acceptable heat transfer geometry. This requirement is met by demonstrating that, under the most severe anticipated loading of fuel assemblies for postulated accidents, no damage to the fuel assembly structure is severe enough to prevent a coolable geometry from being maintained or to preclude CEA insertion.

The fuel assembly structural component stresses under faulted conditions are evaluated using primarily the methods in Appendix F of ASME Section III. The faulted condition stress limits for fuel assembly structural components are:

a. General primary membrane stress intensity limit: S_m'

b. Primary membrane plus bending stress intensity: 1.5 S_m'

Where:

S_m' = smaller value of 2.4 S_m or 0.7 S_u

4.2.1.6 In-Core Control Components

4.2.1.6.1 Control Element Assembly

The mechanical design of the control element assemblies is based on compliance with the functional requirements, as follows:

a. CEAs provide short-term reactivity control under all normal and adverse conditions experienced during reactor startup, operation, shutdown, and accidents.

b. Mechanical clearances of the CEAs within the fuel and reactor internals are such that the requirements for CEA positioning and a reactor trip are attained under the most adverse accumulation of tolerances.

c. Structural material characteristics prevent radiation-induced changes to the CEA materials from impairing the functions of the reactivity control system.

4.2.1.6.1.1 Thermal-Physical Properties of Absorber Material

The absorber material used for the full-strength control rods is boron carbide (B_4C). Inconel 625 is used as the absorber material for the part-strength control rods. See Figures 4.2-3, 4.2-4, and 4.2-5 for the application and orientation of the absorber materials. The related dimensions and thermal-physical properties of absorber material are provided in Table 4.2-1.

4.2.1.6.1.2 Compatibility of Absorber and Cladding Materials

The cladding material used for the control elements is Inconel 625. The selection of this material for use as cladding is based on considerations of strength, creep resistance, corrosion resistance, and dimensional stability under irradiation and on the acceptable performance of this material for the application in reactors currently in operation.

a. B_4C/Inconel 625 Compatibility

Because Inconel 625 is more resistant to carbide formation than Type 316 stainless steel and the expected pellet/clad interfacial temperature in the standard design is below 427 °C, it is concluded that B_4C is compatible with Inconel 625.

4.2.1.6.1.3 Cladding Stress-Strain Limits

The stress limits for the Inconel 625 cladding are as follows:

a. Nonoperation, normal operation, and AOOs:

1) $P_m \leq S_m$

2) $P_m + P_b \leq 1.5\ S_m$

The net unrecoverable circumferential strain does not exceed 1 percent of the cladding diameter, considering the effects of pellet swelling and cladding creep.

b. Postulated accidents:

1) $P_m \leq S_m'$

2) $P_m + P_b \leq 1.5\ S_m'$

Where:

S_m' = smaller value of 2.4 S_m or 0.7 S_u

For the Inconel 625 CEA cladding, the value of S_m is two-thirds of the minimum specified yield strength at temperature.

4.2.1.6.1.4 Irradiation Behavior of Absorber Materials

a. Boron carbide

1) Swelling

The swelling of B_4C increases linearly with burnup according to the following relationship:

$$\%\Delta L = (0.1)^{10}\ \text{B Burnup, at \%}$$

This relationship was obtained from experimental irradiations of pellets with densities between 71 and 98 percent theoretical density and high-density (equal to or greater than 90 percent theoretical density) wafers (Reference 18). Dimensional changes were measured as a function of burnup after irradiation at the temperatures expected in the design.

2) Thermal conductivity

The thermal conductivity of unirradiated 73 percent dense B_4C decreases linearly with temperatures from 149 °C to 871 °C, according to the relationship:

$$\lambda = \frac{1 \text{ cal/sec-cm-K}}{2.17\ (6.87\ +\ 0.017T)}$$

Where:

T = temperature, K

This relationship was obtained from measurements performed on pellets ranging from 70 to 98 percent theoretical density (Reference 19).

The following relationship between the thermal conductivity of irradiated 73 percent theoretical density B_4C pellets and temperature was derived from measured values (Reference 19) on higher density pellets irradiated to fluences up to 3×10^{22} nvt (E > 1 MeV):

$$\lambda = \frac{1 \text{ cal/sec-cm-K}}{2.17\ (38\ +\ 0.025T)}$$

Where:

T = temperature, K

3) Helium release

The fraction of helium released from the pellets is important for determining rod internal gas pressure. The relationship between the helium release and irradiation temperature given below was developed at Oak Ridge National Laboratory (ORNL) to fit experimental data obtained from thermal reactor irradiations (Reference 20):

$$\% \text{ He release} = e^{(C-1.85D)}\ e^{-Q/RT}$$

Where,

C = constant, 6.69 for pellets

D = fractional density, 0.73
Q = activation energy content, 3,600 cal/mole
R = gas constant, 1.98 cal/mole-K
T = pellet temperature, K

This expression becomes:

$$\% \text{ He release} = 208\, e^{(-1820/T)} + 5$$

when the preceding parameters are substituted. In this form, design values for helium release as a function of temperature are generated. The 5 percent helium release allowance (the last term in the expression) was added to provide reasonable assurance that design values are above all reported helium release data. Calculated values of helium release obtained from the recommended design expression are above all experimental data points (References 21 and 22) obtained on B_4C pellet specimens irradiated in thermal reactors.

4) Pellet porosity

Irradiation-induced swelling does not change the characteristics of the porosity, but only changes the bulk volume of the specimens. Therefore, the amount of open porosity available at end of life (EOL) is the same as that present at BOL.

b. Inconel 625

1) Swelling

Direct measurements made after exposure of Inconel 625 to a fluence 5×10^{22} nvt (E > 0.1 MeV) at liquid metal fast breeder reactor (LMFBR) conditions showed no evidence of swelling (Reference 23). Further exposure to 6×10^{22} nvt (E > 0.1 MeV) at 500 °C showed essentially no swelling as measured by immersion density but showed small cavities. Thus, Inconel 625 is not expected to swell below a fluence of 3×10^{22} nvt (E > 1 MeV).

2) Ductility

The ductility of Inconel 625 decreases after irradiation. Extrapolation of lower fluence data on Inconel 625 and 500 indicates that the values of uniform and total elongation of Inconel 625 after 1×10^{22} nvt (E > 1 MeV) are 3 and 6 percent, respectively.

3) Strength

The value of yield strength for Inconel 625 increases after irradiation in the manner typical of metals. However, no credit is taken for increases in yield strength in the design analyses above the initially specified value.

4.2.1.6.2 Neutron Source Assembly

The design bases for the primary/secondary neutron sources and neutron sources assembly (NSA) are set with the consideration of irradiation and material behavior and are as follows:

a. The temperatures of the primary and secondary sources during usage do not affect their integrity.

b. The cladding is compatible with the sources and does not undergo any failure that would affect the integrity of the cladding.

c. Cladding stresses during usage meet stress intensity limits in ASME Section III.

d. No failure of cladding is allowed. In case of cladding failure, no reaction between the coolant and the sources with their fission products would occur.

4.2.1.7 Surveillance Program

Subsection 4.2.4.7 describes the results of the surveillance program for the fuel assemblies. The surveillance program includes poolside examination and hot cell examinations. The poolside examinations include visual inspection for overall performance, dimensional

measurements such as fuel assembly growth, bowing, shoulder gap, etc., and cladding oxide measurements.

4.2.2 Description and Design Drawings

This subsection summarizes the mechanical design characteristics of the fuel system and describes the design parameters for the performance of the reactor. A summary of mechanical design parameters is presented in Table 4.2-1. These data are intended to be representative of the design. Limiting values of these and other parameters are provided in the relevant sections.

4.2.2.1 Fuel Rod

The fuel rods consist of slightly enriched UO_2 cylindrical ceramic pellets and a round wire type 302 stainless steel compression spring that are all encapsulated in a ZIRLO tube seal welded with Zircaloy-4 end plugs. The fuel rods are internally pressurized with helium during assembly. Figures 4.2-6 and 4.2-7 depict the fuel rod design.

Each fuel rod assembly has a serial number and a visual identification mark. The serial number can be used to trace the fabrication history of each fuel rod component. The identification mark indicates a visual check of the pellet enrichment batch during fuel assembly fabrication.

The fuel cladding is cold-worked and stress-relief-annealed ZIRLO tubing with a wall thickness of no less than 0.5715 mm. The actual tube forming process consists of a series of cold working and annealing operations, the details of which are selected to provide the combination of properties described in Subsection 4.2.1.1.

The UO_2 pellets are dished at both ends to accommodate thermal expansion and fuel swelling. The nominal density of the UO_2 in the pellets is 10.44 g/cm^3, which corresponds to 95.25 percent of the 10.96 g/cm^3 theoretical density of UO_2. However, because the pellet dishes and chamfers constitute about 1.2 percent of the volume of the pellet stack, the average density of the pellet stack is reduced to 10.313 g/cm^3. This number is referred to as the stack density.

The compression spring at the top of the fuel pellet column maintains the column in its proper position during handling and shipping. The fuel rod plenum, which is located above the pellet column, provides space for axial thermal differential expansion of the fuel column and accommodates the initial helium loading and evolved fission gases. The manner in which these factors are taken into account, including the calculation of temperatures for the gas contained within the various types of rod internal void volume, is described in References 5, 6, and 7.

4.2.2.2 Burnable Absorber Rod

The burnable neutron absorber rods are included in selected fuel assemblies to reduce the moderator temperature coefficient at beginning of cycle (BOC). They replace fuel rods at selected locations. The burnable absorber rod, shown in Figure 4.2-7, is mechanically similar to fuel rods but consists of Gd_2O_3 admixed in enriched UO_2 in the central rod portion (axially) and enriched UO_2 at the top and bottom. The total column length is the same as the column length of fuel rods.

Each burnable absorber rod assembly includes a serial number and visual identification mark. The serial number is used to record fabrication information for each component in the rod assembly. The identification mark is unique to absorber rods and provides a visual check on the pellet poison content during fuel bundle fabrication.

4.2.2.3 Fuel Assembly

The fuel assembly (Figure 4.2-1) consists of 236 fuel rods and burnable absorber rods, 4 guide thimbles, 1 instrument tube, 12 grids, 1 top nozzle, and 1 bottom nozzle. The guide thimbles, grids, top nozzle, and bottom nozzle form the structural frame of the assembly.

4.2.2.3.1 Bottom Nozzle

The bottom nozzle consists of an adapter plate with flow holes, a support leg at each corner (total of four legs), four skirt plates, and a cylindrical instrument guide. The adapter plate filters foreign materials with an Inconel protective grid. The support legs align the lower end of the fuel assembly with the alignment pins in the core support structure. Each alignment pin positions the corners of the four bottom nozzles.

4.2.2.3.2 Top Nozzle

The top nozzle is composed of an adapter plate, four outer guide posts, a holddown plate, four helical holddown springs, and instrument housing. The top nozzle is attached to the guide thimble using inner extension inserted into outer guide post. The top nozzle serves as an alignment and locating device for each fuel assembly and has features to permit lifting of the fuel assembly. The fuel assembly identification number is engraved on the holddown plate to prevent improper orientation or location in the core.

The lower plate of the top nozzle, called the adapter plate, located at the top ends of the guide thimble, is designed to prevent excessive axial motion of the fuel rods. The upper plate of the top nozzle, called the holddown plate, together with the helical holddown springs, comprise the holddown device. The holddown plate is movable, acts on the underside of the extended tubes of the upper guide structure, and is loaded by the holddown springs. Since the springs are located at the upper end of the assembly, the spring load combines with the fuel assembly weight to counteract upward hydraulic forces. The instrument housing is attached at the center of the adapter plate by a threaded joint, and it accommodates and protects the in-core instrumentation.

The top nozzle parts except springs are made of type 304 stainless steel. The helical holddown springs are made of Inconel 718 because of its previous use for springs and good resistance to relaxation during operation.

4.2.2.3.3 Guide Thimble and Instrument Tube

The upper portion of the guide thimble tube is welded to the internally threaded flange, which is attached to the top nozzle by an externally threaded inner extension inserted into the outer guide post (Figure 4.2-8). The upper head of inner extension is crimped at the upper portion of the outer guide post to prevent untorquing.

The internally threaded end plug is welded to the lower end of the guide thimble tube and the guide thimble screw is inserted into the end plug through the adapter plate of the bottom nozzle to connect the guide thimble to the bottom nozzle (Figure 4.2-9). The guide thimble screws are locked in place by expanding a thin-walled section of the guide thimble screw cap into a cutout in the underside of the adapter plate of the bottom nozzle.

The lower portions of the four-guide thimble tubes are tapered gradually to form a region of reduced diameter to lessen CEA deceleration loads at the end of a trip stroke.

The instrument tube is inserted into sockets in the top and bottom nozzles, respectively, and is retained laterally by the relatively small clearance at these locations. The top nozzle socket is created by the instrument housing, which is threaded into the adapter plate and tack welded in four places. There is no positive axial connection between the instrument tube and the top and bottom nozzles. The 40 dimples formed axially along the instrument tube support the in-core instrumentation laterally when it is inserted into the instrument tube.

4.2.2.3.4 Grid

The 12 grids consist of nine ZIRLO mid-grids, one Inconel top grid, one Inconel bottom grid, and one Inconel protective grid as shown in Figure 4.2-1. The nine mid-grids (Figure 4.2-10), one top grid and one bottom grid (Figure 4.2-11), and one protective grid (Figure 4.2-12) maintain the fuel rod array by providing positive lateral restraint to the fuel rod but only friction restraint to axial fuel rod motion. The grids, fabricated from preformed ZIRLO or Inconel straps, are interlocked in an eggcrate fashion and welded together.

Each cell of the mid-grid contains two conformal springs and four conformal dimples. The mid-grids have a mixing vane to improve the thermal performance by enhancing coolant mixing.

Top and bottom grids consist of two springs and four dimples. The top grid is designed to have reduced spring force to minimize the potential for fuel rod bow, whereas the bottom grid has a high spring force that is capable of providing fuel rod support up to the design burnup.

The protective grid contains four dimples that provide a coplanar four-point contact with the fuel rod in each grid cell. With the small-holed nozzle and fuel rod solid end plug, the protective grid is designed to trap and filter foreign materials.

The grid outer strap is designed to prevent grid hang-up of adjacent fuel assemblies during the reloading operation.

Using the mid-grid sleeve that is attached to mid-grid by welding, the mid-grids are welded to the guide thimble tubes and the instrument tube to fix their axial position in the fuel assembly. Top and bottom grids are fixed through the sleeves, which are welded to the guide thimble tube and the instrument tube.

4.2.2.4 In-Core Control Components

4.2.2.4.1 Control Element Assembly

Control element assemblies (CEAs) consist of either 4 or 12 neutron absorber elements arranged to engage the peripheral guide thimbles of fuel assemblies. The neutron absorber elements are connected by a spider structure that couples to the control element drive mechanism (CEDM) driveshaft extension. The neutron absorber elements of a four-element CEA engage the four guide thimbles in a single fuel assembly. The four-element CEAs are used for control of power distribution and core reactivity in the power operating range. The 12-element CEAs engage the four guide thimbles in a fuel assembly and the two nearest guide thimbles in adjacent fuel assemblies. The 12-element CEAs provide the core with strong shutdown rods. CEAs are shown in Figures 4.2-3, 4.2-4, and 4.2-5.

All control elements are sealed by welds that join the CEA cladding to an Inconel 625 nose cap at the bottom and an Inconel 625 connector at the top that makes up part of the end fitting. The end fittings are threaded and crimped in place by a locking nut to the spider structure that provides rigid lateral and axial support for the control elements. The spider hub bore is specially machined to provide a point of attachment for the CEA extension shaft.

The control elements of 4-element and 12-element full-strength CEAs consist of an Inconel 625 tube loaded with a stack of cylindrical absorber pellets. The absorber material consists of 73 percent theoretical density boron carbide (B_4C) pellets, with the exception of the lower portions of the elements, which contain reduced-diameter B_4C pellets wrapped in a sleeve of Type 347 stainless steel (felt metal).

During normal power operation, all of the 12-element CEAs are considered to be in the fully withdrawn position so the local B^{10} burnup progresses at a lower rate and CEA life is prolonged. A plenum above the absorber column provides expansion volume for helium released from the B_4C. The plenum volume contains a Type 302 stainless steel holddown spring that restrains the absorber material against longitudinal shifting with respect to the

clad while allowing for differential expansion between the absorber and the clad. The spring develops a load that is sufficient to maintain the position of the absorber material during shipping and handling.

The control elements of a four-element part-strength CEA consist of an Inconel 625 tube loaded with Inconel 625 bars over the full active length. Part-strength CEAs, which have lower worth compared to full-strength CEAs, are provided for reactivity and axial power shape control during power operations, including load maneuvering. Because of the use of the Inconel 625 absorber, the cladding dimensional stability is not degraded with long-term exposure of the part-strength CEA to reactor operating conditions.

Full- and part-strength CEAs are positioned by a magnetic jack CEDM mounted on the reactor vessel closure head. The extension shaft joins with the CEA spider and connects the CEA to the CEDM. Full- and part-strength CEAs may be connected to any extension shaft depending on control requirements. Mechanical reactivity control is achieved by positioning groups of CEAs by the CEDMs.

4.2.2.4.2 Neutron Source Assembly

As shown in Figure 4.2-13, the primary source and secondary source are enclosed in NSA cladding. Material for the primary neutron source is Cf-252, and material for the secondary neutron source is antimony and beryllium mixed with volume ratio of 50 percent each.

The function of the two neutron sources is to provide a base neutron flux level so that the neutron flux level can be monitored, as required, during fuel loading, refueling, and shutdown conditions.

4.2.3 Design Evaluation

Design evaluations of the fuel rod, fuel assembly, and in-core control components are described in this subsection. The fuel rod design considers all events expected during normal operation and AOOs; the fuel assembly design during shipping and handling, normal operation, AOOs, and postulated accidents; and the in-core control components design during normal operation, AOOs, and postulated accidents.

The AOO events and postulated accident events such as reactivity initiated accident (RIA) events, loss of coolant accident (LOCA) events and anticipated transients without scram (ATWS) are evaluated in Chapter 15.

Fuel rod designs are performed to confirm the fuel rod integrity for the events expected during normal operation and AOOs. The evaluations are carried out for the limiting conditions. Limiting conditions are defined as those subsets of conditions, such as rod geometry, power history, and thermal-hydraulic parameters, that yield the minimum margin to each of the design criterion. No single subset of limiting conditions will be limiting condition for all design criteria. A conception of composite fuel rod and composite power history for subsets of fuel rods are used for limiting rod power history. For convenience, all rods in the core can be included in a single subset. Thus, evaluation is performed using the most limiting fuel rod fabrication parameters and appropriate linear heat rate over time for the subset being considered up to the rod design burnup of *[60,000 MWD/MTU]** for the APR1400.

4.2.3.1 Cladding

4.2.3.1.1 Vibration Analysis

The mid-grid has mixing vanes that are arranged to provide hydraulic balance to prevent fluid-induced fuel assembly vibration. The conformal spring and dimple of the mid-grid support the fuel rod with increased support area to decrease fuel rod fretting wear.

The grid-to-rod fretting wear resistance performance was verified by the following hydraulic flow tests:

a. Fluid-induced fuel assembly vibration test

b. 500-hour long-term wear resistance test

Based on the fluid-induced fuel assembly vibration test, fuel assembly vibration was small over the range of flow rates of the plants.

The 500-hour long-term wear resistance test results showed that the fuel assembly did not generate a fretting wear-induced fuel failure for the fuel lifetime. In addition, fuel rod fretting wear performance of the fuel assembly was verified by conclusive operating experience without any fuel rod fretting wear failure (*[Reference 1]**).

4.2.3.1.2 Fuel Rod Internal Pressure

The first part of the criteria precludes the outward clad creep rate from exceeding the fuel solid swelling rate, and therefore provides reasonable assurance that the fuel-clad diametral gap will not reopen following contact or increase in size during steady-state operation. The PLUS7 fuel rod with upper plenum has enough free volume to accommodate the fission gas release. The internal pressure of the limiting rod is below the lift-off pressure (*[Reference 1]**).

The increase in fuel rod internal pressure to values above the reactor coolant system pressure allowed by the maximum pressure criterion raises concern about the potential for degraded fuel rod DNB propagation due to clad ballooning and channel flow starvation. Conservative DNB design makes it unlikely that DNB will occur anywhere in the core during normal operation, that is, during steady state and during all anticipated operational occurrences. Therefore, DNB-induced clad ballooning will not occur during normal operation. Furthermore, evaluations of clad strain rate equations, which model conditions where clad temperature and stresses are consistent with both DNB and high-pressure loads, indicate that clad strain was expected to be relatively small compared to the spacing between rods because the duration of the postulated DNB transients is typically relatively short (References 2 and 24).

Some of the hydrides from fabrication and in-reactor formation are returned to solution in the Zircaloy matrix at operating temperatures in the reactor, but re-precipitate when the plant returns to cold shutdown. It has been demonstrated that these hydrides precipitate in the circumferential direction as long as compressive cladding stresses are maintained, but precipitate in the undesirable radial direction if cladding tensile stresses are maintained above a given stress range during cooldown.

The maximum cladding tensile hoop stress resulting from the rod internal pressure considered in DNB propagation evaluation was found to be less than that required to initiate hydride reorientation in the radial direction (Reference 2 and 24).

4.2.3.1.3 Cladding Stresses

The fuel rod mechanical design analyses are performed to determine the stresses in cladding for applicable design conditions. The following describe the method and results of fuel rod stress analysis.

a. Stress associated with normal operation

Internal pressure calculations are used to establish the maximum and minimum for normal operation that can occur during fuel lifetime. A range in external pressure is determined based on normal operation. The resulting differential pressures for the various situations are used in standard formulas for primary stress, along with worst-case clad end-plug dimensions. The calculated stresses are then compared to stress limits for normal operation. Bending and axial stresses are calculated for fuel handling, shipping, and reconstitution, and are compared to allowable limits.

b. Stress associated with AOOs

Fuel rod internal and differential pressures and primary cladding stresses are calculated under AOOs. The conditions at the start of each transient analysis represent normal operation prior to the transient.

The results of the analysis indicate that the primary tensile and compressive stresses in the cladding during normal operation and AOOs are within the allowable limits (*[Reference 1]**).

4.2.3.1.4 Potential for Chemical Reaction

a. Corrosion

Oxide thickness of fuel cladding is affected by design parameters such as cycle length, local heat flux, coolant temperature, and coolant chemistry. The evaluation results, with the aid of a corrosion evaluation model, show that the design limit for cladding corrosion is satisfied up to a rod average burnup of *[60,000 MWD/MTU]* ([Reference 1]*).*

b. External hydriding

During operation of the reactor, cladding reacts to form a protective oxide film in accordance with the following equation:

$Zr + 2H_2O \rightarrow ZrO_2 + 2H_2$

The evaluated hydrogen content absorbed in the cladding is less than the design limit to maintain cladding integrity (*[Reference 1]**).

c. Internal hydriding

A number of reported fuel rod failures have resulted from excessive moisture available in the fuel. Under operation, this moisture oxidizes the cladding. A fraction of the hydrogen that is generated during normal oxidation would be absorbed into the cladding. This localized hydrogen absorption by the cladding would result in localized fuel rod failure.

Work performed at the Organization for Economic Cooperation and Development (OECD) reactor project in Halden, Norway, demonstrated that a threshold value of water moisture is required for hydride sunbursts to occur (Reference 25). Through a series of in-pile experiments, the level of this threshold value was established. The allowable hydrogen limit in the fuel complies with this requirement, providing reasonable assurance that hydride sunbursts will not occur.

It was found that the moisture levels absorbed in fuel pellet during the fabrication have been shown to be insufficient for primary hydride formation because the moisture levels of fuel pellets during fuel pellet fabrication are tightly controlled.

d. Crud layers on zirconium oxide films are usually porous and non-insulating. With porous crud, water is free to flow through the crud and provide heat transfer by convection. Under these conditions, crud-enhanced corrosion should not occur. Coolant chemistry parameters have been specified that minimize corrosion product release rates and their mobility in the primary system. Specifically, the pre-core hot functional environment is pH and oxygen controlled to provide a thin, tenacious, adherent, protective oxide film. This approach minimizes corrosion

product release and associated inventory on initial startup and subsequent operation. During operation, the recommended lithium concentration range (0.2 – 3.5 ppm) effects a chemical potential gradient or driving force between hotter and cooler surfaces (fuel cladding and steam generator tubing, respectively) in such a way that soluble iron and nickel species preferentially deposit on the steam generator surfaces. The associated pH also minimizes general corrosion product release rates from primary system surfaces. During operation, lithium, dissolved oxygen, and dissolved hydrogen are monitored at a frequency consistent with maintaining these parameters within their specifications. Post-operational examinations of fuel cladding that has operated within these specifications have shown no significant crud buildup.

e. Fuel-cladding chemical reaction

Fuel-cladding chemical reactions were investigated in an in-depth post-irradiation study (Reference 26). The study concluded that early unpressured elements containing unstable fuel are more susceptible to stress corrosion cracking than are the design, which uses stable fuel and pressurized cladding. Through the program conducted at Halden in Norway, at Petten in the Netherlands, and at Studsvik in Sweden, it was confirmed that the PLUS7 fuel designs are susceptible to stress corrosion cracking during normal plant operation.

Since stress corrosion cracking is the result of a combination of stresses imposed by the fuel on the cladding and the corrosive chemical species available to the cladding, irradiation programs have been conducted to define the conditions under which pellet-clad interaction damages the cladding. Through the program conducted at Halden in Norway, at Petten in the Netherlands, and at Studsvik in Sweden, it was confirmed that the PLUS7 fuel designs are not susceptible to failure by stress corrosion cracking during normal plant operation.

4.2.3.1.5 Fretting Wear

Because irradiation-induced stress relaxation causes a reduction in grid spring load, grids are designed for EOL conditions as well as BOL conditions to prevent fretting caused by flow-induced vibrations. The fretting wear evaluation is described in Subsection 4.2.3.1.1.

4.2.3.1.6 Cladding Fatigue and Strain

The fatigue damage factor is calculated under daily power cycling. The calculation accounts for power-dependent and time-dependent phenomena by using rod internal pressure, cladding diameter, and pellet diameter change models. The cladding is assumed to conform to the predicted diameter of the pellet during periods of contact. Conservative assumptions are used to select the starting dimensions and properties of the fuel rod chosen for analysis.

For the initial design analyses, daily power cycling between 10 percent and 100 percent power is assumed throughout the life of the plant. The conservative number of reactor heatups/cooldowns and trips are also represented. The method for fatigue analysis results in a series of cladding strain range values covering the fuel lifetime. The cumulative fatigue usage factor is determined by summing the ratios of the number of cycles in a given strain range to the permitted number in that range. The permitted number of cycles in any strain range is based on the O'Donnell and Langer design curve and considers a safety factor of 2 on the stress amplitude or a safety factor of 20 on the number of cycles.

At normal operation, the strain is calculated at end of life. The strain in AOOs is also calculated. The sum of the strains resulting from normal operation and from any single AOO is then compared to the allowable limit. The analysis has been completed, and the results meet the fatigue and strain criteria (*[Reference 1]*[*]).

4.2.3.1.7 Material Wastage Attributable to Mass Transfer

As described in Subsection 4.2.3.1.4, the oxidation and crud buildup on cladding are limited because of the tight coolant water chemistry control and use of ZIRLO cladding. Therefore, the material waste from mass transfer is not significant.

4.2.3.1.8 Fuel Rod Bowing

The phenomenon of fuel rod bowing is observed in irradiated fuel assemblies. Significant fuel rod bowing may cause an adverse effect on thermal-hydraulic characteristics such as the departure from nucleate boiling ratio (DNBR).

The top grid spring restraint force on the fuel rods in the fuel assembly is designed to reduce the fuel rod bowing and the consequent DNBR penalty to an acceptable level. The maximum channel closure for fuel rods is less than the DNBR penalty limit at the EOL. Additionally, the rod-to-rod spacing on all four faces of each fuel assembly were measured during the poolside examinations of the irradiated PLUS7 assemblies, and the measurements were all less than the DNBR penalty limit (*[Reference 1]**).

4.2.3.1.9 Consequences of Power Coolant Mismatch

The consequences of power coolant mismatch (DNB) are addressed in Chapter 15.

4.2.3.1.10 Irradiation Stability of the Cladding

The combined effects of fast flux and cladding temperature are considered in fuel rod design in three ways as follows:

a. Cladding creep rate

   The in-pile creep performance of cladding is dependent upon both the local material temperature and the local fast neutron flux. The functional form of the dependencies is presented in Reference 2.

b. Cladding mechanical properties

   The yield strength, ultimate strength, and ductility of cladding are dependent upon temperature and accumulated fast neutron fluence. Unirradiated properties were used depending upon which is more restrictive for the phenomenon evaluated.

c. Irradiation-induced dimensional changes

   Fuel cladding has been shown to sustain dimensional changes (in the unstressed condition) as a function of the accumulated fast fluence. The irradiation-induced growth correlation method is described in References 2 and 3.

4.2.3.1.11 Creep Collapse and Creepdown

The PLUS7 fuel design uses high-density fuel pellets of more than 95 percent theoretical density (T.D), which are stable with respect to fuel densification. In addition, the fuel rods are initially pressurized with helium. The combination of stable fuel and pre-pressurized fuel rods has been quite effective in eliminating the formation of axial gaps in the fuel column due to densification, and in avoiding cladding collapse.

On the basis of the operating experience of PLUS7 fuel, cladding collapse does not occur for fuel rods with initial fuel pellet density of 95 percent T.D or greater and having initial fuel rod pressurization with helium. Maintaining current pellet fabrication process controls with initial pellet density of 95 percent T.D or greater and with current initial helium pressurization levels is therefore sufficient to prevent cladding collapse. Cladding collapse analyses, if required, would be performed using the models described in Reference 27.

4.2.3.2 Fuel

4.2.3.2.1 Dimensional Stability

Fuel swelling due to irradiation (accumulation of solid and gaseous fission products) and thermal expansion results in an increase in the fuel pellet diameter. The fuel design accommodates both forms of pellet growth. The fuel-clad diametric gap is sufficient to accommodate the thermal expansion of the fuel. Thermal- and irradiation-induced creep of the restrained fuel results in a redistribution of fuel so that the swelling due to irradiation is accommodated by the free volume. The volume of the PLUS7 fuel rod is sufficient to accommodate fuel pellet swelling even under the most adverse burnup and tolerance conditions.

4.2.3.2.2 Potential for Waterlogging Rupture and Chemical Interaction

The potential for a waterlogging rupture is considered remote. The factors, or combination of factors, that are necessary to prevent a waterlogging rupture include a small opening in the cladding, time to permit filling of the fuel rod with water, and a rapid power transient. The size of the opening necessary to cause a problem falls within a fairly narrow band.

With defects that are above a certain size, the rod can fill rapidly, but during a power increase, the rod can also expel water or steam readily without a large pressure buildup. Defects that could result in an opening in the cladding are checked for during fuel rod manufacturing by both ultrasonic and helium leak testing. Clad defects that could develop during reactor operation as a result of hydriding are also controlled by limiting the factors that contribute to hydriding (e.g., hydrogen content of fuel pellets).

The most likely time for a waterlogging rupture incident is after an abnormally long shutdown period, but the startup rate is controlled so that even if a fuel rod is fills with coolant, it would "bake out," thus minimizing the possibility of additional cladding ruptures. The combination of control and inspection during the manufacturing process and the limits on the rate of power change restrict the potential for waterlogging rupture to a small number of fuel rods.

The UO_2 fuel pellets are highly resistant to attack by reactor coolant in the event that cladding defects occur. Extensive experimental work and operating experience have shown that conservative design parameters account for changes in thermal performance during operation and that coolant activity buildup resulting from cladding rupture is limited by the ability of UO_2 to retain solid and gaseous fission products.

4.2.3.2.3 Thermal Stability

Fuel melting does not occur during normal operation or AOOs. To preclude fuel melting, the peak local power attained in normal operation and AOOs can be limited to a maximum value that is sufficient to provide reasonable assurance that the fuel centerline temperatures remain below the melting temperature at all burnups. Design evaluations for normal operation and AOOs have shown that fuel melting will not occur for achievable local powers and licensed fuel rod burnup (*[Reference 1]**).

4.2.3.2.4 Irradiation Stability

The irradiation behaviors of the fuel, including fission product swelling and fission gas release, are described in References 5, 6, and 7. These irradiation behaviors are accounted for in evaluation of fuel rod performance.

4.2.3.3 Fuel Rod Performance

Fuel rod behavior during operation is predicted by a fuel rod analysis code in which the following phenomena are incorporated, in References 5, 6, and 7.

a. Radial power distribution

b. Fuel and cladding temperature distribution

c. Burnup distribution in the fuel

d. Thermal conductivity of the fuel and cladding

e. Densification of the fuel

f. Thermal expansion of the fuel and cladding

g. Fission gas production and release

h. Solid and gaseous fission product swelling

i. Fuel restructuring and relocation

j. Fuel and cladding dimensional change

k. Fuel-to-cladding heat transfer coefficient

l. Thermal conductivity of the gas mixture

m. Thermal conductivity in the Knudsen domain

n. Growth and creep of the cladding

o. Rod internal gas pressure and composition

p. Sorption of helium and other fill gases

q. Cladding-to-coolant heat transfer coefficient

4.2.3.3.1 Fuel-Cladding Mechanical Interaction

The gap between the fuel and cladding is initially sufficient to prevent hard contact between the two. However, during power operation, the fuel and cladding come into contact due to a gradual compressive creep of the cladding inward on the fuel pellets. Thermal- and irradiation-induced distortions that occur during the service life of a fuel rod lead to local cladding stresses and strains.

To preclude the pellet-cladding mechanical interaction, the following two general criteria are established.

a. The total (elastic plus plastic) strain shall not exceed 1 percent.

b. Fuel melting shall not occur.

The strain change and fuel centerline temperature are evaluated for the APR1400 fuel rod design and meet the design criteria.

4.2.3.3.2 Burnup Experience

Burnup experience of PLUS7 fuel is presented in *[Reference 1]**.

4.2.3.3.3 Fuel and Cladding Temperature

The fuel and cladding temperatures are calculated using the fuel rod performance code for normal operation and AOOs. The models of thermal conductivity and gap conductance used for predicting fuel and cladding temperatures are described in References 5, 6, and 7.

The evaluation of fuel temperature for overheating of the fuel pellet is described in Subsection 4.4.1.2, including the maximum linear heat generation rate. The evaluation of overheating of the cladding is described in Chapter 15.

4.2.3.3.4 Potential Effects of Temperature Transients

The potential for a fuel rod to become waterlogged during normal operation is addressed in Subsection 4.2.3.2.2. In the event that a fuel rod does become waterlogged at low or zero power, it is possible that a subsequent power increase could cause a buildup of hydrostatic pressure. However, it is unlikely that pressure would build up to a level that could cause cladding rupture because a fuel pin with the potential for rupture requires the combination of a very small defect together with a long period of operation at low or zero power.

It is therefore concluded that the effect of normal power transients on waterlogged fuel rods is not likely to result in cladding rupture and, even if rupture does occur, it will not produce the sort of postulated burst failures that expel fuel material or damage adjacent fuel rods or fuel assembly structural components.

4.2.3.3.5 Energy Release during Fuel Element Burnout

The reactor protective system provides fuel clad protection so that the probability of fuel element burnout during normal operation and anticipated operational occurrences is extremely low. Thus, the potential for fuel element burnout is restricted to faulted conditions. The LOCA is the limiting event since it results in the larger number of fuel rods exhibiting burnout; thus, the LOCA analysis, which is conservative in predicting fuel element burnout, provides an upper limit for evaluating the consequences of burnout. The LOCA analysis explicitly accounts for the additional heat release due to the chemical reaction between the fuel cladding and the coolant following fuel element burnout in evaluating the consequences of this accident. LOCA analysis results are provided in Subsection 15.6.5.

4.2.3.3.6 Energy Release and Pressure Pulse Effects

The evaluation of energy release and pressure pulse with a sudden increase in fuel enthalpy from a reactivity initiated accident below fuel melting is addressed in Section 15.4.

4.2.3.3.7 Fuel Rod Behavior Effects from Coolant Flow Blockage

An experimental and analytical program was conducted to determine the effects of fuel assembly coolant flow maldistribution during normal reactor operation. In the experimental phase, velocity and static pressure measurements were made in cold, flowing water in an oversized model of a Combustion Engineering (C-E) 14 × 14 fuel assembly to determine the three-dimensional flow distributions in the vicinity of several types of flow obstructions. The effects of the distributions on thermal behavior were evaluated as necessary with the use of a preliminary version of the TORC thermal and hydraulic code (Reference 28).

The issues that were investigated included:

a. Assembly inlet flow maldistribution caused by blockage of a core support plate flow hole. Evaluation of the flow recovery data indicated that even the complete blockage of a core support plate flow hole would not produce a W-3 DNBR of less than 1.0 even if the reactor is operating at a power level that is sufficient to produce a DNBR of 1.3 without the blockage.

b. Flow maldistribution within the assembly caused by complete blockage of one to nine channels. Flow distributions were measured at positions upstream and downstream of a blockage of one to nine channels. The influence of the blockage diminished rapidly in the upstream direction. Analysis of the data for a single channel blockage indicated that such a blockage would not block a W-3 DNBR of less than 1.0 downstream of the blockage even if the reactor is operating at a power level that is sufficient to produce a DNBR of 1.3 without the blockage.

The preceding results were obtained by flow testing an oversized model of a standard 14 × 14 fuel assembly. Because of the similarity in the design of the APR1400 16 × 16 assembly and the early 14x14 array, the test results constitute an adequate demonstration of the effects that flow blockage would have on the 16 × 16 assembly. The 16 × 16 assembly has been demonstrated to have a greater resistance to axial flow than the 14 × 14 array. Increasing flow resistance to produce a more rapid flow recovery (i.e., a more uniform flow) is analogous to the common use of flow-resistance devices to smooth non-uniform velocity profiles in ducts or process equipment.

4.2.3.4 Grid

Fuel assemblies are designed so that the combination of fuel rod rigidity, grid spacing, and grid preload do not result in significant fuel rod deformation under axial loads. Axial forces applied by the grids on the fuel rod will not result in a significant degree of fuel rod bow (*[Reference 1]**).

The capability of the grids to support the clad without excessive clad wear was verified by out-of-pile flow testing on the fuel assembly design and conclusive operating experience as described in Subsection 4.2.3.1.1.

The grid width measurement results of irradiated PLUS7 fuel assemblies show that there is no significant interference with adjacent fuel assemblies or core baffle plates due to the irradiation growth of the mid-grid (*[Reference 1]**).

For axial or lateral shipping loads, the grid springs have an initial preload that exceeds four times (axial) and six times (lateral) the fuel rod weight. Therefore, the grid springs have no additional deflection and the fuel rod is supported sufficiently without movement as a result of 4 g axial or 6 g lateral acceleration of the shipping container. In addition, the permanent deformation of the grid does not occur since the grid buckling strength is greater than the lateral load imposed during shipping and handling (*[Reference 1]**).

The grid materials are Inconel 718 and ZIRLO, which have a corrosion resistance to the reactor internal environment as described in the Subsection 4.2.1.4.1.

The capability of the grid to withstand the lateral loads produced during the postulated seismic and LOCA events was verified by the grid impact test, and comparing the test results with the analytical predictions of the seismic and LOCA loads (*[Reference 30]**). Grid loads resulting from a combined seismic and LOCA event do not cause unacceptable grid deformation as to preclude core cooling.

4.2.3.5 Fuel Assembly

4.2.3.5.1 Nonoperational Load

The fuel assembly is capable of sustaining the effect of 4 g axial and 6 g lateral without sustaining stress levels in excess of those allowed for normal operation.

Accelerometers are included with each shipment that indicates if loadings in excess of 4 g axial or 6 g lateral acceleration are sustained. A record of shipping loads in excess of 4 g axial or 6 g lateral acceleration indicates an unusual shipping occurrence, in which case the fuel assembly is inspected for damage prior to releasing it for use.

The axial shipping load path is through either top or bottom nozzle to the guide thimble. A 4 g axial load produces a compressive stress level in the guide thimble tubes of less than the stress limit that is allowed for normal operational conditions. The fuel assembly is prevented from buckling by being clamped at grid locations (*[Reference 1]**).

The fuel assembly has the capability of sustaining a 4 g axial load at the top nozzle by the refueling grapple (and resisted by an equal load at the bottom nozzle) without sustaining stress levels in excess of those allowed for normal operation. There is no severe force on the fuel assembly in the case of misaligned handling tools, since a low handling speed is required for the fuel assembly, and the fuel assembly handling crane is equipped with an interlock mechanism to prevent overloading to the fuel assembly.

4.2.3.5.2 Normal Operational and Anticipated Operational Occurrence Load

The main loads acting on the fuel assembly structural components, guide thimbles, and nozzles, are holddown force, their own weight, and hydraulic lift force. The fuel assembly is restrained from lifting off except during a pump overspeed transient. The stress level from resulting from a pump overspeed condition is significantly less than the design limits described in Subsection 4.2.1.5.

Fatigue in the guide thimbles caused by CEA drop is significantly less than the design limits because a CEA drop is considered unlikely during the fuel assembly lifetime.

Clearance between the fuel rods and top nozzle is provided so that irradiation growth of fuel rods does not result in rod-to-nozzle interference throughout the fuel assembly lifetime. Clearance between the top nozzle of the fuel assembly and the upper guide structure is provided so that zirconium alloy irradiation growth does not result in fuel assembly or core damage throughout the fuel assembly lifetime. The clearance measurement results of irradiated PLUS7 fuel assemblies show that there is no significant interference between the fuel rod and the top nozzle or between the top nozzle and the upper guide structure (*[Reference 1]**).

The capability of the fuel assembly to sustain the effects of flow-induced vibration without adverse effects has been demonstrated in the full-scale hot loop testing. These tests evaluated fretting and wear of components, fuel assembly uplift forces, and holddown performance. The details of PLUS7 hot loop testing are reported in *[Reference 1]**.

4.2.3.5.3 Postulated Accident Load

During safe shutdown earthquake (SSE) events, the fuel assembly is subjected to lateral and axial loads that cause the fuel assembly to deflect from its normal shape. In the event of a LOCA, rapid changes in pressure and flow will occur within the reactor vessel. The response of a fuel assembly to the mechanical loads produced by a seismic event coincident with a LOCA is considered acceptable if the fuel rods are maintained in a coolable array.

The structural integrity of the fuel assembly is evaluated analytically for the combined seismic and LOCA loads using the methodology in accordance with Reference 29. The analysis confirms that fuel assembly components are not deformed severely to interfere with CEA insertion and the allowable stresses described in Subsection 4.2.1.5 are not exceeded for major components of the fuel assembly even under the added conservatism provided by seismic and LOCA load combination (*[Reference 30]**). Dimensional stability and coolable geometry are maintained.

Fuel assembly characteristics, such as stiffness, frequency, and damping, are determined based on structural testing, and the results are used in seismic/LOCA evaluation.

4.2.3.6 In-Core Control Components

4.2.3.6.1 Control Element Assembly

The CEAs are designed for a 10-year lifetime based on estimates of neutron absorber burnup for each type of CEA, allowable plastic strain of Inconel 625 cladding, and internal pressure.

a. Internal pressure

Internal pressure in the control elements of full-strength CEAs containing B_4C pellets depends on the following parameters:

1) Initial fill gas pressure

2) Gas temperature

3) Volume of helium that is generated and released

4) Available volume including B_4C porosity

The results of the CEA analyses confirm that the design criteria in Subsection 4.2.1.6 regarding stress, strain, and strain fatigue are met.

b. Thermal stability of absorber materials

None of the materials selected for the control elements is susceptible to thermally induced phase changes in reactor operating conditions.

c. Irradiation stability of absorber materials

Accommodations for swelling of the absorbers are incorporated in the design of the control elements and include the following:

1) All B_4C pellets have rounded edges to promote sliding of the pellets in the cladding from differential thermal expansion and irradiation-enhanced swelling

2) Dimensionally stable Type 304 stainless steel spacers are located at the bottom of all absorber stacks adjacent to the nose cap to minimize strain at the weld joint

3) A compression sleeve containing reduced-diameter B_4C pellets is located in the bottom length of the absorber stacks in full-strength CEAs. The compression sleeve laterally positions the reduced-diameter B_4C pellets uniformly with respect to the clad and absorbs the differential thermal expansion and irradiation-induced swelling of the B_4C pellets, thereby limiting the amount of induced strain in the cladding

d. Potential for and consequences of CEA functional failure

The probability of a functional failure of the CEA within the design lifetime is considered to be small. This conclusion is based on the conservatism used in the design, the quality control procedures used during manufacturing, and the testing of similar full-size CEA/CEDM combinations under simulated reactor conditions for lengths of travel and numbers of trips greater than those expected to occur during the design lifetime. The consequences of CEA/CEDM functional failure are addressed in Chapter 15.

A postulated CEA failure mode is a cladding failure. In the event that an element is assumed to partially fill with water under low- or zero-power conditions, the possibility exists that when power is resumed, the path of the water to the outside could be blocked, and expansion of the entrapped water could cause the element to swell. The probability of a CEA functional failure is low because of the low probability of a cladding failure leading to a waterlogged rod.

Another possible consequence of failed cladding is the release of small quantities of CEA filler materials and of helium and lithium from the neutron-boron reactions. However, the amounts that would be released are too small to have a significant effect on coolant chemistry.

4.2.3.6.2 Neutron Source Assembly

The primary source material is Cf-252, and the secondary source material is Sb-Be. The temperature of these materials does not reach a level that would affect the integrity of the sources.

The probability of coolant penetration of the duplex cladding is low. Because of the low activity of the duplex cladding with the coolant, the integrity of the neutron sources is not affected by a cladding failure.

Cladding stresses during usage satisfy stress intensity limits of ASME Section III.

Because of the mechanical stability, chemical stability, and compatibility with neutron sources, stainless steel is used for the components of the neutron sources assembly.

4.2.4 Testing and Inspection Plan

The quality assurance program of KEPCO Nuclear Fuel (KEPCO NF) was developed to plan and monitor KEPCO NF's activities in the design and manufacture of nuclear fuel assemblies and the associated components. The program provides for control of all activities affecting quality, from design and development to procurement, materials handling, fabrication, testing and inspection, storage, and transportation. Inspection and testing are performed on both purchased and manufactured items to verify compliance with acceptance criteria according to the program. Acceptance criteria include the requirements in drawings, specifications, codes and standards, and contractual requirements that are approved by KEPCO NF's design organization. The program also provides training for personnel and a formal auditing program for activities that affect quality (Reference 31).

4.2.4.1 Fuel Assembly

A comprehensive quality control plan is established to provide reasonable assurance that dimensional requirements of the drawings are met. When a large number of measurements are required and inspecting all of the measurements is impracticable, the plan provides a high statistical confidence that the dimensions are within tolerance.

The basic quality assurance measures that are performed, in addition to dimensional inspections and material verifications, are described in the following subsections.

4.2.4.1.1 Weld Quality Assurance Measures

The welded joints used in the fuel assembly design are described in the following paragraphs. The type and function of each weld and weld testing (both destructive and nondestructive) are also described. Weld tests are performed to provide reasonable assurance of the structural integrity of the joints.

The guide thimble joints are made by butt welds between the tube and the threaded upper and the lower ends. The welds are full-penetration welds and do not violate the dimensional or corrosion resistance standards.

The joint between the top nozzle outer guide posts / instrument housing and adapter plate has a threaded connection that is prevented from unthreading by tack welding of the outer guide posts/instrument housing and adapter plate using gas tungsten arc welding. Each weld is inspected for compliance with a visual standard.

The mid-grid welds at the intersection of the perpendicular ZIRLO grid straps are laser welds. Each intersection is welded top and bottom, and each weld is inspected by comparison with a visual standard.

The top and bottom grid welds at the intersection of the perpendicular Inconel grid straps are braze welds and are inspected by comparison with a visual standard.

The protective grid welds at the intersection of perpendicular Inconel grid straps, as well as the protective grid and protective grid washer weld at the intersection, are laser welds and are inspected by comparison with a visual standard.

The grid sleeve and the guide thimble tube (both ZIRLO components) are welded at four points. Each weld is required to be free of cracks and burn-through, and each weld is inspected by comparison to a visual standard. In addition, sufficient testing of sample welds is required to establish acceptable corrosion resistance of the weld region. Each

guide thimble is inspected after welding to show that welding has not affected clearance for CEA motion.

The bottom nozzle consists of an adapter plate, four legs, four skirt plates, and an instrument guide. The four skirt plates are manufactured as one structure by a casting process with four legs of quarter-cylindrical cross-section. The instrument guide is fastened to the underside of the adapter plate center and tack welded, and each weld is inspected for compliance with a visual standard.

The inspection requirements and acceptance standards for each of the welds are established on the basis of providing reasonable assurance that the connections will perform their required functions.

4.2.4.1.2 Other Quality Assurance Measures

All guide thimbles are internally gauged, providing reasonable assurance of free passage of CEAs within the tubes, including the reduced-diameter buffer region.

The clamping status of inner extension tubes that link each post with guide thimbles is checked using a torque wrench.

Each completed fuel assembly is inspected for cleanliness, wrapped to preserve its cleanliness, and loaded in shipping containers that are later purged and filled with dry air.

4.2.4.2 Fuel Rod

4.2.4.2.1 Pellets

During the conversion of UF_6 to ceramic-grade uranium dioxide powder, UO_2 powder is divided into lots that are blended to form uniform isotopic, chemical, and physical characteristics. Samples are taken from each lot and analyzed to verify that the samples are within the UO_2 powder specification limits.

Pellets are divided into lots during fabrication, and all pellets in one lot are processed under the same conditions. Representative samples are obtained from each lot for product acceptance tests. The total hydrogen content of finished ground pellets is restricted.

The pellet diameter and perpendicularity values meet a 95/95 confidence level. All other pellet dimensions conform to the applicable drawing requirements. Density requirements of sintered pellets meet a 95/95 confidence level. Longitudinal sections of two sample pellets from each pellet lot are prepared for metallographic examination to provide reasonable assurance of conformance to microstructure requirements. Pellet surfaces are inspected for chips, cracks, and fissures in accordance with approved standards.

4.2.4.2.2 Cladding

Lots are formed of tubing produced from the same ingot, annealed in the same final vacuum annealing charge, and fabricated using the same procedures. Samples randomly selected from each lot of finished tubing or ingot are chemically analyzed to provide reasonable assurance of conformance to specified chemical requirements and to verify tensile properties, hydride orientation, and metallographic tests. Each finished tube is ultrasonically tested over its entire length for internal soundness and dimensions; visually inspected for cleanliness and the absence of acid stains, surface defects, and deformation; and inspected for inside dimensions and wall thickness.

The following is a summary of the test items:

a. Chemical analysis

   Ingot analysis is performed for the top, middle, and bottom of each ingot. The finished product is tested for hydrogen, nitrogen, and oxygen per ASTM E146.

b. Tensile test at room temperature (ASTM E8)

c. Corrosion resistance test (ASTM G2)

d. Grain size (ASTM E112)

e. Surface roughness

f. Visual examination

g. Ultrasonic test

h. Wall thickness

i. Straightness

j. Inside diameter

4.2.4.2.3 Pellet Stack and Helium Gas Charging

Pellets pass visual standards immediately prior to loading. Cleanliness and dryness of all internal fuel rod components are maintained during the loading process until the final end-plug weld is completed. The loading and handling pellets are carefully controlled to minimize chipping.

4.2.4.2.4 Fuel Rod Weld

The fuel rod end plug to fuel rod cladding tube welds are butt welds between the ZIRLO cladding tube and the Zircaloy-4 end plug machined from bar stock. The weld process is resistance pressure welding. Quality assurance for the end-plug weld includes:

a. Destructive examination of a sufficient number of weld samples to verify the integrity of the weld region

b. Visual examination of all end-plug welds to establish freedom from cracks, seams, inclusions, and foreign particles after final machining of the weld region

c. Helium leak checking of all end-plug welds

d. Corrosion testing of a sufficient number of samples to establish that weld zones do not exhibit excessive corrosion compared to a visual standard

4.2.4.2.5 Fuel Rod Inspection

Finished fuel rods, prior to being loaded into assemblies, are scanned to provide reasonable assurance that no significant gaps exist in the fuel column and to check the fissile content deviation of pellets.

All finished fuel rods are visually inspected to provide reasonable assurance of a proper surface finish for individual surface defects such as scratches, dents, nicks, or gouges.

4.2.4.3 Burnable Absorber Rod

The fabrication of Gd_2O_3-UO_2 pellets is the same as for UO_2 fuel pellets except that there are tighter restrictions on the Gd_2O_3 and UO_2 particle size. Restrictions on particle size promote homogeneity of the Gd_2O_3-UO_2 mixture. For this burnable absorber application, natural UO_2 is used as a carrier for the gadolinium. The fabrication of Gd_2O_3-UO_2 pellets uses dry blending and mixing of the necessary quantities of UO_2 and Gd_2O_3 powders. As with UO_2 pellets, these powders are then pelletized by blending and sintering processes similar to those in the manufacture of UO_2 pellets. The sintering process promotes formation of a solid solution of UO_2 and Gd_2O_3. As with UO_2 pellets, the Gd_2O_3-UO_2 pellets meet specifications on density, grain size, and homogeneity.

The test and inspection plan for the cladding and assembly of the burnable absorber rod is identical to that for the fuel rod, which is described in Subsection 4.2.4.2.

4.2.4.4 Control Element Assembly

The CEAs (full-strength and part-strength) are subjected to inspections and tests during manufacturing and after installation in the reactor.

During manufacturing, the following are performed:

a. The loading of each control element is carefully controlled to obtain the proper amounts and types of filler materials for each type of CEA application (e.g., full-strength B_4C or part-strength Inconel 625)

b. All end cap welds are liquid penetrant examined and helium leak tested

c. Each type of control element has unique external features that distinguish it from other types

d. Each CEA is serialized to distinguish it from the others. Refer to Figures 4.2-3, 4.2-4, and 4.2-5

e. Fully assembled CEAs are checked for proper alignment of the neutron absorber elements using a special fixture. The alignment check provides reasonable assurance that the frictional force that could result from adverse tolerances is below the force that could significantly increase scram time

In addition to the basic measures described above, the manufacturing process includes quality control steps for providing reasonable assurance that the individual CEA components satisfy design requirements for material quality, detail dimensions, and process control.

After installation in the reactor, prior to criticality, each CEA is traversed through its full stroke and tripped. A similar procedure is also conducted at refueling intervals. The required 90 percent insertion scram time for CEAs is 4.0 seconds under the worst-case conditions. The required scram time is shown Figure 4.2-14.

4.2.4.5 Onsite Inspection

Visual inspection of the conveyance vehicle, shipping container, and fuel assembly are performed at the reactor site. Following unloading the fuel assembly in accordance with approved procedures, exterior portions of the fuel assembly components are inspected for shipping damage and cleanliness. If damage is detected, the assembly may be repaired onsite or returned to the manufacturing facility for repair. In the event the repair process is other than one normally used by the manufacturing facility, or that the repaired assembly does not meet the standard requirements for new fuel, the specific process or assembly is reviewed before it is accepted. Each grid is checked for outside dimensions and fuel rod gap.

4.2.4.6 Fuel Rod Failure Monitoring

To monitor fuel rod failure, periodic sampling of the coolant for radioactivity is performed. Failure monitoring is performed by analyzing iodine, noble gases, and cesium isotope. If the radiation level of an isotope changes suddenly, one or more fuel rod failures are predicted depending on radiation levels. Radiation monitoring and the sampling system are addressed in Sections 9.3 and 11.5.

4.2.4.7 Inservice Surveillance

A surveillance program for the PLUS7 lead test assembly was conducted at Ulchin Unit 3. Four PLUS7 lead test assemblies were loaded from cycle 5 through 7, and poolside examinations were conducted after each of the three operational cycles. The examinations included visual inspections and performance factor measurements for fuel assembly dimensions and fuel rod diameters. In addition, the fretting and corrosion performance of one thrice-burned PLUS7 lead test assembly was evaluated. Visual and destructive hot cell examinations of one thrice-burned PLUS7 lead test assembly had been performed using the hot cell examination facility at Korea Atomic Energy Research Institute (KAERI).

A poolside examination was conducted to verify the performance of the commercially supplied PLUS7 fuel loaded in Yonggwang Unit 5 cycle 5 in 2006. Four fuel assemblies were examined after the first operational cycle, two discharged fuel assemblies after the second cycle, and the remaining two discharged fuel assemblies after the third cycle. Poolside examination program information for the PLUS7 fuel assembly is summarized in Table 4.2-3. Based on the surveillance program results, the performance of the PLUS7 fuel assembly was found to be satisfactory within all design criteria (*[Reference 1]**).

There are monitoring systems to check radioactivity during operation. Based on the information gathered from the monitoring systems, fuel assembly degradation is monitored and plant shutdown is decided depending on the degree of the radiation level. If the monitoring results indicate leakage in the loaded fuel, inspection techniques, such as ultrasonic test, are used to identify the leaking fuel rod(s). The cause of the leaking fuel rod(s) is identified and removed. Visual examination is performed for the irradiated fuel assemblies from each refueling to confirm their integrity. If the fuel assembly fails in the visual examination, it is not inserted into the core until a more detailed inspection and/or evaluation can be performed.

4.2.5 Combined License Information

No COL information is required with regard to Section 4.2.

4.2.6 References

1. *[Korea Hydro & Nuclear Power Co., Ltd., "PLUS7 Fuel Design for the APR1400," APR1400-F-M-TR-13001-P, Rev. 0 (Proprietary) and APR1400-F-M-TR-13001-NP, Rev. 0 (Non-Proprietary), August 2013.]**

2. "Implementation of ZIRLO™ Cladding Material in CE Nuclear Power Fuel Assembly Designs," CENPD-404-P-A, Rev. 0, November 2001.

3. "VANTAGE+ Fuel Assembly Reference Core Report," WCAP-12610-P-A, April 1995.

4. W.J. O'Donnell and B.F. Langer, "Fatigue Design Basis for Zircaloy Components," Nuc. Sci. Eng., Vol. 20, pp. 1-12, 1964.

5. Combustion Engineering, Inc., "C-E Fuel Evaluation Model Topical Report," CENPD-139 (proprietary), CENPD-139 Rev. 01 (non-proprietary), CENPD-139 Supplement 1, Rev. 01 (non-proprietary), July 1974.

6. "Improvements to Fuel Evaluation Model," CEN-161(B)-P, July 1981.

7. "Improvements to Fuel Evaluation Model," CEN-161(B)-P Supplement 1-P, April 1986.

8. Conway, J.B., "The Thermal Expansion and Heat Capacity of UO_2 to 2200 °C," E-NMPD-TM-63-6-6.

9. Christensen, J.A., "Thermal Expansion of UO_2," HW-75148, 1962.

10. Jones, J.M. et al., "Optical Properties of Uranium Oxides," Nature, 205,663-65, 1965.

11. Cabannes, F. and Stora, J.P., "Reflection and Emission Factors of UO_2 at High Temperatures," C. R. Acad. Sci., Paris, Ser. B. 264(1) 45-48, 1967.

12. Held, P.C. and Wilder, D.R, "High Temperature Hemispherical Spectral Emittance of Uranium Dioxide at 0.65 and 0.70 m," J. Am. Cer. Soc., Vol. 52, No. 4, 1969.

13. Brassfield, M.C., "Recommended Property and Reaction Kinetics Data for Use in Evaluating a Light Water Cooled Reactor Loss-of-Coolant Incident Involving Zircaloy-4 or 324-53 Clad UO_2," GEMP-482, 1968.

14. R.J. Beals, " High Temperature Mechanical Properties of Oxide Fuels," ANL-7577, p. 160, April-May 1969.

15. M.O. Marlowe, "High Temperature Isothermal Elastic Moduli of UO_2," Journal of Nuclear Materials, Vol. 33 (1969), pp. 242-244, 1969.

16. Combustion Engineering, Inc., "C-E Methodology for Core Designs Containing Gadolinia-Urania Burnable Absorbers," CENPD-275-P (proprietary), March 1987.

17. Combustion Engineering, Inc., "STRIKIN-II, A Cylindrical Geometry Fuel Rod Heat Transfer Program," CENPD-135P (proprietary), CENPD-135 (non-proprietary), August 1974.

18. R.G. Gray and L.R. Lynam, "Irradiation Behavior of Bulk B_4C and B_4C-SiC Burnable Poison Plates," WAPD-261, October 1963.

19. D.E. Mahagan, "Boron Carbide Thermal Conductivity," HEDL-TME-73-78, September 1973.

20. F.J. Homan, "Performance Modeling of Neutron Absorbers," Nuclear Technology, Vol. 16, pp. 216 -225, October 1972.

21. A.L. Pitner and G.E. Russcher, "Irradiation of Boron Carbide Pellets and Powders in Hanford Thermal Reactors," WHAN-FR-24, December 1970.

22. A.L. Pitner and G.E. Russcher, "A Function to Predict LMFBR Helium Release Bound on Boron Carbide Irradiation Data from Thermal Reactors," HEDL-TME-71-127, September 30, 1971.

23. "Quarterly Progress Report – Irradiation Effects on Reactor Structural Materials," HEDL-TME-71-161, pp. GE-5 to GE-10, Aug. -Oct. 1971.

24. CEN-372-P-A, "Fuel Rod Maximum Allowable Gas Pressure," May 1990.

25. K. Joon, "Primary Hydride Failure of Zircaloy Clad Fuel Rods," ANS Transactions, Vol. 15, No. 1.

26. "Evaluation of Fuel Rod Performance in Maine Yankee Core I," EPRI NP-218, Project 586-1, Final Report, November 1976.

27. Combustion Engineering, Inc., "CEPAN – Method of Analyzing Creep Collapse of Oval Cladding," CENPD-187 P-A, March 1976.

28. Combustion Engineering, Inc., "TORC Code: A Computer Code for Determining the Thermal Margin of a Reactor Core," CENPD-161-P-A (proprietary), April 1986.

29. Combustion Engineering, Inc., "Structural Analysis of Fuel Assemblies for Seismic and Loss of Coolant Accident Loading," CENPD-178-P, Rev. 1-P, August 1981.

30. *[Korea Hydro & Nuclear Power Co., Ltd., "Structural Analysis of Fuel Assemblies for Seismic and Loss of Coolant Accident Loading for the APR1400," APR1400-Z-M-NR-13012-P, Rev. 0 (Proprietary) and APR1400-Z-M-NR-13012-NP, Rev. 0 (Non-proprietary), September 2013.]**

31. KEPCO Nuclear Fuel Co., Ltd., "Quality Assurance Manual for APR 1400 DC Project," KN-QAM3, Rev. 1, December 10, 2012.

Table 4.2-1 (1 of 5)

Mechanical Design Parameters

Fuel Assemblies	
Fuel rod array	Square, 16 × 16
Fuel rod pitch, cm (in)	1.285 (0.506)
Mid-Grid	
Type	Conformal spring
Material	ZIRLO
Number per assembly	9
Weight each, kg (lb)	0.895 (1.972)
Top and Bottom Grid	
Type	Vertical spring
Material	Inconel 718
Number per assembly	2
Weight each, kg (lb)	0.65 (1.433)
Protective Grid	
Type	Dimple
Material	Inconel 718
Number per assembly	1
Weight each, kg (lb)	0.38 (0.837)
Weight of fuel assembly (nominal), kg (lb)	638.9 (1,408.55)
Outside Dimensions	
Fuel rod to fuel rod, cm (in)	20.23 × 20.23 (7.964 × 7.964)

Table 4.2-1 (2 of 5)

Fuel Rod	
Fuel rod material (sintered pellet)	UO_2
Pellet diameter (nominal), cm (in)	0.819 (0.3225)
Pellet length, cm (in)	0.983 (0.387) (enriched uranium)
Pellet density (nominal), g/cm^3	10.44
Pellet theoretical density, g/cm^3	10.96
Pellet density (nominal) (% theoretical)	95.25
Stack height density (nominal), g/cm^3	10.313
Clad material	ZIRLO
Clad inner diameter (ID), cm (in)	0.836 (0.329)
Clad outside diameter (OD), (nominal), cm (in)	0.950 (0.374)
Clad thickness (nominal) cm (in)	0.05715 (0.0225)
Diametral gap (cold, nominal) cm (in)	0.0165 (0.0065)
Active length cm (in)	381 (150)
Plenum length (nominal) cm (in)	25.40 (10.00)

Table 4.2-1 (3 of 5)

Full-strength Control Element Assemblies		
Full-strength CEA	12-Element	4-Element
Full-strength CEA Number in Core	48	33
Absorber elements, No. per assy.	12	4
Type	Cylindrical rods	
Clad material	Inconel 625	
Clad thickness, cm (in)	0.089 (0.035)	
Clad OD, cm (in)	2.073 (0.816)	
Diametral gap, cm (in)	0.0229 (0.009)	
Elements		
Burnable absorber material	B_4C pellets / felt metal and reduced-dia. B_4C pellets	
Burnable absorber length, cm (in)	344.17/31.75 (135.5/12.5)	
B_4C Pellet		
Diameter, cm (in)	1.87/1.69 (0.737/0.664)	
Density, % of theoretical density of 2.52 g/cm^3	73	
Weight % boron, minimum	78	
Thermal conductivity, Cal/sec-cm-°K (Btu/hr-ft-°F)	Irradiated	Unirradiated
	8.3×10^{-3} (2.0) at 427 °C (800 °F)	28×10^{-3} (6.8) at 427 °C (800 °F)
	7.9×10^{-3} (1.9) at 538 °C (1,000 °F)	24×10^{-3} (5.8) at 538 °C (1,000 °F)
Felt metal		
Thickness, cm (in)	0.08 (0.032)	
Length, cm (in)	31.35 (12.34)	
Density, g/cm^3 (lb/in^3)	1.772 (0.064)	
Thermal conductivity, Cal/sec-cm-°K (Btu/hr-ft- °F)	1.26×10^{-3} (0.305) at 260 °C (500 °F)	
	1.41×10^{-3} (0.341) at 538 °C (1,000 °F)	

Table 4.2-1 (4 of 5)

Part-strength Control Element Assemblies	
Part-strength CEA	4-element
Part-strength CEA, number in core	12
Absorber elements, number per assembly	4
Type	Cylindrical rods
Clad material	Inconel 625
Clad thickness, cm (in)	0.089 (0.035)
Clad OD, cm (in)	2.073 (0.816)
Diametral gap, cm (in)	0.0229 (0.009)
Elements	
Burnable absorber material	Inconel 625
Burnable absorber length, cm (in)	378.5 (149)
Inconel 625 Cylindrical Bar	
Diameter, cm (in)	1.872 (0.737)
Length of bar, cm (in)	18.923 (7.45)
Density, g/cm^3 (lb/in^3)	8.442 (0.305)
Thermal conductivity, Cal/sec-cm-°K (Btu/hr-ft- °F)	2.35×10^{-2} (5.7) at 21 °C (70 °F)
	3.39×10^{-2} (8.2) at 316 °C (600 °F)

Table 4.2-1 (5 of 5)

Gadolinia-Urania Burnable Absorber Rod Design	
Absorber material	Gd_2O_3-UO_2
Pellet diameter, cm (in)	0.819 (0.3225)
Pellet length (nominal), cm (in)	0.983 (0.387)
Pellet density (% theoretical), (nominal)	95.25
Theoretical density, UO_2, g/cm^3	10.96
Theoretical density, Gd_2O_3, g/cm^3	7.41
Clad material	ZIRLO
Clad ID, cm (in)	0.836 (0.329)
Clad OD, cm (in)	0.950 (0.374)
Clad thickness (nominal), cm (in)	0.05715 (0.0225)
Diametral gap (cold, nominal), cm (in)	0.01651 (0.0065)
Active length, cm (in)	381 (150)
Plenum length (nominal), cm (in)	25.40 (10.00)

Table 4.2-2

Results of Tests of ZIRLO Cladding Tubes

Reactor	Testing Temperature, °C (°F)	Fast Fluence, 10^{21} n/cm^2	Yield Strength, 10^2 kg/cm^2 (ksi)	Uniform Strain Length, %	Total Strain Length, %
BR-3	343.3 (650)	6.4	62.2 (88.5)	1.9	3.6
BR-3	343.3 (650)	6.4	60.4 (85.9)	1.1	1.6
BR-3	343.3 (650)	7.1	62.6 (89.1)	2.0	4.2
BR-3	343.3 (650)	7.1	48.0 (68.2)	2.5	3.2

Table 4.2-3

Poolside Fuel Inspection Program Summary for the PLUS7 Fuel Assembly

Reactor	Shutdown Date/Cycle	Burnup (GWD/MTU)	Inspection Program Scope
Ulchin Unit 3	End of cycle (EOC)-5	19.6 (assembly average)	Visual exam, fuel assembly length, shoulder gap, fuel assembly bowing and twist, grid width, fuel rod OD, cladding oxide thickness
	EOC-6	38.6 (assembly average)	Visual exam, fuel assembly length, shoulder gap, fuel assembly bowing and twist, grid width, fuel rod OD, cladding oxide thickness
	EOC-7	53.2 (assembly average)	Visual exam, fuel assembly length, shoulder gap, fuel assembly bowing and twist, grid width, fuel rod OD, cladding oxide thickness
Yonggwang Unit 5	EOC-5	23.4 (assembly average)	Visual exam, fuel assembly length, shoulder gap, fuel assembly bowing, fuel rod OD
	EOC-6	42.6 (assembly average)	Visual exam, fuel assembly length, shoulder gap, fuel assembly bowing and twist, grid width, fuel rod OD, cladding oxide thickness
	EOC-7	55.0 (assembly average)	Visual exam, fuel assembly length, shoulder gap, fuel assembly bowing and twist, grid width, fuel rod OD, cladding oxide thickness

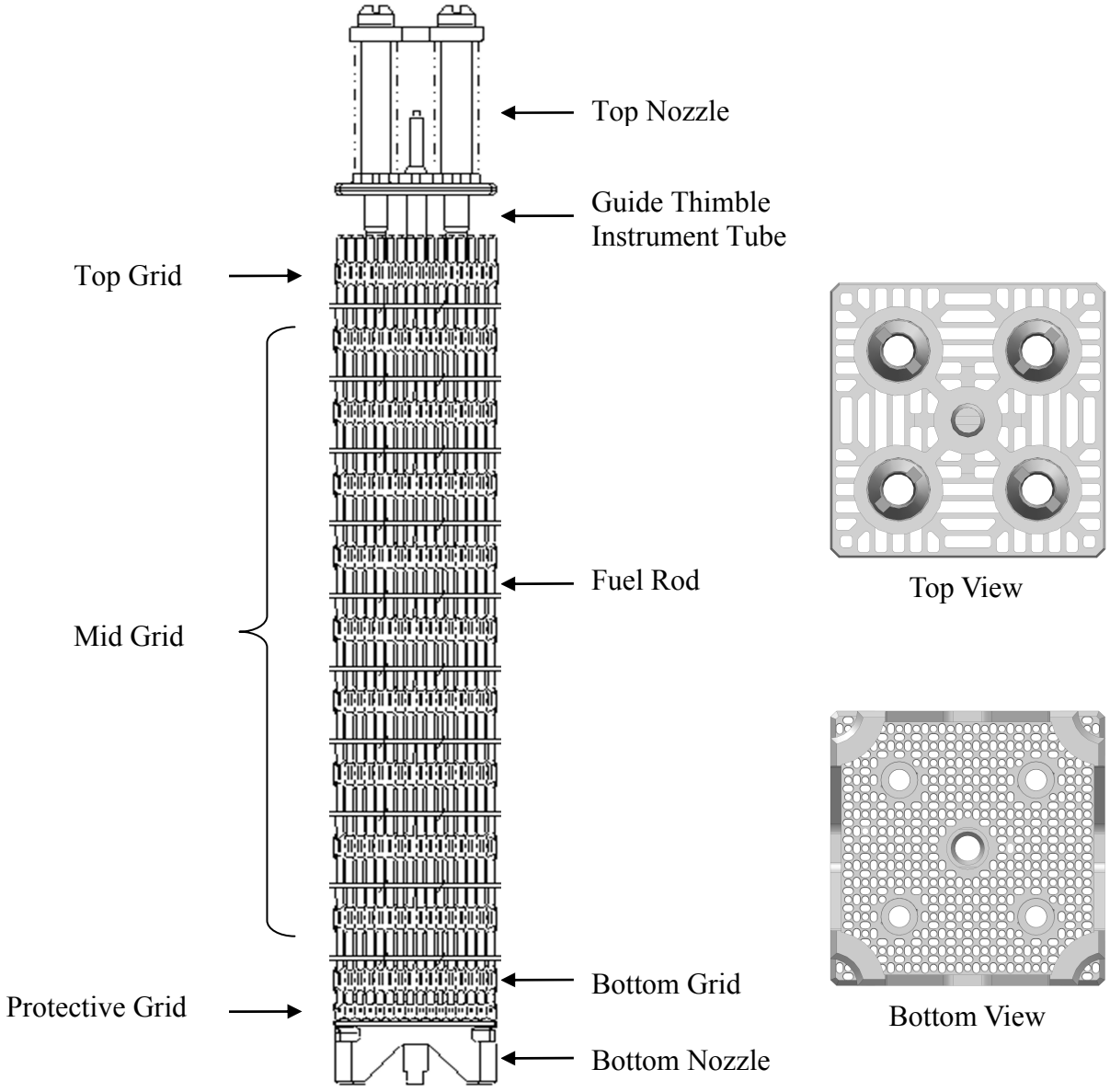

Figure 4.2-1 Fuel Assembly

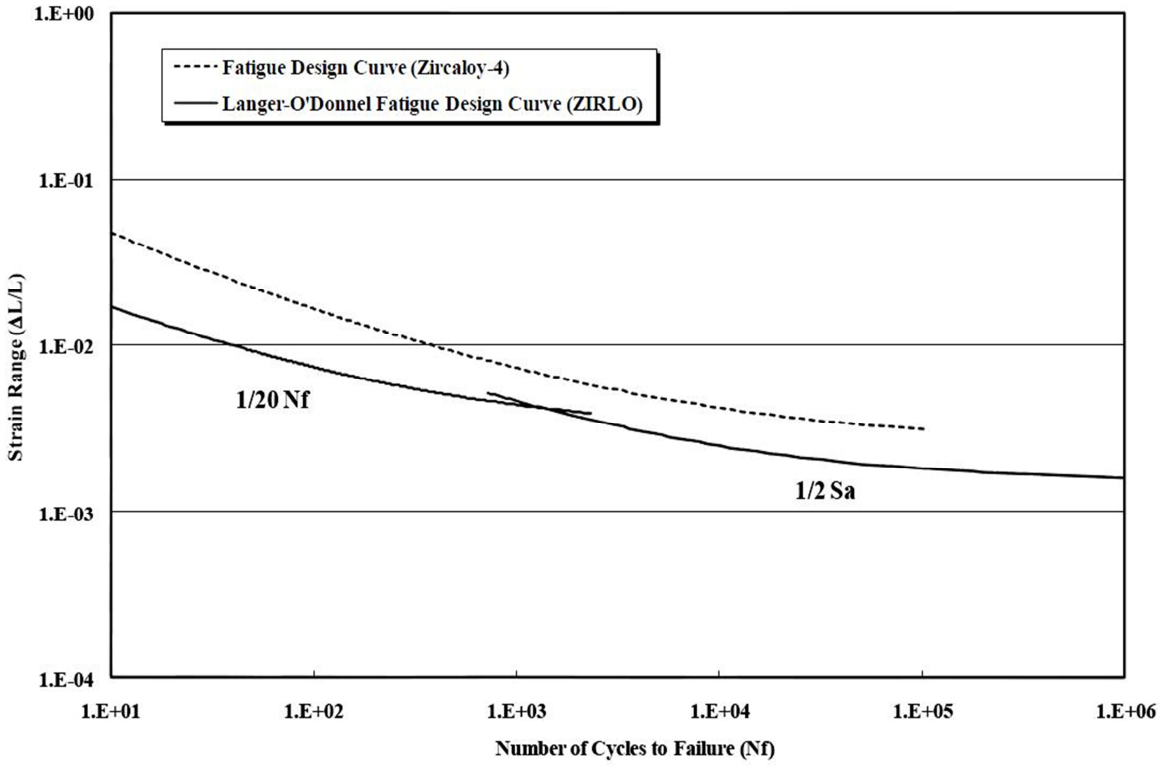

Figure 4.2-2 Design Curves for Cyclic Strain Usage of Zircaloy-4 and ZIRLO

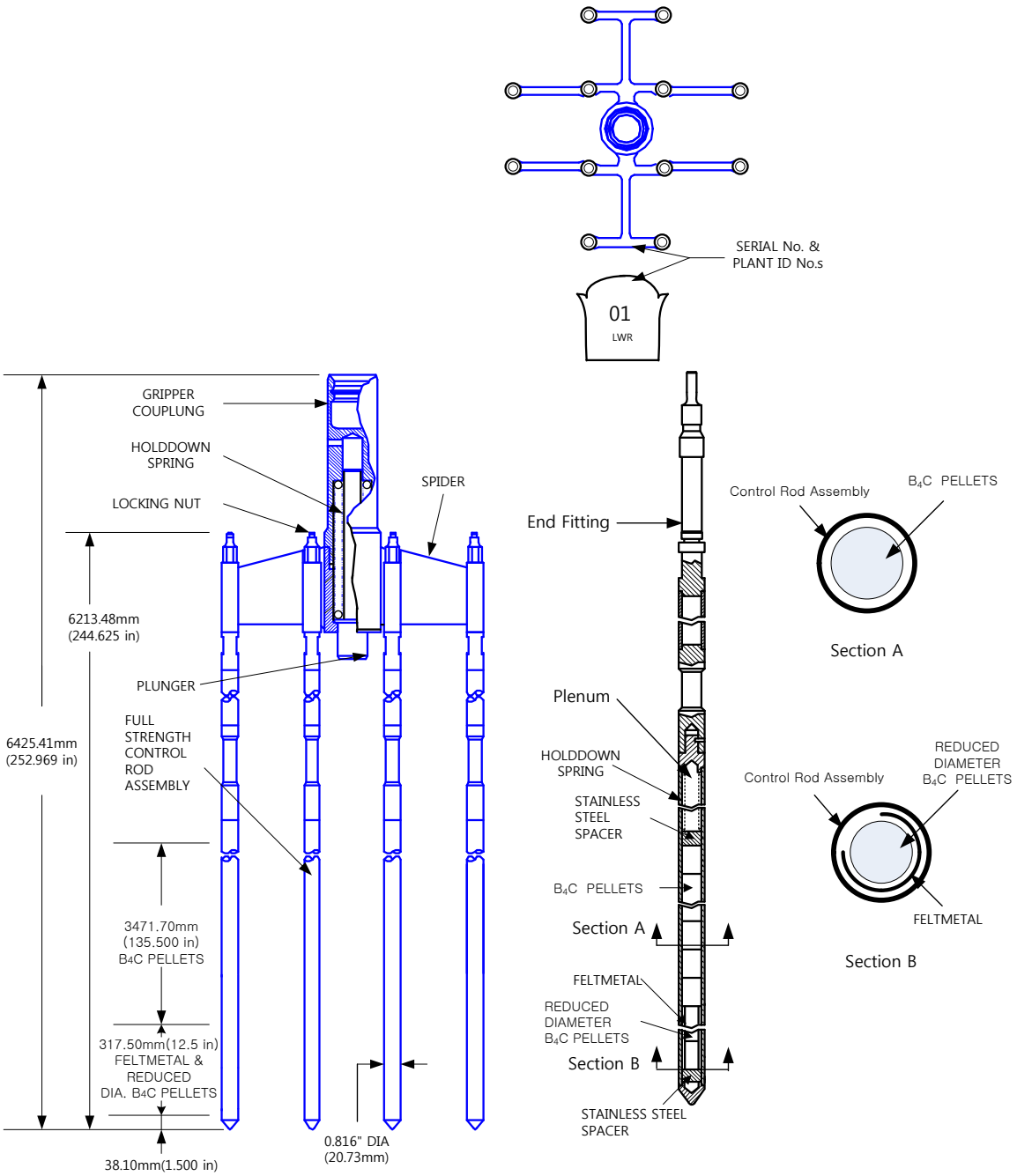

Figure 4.2-3 Full Strength Control Element Assembly (12 Element)

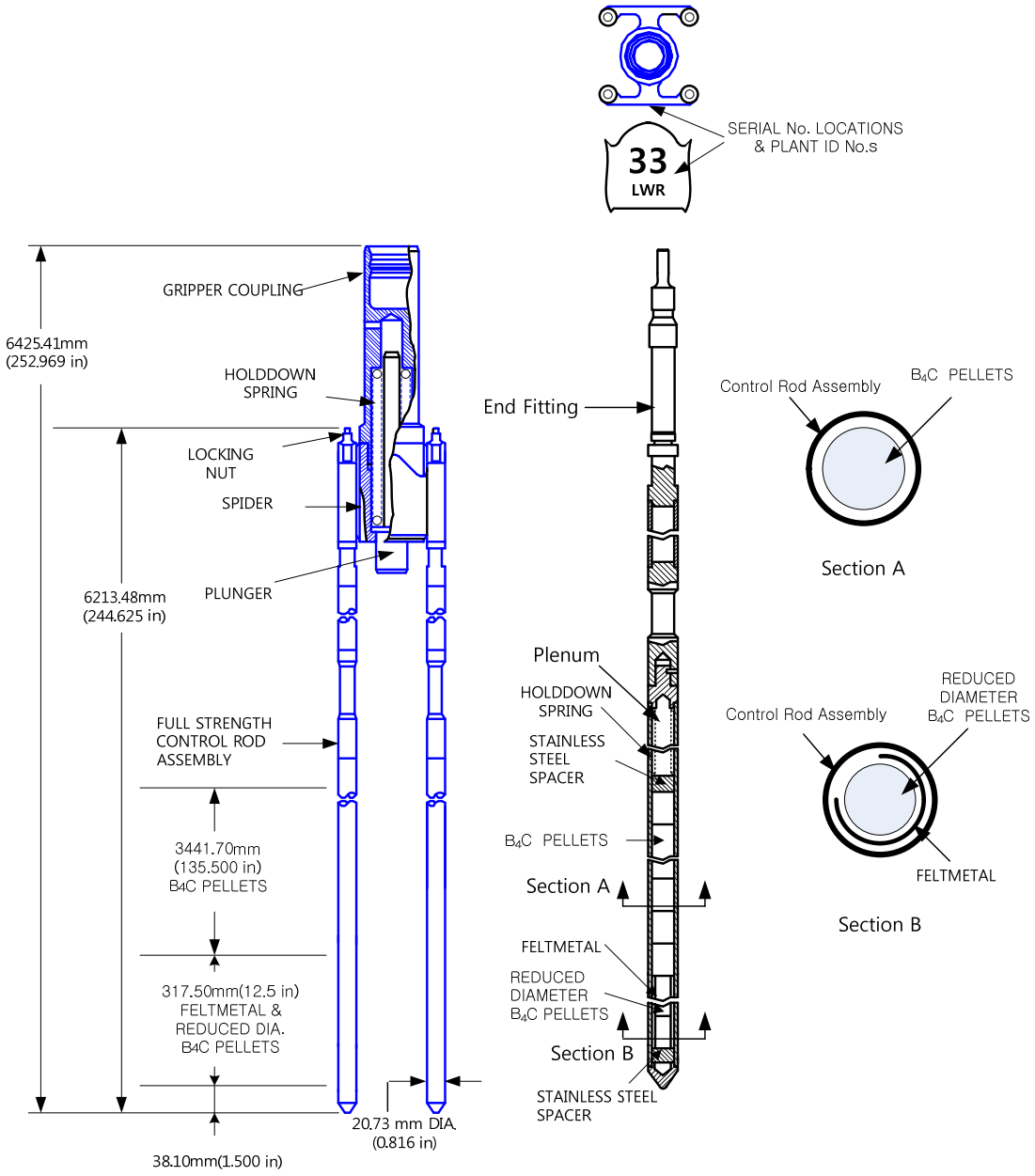

Figure 4.2-4 Full Strength Control Element Assembly (4 Element)

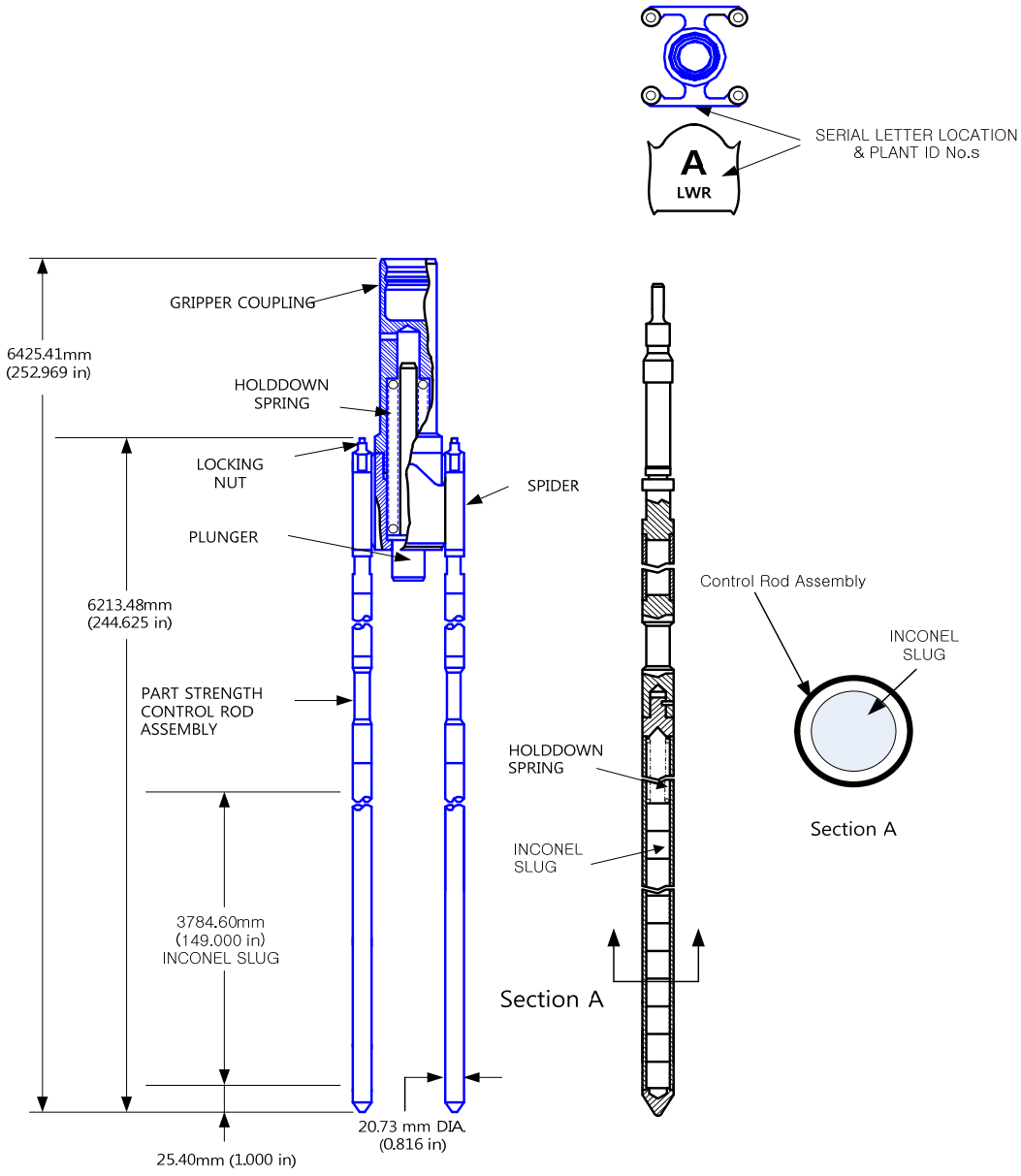

Figure 4.2-5 Part Strength Control Element Assembly

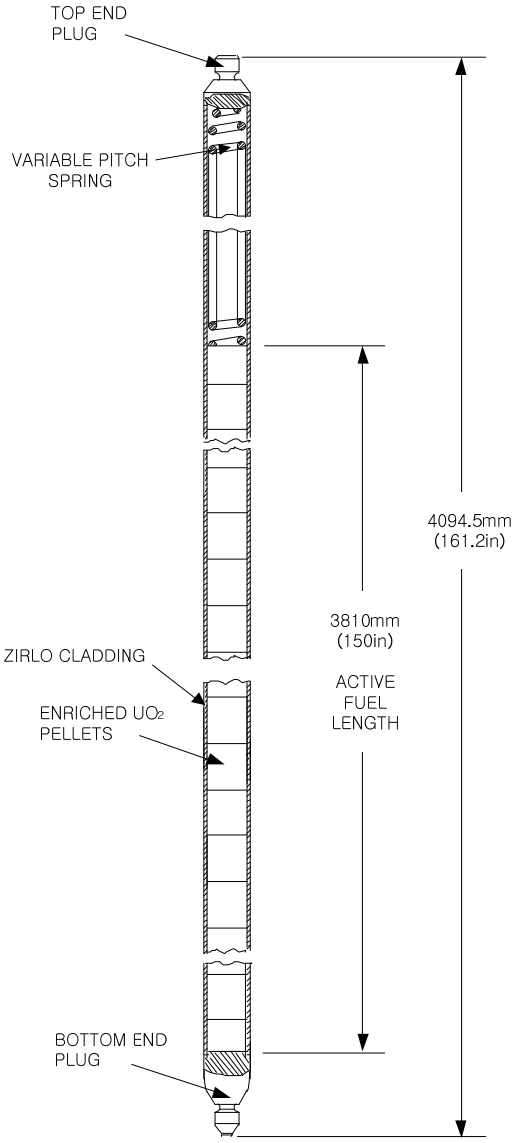

Figure 4.2-6 Fuel Rod

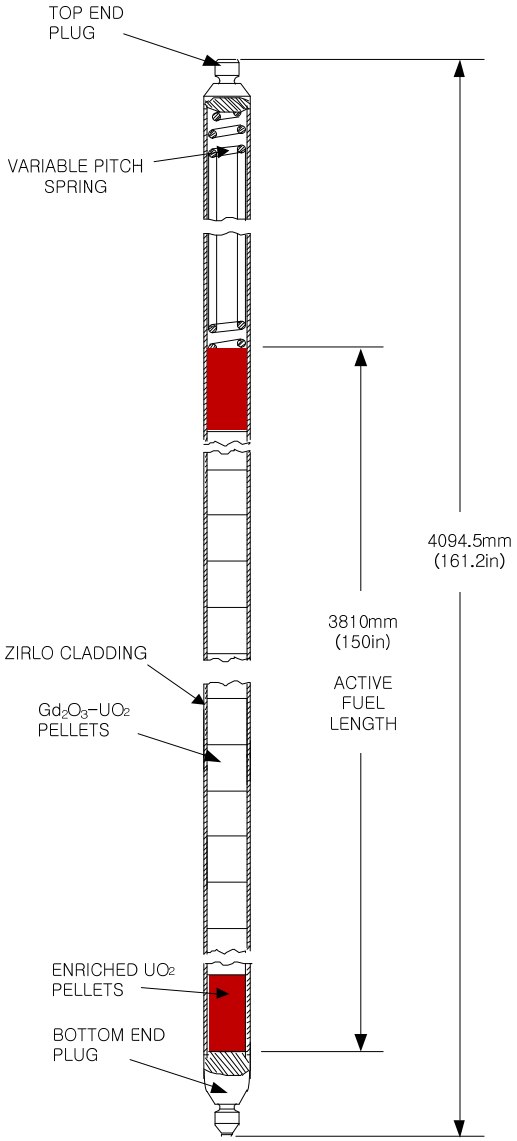

Figure 4.2-7 Gd_2O_3-UO_2 Burnable Absorber Rod

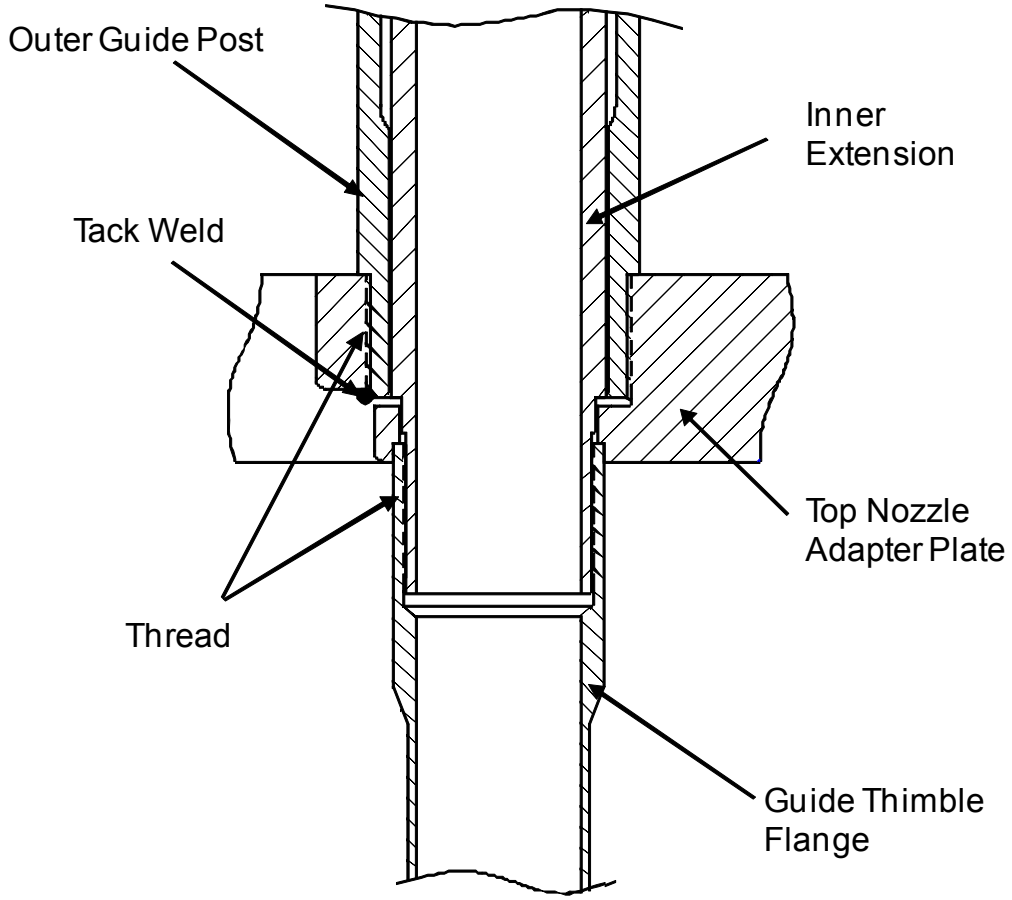

Figure 4.2-8 Guide Thimble to Top Nozzle Joint

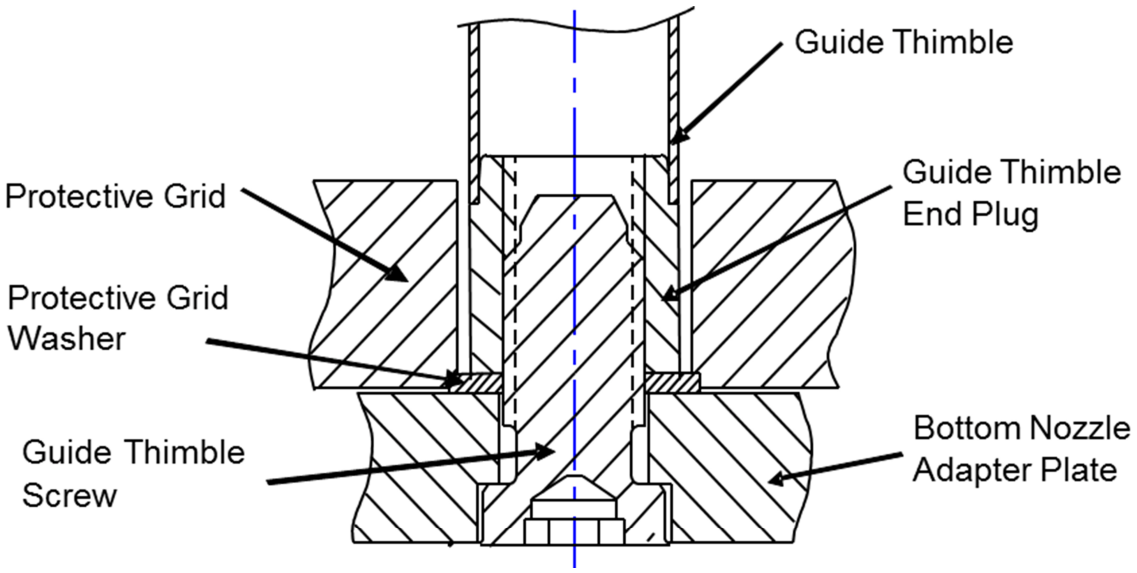

Figure 4.2-9 Guide Thimble to Bottom Nozzle Joint

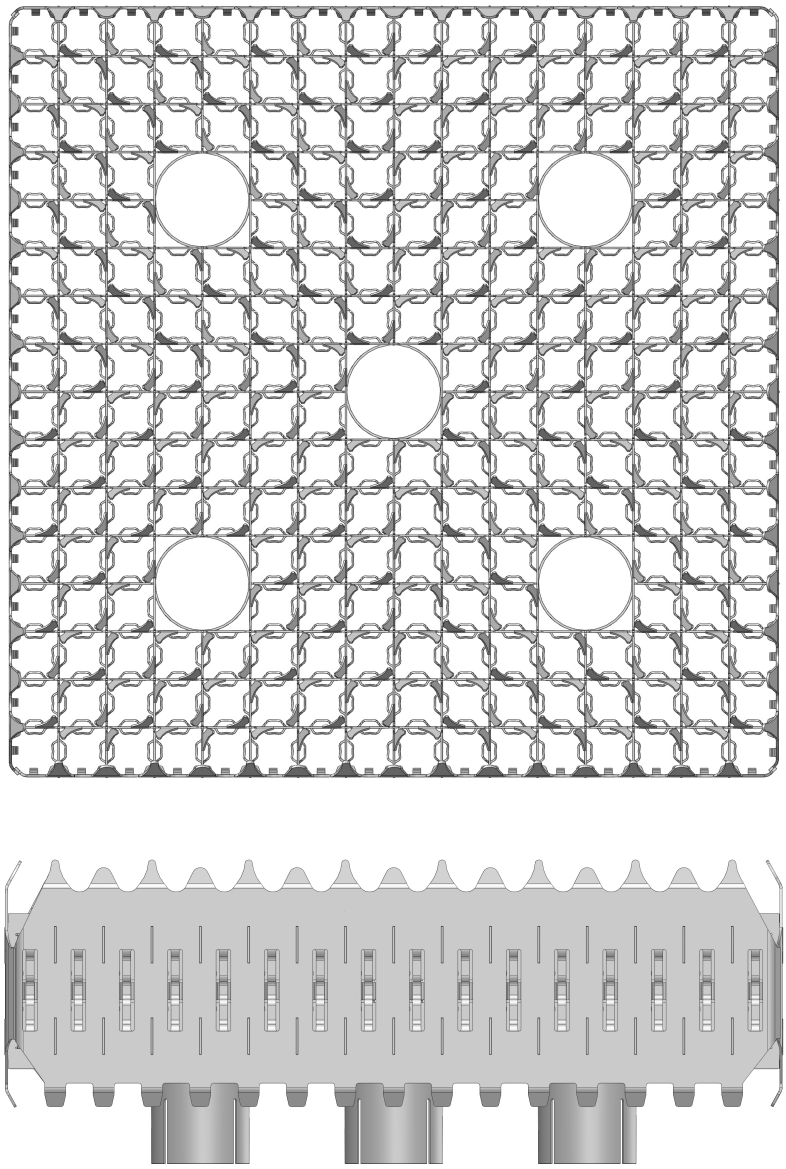

Figure 4.2-10 Mixing Vaned Mid Grid

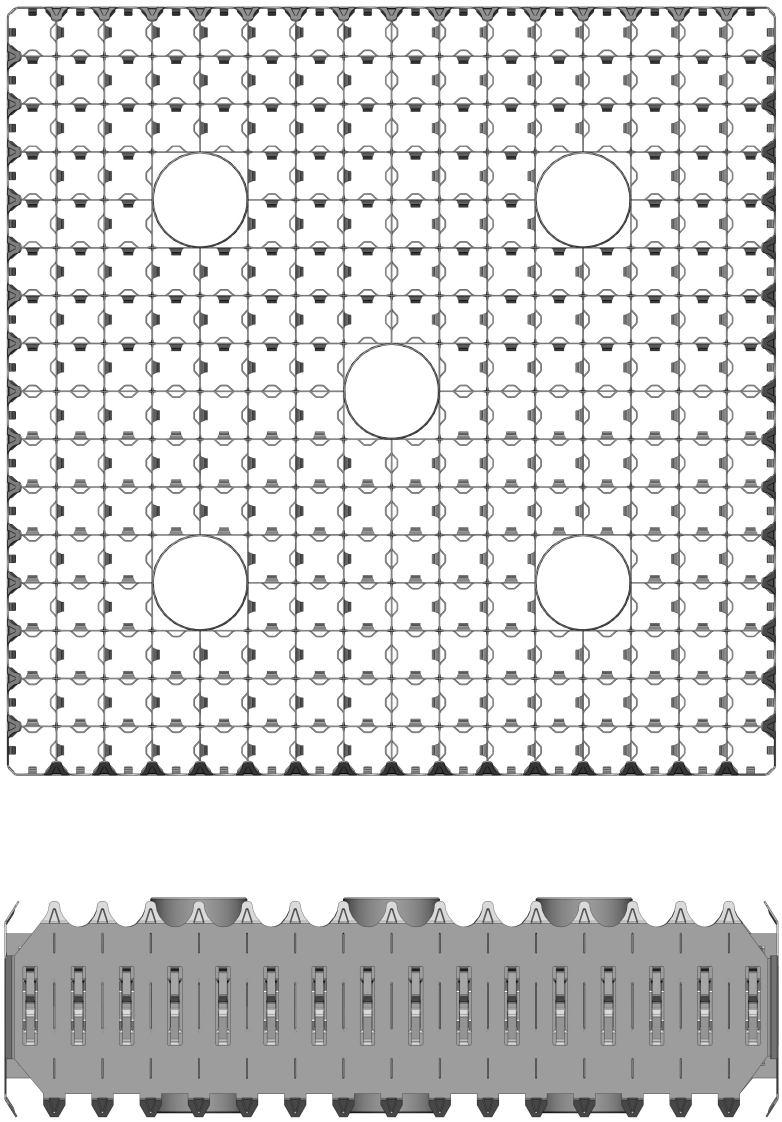

Figure 4.2-11 Top and Bottom Inconel Grid

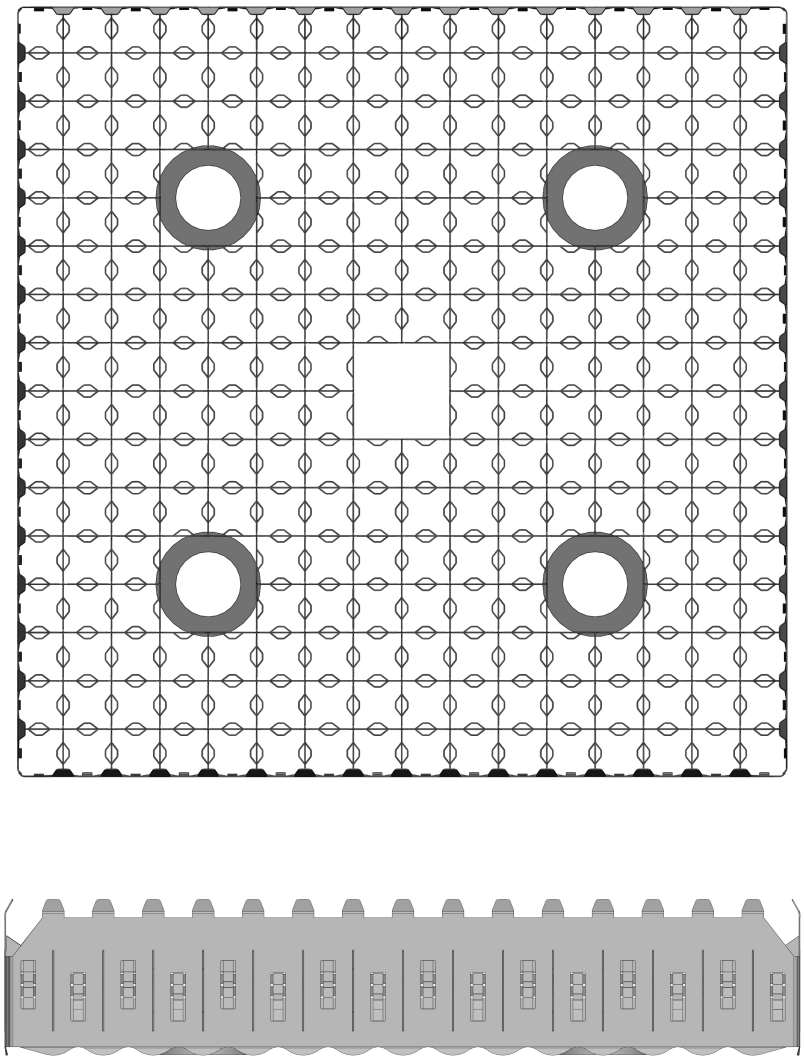

Figure 4.2-12 Protective Grid

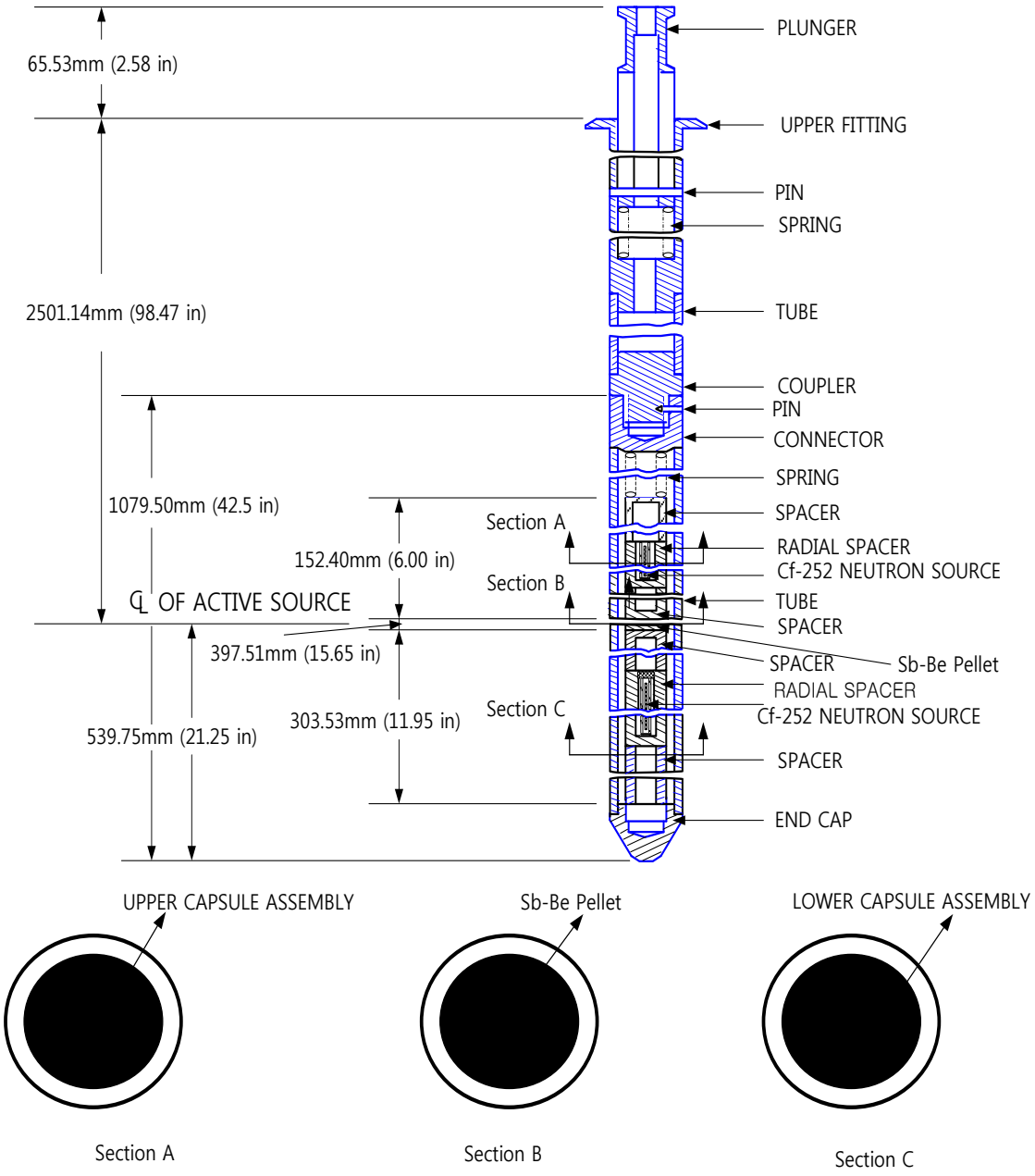

Figure 4.2-13 Neutron Source Assembly

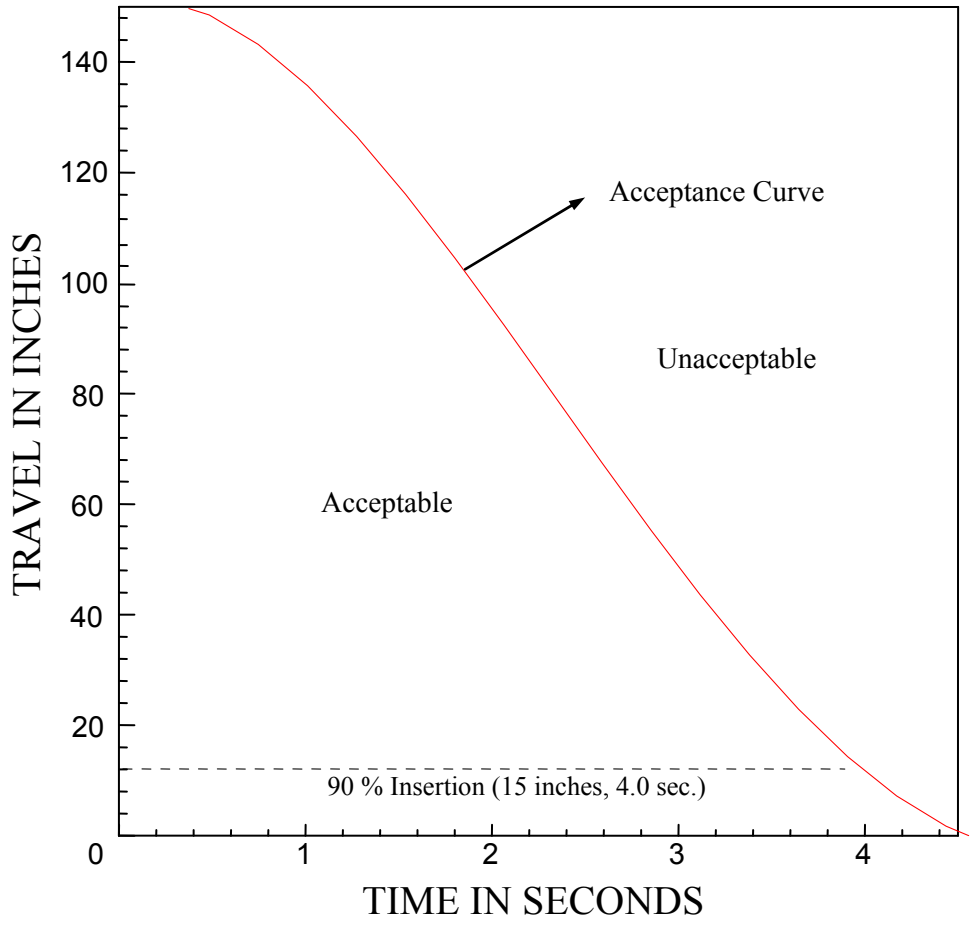

Figure 4.2-14 CEA Position Requirements during Reactor Scram

4.3 Nuclear Design

4.3.1 Design Bases

The bases for the nuclear design of the fuel and reactivity control systems are described in the following subsections. The GDC in 10 CFR 50, Appendix A, provide the regulatory requirements for the nuclear design bases used to design the fuel and reactivity control systems. The following GDC apply to Section 4.3.

a. GDC 10 requires that the acceptable fuel design limits are not exceeded during normal operation, including the effects of anticipated operational occurrences.

b. GDC 11 requires that, in the power operating range, the net effect of the prompt inherent nuclear feedback characteristics tends to compensate for a rapid increase in reactivity.

c. GDC 12 requires that power oscillations that could result in conditions exceeding specified acceptable fuel design limits are not possible or can be reliably and readily detected and suppressed.

d. GDC 13 requires the provision of instrumentation and controls (I&C) to monitor variables and systems over anticipated operational occurrences, and of accident conditions as appropriate to ensure adequate safety, including the variables and systems that can affect the fission process, the integrity of the reactor core, the reactor coolant pressure boundary, and the containment and its associated systems. Appropriate controls must be provided to maintain these variables and systems within the prescribed operating ranges

e. GDC 20 requires the automatic initiation of appropriate systems including the reactivity control systems to ensure that acceptable fuel design limits are not exceeded as a result of anticipated operational occurrences, to sense accident conditions, and to initiate the operation of systems and components important to safety.

f. GDC 25 requires that the protection system be designed to ensure that specified acceptable fuel design limits are not exceeded for any single malfunction of the reactivity control systems such as accidental withdrawal (not including rod ejection or dropout) of the control rods.

g. GDC 26 requires that two independent reactivity control systems of different design principles be provided. One of the systems must use control rods, preferably including a positive means for inserting the rods, and be capable of reliably controlling reactivity changes to ensure that under conditions of normal operation, including anticipated operational occurrences, and with appropriate margin for malfunctions such as stuck rods, specified acceptable fuel design limits are not exceeded. The other system must be capable of reliably controlling the rate of reactivity changes resulting from planned, normal power changes (including xenon burnout) to ensure that the acceptable fuel design limits are not exceeded. One of the two systems must be capable of holding the reactor core subcritical under cold conditions.

h. GDC 27 requires that the RCSs have a capability, in conjunction with the addition of poison by the emergency core cooling system, of reliably controlling reactivity changes to ensure that under postulated accident conditions and with the appropriate margin for stuck rods, the capability to cool the core is maintained.

i. GDC 28 requires that the reactivity control systems be designed with appropriate limits on the potential amount and rate of reactivity increase to ensure that the effects of postulated reactivity accidents neither result in damage to the reactor coolant pressure boundary greater than limited local yielding nor sufficiently disturb the core, its support structure or other reactor pressure vessel internals to significantly impair the capability to cool the core.

Compliance with GDC 10, 11, 12, 25, 26, 27, and 28 is addressed in Subsection 4.3.1. The systems that demonstrate compliance with GDC 13 are addressed in Chapters 3, 7, and 9. The protection system complies with GDC 20 and is addressed in Chapters 3, 6, and 7.

4.3.1.1 Excess Reactivity and Fuel Burnup

The excess reactivity provided for each cycle is based on the depletion characteristics of the fuel and burnable absorber and on the desired burnup for each cycle. The desired burnup is based on an economic analysis of the fuel cost and the projected operating load cycle for the plant. *[The average burnup is chosen to provide reasonable assurance that the peak burnup is within the limits that are described in Subsection 4.2.1.]** This design basis, along with the design basis in Subsection 4.3.1.8, meets 10 CFR 50, Appendix A, GDC 10.

4.3.1.2 Negative Reactivity Feedback

The net effect of the prompt inherent nuclear feedback characteristics, such as fuel temperature coefficient, moderator temperature coefficient, moderator void coefficient, and moderator pressure coefficient, tends to compensate for a rapid increase in reactivity in the power operating range. The negative reactivity feedback design meets GDC 11.

4.3.1.3 Core Design Lifetime and Fuel Replacement Program

The core design lifetime and fuel replacement program presented are based on a refueling interval of approximately 18 months with one-third of the fuel assemblies replaced during each refueling outage.

4.3.1.4 Reactivity Coefficients

The values of each coefficient of reactivity are consistent with the design basis for net reactivity feedback (Subsection 4.3.1.2) and analyses that predict acceptable consequences of postulated accidents and AOOs, where such analyses include the response of the reactor protection system (RPS).

4.3.1.5 Burnable Absorber Requirements

The burnable absorber reactivity worth in the design provides reasonable assurance that the moderator coefficients of reactivity are consistent with the design bases in Subsection 4.3.1.4.

4.3.1.6 Stability Criteria

The reactor and the instrumentation and control systems are designed to detect and suppress xenon-induced power distribution oscillations that could, if not suppressed, result in conditions that exceed the specified acceptable fuel design limits (SAFDLs). The design of the reactor and associated systems precludes the possibility of power level oscillations. This design basis satisfies GDC 12.

4.3.1.7 Maximum Controlled Reactivity Insertion Rate

The reactivity control systems control element assemblies (CEAs), reactor regulating system (RRS), and boron charging portion of the chemical and volume control system (CVCS) are designed so that the potential amount and rate of reactivity insertion from normal operation and postulated reactivity accidents do not result in:

a. Violation of the SAFDLs for any single malfunction of the reactivity control systems (excluding CEA ejection)

b. Damage to the reactor coolant pressure boundary (RCPB)

c. Disruption of the core or other reactor internals sufficient to impair the effectiveness of safety injection

This design basis, together with Subsection 4.3.1.11, meets GDC 25 and 28.

4.3.1.8 Control of Power Distribution

The core power distribution is controlled so that, in conjunction with other core operating parameters, the power distribution does not result in violating the limiting conditions for operation (LCOs). LCOs and limiting safety system settings (LSSSs) are determined based on the accident analyses described in Chapters 6 and 15 to provide reasonable assurance that the SAFDLs and other criteria are not exceeded for accidents. This design basis, together with the information in Subsection 4.3.1.1, meets GDC 10.

4.3.1.9 Excess Control Element Assembly Worth with Stuck Rod Criteria

The amount of reactivity available from insertion of withdrawn CEAs under all power operating conditions, even when the highest-worth CEA fails to insert into the core, provides for excess CEA worth after cooldown to hot zero power, plus any additional shutdown reactivity requirements assumed in the accident analyses. This design basis, together with Subsection 4.3.1.10, meets GDC 26 and 27.

4.3.1.10 Chemical Reactivity Control

The CVCS, described in Subsection 9.3.4, is used to adjust the dissolved boron concentration in the moderator. After a reactor shutdown, the CVCS system is able to compensate for the reactivity changes associated with xenon decay and reactor coolant temperature decreases to ambient temperature, and it provides adequate shutdown margin during refueling. This system also has the capability of controlling, independent of the CEAs, long-term reactivity changes due to fuel burnup and reactivity changes during xenon transients resulting from changes in the reactor load. This design basis, together with Subsection 4.3.1.9, meets GDC 26 and 27.

4.3.1.11 Maximum Control Element Assembly Speeds

Maximum CEA speeds are consistent with the maximum controlled reactivity insertion rate design basis described in Subsection 4.3.1.7. Maximum CEA speeds are also provided in Subsection 15.4.2.

4.3.2 Description

4.3.2.1 Nuclear Design Description

This subsection summarizes the nuclear characteristics of the core and describes the important design parameters that affect the performance of the core in steady-state and normal transient operation. *[Summaries of nuclear design parameters are presented in Tables 4.3-1 and 4.3-2 and Figures 4.3-1 and 4.3-2 and are intended to be descriptive of the first-cycle design.]**

The first-cycle design features a three-batch loading scheme in which type B and C fuel assemblies contain rods of two different enrichments and of gadolinia burnable absorber. This system of enrichment zoning, shown in Figure 4.3-2, offers improved long-term control of the local assembly power distribution.

*[The fuel loading pattern, fuel enrichment, and burnable absorber distributions are shown in Figures 4.3-1 and 4.3-2 for the first cycle.]** The typical fuel loading pattern and fuel enrichments for the equilibrium cycle are shown in Figure 4.3-3. The other three quadrants of the core are symmetric to the displayed quadrant. Physical features of the lattice, fuel assemblies, and CEAs are described in Section 4.2.

The critical boron concentration versus core average burnups are shown in Figure 4.3-47 for first and equilibrium cycles, unrodded full power, and equilibrium xenon.

Core average enrichment, core burnup, critical soluble boron concentrations and worths, plutonium buildup, and delayed neutron fractions and neutron lifetime for the first cycle are shown in Table 4.3-1. The soluble boron insertion rates available, as described in Subsection 9.3.4, are sufficient to compensate for the maximum reactivity addition due to xenon burnout and normal plant cooldown. The amount of maximum reactivity addition for which the CVCS is required to compensate is given in Table 4.3-1. The rate of maximum reactivity addition occurs for an end-of-cycle (EOC) cooldown, in which the moderator temperature coefficient is the most negative.

Table 4.3-2 shows the k_{eff} and reactivity data associated with the cold zero power, hot standby, hot full power without xenon or samarium, and hot full power with equilibrium xenon and samarium conditions for the first cycle.

4.3.2.2 Power Distribution

4.3.2.2.1 General

Power distribution and coolant conditions are controlled so that the peak linear heat rate (LHR) and the minimum departure from nucleate boiling ratio (DNBR) are maintained within operating limits supported by the accident analyses (Chapters 6 and 15) in regard to

the correlations between measured quantities, power distribution, and uncertainties in the determination of power distribution.

Methods of controlling the power distribution include the use of full- or part-strength CEAs to alter the axial power distribution; decreasing CEA insertion by boration, thereby improving the radial power distribution; and correcting off-optimum conditions that cause margin degradations such as CEA misoperation.

The core operating limit supervisory system (COLSS) indicates to the operator how far the core is from operating limits and provides an audible alarm should an operating limit be exceeded. Such a condition signifies a reduction in the capability of the plant to withstand an anticipated transient but does not necessarily imply a violation of fuel design limits. If the margin to fuel design limits continues to decrease, the RPS assures that the SAFDLs are not exceeded by initiating a trip.

The COLSS, described in Section 7.7 and Reference 1, continually assesses the margin of the LHR and DNBR operating limits. The data for these assessments include measured in-core neutron flux data, CEA positions and coolant inlet temperature, pressure, and flow rate. In the event of an alarm indicating that an operating limit has been exceeded, power is reduced unless the alarm can be cleared by improving either the power distribution or another process parameter. The accuracy of the COLSS calculations is verified periodically.

In addition to the monitoring performed by COLSS, the RPS core protection calculators (CPCs) described in Section 7.2, continually monitor the core power distribution and DNBR by processing reactor coolant data, signals from ex-core neutron flux detectors, and input from redundant reed switch assemblies that indicate CEA position. In the event the power distributions or other parameters are perturbed as the result of an AOO that would violate fuel design limits, the high local power density or low DNBR trips in the RPS initiate a reactor trip.

4.3.2.2.2 Nuclear Design Limits on the Power Distribution

The design limits on the power distribution were used both as design input and as initial conditions for accident analyses described in Chapters 6 and 15. In COLSS, the power operating limit assures that the consequences of an AOO or postulated accident are not

more severe than the consequences described in Chapters 6 and 15. The initial conditions used in the determination of power operating limit are stated in terms of peak linear heat generation rate (PLHGR) and required power margin for the minimum DNBR.

The design limits on power distribution are as follows:

a. The limiting three-dimensional heat flux peaking factor, F_q^n (Subsection 4.3.2.2.4), was established for full-power conditions at 2.43. This is based directly on the LOCA limit of 446.2 W/cm (13.6 kW/ft) (Subsection 15.6.5.3.1) and the full-power core average LHR of 183.7 W/cm (5.60 kW/ft). A higher F_q^n is allowed for reduced core power levels.

   Implementation in the Technical Specifications is via an operating limit on the monitored PLHGR.

b. The thermal margin to a minimum DNBR of 1.29 (using the KCE-1 critical heat flux (CHF) correlation as described in Subsections 4.4.2.2 and 4.4.4.1), which is available to accommodate AOOs, is a function of several parameters, including:

   1) Coolant conditions

   2) Axial power distribution

   3) Axially integrated radial peaking factor, F_r^n, where F_r^n is the rod radial peaking factor, which is defined and termed as rod radial power factor in Subsection 4.4.2.2.2

   The coolant conditions assumed in the safety analysis, the expected set of unrodded or rodded F_r^n in Table 4.3-10, and the set of axial shapes displayed in Figure 4.4-3 constitute one possible set of limiting combinations of parameters for full power operation. Other combinations giving acceptable accident analysis consequences are also equally acceptable. Implementation in the technical specifications is via a power operating limit based on DNBR which maintains an appropriate amount of thermal margin to the DNBR limit.

It is shown in the following subsections that operation within these design limits is achievable.

4.3.2.2.3 Expected Power Distributions

Figures 4.3-4 through 4.3-18 show planar average radial power distributions of typical first cycle and Figures 4.3-19 through 4.3-24 show unrodded core average axial power distributions, respectively. They illustrate conditions expected at full power for various times in the fuel cycle. It is expected that for normal, base load operation of the plant, the operation of the reactor will be with limited CEA insertion so that the unrodded power distributions in Figures 4.3-4 through 4.3-24 represent the expected power distribution during most of the cycle. Normal operation of the reactor may include full insertion of the part-strength CEA group during load transients. Therefore, Figures 4.3-4 through 4.3-18 show radial power distributions both for unrodded operation and for steady-state operation with the part-strength CEA group fully inserted. The three-dimensional peaking factor, F_q^n, expected during steady-state operation, is the product of the planar radial peaking factor and the axial peaking factor.

Figures 4.3-25 through 4.3-27 show a loading pattern and planar radial power distributions of typical equilibrium cycle based on a refueling interval of approximately 18 months. The expected power distributions for this cycle are similar to those of the first cycle except for the reduced power in fuel assemblies located on the periphery of the core and consequently higher radial peaking factors in the interior region of the core. The expected power distributions are well within the nuclear design limits described in Subsection 4.3.2.2.2. The uncertainty associated with these calculated power distributions is described in Subsection 4.3.3.1.2.2.2.

The capability of the core to follow load transients without exceeding power distribution limitations depends on the margin to operating limits during a load-follow operation compared to the margin required for base-loaded, unrodded operation. The radial and axial power distributions and estimates of F_q^n and F_r^n are obtained from ROCS (Reference 5).

The radial power distribution in an assembly is a function of the location of the assembly in the core, the time in the fuel cycle, CEA insertion, and other considerations. A normalized assembly power distribution used for a sample DNB calculation is described in Subsection 4.4.2.2 and shown in Figure 4.4-2. Figures 4.3-28 and 4.3-29 show typical rodwise power

distributions of the assembly with the highest relative power at BOC and EOC, respectively. In Subsection 4.3.3.1.2, the accuracy of calculations of the power distribution within a fuel assembly is addressed.

4.3.2.2.4 Allowances and Uncertainties on Power Distributions

Consideration is given to the uncertainty and the allowances associated with COLSS online monitoring (Reference 1), and to calculation uncertainties in comparing the expected power distributions and the PLHGR produced by analysis with the design limits, as addressed in Subsection 4.3.2.2.2. The design limit F_q^n, mentioned in Subsection 4.3.2.2.2 for hot full power (HFP), is determined to have been reached if a COLSS measured F_q^n multiplied by the power level measurement uncertainty (1.02) and the COLSS LHR measurement uncertainty, is the same as the design limit F_q^n. In this case, COLSS would actuate an alarm on PLHGR.

4.3.2.2.5 Comparisons Between Limiting and Expected Power Distributions

As presented in Subsection 4.3.2.2.3, the maximum expected unrodded F_q^n determined by the product of planar radial peaking factor and the axial peaking factor for the first cycle, is limited below the design limit F_q^n, considering uncertainties. Additionally, the calculations addressed in Subsection 4.3.2.2.3 show that, with proper use of the part-strength CEAs, acceptable margin is maintained for the peak LHR during these maneuvering transients. In the event that part-strength CEAs are not moved properly, the power distribution could become unacceptable. In this case, the COLSS would indicate an insufficient margin and direct the operator to improve the core power distribution, improve the coolant conditions, or reduce core power.

The power distributions expected to occur during maneuvering transients in the first cycle of the APR1400 operation are used for a thermal margin analysis described in Subsection 4.4.2. According to the analysis results, the minimum DNBR of 1.29 is satisfied throughout the first cycle of the APR1400.

4.3.2.3 Reactivity Coefficients

Reactivity coefficients relate changes in core reactivity to variations in fuel or moderator conditions. The data presented in Subsection 4.3.2.3 and associated tables and figures illustrate the range of reactivity coefficient values calculated for a variety of operating and accident conditions. Subsection 4.3.3 presents comparisons of calculated and measured moderator temperature coefficients and power coefficients for operating reactors. The data agreement shown in Subsection 4.3.3 provides confidence that the data presented in Subsection 4.3.2.3 adequately characterize the APR1400 core design. Table 4.3-3 presents a comparison of the calculated reactivity coefficients with those used in the accident analyses that are described in Chapters 6 and 15. For each accident analysis, conservative reactivity coefficient values are used. Values used in the accident analyses may fall outside the calculated data ranges in a conservative direction because uncertainties in the coefficient values, as described in Subsection 4.3.3.1.2, and other conservatisms are taken into account in the accident analyses. A more extensive list of reactivity coefficients is given in Table 4.3-4.

The calculation methods used to compute reactivity coefficients are described in Subsection 4.3.3.1.1. All data presented in subsequent subsections were calculated with a three-dimensional nuclear model. Spatial distributions of materials and flux weighting are explicitly performed for the particular conditions at which the reactivity coefficients are calculated. The adequacy of this method is addressed in Subsection 4.3.3.1.2.

4.3.2.3.1 Fuel Doppler Coefficient

The fuel temperature coefficient is the change in reactivity per unit change in fuel temperature. A change in fuel temperature affects the reaction rates in both the thermal and epithermal neutron energy regions. The principal contributor to the change in reaction rate, with fuel temperature in the epithermal range is the Doppler effect, which arises from the increase in absorption widths of the resonances with an increase in fuel temperature. The ensuing increase in absorption rate with fuel temperature causes a negative fuel temperature coefficient. In the thermal energy region, a change in reaction rate with fuel temperature arises from the effect of temperature-dependent scattering properties of the fuel matrix on the thermal neutron spectrum. In typical PWR fuels containing strong resonance absorbers such as U-238 and Pu-240, the magnitude of the component of the fuel temperature

coefficient arising from the Doppler effect is more than a factor of 10 larger than the magnitude of the thermal energy component.

Figure 4.3-30 shows the dependence of the calculated fuel temperature coefficient on the fuel temperature, both at the beginning and at the end of the first cycle.

4.3.2.3.2 Moderator Temperature Coefficient

The moderator temperature coefficient relates changes in reactivity to uniform changes in moderator temperature, including the effects of moderator density changes, with changes in moderator temperature. Typically, an increase in the moderator temperature causes a decrease in the core moderator density and therefore less thermalization, which reduces core reactivity. When soluble boron is present in the moderator, a reduction in moderator density causes a reduction in the content of soluble boron in the core, producing a positive contribution to the moderator temperature coefficient. In order to limit the dissolved boron concentration, rods with burnable absorbers are provided in the form of slightly enriched uranium with uniformly dispersed gadolinia particles. The number and type of burnable absorber rods are given in Table 4.3-1 and their distribution in one quadrant of the core is shown in Figures 4.3-1 and 4.3-2. The reactivity control provided by the burnable absorber rods is given in Table 4.3-1 and allows a reduction in the dissolved boron concentration to the values given in Table 4.3-1.

The calculated moderator temperature coefficients for various core conditions at the beginning and end of the first cycle are given in Table 4.3-4. The moderator temperature coefficients are more negative at EOC because the soluble boron in the coolant is reduced. The buildup of equilibrium xenon produces a net negative change of -0.70×10^{-4} $\Delta\rho/°C$ (-0.39×10^{-4} $\Delta\rho/°F$) in the moderator temperature coefficient; this change is mainly due to the accompanying reduction in critical soluble boron. The changing fuel isotopic concentrations and changing neutron spectrum during fuel depletion also contribute a small negative component to the moderator temperature coefficient.

The dependence of the moderator temperature coefficient on moderator temperature at the beginning and end of the first cycle (at constant soluble boron) is shown in Figures 4.3-31 and 4.3-32, respectively. These figures also show the expected moderator temperature coefficient at reduced power levels (corresponding to a reduced moderator temperature)

based on power reductions accomplished with soluble boron only and with CEAs only. These two modes of power reduction result in the most positive and most negative moderator temperature coefficients expected to occur at reduced power levels. Figures 4.3-31 and 4.3-32 show the expected moderator temperature coefficient for the full range of expected operating conditions and accident conditions addressed in Chapter 15.

4.3.2.3.3 Moderator Density Coefficient

The moderator density coefficient is the change in reactivity per unit change in the core average moderator density at constant moderator temperature. A positive moderator density coefficient translates into a negative contribution to the total moderator temperature coefficient, which is defined in Subsection 4.3.2.3.2. The density coefficient is generally positive in the operating range, although the magnitude decreases as the soluble boron level in the core is increased. The calculated density coefficient is shown in Table 4.3-4 and curves of density coefficient as a function of density for several soluble boron concentrations are presented in Figure 4.3-33. These curves are based on ROCS calculations and have been generated over a wide range of core conditions. The density coefficients explicitly used in the accident analyses are based on core conditions with the most limiting temperature coefficients allowed by the Technical Specifications. Table 4.3-3 shows a comparison of the expected values of the moderator temperature coefficients with those actually used in the accident analyses.

4.3.2.3.4 Moderator Nuclear Temperature Coefficient

The moderator nuclear temperature coefficient is the change in reactivity per unit change in core average moderator temperature, at constant moderator density. The source of this reactivity dependence is the spectral effects associated with the change in thermal scattering properties of water molecules as the internal energy, which is represented by the bulk water temperature, is changed. The magnitude of the moderator nuclear temperature coefficient is equal to the difference between the moderator temperature coefficient, defined in Subsection 4.3.2.3.2, and the moderator density coefficient, defined in Subsection 4.3.2.3.3.

4.3.2.3.5 Moderator Pressure Coefficient

The moderator pressure coefficient is the change in reactivity per unit change in reactor coolant system (RCS) pressure. Since an increase in pressure, at constant moderator temperature, increases water density, the pressure coefficient is merely the density coefficient expressed in a different form. The calculated pressure coefficient at full power is shown in Table 4.3-4.

4.3.2.3.6 Moderator Void Coefficient

Small amounts of local subcooled boiling in the reactor during full-power operation result in a predicted core average steam (void) volume fraction of less than 1 percent. Changes in the moderator void fraction produce reactivity changes that are quantified by the void coefficient of reactivity. An increase in voids decreases core reactivity, but the presence of soluble boron tends to add a positive contribution to the coefficient.

The calculated values of moderator void coefficient are shown in Table 4.3-4. Curves showing void coefficient versus void content can be inferred directly from the density coefficient curves provided in Figure 4.3-33.

4.3.2.3.7 Power Coefficient

The power coefficient is the change in reactivity per unit change in core power level. All previously described coefficients contribute to the power coefficient, but only the moderator temperature coefficient and the fuel temperature coefficient contributions are significant. The contributions of the pressure and void coefficients are negligible because the magnitudes of these coefficients and the changes in pressure and void fraction per unit change in power level are small. The contribution of moderator density change is included in the moderator temperature coefficient contribution.

In order to determine the change in reactivity with power, the changes in the nodal average moderator and effective fuel temperature with power are determined. The average moderator (coolant) temperature is controlled to be a linear function of power.

The core average LHR is also linear with power. The nodal average effective fuel temperature dependence on the core average LHR is calculated from the following semi-empirical relation:

$$T_f(p) = T_{MOD}(p) + \left(\sum_{i=0}^{3} B_i \times M^i\right) \times p + \left(\sum_{j=0}^{3} C_j \times M^j\right) \times p^2 + \left(\sum_{k=0}^{3} D_k \times M^k\right) \times p^3$$

(Eq. 4.3-1)

Where:

T_{MOD} = average moderator temperature (°F)

M = exposure in MWD/MTU

p = linear heat generation rate (LHGR) in the fuel in kW/ft

T_f = average effective fuel temperature (°F)

The coefficients B_i, C_j, and D_k are determined from least-squares fitting of the fuel temperature generated by FATES (References 2 and 3). For the APR1400 fuel pins, the following values apply:

$B_0 = +1.280 \times 10^{2}$	$C_0 = -5.793 \times 10^{-1}$	$D_0 = -8.422 \times 10^{-2}$
$B_1 = +1.767 \times 10^{-3}$	$C_1 = -9.705 \times 10^{-4}$	$D_1 = +1.597 \times 10^{-5}$
$B_2 = -2.376 \times 10^{-7}$	$C_2 = +5.008 \times 10^{-8}$	$D_2 = +2.712 \times 10^{-9}$
$B_3 = +2.348 \times 10^{-12}$	$C_3 = -6.352 \times 10^{-13}$	$D_3 = -1.278 \times 10^{-13}$

The basis for this relation is described in References 4 and 20.

The total power coefficient at a given core power can be determined by evaluation, for the conditions associated with the given power level, of the following expression:

$$\frac{d\rho}{dp} = \frac{\delta\rho}{\delta T_f} \times \frac{\delta T_f}{\delta p} + \frac{\delta\rho}{\delta T_m} \times \frac{\delta T_m}{\delta p}$$

(Eq. 4.3-2)

The first term of Equation 4.3-2 provides the fuel temperature contribution to the power coefficient, which is shown as a function of power in Figure 4.3-34.

The first factor ($\delta\rho/\delta T_f$) of the first term is the fuel temperature coefficient of reactivity, described in Subsection 4.3.2.3.1 and shown in Figure 4.3-30. The second factor ($\delta T_f/\delta\rho$) of the first term is obtained by calculating the derivative of Equation 4.3-1.

$$\frac{\delta T_f(p)}{\delta p} = \frac{\delta T_{MOD}(p)}{\delta p} + \left(\sum_{i=0}^{3} B_i \times M^i\right) + 2\left(\sum_{j=0}^{3} C_j \times M^j\right) \times p + 3\left(\sum_{k=0}^{3} D_k \times M^k\right) \times p^2$$

(Eq. 4.3-3)

The second term in Equation 4.3-2 provides the moderator contribution to the power coefficient. The first factor ($\delta\rho/\delta T_m$) of the second term, the moderator temperature coefficient, is described in Subsection 4.3.2.3.2 and shown in Figures 4.3-31 and 4.3-32. The second factor ($\delta T_m/\delta p$) of the second term is a constant because the moderator temperature is controlled to be a linear function of power.

Because the fuel temperature coefficient ($\delta\rho/\delta T_f$) and moderator temperature coefficient ($\delta\rho/\delta T_m$) are functions of one or more independent variables (e.g., burnup, temperature, soluble boron content, xenon worth, CEA insertion), the total power coefficient, dρ/dp, also depends on these variables.

The power coefficient tends to become more negative with burnup because the fuel and moderator temperature coefficients become more negative as shown in Figures 4.3-30 through 4.3-32. Insertion of the CEAs, while maintaining constant power, results in a more negative power coefficient because the soluble boron level is reduced and because of the spectral effects of the CEAs themselves. The full-power values of the overall power coefficient for the unrodded core at the beginning and end of the first cycle are shown in Table 4.3-4.

4.3.2.4 Control Requirements

The three basic types of control requirements that influence the design of this reactor are:

a. Reactivity control so that the reactor can be operated in the unrodded critical, full-power mode for the design cycle length

b. Power level and power distribution control so that reactor power can be safely varied from full power to cold shutdown and power distribution at any given power level is controlled within acceptable limits

c. Shutdown reactivity control sufficient to mitigate the effects of postulated accidents

Reactivity control is provided by several means. The amount and enrichment of the fuel and burnable absorber rods are design variables that determine the initial and EOC reactivity for an unrodded, unborated condition. Soluble boron and CEA absorbers are flexible means of controlling long-term and short-term reactivity changes, respectively.

The following subsections describe the reactivity balances associated with each type of control requirement.

4.3.2.4.1 Reactivity Control at BOC and EOC

The reactivity data for the unrodded core with no soluble boron are shown in Table 4.3-2. This table includes the reactivity worth of equilibrium xenon and samarium, and shows the reactivity available to compensate for burnup and fission product absorption. Soluble boron concentrations required for criticality at various core conditions are shown in Table 4.3-1. Soluble boron is used to compensate for slow reactivity changes such as those due to burnup and changes in xenon content. The reactivity controlled by burnable absorber rods is also given in Table 4.3-1. At EOC, the residual reactivity worth of the burnable absorber is less than 1 percent, and the soluble boron concentration is near zero. The reactor is to be operated in an unrodded condition at power. The CEA insertion at power is limited by the power-dependent insertion limit (PDIL) for short-term reactivity changes.

4.3.2.4.2 Power Level and Power Distribution Control

The regulating CEA groups can be used to compensate for changes in reactivity associated with routine power level changes. In addition, they can be used to compensate for minor variations in moderator temperature and boron concentration during operation at power and to dampen axial xenon oscillations. The reactivity worth of the regulating CEA groups is shown in Table 4.3-6. Soluble boron is used to maintain shutdown reactivity at cold zero-

power conditions. Soluble boron can also be used to compensate for changes in reactivity due to power level changes and minor changes in reactivity that may occur during normal reactor operation. Twelve part-strength CEAs are provided in the design. A major function of the part-strength CEAs is to assist in the control of core power distribution, including suppression of xenon-induced axial power oscillations during power operations, and control of axial power shape during load-following transients. The part-strength CEAs can also provide reactivity control to compensate for minor variations in moderator temperature and boron concentration during power operations and to assist in compensating for changes in reactivity from power level and xenon during load-following transients. The reactivity worth of the part-strength CEA groups is shown in Table 4.3-6.

4.3.2.4.3 Shutdown Reactivity Control

The reactivity worth requirements of the full complement of CEAs is determined primarily by the power defect, the excess CEA worth with the stuck-rod criteria described in Subsection 4.3.1.9, and the total CEA reactivity allowance for the cycle. Table 4.3-8 shows the reactivity component allowances. These data are based on EOC conditions, when the fuel and moderator temperature coefficients are most negative and the shutdown reactivity requirement is at maximum. Each allowance component is described in subsequent subsections. No CEA allowance is provided for xenon reactivity effects because these effects are controlled with soluble boron rather than with CEAs.

As shown in Table 4.3-9 for the end of the first cycle, the worth of all CEAs except for the most reactive, which is assumed to be stuck in the fully withdrawn position, provides shutdown capability required by the total reactivity allowance shown in Table 4.3-8. The margin is sufficient to compensate for calculated uncertainties in the nominal design allowances and in the CEA reactivity worth. Therefore, the shutdown reactivity control provided in this design is sufficient at all times during the cycle.

4.3.2.4.3.1 Fuel Temperature Variation

The increase in reactivity that occurs when fuel temperature decreases from the full-power value to the zero-power value is due primarily to the Doppler effect from U-238. The CEA reactivity allowance for fuel temperature variation, shown in Table 4.3-8, is a conservative allowance for the EOC conditions.

4.3.2.4.3.2 Moderator Temperature Variation

The moderator temperature variation allowance is large enough to compensate for any reactivity increase that may occur when the moderator temperature decreases from the full-power value to the zero-power (hot standby) value. This reactivity increase, which is due primarily to the negative moderator temperature coefficient, is largest at EOC, when the soluble boron concentration is near zero and the moderator coefficient is strongly negative. At BOC, when the moderator temperature coefficient is less negative, the reactivity change is smaller.

The CEA reactivity allowance for moderator temperature variation given in Table 4.3-8 is the sum of three allowances. The first, and most important, is the allowance for the moderator temperature coefficient effect. The second is an allowance for the reduction in CEA worth resulting from the shorter neutron diffusion length at the zero-power moderator density relative to the full-power moderator density. This allowance is necessary because the CEA worths shown in Table 4.3-6 were calculated at full power. The third allowance is intended to cover the reactivity effects associated with the greatest expected axial flux redistribution resulting from the difference in moderator temperature profile between full and zero power and the asymmetric axial isotopic distribution at EOC.

4.3.2.4.3.3 Moderator Voids

Reducing the power level from full power to zero power causes an increase in reactivity resulting from the collapsing of steam bubbles caused by local boiling at full power. The amount of void in the core is estimated to be less than 1 percent at full power. As with the moderator temperature effect, the maximum increase in reactivity from full to zero power occurs at EOC when the smallest amount of dissolved boron is present. The reactivity effect is small. The allowance for this effect is shown in Table 4.3-8.

4.3.2.4.3.4 Control Element Assembly Bite

The CEA bite is the amount of reactivity worth in CEAs that can be inserted in the core at full power to initiate ramp changes in reactivity associated with load changes and to compensate for minor variations in moderator temperature, boron concentration, xenon concentration, and power level. The insertion of part-strength CEAs (PSCEAs) at full

power, for load change operations, is included in the CEA bite allowance. The reactivity allowance for this effect is shown in Table 4.3-8.

4.3.2.4.3.5 Accident Analysis Allowance

The allowance shown in Table 4.3-8 for accident analysis is more conservative than that assumed under various postulated accident conditions addressed in Chapter 15, which result in acceptable consequences.

4.3.2.4.3.6 Available Reactivity Worth

Table 4.3-9 shows the reactivity worths of all CEAs and the highest reactivity worth of a single CEA in the fully withdrawn position for the end of the first cycle. This table also compares the available net shutdown worth (including the effects of the stuck CEA) to the reactivity worth requirements from Table 4.3-8. All required biases and uncertainties have been included in the CEA worths in Table 4.3-9. Subsection 4.3.3 presents detailed information on biases and uncertainties.

4.3.2.5 Control Element Assembly Patterns and Reactivity Worths

The locations of all CEAs are shown in Figure 4.3-35. The CEAs designated as regulating control rods are divided into five groups, the shutdown CEAs are divided into two groups, and the PSCEAs are assigned as a single group. *[These groups are identified for the first cycle operation in Figure 4.3-36]*,* and the location of the ex-core detectors is shown in Figure 4.3-37. All CEAs in a group are withdrawn or inserted quasi-simultaneously. Shutdown groups are inserted following the regulating groups and withdrawn before the regulating groups. *[The reactivity worths of sequentially inserted CEA groups are shown in Table 4.3-6 for the beginning, middle, and end of the first cycle.]** The values of F_r^n for these cases are shown in Table 4.3-10.

It is expected that the core will operate unrodded during full-power, base-load operation, except for limited insertion of the PSCEA group or the lead regulating group to compensate for minor variations in moderator temperature and boron concentration. Movement of the PSCEAs is restricted only by their effect on axial power distribution. For operation with substantial insertion of regulating CEAs, the relationship between power level and

maximum permitted CEA insertion is typified in Figure 4.3-38. This figure also illustrates the regulating group insertion order (5-4-3) and the 40 percent fixed overlap between successive regulating groups. Compliance with the power-dependent insertion limits throughout the cycle provides reasonable assurance that adequate shutdown margin is maintained and the core conditions are no more severe than the initial conditions assumed in the accident analyses described in Chapter 15.

Reactivity insertion rates for the accident analysis of the core are presented in Chapter 15. The full-power CEA ejection accident assumes the ejection of one CEA from the maximum insertion of the lead regulating bank allowed by the PDIL. The ejected CEA worth is calculated by taking the difference between the pre-ejected and post-ejected reactivity of the core computed by static methods. Similar CEA ejection event analyses are performed for zero power and several intermediate powers. The assumed initial rod configuration is the maximum transient insertion limit allowed by the power-dependent insertion limit of the CEA groups at that power.

The CEA withdrawal incident from low power is analyzed with the maximum calculated differential reactivity insertion rate resulting from a sequential CEA bank withdrawal with a 40 percent overlap. The CEA withdrawal incident from full power is analyzed from the insertion of the lead bank that corresponds to the PDIL at full power. Reactivity insertion rates are calculated by a static axial model of the APR1400 core. The calculated reactivity insertion resulting from a sequential CEA withdrawal is presented in Figures 4.3-39 and 4.3-40.

The full-strength CEA drop incident is analyzed by selecting the dropped CEA that maximizes the increase in the radial peaking factor. The radial peaking factors include an allowance for 30 minutes of xenon redistribution. A conservatively small negative reactivity insertion is used in the accident analysis.

The typical reactivity insertion during a reactor scram is presented in Section 15.0. This reactivity insertion is computed conservatively using the HERMITE (Reference 10) code for various axial power shapes. And it is used for all accidents that are terminated by a scram, unless otherwise indicated. The reactivity insertion is conservative because only the minimum shutdown worth of 8.0 percent $\Delta\rho$ is assumed to be available at hot full power. The scram reactivity insertion for the loss-of-flow event is implicit in the kinetic axial analysis.

4.3.2.6 Criticality of Reactor During Refueling

The soluble boron concentrations during refueling are shown in Table 4.3-1. These concentrations assure that the k_{eff} of the core does not exceed 0.95.

4.3.2.7 Stability

4.3.2.7.1 General

Pressurized water reactors (PWRs) with negative overall power coefficients are inherently stable with respect to power oscillations. Therefore, this discussion is limited to xenon-induced power distribution oscillations. Xenon-induced oscillations occur as a result of rapid perturbations to the power distribution, which cause the xenon and iodine distributions to be out of phase with the perturbed power distribution. This results in a shift in the iodine and xenon distribution that causes the power distribution to change in an opposite direction from the initial perturbation and causing oscillation of the power distribution. The magnitude of the power distribution oscillation can either increase or decrease with time. Thus, the core can be considered to be either unstable or stable with respect to these oscillations. The methods of analyzing the stability of the core considering xenon oscillations are described in Subsection 4.3.2.7.2. The tendency of certain types of oscillations to increase or to decrease is calculated, and the method of controlling unstable oscillations is presented.

4.3.2.7.2 Xenon Oscillation Analysis Methods

Two methods of analyzing xenon oscillations are available. The first method consists of an analysis of the spatial flux distribution, accounting for the space-time solution of the xenon concentration. This method is useful for testing various control strategies and evaluating transitional effects such as power maneuvers. The second method consists of modal perturbation theory analysis, which is useful for evaluating the sensitivity of the stability to changes in the reactor design characteristics and for the determination of the degree of stability for a particular oscillatory mode.

The stability of a reactor can be characterized by a stability index or a damping factor that is defined as the natural exponent that describes the growing or decaying amplitude of the oscillation. A xenon oscillation can be described by the following equation:

$$\phi(\bar{r},t) = \phi_o(\bar{r}) + \Delta\phi_o(\bar{r})e^{bt}\sin(\omega t + \delta) \quad \text{(Eq. 4.3-4)}$$

Where:

$\phi(\bar{r},t)$	=	space-time solution of the neutron flux
$\phi_o(\bar{r})$	=	initial fundamental flux
$\Delta\phi_o(\bar{r})$	=	perturbed flux mode
b	=	stability index
ω	=	frequency of the oscillation
δ	=	phase shift

Modal analysis consists of an explicit solution of the stability index b using known fundamental and perturbed flux distributions. A positive stability index b indicates an unstable core, and a negative value indicates stability for the oscillatory mode being investigated. The stability index is generally expressed in units of inverse hours, so that a value of -0.01/hr would mean that the amplitude of each subsequent oscillation cycle decreases by approximately 25 percent (for a period of approximately 30 hours for each cycle).

Xenon oscillation modes in PWRs can be classified into three general types: radial, azimuthal, and axial. To analyze the stability for each oscillation mode, only the first overtone needs to be considered since higher harmonic modes decay more rapidly than the first overtone.

4.3.2.7.3 Expected Stability Indices

4.3.2.7.3.1 Radial Stability

A radial xenon oscillation consists of a power shift inward and outward from the center of the core to the periphery. This oscillatory mode is generally more stable than an azimuthal mode. This effect is illustrated in Figure 4.3-41, which shows that for a bare cylinder, the radial mode is more stable than the azimuthal mode. Discussion of the stability for radial oscillatory modes is therefore deferred to that for the azimuthal mode.

4.3.2.7.3.2 Azimuthal Stability

An azimuthal oscillation consists of an X-Y power shift from one side of the reactor to the other. Simulation of this type of oscillation is performed for a range of expected reactor operating conditions.

The expected variation of the stability index during the first cycle is shown in Figure 4.3-42. These results are obtained from analyses that consider the spatial flux shape changes during the cycle, the changes in the moderator and Doppler coefficient during the cycle, and the change in xenon and iodine fission yield as a result of plutonium buildup during the cycle. As shown in Figure 4.3-42, the expected stability index is no greater than -0.095/hr at any time during the cycle for the expected mode of reactor operation.

4.3.2.7.3.3 Axial Stability

An axial xenon oscillation consists of a power shift toward the top and bottom of the reactor core. This type of oscillation can be unstable during the first cycle. Table 4.3-11 shows the calculated variation of the axial stability index during the first cycle. Control action with part-strength rods or full-strength rods may be required to limit the magnitude of the oscillation. As addressed in Subsection 4.3.2.2, the axial power distribution is monitored by COLSS and the RPS. Based on the COLSS measurement of the axial power distribution, the operator may move the full-strength or part-strength CEAs to control any axial oscillations.

4.3.2.7.4 Control of Axial Instabilities

Control of axial oscillations during a power maneuver is accomplished through the use of full-strength and/or part-strength control element assemblies (PSCEAs). PSCEAs are mainly used throughout these maneuvers to limit the change in power distribution as well as to control core reactivity. The difference between an uncontrolled and a controlled xenon oscillation is illustrated in Figure 4.3-43. It was assumed in the calculation of the controlled oscillation that the PSCEAs were moved in such a way as to preserve the initial shape in the core prior to the initiating perturbation. The calculations are performed at the end of the first cycle, which corresponds to the expected least-stable condition for axial xenon oscillations.

4.3.2.7.5 Summary of Special Features Required by Xenon Instability

The RPS, described in Subsection 7.2.2, is designed to prevent exceeding acceptable fuel design limits and to limit the consequences of postulated accidents. The RPS also provides reasonable assurance that under all allowed operating modes, the state of the reactor is confined to conditions not more severe than the initial conditions assumed in the design and analysis of the protective system.

Because the reactor is predicted to be stable with respect to radial and azimuthal xenon oscillations, no special protective system features are needed to accommodate radial or azimuthal mode oscillations. Nevertheless, a maximum quadrant tilt is prescribed along with prescribed operating restrictions if the tilt is exceeded. The azimuthal power tilt is determined by COLSS and included in the COLSS determination of core margin. The azimuthal power tilt limit is accounted for in the RPS.

4.3.2.7.5.1 Features Provided for Azimuthal Xenon Effects

a. Administrative limits on azimuthal power tilt

b. Monitoring and indicating the azimuthal power tilt in COLSS as well as accounting for the tilt in the COLSS determination of core margin

c. Accounting for the azimuthal power tilt limit in the RPS (CPC)

4.3.2.7.5.2 Features Provided for Axial Xenon Effects and Power Distribution Effect and Control

a. PSCEAs or regulating CEAs for control of the axial power distribution, if required

b. Monitoring and accounting for changes in the axial power distribution in the COLSS

c. Monitoring and accounting for the axial power distribution in the RPS (CPC)

4.3.2.8 Vessel Irradiation

Typical neutron fluxes inside the reactor vessel obtained by the calculation model described in Subsection 4.3.3.3 are shown in Table 4.3-5. In addition, fast neutron fluences (time-integrated neutron flux) at reactor vessel are shown in Table 4.3-7. The time integration is based on a 93 percent capacity factor for 60 years of design life.

Calculation uncertainty of neutron flux estimation methodology is within 20 percent, which is evaluated by uncertainty analysis covering uncertainties from geometrical modeling, material composition, core neutron source, and deviation from measurement data. The reactor vessel surveillance program is described in Subsection 5.3.1.6.

4.3.3 Analytical Methods

4.3.3.1 Reactivity and Power Distribution

4.3.3.1.1 Methods of Analysis

The nuclear design analysis of low-enrichment PWR cores is based on the three-dimensional ROCS nodal code and the two-dimensional transport code DIT (References 5 and 6). DIT provides cross sections averaged over a few broad energy groups for the whole assembly or individual cells, and few-group one-dimensional, two-dimensional, and three-dimensional diffusion theory calculations of integral and differential reactivity effects and power distributions. Differences between calculated and measured data for various nuclear parameters in the nuclear design and safety analysis are presented in Subsection 4.3.3.1.2.

The primary nuclear parameters used in the safety analysis are adjusted to account for known uncertainties and biases based on comparisons to measurement. As improvements in analytical procedures are developed, and improved data become available, they are incorporated into the design procedures after validation with relevant experimental data.

4.3.3.1.1.1 Cross Section Generation

Few-group cross sections for coarse-mesh and fine-mesh diffusion theory codes are prepared by the discrete integral transport (DIT) lattice code to be used in ROCS. The ROCS/DIT code system is documented in an NRC-approved topical report (Reference 5).

The essential components of the DIT lattice code are:

a. Spectral calculations using DIT theory in up to 85 energy groups for typical portions of the assembly geometry (e.g., fuel cell, fuel cell and burnable absorber, fuel cell, waterhole)

b. Few-group spatial calculations in exact assembly geometry followed by a leakage calculation to maintain a critical spectrum

c. Isotopic depletion calculations for every cell in the assembly

The use of the two-dimensional DIT code provides reasonable assurance that the effects of lattice heterogeneities are treated. Few-group cross sections for coarse-mesh spatial calculations are obtained and include accurate weighting of the various types of fuel, burnable absorber, and waterhole cells.

The assembly calculation, which is performed in several broad energy groups (ranging from 2 to 12), is preceded by a sequence of spectrum calculations performed in the basic cross section library of the energy group structure of up to 85 groups.

The geometries used in the spectrum calculations are replicas of portions of the true assembly geometry. Boundary conditions recycled from the assembly calculation are used for each spectrum geometry.

Group condensation based on the spectra calculated for all the different types of cells and subregions within them is performed to obtain few-group macroscopic cross sections that are passed on directly to the assembly calculations. Because the accuracy of the spectrum calculations is high, the group condensation can normally be performed with a standard four-group structure. More groups can sometimes be used in the assembly calculation. For example, a seven-group condensation is typically used for gadolinia-bearing assemblies.

The assembly and spectrum calculations are performed by integral transport theory with multigroup interface currents used to couple adjacent cells.

The entire sequence of calculations is normally performed assuming that there is no net leakage from the assembly geometry. Following the assembly calculation, fine-group spectra are constructed for all subregions in the assembly based on the spatial distribution of the few-group assembly flux and on the energy and spatial distribution of the fine-group flux from the spectrum calculations. A correction for the influence of global leakage is then made on the basis of a B1 calculation with the fine energy group structure for the homogenized assembly to maintain criticality of the assembly.

Few-group microscopic cross sections for use in the depletion stage of DIT are formed using the basic cross section library and the spectra calculated as described.

Spatial averages of microscopic and macroscopic cross sections are performed for editing purposes and are passed on to ROCS.

The DIT code uses a data library containing multigroup cross sections, fission spectra, fission product yields, and other supplemental data. The principal source of data for the library is ENDF/B-IV. Three adjustments to the library data have been made to reflect changes to ENDF/B-IV recommended by the cross-sectional evaluation working group for ENDF/B-V.

The adjustments are as follows:

a. Reduction of about 3 percent in the shielded resonance integral of U-238

b. Adoption of the harder Watt fission spectra for U-235 and Pu-239

c. A moderate upward adjustment of U-235 and Pu-239 thermal $\bar{\nu}$ values of about 0.1 percent, improving the $\bar{\nu}$ and η discrepancy

Several improvements have been made to the DIT calculation methodology described in Reference 5. These improvements, described and approved in References 7 and 8, include the use of anisotropic scattering and higher-order interface currents.

4.3.3.1.1.2 Coarse-Mesh Methods

Static and depletion-dependent reactivity and nuclide concentrations, flux and power distributions in two-dimensional and three-dimensional representations of the core are determined by a diffusion-depletion program, ROCS, which is described in Reference 5. The ROCS program was approved for use as a PWR core design and analysis code by the NRC in Reference 5. The ROCS program is designed to perform two-dimensional or three-dimensional coarse-mesh reactor core calculations based on a two-group nodal expansion method, with full-core, half-core, or quarter-core symmetric geometries. The mesh consists of rectangular parallelepiped "nodes" arranged contiguously in the X-Y plane, with one or more axial meshes (or planes) in the Z direction. In most applications, only the active core region is represented, with albedo-like boundary conditions assigned to exterior nodes. A typical ROCS core geometry uses four nodes per assembly in the X-Y plane and 20 to 30 axial planes depending on core height and in-core instrument locations.

The nodal macroscopic group constants used in the neutronics calculation are constructed from detailed isotopic concentrations and microscopic cross sections processed by the code. The specified isotopes include fixed-depletable isotopes and a lumped residual representing non-depletable isotopes. The depletable isotopes include fission chain isotopes, fission products, and burnable absorbers. Control rods are represented by macroscopic cross sections specific to different rod banks.

The ROCS system performs coarse-mesh depletion calculations for each node in a two-dimensional or three-dimensional core configuration. The allowed depletion chains are internally modeled with fixed-depletion equations so that beyond the input cross-section data, the user need to supply only data such as initial concentrations, decay constants, and fission yields for each depletion nuclide. These include the principal uranium and plutonium isotopes; a fuel exposure chain; xenon and samarium fission product chains; and boron, gadolinium, and erbium burnable absorber chains.

The fixed-depletion equations used in the ROCS code are derived through the standard procedure of analytically integrating the coupled linear rate equations, which represent each chain. The depletion equations are solved using the flux and microscopic cross-section values based on the neutronic and thermal-hydraulic feedback calculations preceding the depletion time step. The initial flux and cross sections are assumed to be constant over the depletion time step.

Cross-section information used in the ROCS system is derived from microscopic cross sections supplied by DIT for each nuclide in two energy groups. This information is used in two basic forms. First, two-group macroscopic cross sections are used in the basic flux and eigenvalue calculation. The microscopic contributions from thermal-hydraulic feedbacks, xenon, soluble boron, and control rods are added before the flux calculation. Second, two-group microscopic cross sections are used in the depletion and xenon short-term time-stepping calculations.

4.3.3.1.1.3 Fine-Mesh Methods

The ROCS code, which is described and approved in Reference 5, performs mesh-centered pin-peaking calculations for each node in two-dimensional or three-dimensional core geometries. The ROCS uses an embedded fine-mesh diffusion theory method for obtaining pin power distributions from coarse-mesh calculations. The improvements made to the ROCS methodology described in Reference 5 include the use of a predictor/corrector method for gadolinia-bearing fuel described and approved for use in Reference 9 and the use of assembly discontinuity factors described in Reference 8 and approved for use in Reference 7.

A method has been developed for determining diffusion coefficients that permits the inclusion of transport effects when combined with the finite difference formulation of ROCS. The diffusion coefficients conserve cell averaged fluxes, reaction rates, and net leakage across cell boundaries. Thus, the ROCS program can effectively reproduce DIT local power distributions.

Having determined diffusion coefficients that exactly reproduce average fluxes, reaction rates, and net currents from transport theory for a particular geometry, it is then asserted that they are universally applicable independent of the size of the flux gradients seen in the core.

The nodal diffusion equations are solved as a boundary source problem for the embedded calculation. The partial in-currents on each nodal face and the global eigenvalue are supplied by the ROCS coarse-mesh calculation.

After completion of the fine-mesh embedded calculation, the fine-mesh power distribution is renormalized to the coarse-mesh power level to assure that coarse-mesh and fine-mesh node average powers and burnups will remain the same during depletion.

The ROCS embedded calculation uses a macroscopic cross-section model based on interpolation of multi-dimensional macroscopic tables. These tables are created by the MCXSEC code, which processes DIT results for all assembly types, and are typically burnup, enrichment, moderator, and fuel temperature dependent for each fine-mesh pin cell type. Lagrange linear interpolations are performed to obtain the macroscopic cross sections. The interpolated absorption cross section is then corrected for soluble boron and xenon changes by using boron and xenon microscopic cross sections along with number densities obtained from the core soluble boron and local xenon equilibrium concentrations. Axial leakage is represented by adding a DB^2 term to the absorption cross section.

4.3.3.1.1.4 Other Analysis Methods

As the size of large power reactors increases, space-time effects during reactor transients become more important. In order not to penalize reactor performance unduly with overly conservative design methods, it is desirable to have the capability to perform detailed space-time neutronics calculations for both design and off-design transients.

The HERMITE code (Reference 10) solves the few-group, space and time-dependent neutron diffusion equation including feedback effects of fuel temperature, coolant temperature, coolant density, and control rod motion. The neutronics equations in one, two, and three dimensions are solved by the fourth-order nodal expansion method. The fuel temperature model explicitly represents the pellet, gap, and clad regions of the fuel pin, and the governing heat conduction equations are solved by a finite difference method. Continuity and energy conservation equations are solved to determine the coolant temperature and density. In the one-dimensional mode, HERMITE also has the option of finding the axially dependent absorber distribution required to produce a particular user-specified axial power shape. This option is often used to produce conservative axial power

shapes corresponding to the LCO limits on axial power shape from which simulations of core transients are subsequently initiated.

CEA shadowing is the change in ex-core detector response resulting from changing the core configuration from an unrodded condition to a condition with CEAs inserted, while maintaining constant power operation. Although CEA shadowing is a function of the relative azimuthal locations of the higher-power peripheral assemblies and the ex-core detectors, its effect is minimized by placing the ex-core detectors at azimuthal locations where minimum CEA shadowing occurs. CEA shadowing factors can be determined using detailed two- or three-dimensional power distributions calculated by ROCS, representing the cumulative presence of the various CEA banks and the DORT code (Reference 11).

Normalized CEA shadowing factors are relatively constant with burnup and power level changes made without moving CEAs. CEA shadowing factors at the beginning and end of the first cycle are as shown in Table 4.3-12.

Shadowing factors account for the radial power distribution effects and the shape-annealing function accounts for the axial power distribution effects on the ex-core detector responses. Each detector subchannel responds to neutrons from the entire length of the core, not just from the section immediately opposite the subchannel due to neutron scattering in the various regions that separate the core and the ex-core detectors. This effect is independent of the power shape and the azimuthal CEA shadowing factors. Typical axial annealing functions, given as fractional response per percent of core height for a three-subchannel system, are shown in Figure 4.3-44.

Axial shape-annealing functions are determined utilizing a fixed-source adjoint MCNP calculation. MCNP (Reference 21) is a Monte Carlo N-particle transport code. The three-dimensional geometry model is used for the annealing calculation with representation of the core, vessel, vessel internals, air gap, and biological shield. Three adjoint MCNP calculations are performed with an adjoint source in each ex-core detector subchannel. Figure 4.3-45 illustrates the MCNP calculation model used.

The subchannel responses for each axial slice of reactor core can be determined by integrating the fission spectrum weighted adjoint fluxes ascribed to the adjoint source located at one of the subchannels. The annealing curves shown in Figure 4.3-44 are

determined using this same technique for other subchannels and normalizing the responses to the total ex-core detector response of all three subchannels,.

Because the annealing curve is determined regardless of the axial power shape, the resulting annealing functions, S(z), is multiplied by the peripheral axial power distributions, P(z), to obtain the ex-core detector responses for each subchannel as follows:

$$D_{lower} = \int_0^H P(z)S(z)_{lower}\,dz = \text{Lower detector response} \quad \text{(Eq. 4.3-5)}$$

$$D_{middle} = \int_0^H P(z)S(z)_{middle}\,dz = \text{Middle detector response} \quad \text{(Eq. 4.3-6)}$$

$$D_{upper} = \int_0^H P(z)S(z)_{upper}\,dz = \text{Upper detector response} \quad \text{(Eq. 4.3-7)}$$

The shape-annealing functions are essentially geometric correction factors applied to the peripheral axial power distribution. As such, the effects of time in fuel cycle, transient xenon redistribution and CEA insertion, although affecting the peripheral bundle power shape, do not affect the geometric shape-annealing correction factors.

The ex-core detector temperature decalibration effect is the relative change in detector response as a function of reactor water inlet temperature at constant power. The temperature decalibration effect is calculated using the ANISN one-dimensional transport code (Reference 11), with explicit representation of core, vessel internals, vessel, and ex-core detector for various reactor inlet temperatures. Figure 4.3-46 shows the typical detector temperature decalibration effects as a function of inlet temperature normalized to an inlet temperature of 290.6 °C (555 °F).

Final normalization of the CEA shadowing factors, shape-annealing functions, and temperature decalibration constants is accomplished during startup testing.

4.3.3.1.2 Comparisons with Experiments

The nuclear analytical design methods in use for the APR1400 were checked against a variety of critical experiments and operating power reactors. In the first type of analysis, reactivity and power distribution calculations were performed, which produced information concerning the validity of the basic fuel cell calculation. The second type of analysis consisted of a core-follow program in which power distributions, reactivity coefficients,

reactivity depletion rate, and CEA worths were analyzed to provide a global verification of the nuclear design package.

The comparison between calculations and measurements served not only to verify the calculation methodology but also provided a set of calculation biases and uncertainties that are applied to the calculation results to yield best-estimate and 95/95 confidence limit predictions for use in the safety analysis. Verification of the basic methodology was demonstrated and approved by the NRC (Reference 5). Biases and uncertainties for the DIT/ROCS code system were also documented and approved (Reference 5). Implementation of the improvements for the core design and accumulation of measurement data necessitated an update of the biases and uncertainties to provide reasonable assurance that 95/95 confidence limits are maintained in all results used for licensing-related analyses. These updated biases and uncertainties are summarized in Reference 12. The revisions do not represent a change in methodology but are intended to maintain the approved level of accuracy in Reference 5.

4.3.3.1.2.1 Critical Experiments

Selected critical experiments have been analyzed with the DIT code. The selection of critical experiments is based on the following criteria:

a. Applicability to Combustion Engineering (C-E) fuel and assembly designs

b. Self-consistency of measured parameters

c. Availability of adequate data to model the experiments

Two groups of critical experiments using rod arrays representative of the 14 × 14 assembly have been used in this evaluation. The first is a series of clean experiments with UO_2 fuel carried out in 1967 (Reference 13), and the second is a set of experiments carried out in 1969 (Reference 5). Tables 4.3-13 and 4.3-14 give the principal parameters for each experimental configuration. The moderator-to-fuel volume ratios were varied by changing the cell pitch of the fuel rod arrangement. The moderator and reflector material for all cores was water.

Measurements included the criticality parameters and the fission rate distributions in selected fuel rods. Subsection 4.3.3.1.2.1 addresses the comparisons between measured and calculated criticality, as well as between measured and calculated fission rate distributions that were completed to establish calculative biases and uncertainties in predicting intra-assembly power peaking for both 14 × 14 and 16 × 16 arrays.

a. Description of the experiments

1) C-E sponsored UO_2 critical experiments

A series of critical experiments was performed by C-E at the Westinghouse Reactor Evaluation Center using the Canadian Research Reactor (CRX). The experimental program consisted of approximately 70 critical configurations of fuel rods. The basic core configuration was a 30 × 30 square fuel rod array of Zircaloy-4 clad UO_2 fuel with an enrichment of 2.72 weight percent U-235. Fuel rods were removed to create internal waterholes or channels to accommodate control rods or to simulate control rod channels and water gaps representative of the C-E 14 × 14 fuel assembly design.

The majority of the experiments used a lattice pitch of 1.524 cm (0.600 in) with several experiments repeated for a lattice pitch of 1.4605 cm (0.575 in). These pitch values, together with the fuel pellet dimensions, enrichment, and rod diameter resulted in hydrogen-to-fuel ratios representative of the 14 × 14 design at both room and operating temperatures.

2) KRITZ experiments

A program of critical experiments, sponsored jointly by C-E and SIEMENS/Kraftwerk Union AG (KWU), was performed at the KRITZ critical facility of AB Atomenergi, Studsvik, Sweden. The program consisted of analyzing a number of core configurations of interest to C-E and SIEMENS/KWU. The C-E configurations were representative of the 14 × 14 fuel assembly, including the five large control rod channels. A basic cell pitch of 1.4351 cm (0.5650 in) was used for all lattices. The cores were relatively large both in cross-sectional area and height. Each core contained about 1,450

rods that were 265 cm (104.3 in) long. The core was reflected with water on the four sides and the bottom. Soluble boron was used for gross reactivity control.

b. Results of analyses

The results of the analyses of the six critical experiments are summarized in Table 4.3-15. The average k_{eff} was 1.0016.

As part of the C-E and KRITZ critical experimental programs, pin-by-pin power distributions were measured to provide a database with which to define biases and uncertainties in predicted waterhole peaking factors. This analysis is described in detail in Reference 14. The bias and 95/95 tolerance range for assembly peaking factors is 0.0 percent and 2.78 percent, respectively (Reference 12).

4.3.3.1.2.2 Operating Power Reactors

The accuracy of the calculation system is assessed through the analysis of experimental data collected on operating power reactors. The data under investigation consist of the core reactivity balance data, reactivity coefficients, power distributions, and rod worths measured during the startup period and at power operation.

4.3.3.1.2.2.1 Startup Data

Measured data obtained during reactor startup are the most reliable because they are obtained under well-controlled conditions.

The analysis of the errors in the calculated reactivity as a function of the difference between a core average moderator temperature and a base temperature showed that the gradient of the reactivity bias against the temperature difference is 0.001 (Reference 12). These values have been incorporated into the total reactivity bias for DIT/ROCS, described in the depletion data of the next section.

a. Isothermal temperature coefficient

The isothermal temperature coefficient (ITC) is the change in core reactivity resulting from a 1 °C (1 °F) change in moderator and fuel temperatures.

The error in the calculated ITC has been determined by comparing the isothermal temperature coefficients measured for a number of reactors and cycles, both at power and at zero power, and for a wide range of soluble boron concentrations, with three-dimensional ROCS calculations performed at the same conditions as the measurements.

The best-estimate ITC and the 95/95 tolerance limit ITC are computed as follows:

$$ITC_{be} = ITC_{calc} + B_{itc}$$
$$= ITC_{calc} - 0.0152 - 0.9825 \times 10^{-4} \times PPM \ (10^{-4}\Delta\rho/^{\circ}F) \qquad \text{(Eq. 4.3-8)}$$

and

$$ITC\ (\pm\ 95/95) = ITC_{calc} + B_{itc} \pm K\ (95/95) \times \sigma\ (10^{-4}\Delta\rho/^{\circ}F) \qquad \text{(Eq. 4.3-9)}$$

Where:

ITC_{be} = the best-estimate ITC

ITC_{calc} = the calculated ITC

PPM = soluble boron concentration

B_{itc} = the ITC bias

K (95/95) = 2.120

σ = 0.0736

b. Control rod bank worths

The bias and uncertainty in calculated CEA worths (Reference 12) were found to be +1.87 percent and ±6.52 percent for total or net worths. The bias and uncertainty for group or bank worth were found to be +2.42 percent and ±15.5

percent, respectively. The difference in uncertainties between total and group or bank worths is due to the fact that most of the bank worths were small, resulting in greater relative errors because of the measurement uncertainty effects.

c. Dropped, ejected, and net rod worths

The dropped-worth bias and uncertainty are chosen as those of the bank worth. The dropped-worth bias and uncertainty are comparable to those of the bank worth because they both have similar and small biases and uncertainties in absolute units. The large relative uncertainties are misleading because they apply to very small worths.

The ejected-worth bias and uncertainty are expressed in relative units for small worths and absolute units for larger worths:

	Bias	Kσ
Worth < 0.24 %Δρ	4.0 %	31 %
Worth ≥ 0.24 %Δρ	0.006 %Δρ	0.077 %Δρ

The net-worth bias and uncertainty are chosen as those of the total worth because the total worth is representative of the rod density at the N-1 condition. The assumption is conservative because the N-1 configuration is strongly affected by the reactivity of the unrodded zone. The N-1 configuration is less sensitive to the precision of the calculated control rod cross section than the fully rodded configuration of the total worth.

d. Power coefficient

The error in DIT/ROCS power coefficients is characterized by a power-dependent bias given by:

$$B_{pc} = -5.78 + 7.43 \times 10^{-4} \times BU + 0.145 \times P \ (\%) \qquad \text{(Eq. 4.3-10)}$$

where,

P = % power

BU = core average exposure (MWD/MTU)

and a 95/95 probability/confidence tolerance band of ±14 percent.

4.3.3.1.2.2.2 Power Operation Data

The two quantities that are monitored continually during nominal full-power operation are the reactivity depletion rate and the power distribution. The constant monitoring of these quantities establishes the validity of the nuclear design.

The reactivity depletion rate is monitored by comparing measured critical steady-state conditions with corresponding calculated conditions. These conditions are characterized by exposure, power level, boron concentration, inlet temperature, and control rod insertion.

The reactivity bias and 95/95 probability/confidence tolerance band at BOC and EOC, obtained from comparisons between measurements and calculations (Reference 12) are as follows:

$$B_\rho (F, BOC) = +0.405 - 0.001 \times (T_{mod} - 573) - X \pm 0.24 \ (\%\Delta\rho) \quad \text{(Eq. 4.3-11)}$$

$$B_\rho (L, BOC) = +0.139 - 0.198 \times P - 0.0875 \times \varepsilon - X \pm 0.20 \ (\%\Delta\rho) \quad \text{(Eq. 4.3-12)}$$

$$B_\rho (EOC) = +0.3315 - 0.6478 \times \varepsilon + 1.087 \times 10^{-4} \times BU - 0.198 \times P - X \ (\%\Delta\rho) \quad \text{(Eq. 4.3-13)}$$

Where:

P = fraction of full power

ε = reactor enrichment (w/o U-235 as if all fuel is fresh)

X = differential grid worth (0.04 %Δρ per Reference 12)

T_{mod} = average moderator temperature in °F

BU = cycle length in MWD/MTU

F and L refer to first and later cycles, respectively.

The power dependence of the reactivity bias is measured by the power ascension test performed during startup testing described in Subsection 4.3.3.1.2.2.1. The adjustment for grid worth is required because the DIT/ROCS system does not account for the grid effect on the calculated reactivity.

The uncertainty to be attributed to calculated fuel assembly power distributions is obtained by comparing detailed three-dimensional calculations of the assembly powers with those inferred from in-core measurements with the CECOR (Reference 15) system using fixed in-core rhodium detectors. The resulting differences are a reflection of both measurement and calculative errors.

In order to determine the uncertainty to be attributed to the calculation, the measurement uncertainty is subtracted from these difference distributions. The measurement uncertainty is from an uncertainty evaluation associated with the CECOR system (Reference 16).

Table 4.3-16 summarizes the calculation uncertainties.

4.3.3.2 Spatial Stability

4.3.3.2.1 Methods of Analysis

An analysis of xenon-induced spatial power oscillations may be done by two classes of methods: time-dependent spatial calculations and linear modal analysis. The first method is based on computer simulation of the space, energy, and the time dependence of neutron flux and power density distributions. The second method calculates the damping factor based on steady-state calculations of flux, importance (adjoint flux), xenon and iodine concentrations, and other relevant variables.

The time-dependent calculations are indispensable for studies of the effects of CEA, core margin, ex-core and in-core detector responses, and other factors, and are performed in one, two, and three dimensions with few-group diffusion theory, using tested computer codes and realistic modeling of the reactor core.

4.3.3.2.2 Radial Xenon Oscillations

To confirm that the radial oscillation mode is extremely stable, a space-time calculation was run for a reflected, zoned core of the APR1400 prototype plant, without including the damping effects of the negative power coefficient. The initial perturbation was an absorber worth of 0.4 percent in reactivity placed in the central 20 percent of the core for 1 hour. Following removal of the perturbation, the resulting oscillation was followed in 4-hour time steps for a period of 80 hours. The resulting oscillation died out very rapidly with a damping factor of about –0.06 per hour. When this damping factor is corrected for a finite time step size by the formula in Reference 18, a more negative damping factor is obtained, indicating an even more strongly convergent oscillation. On this basis, it is concluded that radial oscillation instability will not occur. This conclusion is also applicable to the APR1400.

4.3.3.2.3 Azimuthal Xenon Oscillations

The azimuthal xenon stability was analyzed by using the ROCS code to perform explicit simulation of the core behavior following an azimuthal perturbation. The perturbation consisted of a 16.7 °C (30 °F) asymmetry in the core inlet temperature distribution and included the effects of power and moderator feedback. The finite time step length was used in the ROCS simulation.

4.3.3.2.4 Axial Xenon Oscillations

The axial xenon oscillation was analyzed by using the ROCS code to perform a simulation of the core behavior following an axial perturbation. The perturbation induced by power change was maintained at 50 percent of full power for the first 2 hours and returned to 100 percent power after 2 hours and remained unchanged for up to 100 hours. The finite time step length was used in the ROCS simulation.

Axial xenon oscillation experiments performed at the Fort Calhoun Nuclear Power Plant (United States) at a core exposure of 7,075 MWD/MTU and at the Stade Nuclear Power Plant (Germany) at BOC and at 12,200 MWD/MTU (Reference 18) were analyzed with a space-time one-dimensional axial model. The results are given in Table 4.3-17 and show no systematic error between the experimental and analytical results.

4.3.3.3 Reactor Vessel Fluence Calculation Model

The fission neutrons starting from the reactor core are attenuated by the core shroud, core support barrel, and reactor coolant, which exist between the core and reactor vessel. The neutron flux calculation methodology is selected in accordance with Regulatory Position 1 of NRC RG 1.190, "Calculational and Dosimetry Methods for Determining Pressure Vessel Neutron Fluence."

The DORT code (Reference 11) is used to evaluate neutron flux distributions. DORT is widely used in the nuclear industry for flux-distribution evaluations of reactor vessels. DORT is a discrete-ordinates Sn code and can perform calculations in (X, Y), (R, θ), and (R, Z) geometry.

To determine the reactor vessel neutron flux distribution, (R, θ) geometry is selected to effectively model the circular shape of the core support barrel and reactor vessel. Rectangular geometries of the fuel assemblies and the core shroud are finely approximated by giving a sufficient number of (R, θ) meshes. The approximation in the geometrical modeling is considered in the calculation uncertainty. Axial variations of neutron fluxes are considered by applying long-term axial power distributions with a bounding axial peaking factor of 1.15 to two-dimensional (R, θ) calculation results.

For the DORT calculations, the BUGLE-93 (Reference 19) cross-section library is used, which is generated from ENDF/B-VI data collapsed to 47 neutron energy groups. An S_8 fully symmetric angular quadrature set and P_3 angular decomposition of the scattering cross sections are used in the transport calculation.

4.3.4 Changes

The APR1400 plant nuclear design is very similar to the System 80+ design, having the same core size and fuel lattice type (16 × 16 C-E fuel type), which was licensed by the NRC in 1997. There is no significant nuclear design change compared to the System 80+ design.

4.3.5 Combined License Information

No COL information is required with regard to Section 4.3.

4.3.6 References

1. Combustion Engineering, Inc., "COLSS, Assessment of the Accuracy of PWR Operating Limits as Determined by the Core Operating Limit Supervisory System," CENPD-169, C-E Proprietary Topical Report, July 1975; and Combustion Engineering, Inc., "Overview Description of the Core Operating Limit Supervisory System (COLSS)," CEN-312, Rev. 01, C-E Proprietary Report, November 1986.

2. P. H. Gavin and P. C. Rohr, "Development and Verification of a Fuel Temperature Correlation for Power Feedback and Reactivity Coefficient Application," Trans. Am. Nucl. Soc., 30, 765 (1978).

3. Combustion Engineering, Inc., "C-E Fuel Evaluation Model Topical Report," CENPD-139, Rev. 01 (Non-Proprietary), CENPD-139 Supplement 1, Rev. 01 (Non-Proprietary), July 1974.

4. P.C. Rohr, "Burnup Dependent Fuel Temperature Correlation for System 80 (108232), PDP-78-076, August 2, 1978.

5. Combustion Engineering, Inc., "The ROCS and DIT Computer Codes for Nuclear Design," CENPD-266-P-A, CE Proprietary Topical Report, April 1983.

6. A. Jonsson, J.R. Rec, and U.N. Singh, "Verification of a Fuel Assembly Spectrum Code Based on Integral Transport Theory," Trans. Am. Nucl. Soc., 28, 778 (1978).

7. U.S. Nuclear Regulatory Commission, "Safety Evaluation by the Office of Nuclear Reactor Regulation Related to Amendment No. 61 to Facility Operating License No. NPF-41. Arizona Public Service et al., Palo Verde Nuclear Generating Station, Unit No. 1, Docket No. STN 50-528."

8. "Palo Verde Nuclear Generating Station (PVNGS) Unit 1-Proposed Reload Technical Specification Changes-Unit 1 Cycle 4," File: 91-056-026: 91-005-419-5.

9. Combustion Engineering, Inc., "CE Methodology for Core Design Containing Gadolinia-Urania Burnable Absorbers," CENPD-275-P Rev, 1-P-A, May 1988.

10. P. E. Rohan, S. G. Wagner, and S. E. Ritterbusch, "HERMITE, A Multi-Dimensional Space-Time Kinetics Code for PWR Transients," Combustion Engineering Topical Report CENPD-188-A, July 1976.

11. Oak Ridge National Laboratory, "One-Dimensional, Two-Dimensional and Three-Dimensional Discrete Ordinates Transport Code System," CCC-650/DOORS3.2, RSICC, 1998.

12. "Methodology Manual – Physics Biases and Uncertainties," CE-CES-129 Revision 9-P, March 2003.

13 E. G. Taylor, et al., "Combustion Engineering, Inc., Critical Experiments," WCAP-7102, October 16, 1967.

14. P. H. Gavin and H.G. Joo, "Evaluation of Assembly Peaking Factors by DIT with P1 Scattering and DP2 Cell Coupling," PHA-88-109, November 2, 1988.

15. Combustion Engineering, Inc., "A Method of Analyzing In-Core Detector Data in Power Reactor," CENPD-145, C-E Topical Report, April 1975.

16. Combustion Engineering, Inc., "INCA/CECOR Power Peaking Uncertainty," CENPD-153-P, Rev. 1-P-A, May 1980.

17. C.G. Poncelot, "The Effect of a Finite Time Step Length on Calculated Spatial Xenon Stability Characteristics in Large PWRs," Trans. ANS, 10, 2, p 571, 1967.

18. A. Gruen, "Meassung Physikalischer Kenngroessen an Leistungsreakoren," Atomkernenergie, 25, 2, 1975.

19. D. T. Ingersoll, et al., "Production and Testing of the VITAMIN-B6 Fine-Group and the BUGLE-93 Broad Group Neutron/Photon Cross section Libraries Derived from ENDF/B-VI Nuclear Data," DLC-175, ORNL-6795, January 1995.

20. KEPCO Nuclear Fuel Co., Ltd., "Evaluation of Fuel Temperature Correlation of PLUS7 for Korean Standard Nuclear Power Plants," KNF-TR-ND1-05001, Rev. 0, March 2005.

21. Los Alamos National Laboratory, “MCNP-A General Monte Carlo N-Particle Transport Code, Version 5-1. 40,” LA-CC-02-083, November 2005.

Table 4.3-1 (1 of 2)

Nuclear Design Characteristics

Item	Value
Fuel management	3-batch, mixed central zone
Core average burnup (MWD/MTU), 10 ppm soluble boron	17,571
First core average discharge burnup (MWD/MTU)	*[28,914]**
Core average U-235 enrichment (w/o)	2.66
Core average H_2O/UO_2 volume ratio, first cycle, hot (core cell)	*[2.12]**
Number of CEAs	
Full strength	81
Part strength	12
Burnable absorber rods	
Number	1,680
Material	Gd_2O_3-UO_2
Worth at BOC, hot, 308.9 °C (588 °F), %Δρ	8.8
Worth at BOC, cold, 20 °C (68 °F), %Δρ	6.5
Dissolved boron content for criticality, ppm (CEAs withdrawn, BOC)	
Cold, 20 °C (68 °F)	1,238
Hot, zero power, clean, 291.3 °C (556.3 °F)	1,187
Hot, full power, clean, 308.9 °C (588 °F)	1,067
Hot, full power, equilibrium Xe	817
Dissolved boron content, ppm, for:	
Refueling	2,150
5% subcritical, cold, first cycle (all CEAs out) 0 MWD/MTU	*[1,637]**
5% subcritical, hot, first cycle (all CEAs out) 0 MWD/MTU	*[1,695]**
Inverse boron worth, ppm/%Δρ (BOC/EOC)	
Hot, 308.9 °C (588 °F)	91/84
Cold, 20 °C (68 °F)	73/60
Neutron parameters	
Neutron lifetime (cycle average), microseconds	27.5
Delayed neutron fraction (cycle average)	0.0058

Table 4.3-1 (2 of 2)

Item	Value
Plutonium buildup (first cycle)	
g fissile Pu (final) / kg U (original)	*[4.8]**
g total Pu (final) / kg U (original)	*[6.28]**

Table 4.3-2

Effective Multiplication Factors and Reactivity Data(1)

Condition	k_{eff}	Reactivity (ρ)
Cold, 20 °C (68 °F), 0 ppm, BOC	1.214	0.176
Cold, 20 °C (68 °F) at minimum refueling boron concentration (2,150 ppm), BOC	0.899	–0.112
Hot, 291.3 °C (556.3 °F), zero power, clean (0 ppm), BOC	1.154	0.134
Hot, full power, no Xe or Sm, 308.9 °C (588 °F), 0 ppm, BOC	1.132	0.117
Hot, full power, equilibrium Xe (0 ppm), 1,000 MWD/MTU	1.096	0.088
Hot, full power, equilibrium Xe and Sm (0 ppm), 1,000 MWD/MTU	1.090	0.082
Reactivity decrease, hot		
Zero to full power, BOC (817 ppm)		0.012
Fuel temperature		0.011
Moderator temperature		0.001
Reactivity decrease, hot		
Zero to full power, EOC (10 ppm)		0.019
Fuel temperature		0.008
Moderator temperature		0.011

(1) No control element assemblies or dissolved boron except as noted, initial core

Table 4.3-3

Comparison of Core Reactivity Coefficients
with Those Used in Various Accident Analyses

Coefficients from Table 4.3-4	Moderator Temperature Coefficient ($\Delta\rho$/ °C × 10^{-4}) ($\Delta\rho$/ °F × 10^{-4})	Doppler Coefficient(1)	Density Coefficient ($\Delta\rho$/gm/cm^3)
Full power			
BOC	–1.71 (–0.95)	Figure 4.3-30	0.032
EOC	–4.34 (–2.41)	Figure 4.3-30	Not applicable (N/A)
Zero power, CEA groups 5, 4, and 3 inserted			
BOC	–1.59 (–0.88)	Figure 4.3-30	N/A
EOC	–3.73 (–2.07)	Figure 4.3-30	N/A
Coefficients Used in Accident Analyses			
CEA withdrawal			
Full/zero power	0/+0.9(3) (+0.5)	0.819/0.819	N/A
CEA misoperation			
Dropped CEA	–5.4(3) (–3.0)	1.181	N/A
Loss of flow	0.0(3)	0.819	N/A
CEA ejection			
BOC, full/zero power	0/+0.9(3) (+0.5)	0.819/0.819	N/A
Loss-of-coolant accident			
Small break	0	1.0	(2)
Large break	+0.9 (+0.5)	1.0	(2)

(1) Nominal values of the Doppler coefficient, $\Delta\rho$/°C ($\Delta\rho$/°F), as a function of the fuel temperature are shown in Figure 4.3-30. The numbers entered in the 'Doppler Coefficient' column of this table are the multipliers applied to the data used in the analysis of designated accidents.

(2) A curve of reactivity vs. moderator density is used for the LOCA evaluation. The value of density coefficient used corresponds to a 0 MTC for the small break events and +0.9 × 10^{-4} $\Delta\rho$ /°C (+0.5 × 10^{-4} $\Delta\rho$/°F) for the large breaks resulting in rapid depressurization.

(3) These values are the ones used at the nominal T_{avg} = 308.9 °C (588 °F). For other temperatures, the set of curves shown in Figures 4.3-31 and 4.3-32 corresponding to the extreme (i.e., most positive at BOC, most negative at EOC) is used.

Table 4.3-4 (1 of 2)

Reactivity Coefficients

Reactivity Coefficient	Value
Moderator temperature coefficient at: BOC (0 MWD/MTU), Δρ/°C (Δρ/°F)	
Cold, 20 °C (68 °F), Clean, 1,238 ppm	$+0.23 \times 10^{-4}$ $(+0.13 \times 10^{-4})$
Hot zero power, 291.3 °C (556.3 °F), no CEAs, clean, 1,187 ppm	-0.28×10^{-4} (-0.16×10^{-4})
Hot full power, 308.9 °C (588 °F), no CEAs, clean, 1,067 ppm	-1.01×10^{-4} (-0.56×10^{-4})
Hot full power, 308.9 °C (588 °F), no CEAs, equilibrium Xe, 817 ppm	-1.71×10^{-4} (-0.95×10^{-4})
Hot zero power, 291.3 °C (556.3 °F), regulating CEA banks 5, 4, and 3 inserted, 0 MWD/MTU, 817 ppm, hot full power equilibrium Xe	-1.59×10^{-4} (-0.88×10^{-4})
Moderator temperature coefficient at: Middle of cycle (3,000 MWD/MTU), Δρ/°C (Δρ/°F)	
Hot zero power, 291.3 °C (556.3 °F), no CEAs, clean	$+0.25 \times 10^{-4}$ $(+0.14 \times 10^{-4})$
Hot full power, equilibrium Xe, no CEAs, 308.9 °C (588 °F)	-0.84×10^{-4} (-0.47×10^{-4})
Moderator temperature coefficient at: EOC (10 ppm soluble boron, 17,571 MWD/MTU), Δρ/°C (Δρ/ °F)	
Cold, 20 °C (68 °F) (approximate)	$+0.22 \times 10^{-4}$ $(+0.12 \times 10^{-4})$
Hot zero power, 291.3 °C (556.3 °F), no CEAs, hot full power, equilibrium Xe	-3.18×10^{-4} (-1.77×10^{-4})
Hot full power, equilibrium Xe, no CEAs, 308.9 °C (588 °F)	-4.34×10^{-4} (-2.41×10^{-4})
Hot zero power, 291.3 °C (556.3 °F), rodded, regulating CEA banks 5, 4, and 3 inserted, hot full power, equilibrium Xe	-3.73×10^{-4} (-2.07×10^{-4})

Table 4.3-4 (2 of 2)

Reactivity Coefficient	Value
Moderator Density Coefficient, $\Delta\rho/gm/cm^3$	
Hot, operating, 308.9 °C (588 °F)	
BOC, 817 ppm soluble boron, 0 MWD/MTU	+0.030
Fuel temperature contribution to power coefficient,	
$\Delta\rho/(W/cm)$ $\Delta\rho/(kW/ft)$, 817 ppm, 0 MWD/MTU	
Hot zero power	-7.49×10^{-5} (-2.46×10^{-3})
Full power	-5.14×10^{-5} (-1.69×10^{-3})
Moderator void coefficient $\Delta\rho$/% void	
Hot, operating, 308.9 °C (588 °F)	
BOC, 817 ppm soluble boron, 0 MWD/MTU	-0.21×10^{-3}
Moderator pressure coefficient, $\Delta\rho$/psi	
Hot, operating, 308.9 °C (588 °F)	
BOC, 817 ppm soluble boron, 0 MWD/MTU	$+0.44 \times 10^{-6}$
Overall power coefficient, $\Delta\rho/(W/cm)$ $\Delta\rho/(kW/ft)$	
Hot, operating, 308.9 °C (588 °F)	
BOC, 817 ppm soluble boron, 0 MWD/MTU	-6.37×10^{-5} (-2.09×10^{-3})
EOC, 10 ppm soluble boron, 17,571 MWD/MTU	-1.18×10^{-4} (-3.87×10^{-3})

Table 4.3-5

Typical Neutron Flux Inside the Reactor Vessel

Location	E>1MeV (n/cm^2-sec)	1MeV>E>0.1MeV (n/cm^2-sec)	0.1MeV>E>0.414eV (n/cm^2-sec)	E<0.414eV (n/cm^2-sec)
At the inside surface (peak)	5.4×10^{10}	6.9×10^{10}	1.1×10^{11}	1.5×10^{11}
At the 1/4-thickness location (peak)	2.9×10^{10}	7.1×10^{10}	6.1×10^{10}	4.2×10^{09}
Core middle(1) at mid-height (peak)	1.3×10^{14}	1.2×10^{14}	2.2×10^{14}	4.9×10^{13}
Core outer radius at mid-height (peak)	6.9×10^{13}	6.7×10^{13}	1.1×10^{14}	1.7×10^{14}

(1) Between core center and core outer radius

Table 4.3-6

Worths of CEA Groups (%Δρ)

Type of CEA	*[0 MWD/MTU]** (817 ppm)	7,018 MWD/MTU (699 ppm)	13,992 MWD/MTU (318 ppm)	17,571 MWD/MTU (10 ppm)
Shutdown CEAs	–10.63	–11.33	–11.89	–12.32
Regulating CEAs				
Group 1	–1.33	–1.58	–1.49	–1.49
Group 2	–1.03	–1.03	–1.11	–1.16
Group 3	–0.77	–0.87	–0.86	–0.88
Group 4	–0.43	–0.42	–0.48	–0.49
Group 5	–0.3	–0.36	–0.36	–0.36
Part-Strength CEAs				
Group P	–0.19	–0.25	–0.31	–0.33
Total (all CEAs)				
Without PSCEA	–14.49	–15.59	–16.19	–16.7
With PSCEA	–14.68	–15.85	–16.5	–17.03

Table 4.3-7

Fast Neutron Fluence at the Reactor Vessel

Location	Fast neutron fluence (E>1MeV, 55.8EFPY) (n/cm^2)
At the inside surface (peak)	9.5×10^{19}
At the 1/4-thickness location (peak)	5.1×10^{19}

Table 4.3-8

CEA Reactivity Allowances (%Δρ)

Reactivity Component	Reactivity (%Δρ)
Fuel temperature variation	1.18
Moderator temperature variation	2.46
Moderator voids	0.10
CEA bite and part-strength CEA insertion	0.25
Accident analysis allowance	6.19
Total reactivity allowance	10.18

Table 4.3-9

Comparison of Available CEA Worths and Allowances

Condition	Reactivity (%Δρ)
All CEAs inserted, hot, 308.9 °C (588 °F)	16.70
Total reactivity allowance, full power (from Table 4.3-8)	10.18
Stuck rod worth	5.69
Uncertainty in net rod worth	0.69
Excess reactivity	+0.14

Table 4.3-10

Comparison of Rodded and Unrodded Peaking Factors
for Various Rodded Configurations

Configurations	Maximum Rod Radial Peaking Factor (F_r^n)			
	0 MWD/MTU	7,018 MWD/MTU	13,992 MWD/MTU	17,571 MWD/MTU
Unrodded	1.42	1.36	1.33	1.30
P	1.41	1.39	1.38	1.38
P+5	1.55	1.48	1.52	1.50
P+5+4	1.50	1.65	1.69	1.68
P+5+4+3	1.87	1.57	1.58	1.60
P+5+4+3+2	1.93	1.72	1.76	1.77
P+5+4+3+2+1	2.45	2.06	2.12	2.17
5+4+3+2+1	2.40	2.03	2.10	2.13
5+4+3+2	1.90	1.83	1.90	1.87
5+4+3	1.83	1.55	1.63	1.61
5+4	1.48	1.57	1.57	1.55
5	1.53	1.46	1.49	1.46

Table 4.3-11

Calculated Variation of the Axial Stability Index during the First Cycle (hr^{-1})

Power Level	BOC	EOC
100 %	–0.0097	+0.0090

Table 4.3-12

Control Element Assembly Shadowing Factors

Group	BOC	EOC
Group 5 In	1.043	1.043
Group P In	0.997	1.004
Group 5 + P In	1.064	1.072

Table 4.3-13

C-E Critical Experiments

Core Configuration						
Lattice	Fuel Rod Array	Fuel Cell Pitch, cm (in)	No. Fuel Rods	Temp. of Core	Soluble Boron Concentration, ppm	No. Control Rod Channels
#12	30 × 30	1.524 (0.600)	880	20 °C (68 °F)	0	5
#32	30 × 30	1.524 (0.600)	832	20 °C (68 °F)	0	17
#43	30 × 30	1.524 (0.600)	880	20 °C (68 °F)	323	5
#53	30 × 30	1.461 (0.575)	832	20 °C (68 °F)	0	17
#56	30 × 30	1.461 (0.575)	832	20 °C (68 °F)	302	17

Fuel Rod Design	
Clad OD	1.1895 cm (0.4683 in)
Clad thickness	0.07988 cm (0.03145 in)
Clad material	Zircaloy-4
Fuel pellet OD	1.016 cm (0.400 in)
Fuel density	10.40 g/cm^3
Fuel enrichment	2.72 w/o

Table 4.3-14

Fuel Specification (KRITZ Experiments)

Parameter	Unit	Value
Fuel material (pellets)	N/A	UO_2
Fuel density (dishing included)	g/cm^3	10.15
U-235 in U	w/o	3.10
Fuel length	mm	2,650
Pellet length	mm	11
Oxide diameter	mm	9.08
Cladding material	N/A	Zircaloy-4
Cladding density	g/cm^3	6.55
Outer diameter	mm	10.74
Inner diameter	mm	9.30

Table 4.3-15

Comparison of Reactivity Levels for Non-Uniform Core

Core	Vol. Mod/ Vol. Fuel	No. Large Water Holes	Measured Axial Buckling (M^{-2})	Soluble Boron Conc. (ppm)	k_{eff}
CRX (C-E Criticals) 2.7 w/o U-235, 20 °C (68 °F)					
#12	1.49	5	3.53	0	1.0017
#32	1.49	17	3.70	0	1.0006
#43	1.49	5	1.64	323	1.0032
#53	1.26	17	2.82	0	1.0021
#56	1.26	17	1.07	302	1.0006
KRITZ					
UO_2, 229.4 °C (445 °F)	1.79	21	2.20	959	1.0014

Table 4.3-16

Summary of ROCS/DIT Calculative Uncertainties

ROCS Calculation Uncertainty	Fxy	F_q	F_r
Bias, D (%)	0.0	0.0	0.0
Degrees of freedom, f_c	26	230	60
Confidence multiplier, $k_{95/95}$	2.275	1.823	2.022
Percent deviation, S_C (%)	2.40	3.25	2.10
95/95 confidence interval, kS_C (%)	5.46	5.93	4.24

Table 4.3-17

Axial Xenon Oscillations

Reactor	Exposure (MWD/MTU)	Period (hr)		Damping Factor (hr^{-1})	
		Measured	Calculated	Measured	Calculated
Omaha	7,075	29	32	–0.027	–0.030
Stade	BOC	36	36	–0.096	–0.090
Stade	12,200	27	30	–0.021	–0.019

N F	N : BOX Number F : Fuel Type				1 C0	2 B0	3 C0	4 B0
			5 C0	6 C0	7 B2	8 B1	9 B3	10 C2
		11 C0	12 C1	13 B1	14 A0	15 C3	16 A0	17 B3
	18 C0	19 C1	20 B3	21 A0	22 B3	23 A0	24 B1	25 A0
	26 C0	27 B1	28 A0	29 C2	30 A0	31 C3	32 A0	33 B1
34 C0	35 B2	36 A0	37 B3	38 A0	39 B3	40 A0	41 B3	42 A0
43 B0	44 B1	45 C3	46 A0	47 C3	48 A0	49 C2	50 A0	51 C3
52 C0	53 B3	54 A0	55 B1	56 A0	57 B3	58 A0	59 B3	60 A0
61 B0	62 C2	63 B3	64 A0	65 B1	66 A0	67 C3	68 A0	69 A0

Figure 4.3-1 First Cycle Fuel Loading Pattern

Assembly Type	Number of Fuel Assemblies	Fuel Rod Enrichment (w/o)	No. of Rods Per Assembly	No. of Gd_2O_3 Rods per Assembly	Gd_2O_3 Contents (w/o)
A0	77	1.71	236	-	-
B0	12	3.14	236	-	-
B1	28	3.14/2.64	172/52	12	8
B2	8	3.14/2.64	124/100	12	8
B3	40	3.14/2.64	168/52	16	8
C0	36	3.64/3.14	184/52	-	-
C1	8	3.64/3.14	172/52	12	8
C2	12	3.64/3.14	168/52	16	8
C3	20	3.64/3.14	120/100	16	8

NOTES : 1. ALL BURNABLE ABSORBER RODS HAVE AN ENRICHED URANIUM (2.0 WT% U-235).
2. GADOLINIA IS ONLY PRESENT IN THE CENTRAL 92 % OF THE BURNABLE ABSORBER RODS. THE TOP AND BOTTOM 12 INCHES OF THE BURNABLE ABSORBER RODS DO NOT CONTAIN GADOLINIA.

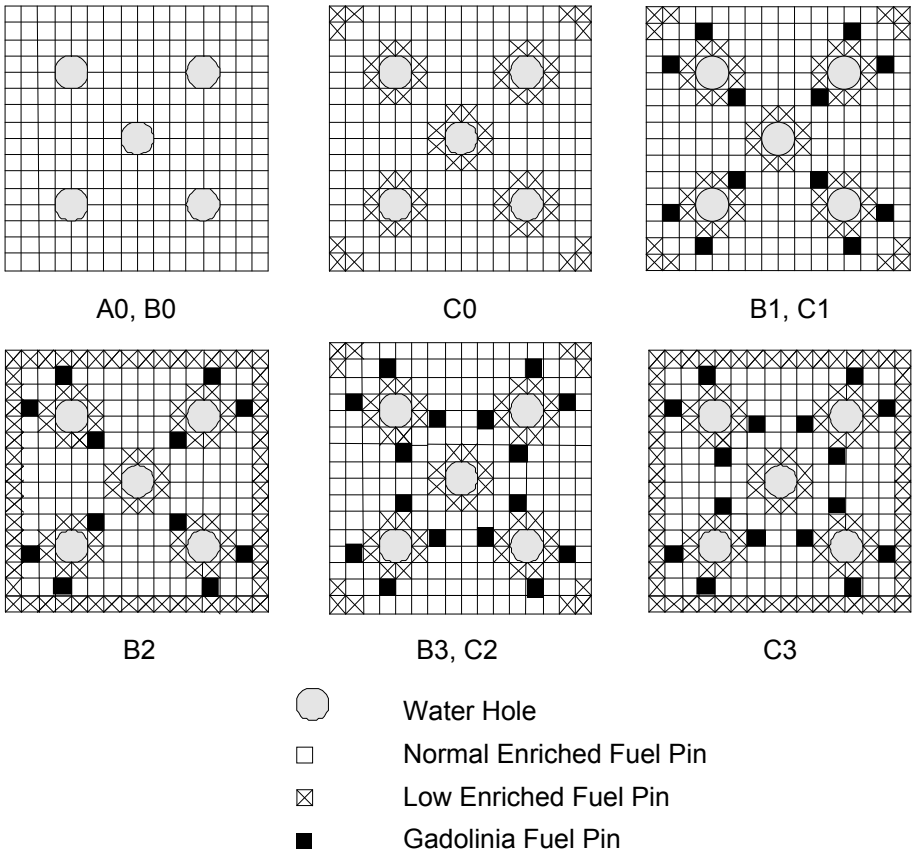

Figure 4.3-2 First Cycle Assembly Fuel Loadings with Water Hole and Burnable Absorber Rod Placement

N F	N : BOX Number F : Fuel Type				1 J1	2 J2	3 K0	4 H1
			5 H0	6 K0	7 J2	8 K1	9 J0	10 K2
		11 H1	12 K1	13 J0	14 K2	15 H1	16 K2	17 H2
	18 H0	19 K1	20 J1	21 K2	22 J2	23 K2	24 J2	25 K2
	26 K0	27 J0	28 K2	29 H2	30 K2	31 J2	32 J1	33 J2
34 J1	35 J2	36 K2	37 J2	38 K2	39 J2	40 J2	41 K2	42 J2
43 J2	44 K1	45 H1	46 K2	47 J2	48 J2	49 K2	50 H0	51 K2
52 K0	53 J0	54 K2	55 J2	56 J1	57 K2	58 H0	59 K1	60 J2
61 H1	62 K2	63 H2	64 K2	65 J2	66 J2	67 K2	68 J2	69 H2

Figure 4.3-3 Equilibrium Cycle Typical Fuel Loading Pattern and Fuel Enrichments (1 of 2)

Assembly Type	Fuel Rod Enrichment (w/o)	No. of Rods Per Assembly	No. of Gd_2O_3 Rods per Assembly	Gd_2O_3 Contents (w/o)
H0	4.50/4.00	184/52	-	-
H1	4.50/4.00	172/52	12	8
H2	4.50/4.00	168/52	16	8
J0	4.50/4.00	184/52	-	-
J1	4.50/4.00	172/52	12	8
J2	4.50/4.00	168/52	16	8
K0	4.50/4.00	184/52	-	-
K1	4.50/4.00	172/52	12	8
K2	4.50/4.00	168/52	16	8

NOTES: 1. ALL BURNABLE ABSORBER RODS HAVE AN ENRICHED URANIUM (2.0 WT% U-235).

2. GADOLINIA IS ONLY PRESENT IN THE CENTRAL 92 % OF THE BURNABLE ABSORBER RODS. THE TOP AND BOTTOM 12 INCHES OF THE BURNABLE ABSORBER RODS DO NOT CONTAIN GADOLINIA.

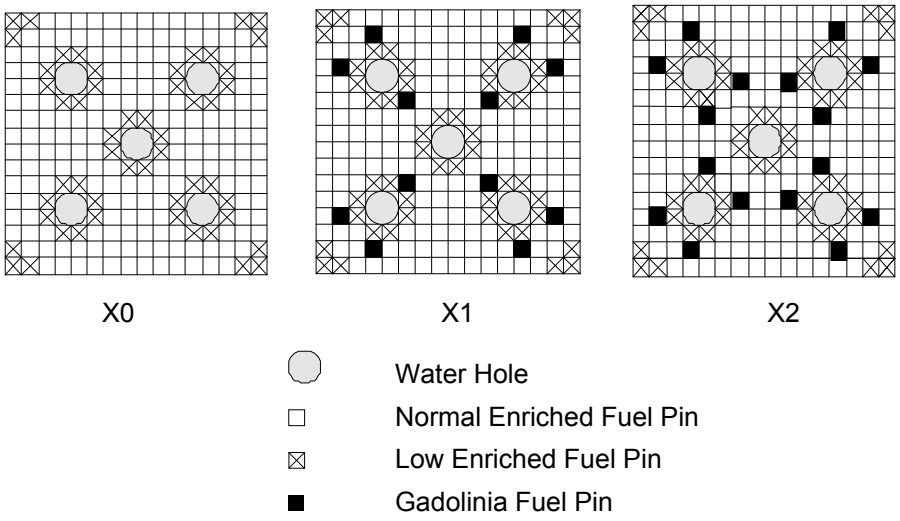

Figure 4.3-3 Equilibrium Cycle Typical Fuel Loading Pattern and Fuel Enrichments (2 of 2)

FORMAT IS

FUEL TYPE	BOX NO.
BOX RPD	
MAX PIN	

	MAXIMUM VALUE	IN BOX
BOX RPD	1.20	27
MAX PIN	1.60	52

					C0 1 0.78 1.34	B0 2 1.01 1.46	C0 3 1.15 1.60	B0 4 1.11 1.55
			C0 5 0.85 1.46	C0 6 1.18 1.56	B2 7 1.06 1.37	B1 8 1.14 1.35	B3 9 1.11 1.42	C2 10 1.20 1.52
		C0 11 0.88 1.38	C1 12 1.16 1.48	B1 13 1.20 1.49	A0 14 0.98 1.09	C3 15 1.16 1.43	A0 16 0.97 1.06	B3 17 1.07 1.33
	C0 18 0.85 1.46	C1 19 1.16 1.49	B3 20 1.08 1.38	A0 21 0.96 1.06	B3 22 1.04 1.33	A0 23 0.93 1.05	B1 24 1.13 1.39	A0 25 0.93 1.08
	C0 26 1.18 1.56	B1 27 1.20 1.49	A0 28 0.96 1.07	C2 29 1.13 1.43	A0 30 0.88 1.01	C3 31 1.06 1.42	A0 32 0.88 1.04	B1 33 1.07 1.38
C0 34 0.78 1.34	B2 35 1.06 1.37	A0 36 0.98 1.10	B3 37 1.04 1.33	A0 38 0.88 1.03	B3 39 0.96 1.27	A0 40 0.83 1.00	B3 41 0.92 1.26	A0 42 0.81 0.99
B0 43 1.01 1.46	B1 44 1.14 1.35	C3 45 1.16 1.43	A0 46 0.93 1.07	C3 47 1.06 1.42	A0 48 0.83 0.98	C2 49 0.98 1.32	A0 50 0.78 0.95	C3 51 0.93 1.28
C0 52 1.15 1.60	B3 53 1.11 1.42	A0 54 0.97 1.08	B1 55 1.13 1.39	A0 56 0.88 1.05	B3 57 0.92 1.25	A0 58 0.78 0.93	B3 59 0.84 1.16	A0 60 0.75 0.91
B0 61 1.11 1.55	C2 62 1.20 1.52	B3 63 1.07 1.33	A0 64 0.93 1.08	B1 65 1.07 1.38	A0 66 0.81 0.99	C3 67 0.93 1.28	A0 68 0.75 0.91	A0 69 0.77 0.90

Figure 4.3-4 Planar Average Power Distribution Unrodded Full Power, No Xenon, 0 MWD/MTU of the First Cycle

FORMAT IS

FUEL TYPE	BOX NO.
BOX RPD	
MAX PIN	

	MAXIMUM VALUE	IN BOX
BOX RPD	1.16	55
MAX PIN	1.46	52

					C0 1 0.72 1.25	B0 2 0.94 1.35	C0 3 1.06 1.46	B0 4 1.02 1.42
			C0 5 0.78 1.35	C0 6 1.09 1.45	B2 7 1.00 1.28	B1 8 1.08 1.26	B3 9 1.05 1.33	C2 10 1.12 1.41
		C0 11 0.82 1.27	C1 12 1.08 1.37	B1 13 1.14 1.41	A0 14 0.97 1.07	C3 15 1.13 1.42	A0 16 0.96 1.07	B3 17 1.05 1.32
	C0 18 0.78 1.35	C1 19 1.08 1.38	B3 20 1.03 1.32	A0 21 0.95 1.05	B3 22 1.05 1.29	A0 23 0.96 1.08	B1 24 1.16 1.38	A0 25 0.97 1.10
	C0 26 1.09 1.45	B1 27 1.14 1.41	A0 28 0.95 1.06	C2 29 1.14 1.39	A0 30 0.92 1.05	C3 31 1.11 1.42	A0 32 0.95 1.09	B1 33 1.14 1.38
C0 34 0.72 1.25	B2 35 1.00 1.29	A0 36 0.97 1.08	B3 37 1.05 1.29	A0 38 0.92 1.05	B3 39 1.02 1.28	A0 40 0.90 1.05	B3 41 1.01 1.30	A0 42 0.91 1.06
B0 43 0.94 1.35	B1 44 1.08 1.26	C3 45 1.13 1.42	A0 46 0.96 1.08	C3 47 1.11 1.42	A0 48 0.90 1.05	C2 49 1.09 1.38	A0 50 0.88 1.04	C3 51 1.05 1.36
C0 52 1.06 1.46	B3 53 1.05 1.33	A0 54 0.96 1.07	B1 55 1.16 1.38	A0 56 0.95 1.09	B3 57 1.01 1.30	A0 58 0.88 1.03	B3 59 0.97 1.26	A0 60 0.88 1.03
B0 61 1.02 1.42	C2 62 1.12 1.41	B3 63 1.05 1.32	A0 64 0.97 1.10	B1 65 1.14 1.38	A0 66 0.91 1.06	C3 67 1.05 1.36	A0 68 0.88 1.03	A0 69 0.92 1.05

Figure 4.3-5 Planar Average Power Distribution Unrodded Full Power, Equilibrium Xenon, 50 MWD/MTU of the First Cycle

FORMAT IS

FUEL TYPE	BOX NO.
BOX RPD	
MAX PIN	

	MAXIMUM VALUE	IN BOX
BOX RPD	1.21	65
MAX PIN	1.43	31

					C0 1 0.62 1.08	B0 2 0.80 1.19	C0 3 0.91 1.26	B0 4 0.88 1.23
			C0 5 0.66 1.15	C0 6 0.94 1.28	B2 7 0.93 1.17	B1 8 1.04 1.19	B3 9 1.04 1.28	C2 10 1.11 1.29
		C0 11 0.72 1.13	C1 12 1.00 1.26	B1 13 1.08 1.28	A0 14 0.94 1.05	C3 15 1.15 1.41	A0 16 0.98 1.09	B3 17 1.11 1.31
	C0 18 0.66 1.15	C1 19 1.00 1.26	B3 20 1.03 1.26	A0 21 0.95 1.06	B3 22 1.10 1.29	A0 23 0.99 1.12	B1 24 1.20 1.37	A0 25 1.02 1.15
	C0 26 0.94 1.28	B1 27 1.08 1.29	A0 28 0.95 1.06	C2 29 1.18 1.38	A0 30 0.98 1.10	C3 31 1.19 1.43	A0 32 1.01 1.15	B1 33 1.21 1.38
C0 34 0.62 1.08	B2 35 0.93 1.17	A0 36 0.94 1.05	B3 37 1.10 1.29	A0 38 0.98 1.10	B3 39 1.12 1.32	A0 40 0.99 1.12	B3 41 1.13 1.33	A0 42 0.99 1.13
B0 43 0.80 1.19	B1 44 1.04 1.19	C3 45 1.15 1.41	A0 46 0.99 1.12	C3 47 1.19 1.42	A0 48 0.99 1.12	C2 49 1.20 1.42	A0 50 0.98 1.12	C3 51 1.16 1.41
C0 52 0.91 1.26	B3 53 1.04 1.29	A0 54 0.98 1.09	B1 55 1.20 1.37	A0 56 1.01 1.15	B3 57 1.13 1.33	A0 58 0.98 1.12	B3 59 1.09 1.31	A0 60 0.96 1.10
B0 61 0.88 1.23	C2 62 1.11 1.29	B3 63 1.11 1.31	A0 64 1.02 1.15	B1 65 1.21 1.38	A0 66 0.99 1.13	C3 67 1.16 1.41	A0 68 0.96 1.10	A0 69 0.96 1.11

Figure 4.3-6 Planar Average Power Distribution Unrodded Full Power, Equilibrium Xenon, 4,000 MWD/MTU of the First Cycle

FORMAT IS

FUEL TYPE	BOX NO.
BOX RPD	
MAX PIN	

	MAXIMUM VALUE	IN BOX
BOX RPD	1.23	49
MAX PIN	1.41	62

					C0 1 0.58 1.03	B0 2 0.75 1.15	C0 3 0.86 1.24	B0 4 0.84 1.19
			C0 5 0.60 1.06	C0 6 0.86 1.21	B2 7 0.94 1.18	B1 8 1.09 1.28	B3 9 1.13 1.37	C2 10 1.21 1.41
		C0 11 0.67 1.09	C1 12 0.99 1.24	B1 13 1.07 1.24	A0 14 0.93 1.04	C3 15 1.21 1.40	A0 16 1.00 1.10	B3 17 1.20 1.38
	C0 18 0.60 1.06	C1 19 0.99 1.23	B3 20 1.08 1.27	A0 21 0.94 1.05	B3 22 1.15 1.30	A0 23 0.98 1.11	B1 24 1.20 1.35	A0 25 0.99 1.14
	C0 26 0.86 1.21	B1 27 1.07 1.24	A0 28 0.94 1.05	C2 29 1.22 1.37	A0 30 0.97 1.10	C3 31 1.22 1.39	A0 32 0.98 1.14	B1 33 1.19 1.35
C0 34 0.58 1.03	B2 35 0.94 1.18	A0 36 0.93 1.04	B3 37 1.15 1.30	A0 38 0.97 1.10	B3 39 1.17 1.33	A0 40 0.98 1.12	B3 41 1.16 1.33	A0 42 0.97 1.13
B0 43 0.75 1.16	B1 44 1.09 1.28	C3 45 1.21 1.40	A0 46 0.98 1.11	C3 47 1.22 1.38	A0 48 0.98 1.12	C2 49 1.23 1.40	A0 50 0.96 1.11	C3 51 1.18 1.37
C0 52 0.86 1.24	B3 53 1.13 1.37	A0 54 1.00 1.10	B1 55 1.20 1.35	A0 56 0.98 1.14	B3 57 1.16 1.34	A0 58 0.96 1.11	B3 59 1.10 1.29	A0 60 0.90 1.07
B0 61 0.84 1.19	C2 62 1.21 1.41	B3 63 1.20 1.38	A0 64 0.99 1.14	B1 65 1.19 1.35	A0 66 0.97 1.13	C3 67 1.18 1.37	A0 68 0.90 1.07	A0 69 0.86 1.04

Figure 4.3-7 Planar Average Power Distribution Unrodded Full Power, Equilibrium Xenon, 8,000 MWD/MTU of the First Cycle

FORMAT IS

FUEL TYPE	BOX NO.
BOX RPD	
MAX PIN	

	MAXIMUM VALUE	IN BOX
BOX RPD	1.23	29
MAX PIN	1.39	62

					C0 1 0.59 1.03	B0 2 0.75 1.08	C0 3 0.83 1.16	B0 4 0.81 1.12
			C0 5 0.63 1.07	C0 6 0.87 1.17	B2 7 0.97 1.21	B1 8 1.10 1.27	B3 9 1.14 1.32	C2 10 1.22 1.39
		C0 11 0.72 1.16	C1 12 1.07 1.32	B1 13 1.10 1.26	A0 14 0.94 1.04	C3 15 1.21 1.35	A0 16 0.98 1.08	B3 17 1.18 1.31
	C0 18 0.63 1.07	C1 19 1.07 1.32	B3 20 1.15 1.29	A0 21 0.97 1.06	B3 22 1.15 1.27	A0 23 0.96 1.05	B1 24 1.14 1.28	A0 25 0.94 1.05
	C0 26 0.87 1.17	B1 27 1.10 1.26	A0 28 0.97 1.06	C2 29 1.23 1.37	A0 30 0.97 1.06	C3 31 1.20 1.34	A0 32 0.94 1.04	B1 33 1.12 1.24
C0 34 0.59 1.02	B2 35 0.97 1.21	A0 36 0.94 1.04	B3 37 1.15 1.27	A0 38 0.97 1.06	B3 39 1.16 1.28	A0 40 0.96 1.05	B3 41 1.14 1.28	A0 42 0.94 1.03
B0 43 0.75 1.08	B1 44 1.10 1.27	C3 45 1.21 1.35	A0 46 0.96 1.06	C3 47 1.20 1.34	A0 48 0.96 1.05	C2 49 1.22 1.38	A0 50 0.95 1.04	C3 51 1.19 1.33
C0 52 0.83 1.16	B3 53 1.14 1.32	A0 54 0.98 1.08	B1 55 1.14 1.27	A0 56 0.94 1.04	B3 57 1.14 1.28	A0 58 0.95 1.04	B3 59 1.12 1.27	A0 60 0.91 1.00
B0 61 0.81 1.12	C2 62 1.22 1.39	B3 63 1.18 1.31	A0 64 0.94 1.05	B1 65 1.12 1.24	A0 66 0.94 1.03	C3 67 1.19 1.33	A0 68 0.91 1.00	A0 69 0.87 0.92

Figure 4.3-8 Planar Average Power Distribution Unrodded Full Power, Equilibrium Xenon, 14,000 MWD/MTU of the First Cycle

FORMAT IS

FUEL TYPE	BOX NO.
BOX RPD	
MAX PIN	

	MAXIMUM VALUE	IN BOX
BOX RPD	1.22	29
MAX PIN	1.34	62

					C0 1 0.61 1.04	B0 2 0.76 1.07	C0 3 0.83 1.14	B0 4 0.81 1.10
			C0 5 0.65 1.07	C0 6 0.88 1.16	B2 7 0.98 1.20	B1 8 1.09 1.24	B3 9 1.12 1.27	C2 10 1.19 1.34
		C0 11 0.74 1.15	C1 12 1.08 1.30	B1 13 1.10 1.24	A0 14 0.95 1.04	C3 15 1.20 1.33	A0 16 0.97 1.07	B3 17 1.15 1.27
	C0 18 0.65 1.07	C1 19 1.08 1.29	B3 20 1.15 1.25	A0 21 0.97 1.06	B3 22 1.14 1.23	A0 23 0.96 1.04	B1 24 1.12 1.22	A0 25 0.94 1.03
	C0 26 0.88 1.17	B1 27 1.10 1.23	A0 28 0.97 1.06	C2 29 1.22 1.33	A0 30 0.97 1.05	C3 31 1.19 1.30	A0 32 0.95 1.02	B1 33 1.11 1.20
C0 34 0.61 1.04	B2 35 0.98 1.19	A0 36 0.95 1.04	B3 37 1.14 1.23	A0 38 0.97 1.05	B3 39 1.15 1.24	A0 40 0.97 1.03	B3 41 1.13 1.24	A0 42 0.95 1.02
B0 43 0.76 1.08	B1 44 1.09 1.25	C3 45 1.20 1.33	A0 46 0.96 1.04	C3 47 1.19 1.29	A0 48 0.97 1.03	C2 49 1.21 1.33	A0 50 0.96 1.04	C3 51 1.19 1.30
C0 52 0.83 1.15	B3 53 1.12 1.27	A0 54 0.97 1.07	B1 55 1.12 1.22	A0 56 0.95 1.02	B3 57 1.13 1.24	A0 58 0.96 1.03	B3 59 1.13 1.24	A0 60 0.93 1.02
B0 61 0.81 1.10	C2 62 1.19 1.34	B3 63 1.15 1.27	A0 64 0.94 1.03	B1 65 1.11 1.20	A0 66 0.95 1.02	C3 67 1.19 1.30	A0 68 0.93 1.02	A0 69 0.90 0.96

Figure 4.3-9 Planar Average Power Distribution Unrodded Full Power, Equilibrium Xenon, 17,571 MWD/MTU of the First Cycle

FORMAT IS

FUEL TYPE	BOX NO.
BOX RPD	
MAX PIN	

	MAXIMUM VALUE	IN BOX
BOX RPD	1.26	27
MAX PIN	1.59	26

					C0 1 0.75 1.26	B0 2 0.93 1.32	C0 3 1.00 1.37	B0 4 0.94 1.30
			C0 5 0.88 1.48	C0 6 1.20 1.59	B2 7 1.06 1.38	B1 8 1.08 1.27	B3 9 0.96 1.23	C2 10 0.97 1.25
		C0 11 0.92 1.44	C1 12 1.22 1.53	B1 13 1.26 1.55	A0 14 1.02 1.15	C3 15 1.13 1.44	A0 16 0.85 0.97	B3 17 0.67 0.86
	C0 18 0.88 1.48	C1 19 1.22 1.54	B3 20 1.16 1.48	A0 21 1.05 1.17	B3 22 1.12 1.41	A0 23 0.96 1.08	B1 24 1.08 1.34	A0 25 0.85 0.99
	C0 26 1.20 1.59	B1 27 1.26 1.55	A0 28 1.05 1.17	C2 29 1.24 1.55	A0 30 0.98 1.12	C3 31 1.13 1.46	A0 32 0.93 1.07	B1 33 1.09 1.33
C0 34 0.75 1.26	B2 35 1.06 1.38	A0 36 1.02 1.15	B3 37 1.12 1.41	A0 38 0.98 1.12	B3 39 1.06 1.37	A0 40 0.92 1.08	B3 41 1.00 1.31	A0 42 0.88 1.04
B0 43 0.93 1.32	B1 44 1.08 1.27	C3 45 1.13 1.44	A0 46 0.96 1.09	C3 47 1.13 1.46	A0 48 0.92 1.07	C2 49 1.08 1.41	A0 50 0.84 1.00	C3 51 0.98 1.32
C0 52 1.00 1.37	B3 53 0.96 1.23	A0 54 0.85 0.97	B1 55 1.08 1.34	A0 56 0.93 1.07	B3 57 1.00 1.31	A0 58 0.84 1.00	B3 59 0.85 1.18	A0 60 0.71 0.87
B0 61 0.94 1.30	C2 62 0.97 1.25	B3 63 0.67 0.86	A0 64 0.85 0.99	B1 65 1.09 1.33	A0 66 0.88 1.04	C3 67 0.98 1.32	A0 68 0.71 0.87	A0 69 0.50 0.60

Figure 4.3-10 Planar Average Power Distribution, Bank 5 Full In, Full Power, Equilibrium Xenon, BOC (0 MWD/MTU) of the First Cycle

FORMAT IS

FUEL TYPE	BOX NO.
BOX RPD	
MAX PIN	

	MAXIMUM VALUE	IN BOX
BOX RPD	1.36	29
MAX PIN	1.52	29

					C0 1 0.60 1.03	B0 2 0.72 1.00	C0 3 0.74 1.04	B0 4 0.70 0.95
			C0 5 0.72 1.20	C0 6 0.95 1.27	B2 7 1.01 1.21	B1 8 1.06 1.21	B3 9 0.98 1.13	C2 10 0.96 1.07
		C0 11 0.83 1.32	C1 12 1.21 1.48	B1 13 1.22 1.40	A0 14 0.99 1.09	C3 15 1.18 1.33	A0 16 0.82 0.95	B3 17 0.68 0.79
	C0 18 0.72 1.21	C1 19 1.21 1.48	B3 20 1.31 1.43	A0 21 1.07 1.17	B3 22 1.23 1.37	A0 23 0.97 1.08	B1 24 1.05 1.24	A0 25 0.80 0.93
	C0 26 0.95 1.27	B1 27 1.22 1.40	A0 28 1.07 1.18	C2 29 1.36 1.52	A0 30 1.05 1.14	C3 31 1.25 1.41	A0 32 0.94 1.06	B1 33 1.09 1.24
C0 34 0.60 1.03	B2 35 1.01 1.21	A0 36 0.99 1.09	B3 37 1.23 1.37	A0 38 1.05 1.14	B3 39 1.25 1.38	A0 40 1.01 1.10	B3 41 1.17 1.31	A0 42 0.96 1.04
B0 43 0.72 1.00	B1 44 1.06 1.21	C3 45 1.18 1.32	A0 46 0.97 1.08	C3 47 1.25 1.40	A0 48 1.01 1.10	C2 49 1.27 1.43	A0 50 0.97 1.06	C3 51 1.19 1.34
C0 52 0.74 1.04	B3 53 0.98 1.13	A0 54 0.82 0.96	B1 55 1.05 1.24	A0 56 0.94 1.06	B3 57 1.17 1.31	A0 58 0.97 1.06	B3 59 1.07 1.24	A0 60 0.82 0.95
B0 61 0.70 0.95	C2 62 0.96 1.07	B3 63 0.68 0.79	A0 64 0.80 0.93	B1 65 1.09 1.24	A0 66 0.96 1.04	C3 67 1.19 1.34	A0 68 0.82 0.95	A0 69 0.55 0.61

Figure 4.3-11 Planar Average Power Distribution, Bank 5 Full In, Full Power, Equilibrium Xenon, MOC (14,000 MWD/MTU) of the First Cycle

FORMAT IS

FUEL TYPE	BOX NO.	MAXIMUM VALUE	IN BOX
BOX RPD		1.35	29
MAX PIN		1.48	29

					C0 1 0.63 1.04	B0 2 0.73 1.01	C0 3 0.75 1.03	B0 4 0.70 0.93
			C0 5 0.74 1.20	C0 6 0.97 1.26	B2 7 1.02 1.20	B1 8 1.06 1.19	B3 9 0.97 1.11	C2 10 0.94 1.05
		C0 11 0.85 1.30	C1 12 1.23 1.45	B1 13 1.23 1.38	A0 14 1.00 1.10	C3 15 1.17 1.31	A0 16 0.81 0.94	B3 17 0.66 0.76
	C0 18 0.74 1.20	C1 19 1.23 1.45	B3 20 1.31 1.41	A0 21 1.08 1.18	B3 22 1.23 1.35	A0 23 0.97 1.07	B1 24 1.03 1.18	A0 25 0.80 0.91
	C0 26 0.97 1.26	B1 27 1.23 1.38	A0 28 1.08 1.18	C2 29 1.35 1.48	A0 30 1.05 1.13	C3 31 1.23 1.36	A0 32 0.94 1.03	B1 33 1.08 1.18
C0 34 0.63 1.04	B2 35 1.02 1.20	A0 36 1.00 1.10	B3 37 1.23 1.35	A0 38 1.05 1.13	B3 39 1.23 1.33	A0 40 1.01 1.08	B3 41 1.16 1.27	A0 42 0.96 1.03
B0 43 0.73 1.01	B1 44 1.06 1.19	C3 45 1.17 1.31	A0 46 0.97 1.07	C3 47 1.23 1.36	A0 48 1.01 1.08	C2 49 1.25 1.38	A0 50 0.97 1.06	C3 51 1.17 1.30
C0 52 0.75 1.03	B3 53 0.97 1.10	A0 54 0.81 0.94	B1 55 1.03 1.18	A0 56 0.94 1.03	B3 57 1.16 1.27	A0 58 0.97 1.05	B3 59 1.06 1.22	A0 60 0.82 0.96
B0 61 0.70 0.93	C2 62 0.94 1.05	B3 63 0.66 0.76	A0 64 0.80 0.91	B1 65 1.08 1.18	A0 66 0.96 1.03	C3 67 1.17 1.30	A0 68 0.82 0.96	A0 69 0.55 0.62

Figure 4.3-12 Planar Average Power Distribution, Bank 5 Full In, Full Power, Equilibrium Xenon, EOC (17,571 MWD/MTU) of the First Cycle

FORMAT IS

FUEL TYPE	BOX NO.
BOX RPD	
MAX PIN	

	MAXIMUM VALUE	IN BOX
BOX RPD	1.16	27
MAX PIN	1.48	26

					C0 1 0.72 1.23	B0 2 0.93 1.35	C0 3 1.06 1.46	B0 4 1.03 1.43
			C0 5 0.80 1.36	C0 6 1.11 1.48	B2 7 1.00 1.29	B1 8 1.06 1.25	B3 9 1.04 1.34	C2 10 1.13 1.39
		C0 11 0.84 1.32	C1 12 1.12 1.41	B1 13 1.16 1.43	A0 14 0.95 1.07	C3 15 1.01 1.29	A0 16 0.94 1.04	B3 17 1.05 1.31
	C0 18 0.80 1.36	C1 19 1.12 1.41	B3 20 1.06 1.36	A0 21 0.96 1.07	B3 22 1.05 1.30	A0 23 0.94 1.06	B1 24 1.15 1.38	A0 25 0.98 1.11
	C0 26 1.11 1.48	B1 27 1.16 1.43	A0 28 0.96 1.07	C2 29 1.14 1.42	A0 30 0.91 1.03	C3 31 1.11 1.44	A0 32 0.96 1.10	B1 33 1.16 1.42
C0 34 0.72 1.23	B2 35 1.00 1.29	A0 36 0.95 1.07	B3 37 1.05 1.30	A0 38 0.91 1.04	B3 39 0.92 1.17	A0 40 0.90 1.05	B3 41 1.03 1.34	A0 42 0.93 1.09
B0 43 0.93 1.35	B1 44 1.06 1.25	C3 45 1.01 1.29	A0 46 0.94 1.06	C3 47 1.11 1.44	A0 48 0.90 1.04	C2 49 1.10 1.42	A0 50 0.91 1.07	C3 51 1.09 1.42
C0 52 1.06 1.46	B3 53 1.04 1.34	A0 54 0.94 1.05	B1 55 1.15 1.38	A0 56 0.96 1.10	B3 57 1.03 1.34	A0 58 0.91 1.06	B3 59 1.01 1.32	A0 60 0.91 1.08
B0 61 1.03 1.43	C2 62 1.13 1.39	B3 63 1.05 1.31	A0 64 0.98 1.11	B1 65 1.16 1.42	A0 66 0.93 1.09	C3 67 1.09 1.42	A0 68 0.91 1.08	A0 69 0.96 1.09

Figure 4.3-13 Planar Average Power Distribution, PSCEA Bank Full In, Full Power, Equilibrium Xenon, BOC (0 MWD/MTU) of the First Cycle

FORMAT IS

FUEL TYPE	BOX NO.
BOX RPD	
MAX PIN	

	MAXIMUM VALUE	IN BOX
BOX RPD	1.28	67
MAX PIN	1.44	49

					C0 1 0.59 1.01	B0 2 0.74 1.06	C0 3 0.83 1.15	B0 4 0.81 1.11
			C0 5 0.66 1.11	C0 6 0.88 1.17	B2 7 0.95 1.14	B1 8 1.06 1.18	B3 9 1.12 1.26	C2 10 1.21 1.35
		C0 11 0.76 1.21	C1 12 1.11 1.36	B1 13 1.12 1.29	A0 14 0.91 1.00	C3 15 1.04 1.17	A0 16 0.95 1.05	B3 17 1.17 1.29
	C0 18 0.66 1.11	C1 19 1.11 1.36	B3 20 1.19 1.30	A0 21 0.98 1.07	B3 22 1.13 1.25	A0 23 0.93 1.02	B1 24 1.13 1.25	A0 25 0.95 1.04
	C0 26 0.88 1.17	B1 27 1.12 1.28	A0 28 0.98 1.07	C2 29 1.23 1.37	A0 30 0.95 1.04	C3 31 1.19 1.32	A0 32 0.96 1.05	B1 33 1.15 1.29
C0 34 0.59 1.01	B2 35 0.95 1.14	A0 36 0.91 1.00	B3 37 1.13 1.25	A0 38 0.95 1.04	B3 39 1.02 1.13	A0 40 0.96 1.06	B3 41 1.19 1.33	A0 42 0.99 1.08
B0 43 0.74 1.06	B1 44 1.06 1.18	C3 45 1.04 1.16	A0 46 0.93 1.02	C3 47 1.19 1.32	A0 48 0.96 1.06	C2 49 1.26 1.44	A0 50 1.02 1.10	C3 51 1.28 1.43
C0 52 0.83 1.16	B3 53 1.12 1.26	A0 54 0.95 1.05	B1 55 1.13 1.25	A0 56 0.96 1.06	B3 57 1.19 1.33	A0 58 1.02 1.10	B3 59 1.21 1.34	A0 60 0.99 1.09
B0 61 0.81 1.11	C2 62 1.21 1.35	B3 63 1.17 1.29	A0 64 0.95 1.04	B1 65 1.15 1.29	A0 66 0.99 1.08	C3 67 1.28 1.43	A0 68 0.99 1.09	A0 69 0.95 1.01

Figure 4.3-14 Planar Average Power Distribution, PSCEA Bank Full In, Full Power, Equilibrium Xenon, MOC (14,000 MWD/MTU) of the First Cycle

FORMAT IS

FUEL TYPE	BOX NO.
BOX RPD	
MAX PIN	

	MAXIMUM VALUE	IN BOX
BOX RPD	1.28	67
MAX PIN	1.42	67

					C0 1 0.61 1.01	B0 2 0.75 1.05	C0 3 0.83 1.13	B0 4 0.81 1.09
			C0 5 0.68 1.10	C0 6 0.90 1.17	B2 7 0.97 1.12	B1 8 1.05 1.15	B3 9 1.10 1.23	C2 10 1.18 1.31
		C0 11 0.78 1.19	C1 12 1.12 1.33	B1 13 1.12 1.26	A0 14 0.92 1.01	C3 15 1.02 1.13	A0 16 0.94 1.04	B3 17 1.14 1.25
	C0 18 0.68 1.10	C1 19 1.12 1.32	B3 20 1.19 1.28	A0 21 0.99 1.07	B3 22 1.12 1.23	A0 23 0.93 1.01	B1 24 1.11 1.21	A0 25 0.95 1.01
	C0 26 0.90 1.17	B1 27 1.12 1.26	A0 28 0.99 1.07	C2 29 1.21 1.34	A0 30 0.94 1.02	C3 31 1.18 1.29	A0 32 0.97 1.03	B1 33 1.14 1.24
C0 34 0.61 1.01	B2 35 0.97 1.12	A0 36 0.92 1.01	B3 37 1.12 1.23	A0 38 0.94 1.02	B3 39 1.00 1.10	A0 40 0.96 1.06	B3 41 1.18 1.30	A0 42 1.01 1.09
B0 43 0.75 1.05	B1 44 1.05 1.15	C3 45 1.02 1.13	A0 46 0.93 1.01	C3 47 1.18 1.29	A0 48 0.96 1.05	C2 49 1.25 1.41	A0 50 1.03 1.12	C3 51 1.28 1.42
C0 52 0.83 1.13	B3 53 1.10 1.23	A0 54 0.94 1.04	B1 55 1.11 1.20	A0 56 0.97 1.03	B3 57 1.18 1.31	A0 58 1.03 1.12	B3 59 1.23 1.34	A0 60 1.02 1.12
B0 61 0.81 1.09	C2 62 1.18 1.31	B3 63 1.14 1.25	A0 64 0.95 1.01	B1 65 1.14 1.24	A0 66 1.01 1.09	C3 67 1.28 1.42	A0 68 1.02 1.12	A0 69 0.99 1.06

Figure 4.3-15 Planar Average Power Distribution , PSCEA Bank Full In, Full Power, Equilibrium Xenon, EOC (17,571 MWD/MTU) of the First Cycle

FORMAT IS

FUEL TYPE	BOX NO.
BOX RPD	
MAX PIN	

	MAXIMUM VALUE	IN BOX
BOX RPD	1.29	27
MAX PIN	1.63	6

					C0 1 0.75 1.26	B0 2 0.94 1.33	C0 3 1.01 1.38	B0 4 0.95 1.31
			C0 5 0.91 1.53	C0 6 1.23 1.63	B2 7 1.06 1.39	B1 8 1.06 1.26	B3 9 0.96 1.20	C2 10 0.97 1.26
		C0 11 0.96 1.50	C1 12 1.27 1.59	B1 13 1.29 1.59	A0 14 1.02 1.15	C3 15 1.01 1.31	A0 16 0.83 0.94	B3 17 0.67 0.85
	C0 18 0.91 1.53	C1 19 1.27 1.59	B3 20 1.20 1.53	A0 21 1.07 1.19	B3 22 1.11 1.42	A0 23 0.94 1.06	B1 24 1.07 1.32	A0 25 0.85 1.00
	C0 26 1.23 1.63	B1 27 1.29 1.59	A0 28 1.07 1.19	C2 29 1.24 1.56	A0 30 0.96 1.11	C3 31 1.12 1.45	A0 32 0.93 1.07	B1 33 1.10 1.35
C0 34 0.75 1.26	B2 35 1.06 1.39	A0 36 1.02 1.15	B3 37 1.11 1.42	A0 38 0.96 1.11	B3 39 0.95 1.24	A0 40 0.91 1.06	B3 41 1.01 1.32	A0 42 0.90 1.06
B0 43 0.94 1.33	B1 44 1.06 1.25	C3 45 1.01 1.30	A0 46 0.94 1.07	C3 47 1.12 1.44	A0 48 0.91 1.05	C2 49 1.08 1.40	A0 50 0.86 1.03	C3 51 1.01 1.36
C0 52 1.01 1.38	B3 53 0.96 1.20	A0 54 0.83 0.94	B1 55 1.07 1.33	A0 56 0.93 1.08	B3 57 1.01 1.32	A0 58 0.86 1.02	B3 59 0.88 1.22	A0 60 0.74 0.90
B0 61 0.95 1.31	C2 62 0.97 1.26	B3 63 0.67 0.85	A0 64 0.85 1.00	B1 65 1.10 1.35	A0 66 0.90 1.06	C3 67 1.01 1.36	A0 68 0.74 0.90	A0 69 0.52 0.62

Figure 4.3-16 Planar Average Power Distribution, PSCEA Bank and Bank 5 Full In, Full Power, Equilibrium Xenon, BOC (0 MWD/MTU) of the First Cycle

FORMAT IS

FUEL TYPE	BOX NO.
BOX RPD	
MAX PIN	

	MAXIMUM VALUE	IN BOX
BOX RPD	1.36	29
MAX PIN	1.55	12

					C0 1 0.60 1.02	B0 2 0.71 0.99	C0 3 0.74 1.02	B0 4 0.69 0.94
			C0 5 0.75 1.26	C0 6 0.98 1.31	B2 7 1.00 1.21	B1 8 1.01 1.15	B3 9 0.96 1.08	C2 10 0.95 1.06
		C0 11 0.88 1.40	C1 12 1.28 1.55	B1 13 1.26 1.46	A0 14 0.97 1.09	C3 15 1.02 1.16	A0 16 0.78 0.90	B3 17 0.67 0.77
	C0 18 0.75 1.26	C1 19 1.28 1.55	B3 20 1.36 1.49	A0 21 1.10 1.22	B3 22 1.22 1.38	A0 23 0.94 1.07	B1 24 1.03 1.23	A0 25 0.80 0.94
	C0 26 0.98 1.31	B1 27 1.26 1.45	A0 28 1.10 1.22	C2 29 1.36 1.55	A0 30 1.02 1.14	C3 31 1.24 1.38	A0 32 0.96 1.08	B1 33 1.12 1.29
C0 34 0.60 1.02	B2 35 1.00 1.21	A0 36 0.97 1.09	B3 37 1.22 1.38	A0 38 1.02 1.14	B3 39 1.09 1.22	A0 40 1.01 1.10	B3 41 1.21 1.35	A0 42 1.00 1.10
B0 43 0.71 0.99	B1 44 1.01 1.15	C3 45 1.02 1.16	A0 46 0.94 1.07	C3 47 1.24 1.37	A0 48 1.01 1.10	C2 49 1.30 1.45	A0 50 1.02 1.11	C3 51 1.26 1.42
C0 52 0.74 1.02	B3 53 0.96 1.07	A0 54 0.78 0.90	B1 55 1.03 1.23	A0 56 0.96 1.08	B3 57 1.21 1.35	A0 58 1.02 1.10	B3 59 1.14 1.32	A0 60 0.88 1.02
B0 61 0.69 0.94	C2 62 0.95 1.06	B3 63 0.67 0.77	A0 64 0.80 0.94	B1 65 1.12 1.29	A0 66 1.00 1.10	C3 67 1.26 1.42	A0 68 0.88 1.02	A0 69 0.59 0.66

Figure 4.3-17 Planar Average Power Distribution, PSCEA Bank and Bank 5 Full In, Full Power, Equilibrium Xenon, MOC (14,000 MWD/MTU) of the First Cycle

FORMAT IS

FUEL TYPE	BOX NO.
BOX RPD	
MAX PIN	

	MAXIMUM VALUE	IN BOX
BOX RPD	1.37	20
MAX PIN	1.53	12

					C0 1 0.63 1.03	B0 2 0.72 0.99	C0 3 0.74 1.01	B0 4 0.69 0.92
			C0 5 0.78 1.26	C0 6 1.00 1.30	B2 7 1.01 1.20	B1 8 1.01 1.13	B3 9 0.94 1.05	C2 10 0.93 1.03
		C0 11 0.91 1.38	C1 12 1.30 1.53	B1 13 1.26 1.43	A0 14 0.98 1.10	C3 15 1.00 1.14	A0 16 0.77 0.88	B3 17 0.65 0.74
	C0 18 0.78 1.26	C1 19 1.30 1.53	B3 20 1.37 1.48	A0 21 1.11 1.22	B3 22 1.21 1.36	A0 23 0.94 1.05	B1 24 1.01 1.17	A0 25 0.80 0.92
	C0 26 1.00 1.30	B1 27 1.26 1.43	A0 28 1.11 1.22	C2 29 1.35 1.51	A0 30 1.02 1.12	C3 31 1.22 1.33	A0 32 0.96 1.05	B1 33 1.11 1.23
C0 34 0.63 1.03	B2 35 1.01 1.20	A0 36 0.98 1.10	B3 37 1.21 1.35	A0 38 1.02 1.12	B3 39 1.07 1.17	A0 40 1.00 1.08	B3 41 1.20 1.31	A0 42 1.01 1.09
B0 43 0.72 0.99	B1 44 1.01 1.14	C3 45 1.00 1.14	A0 46 0.94 1.05	C3 47 1.22 1.33	A0 48 1.00 1.08	C2 49 1.28 1.41	A0 50 1.02 1.10	C3 51 1.25 1.39
C0 52 0.74 1.01	B3 53 0.94 1.05	A0 54 0.77 0.88	B1 55 1.01 1.17	A0 56 0.96 1.05	B3 57 1.20 1.31	A0 58 1.02 1.10	B3 59 1.14 1.30	A0 60 0.89 1.03
B0 61 0.69 0.92	C2 62 0.93 1.03	B3 63 0.65 0.74	A0 64 0.80 0.92	B1 65 1.11 1.23	A0 66 1.01 1.09	C3 67 1.25 1.39	A0 68 0.89 1.03	A0 69 0.60 0.67

Figure 4.3-18 Planar Average Power Distribution, PSCEA Bank and Bank 5 Full In, Full Power, Equilibrium Xenon, EOC (17,571 MWD/MTU) of the First Cycle

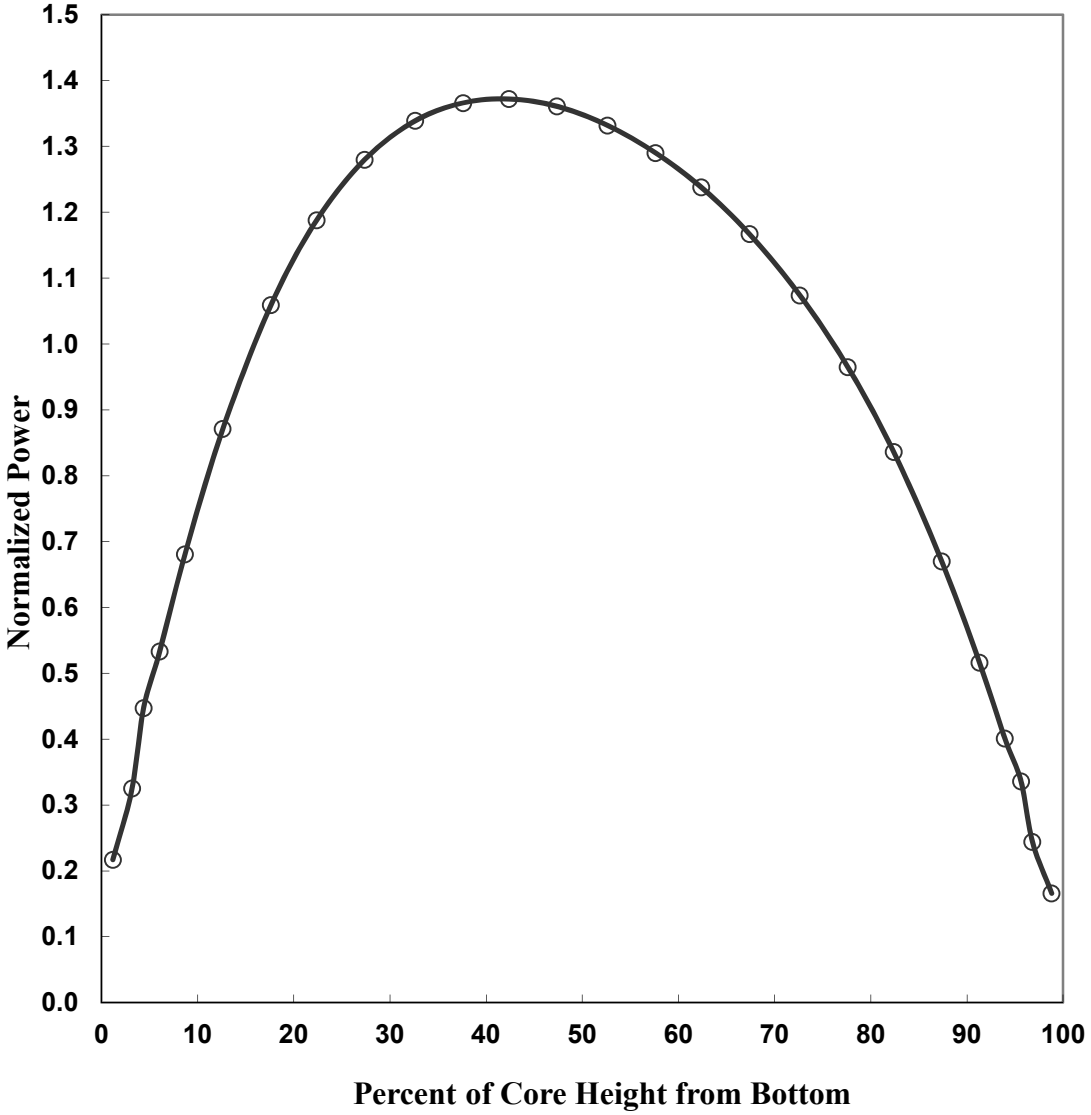

Figure 4.3-19 Unrodded Axial Power Distribution at 0 MWD/MTU of the First Cycle

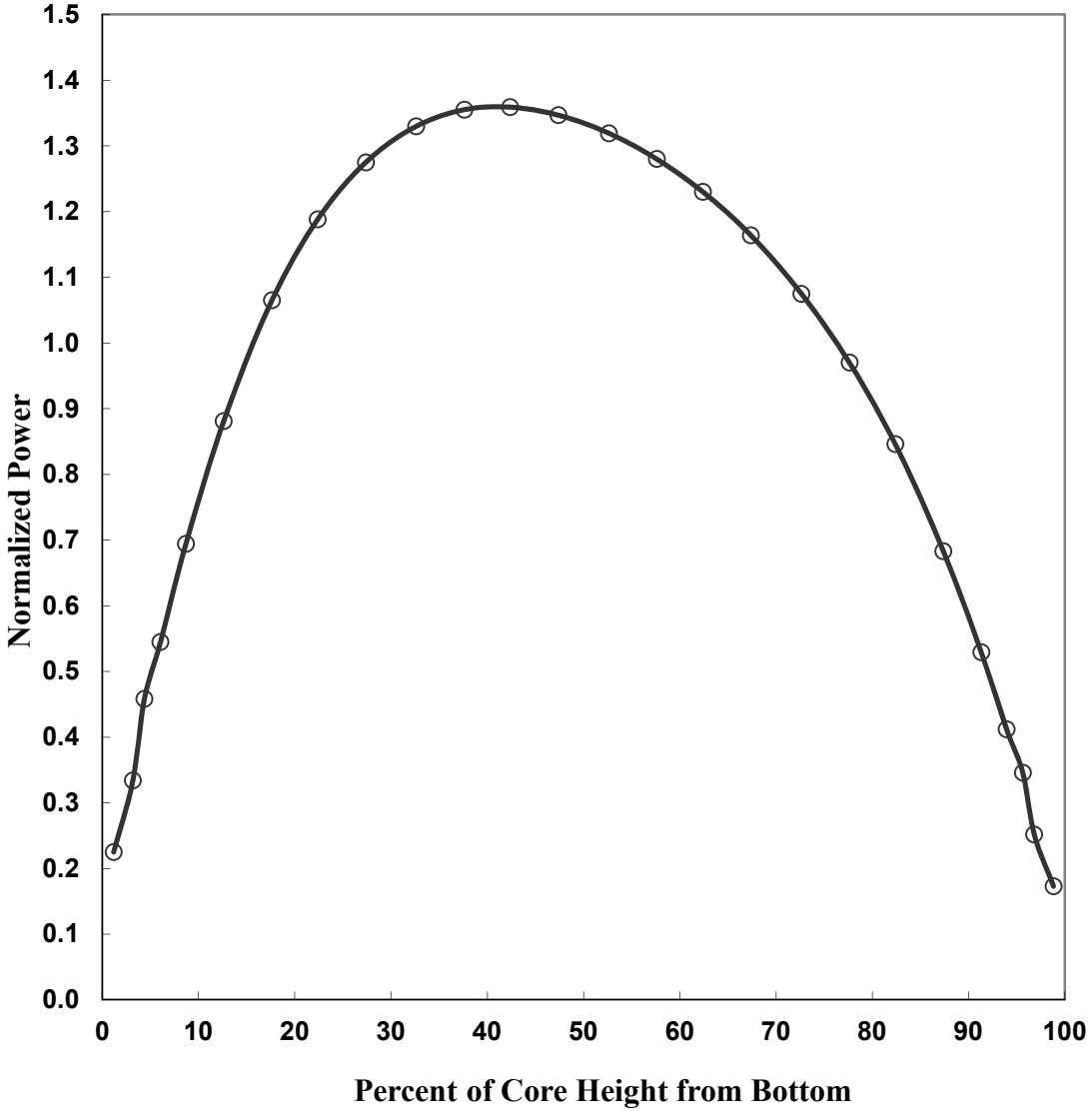

Figure 4.3-20 Unrodded Axial Power Distribution at 50 MWD/MTU of the First Cycle

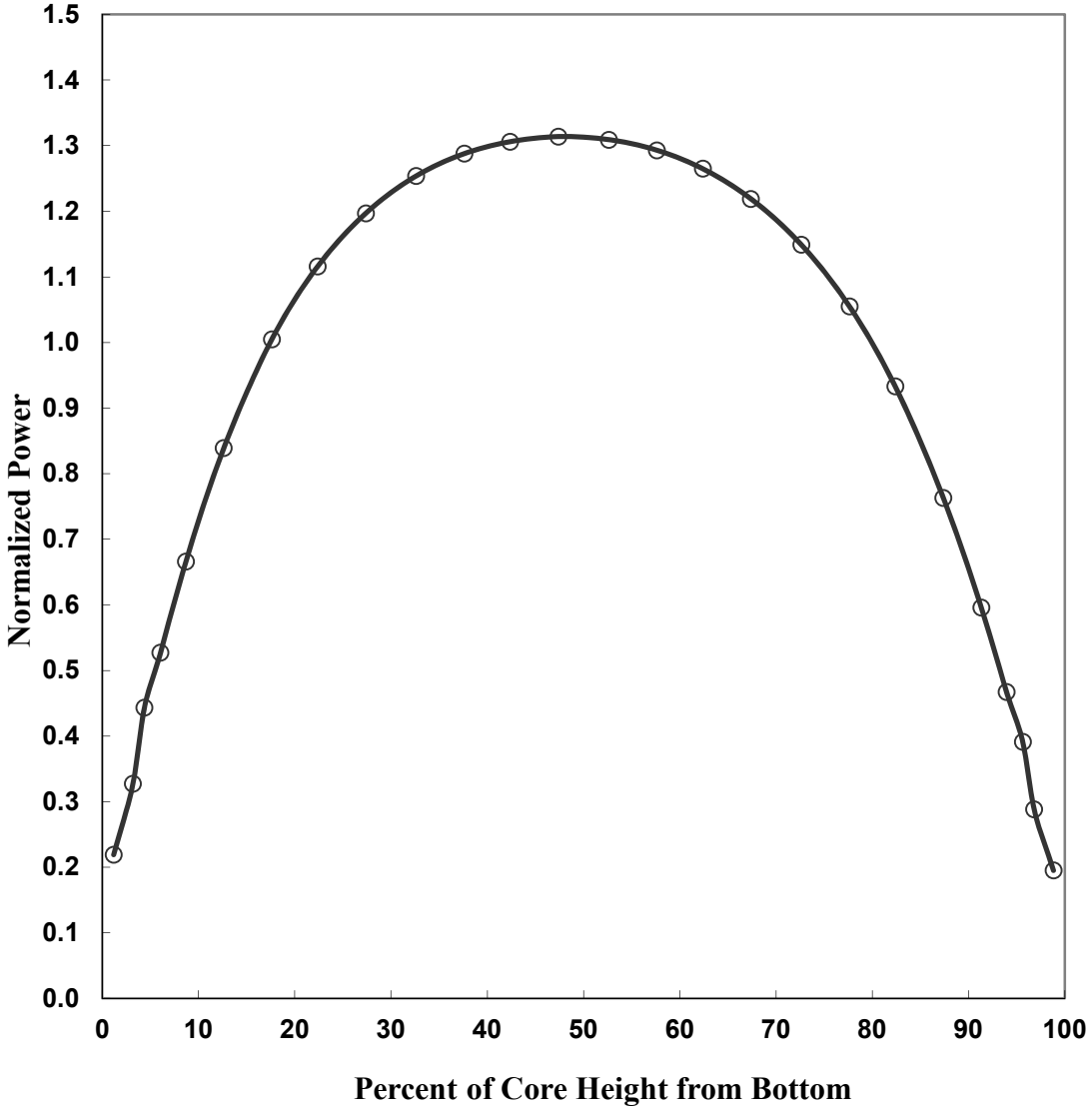

Figure 4.3-21 Unrodded Axial Power Distribution at 4,000 MWD/MTU of the First Cycle

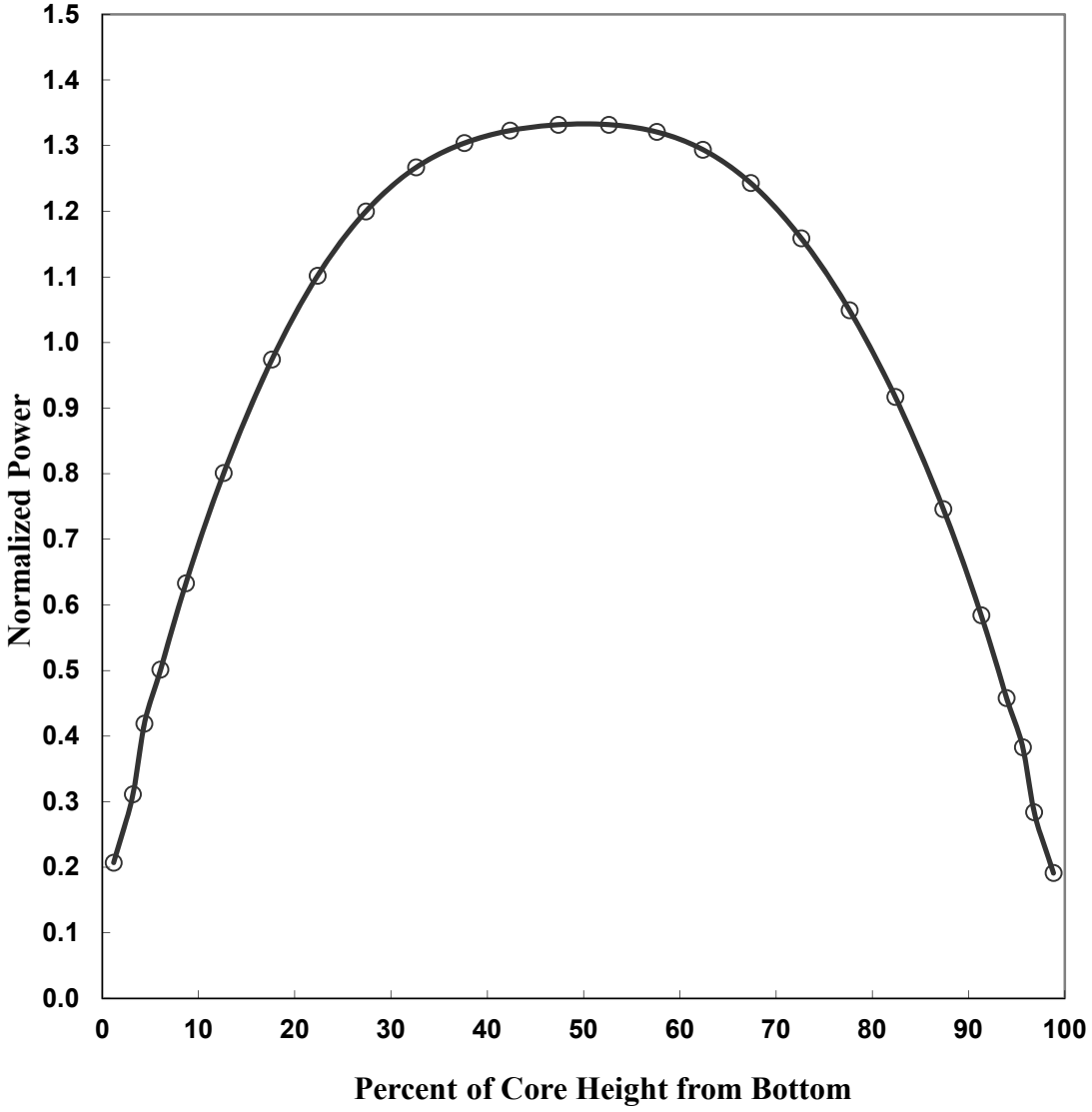

Figure 4.3-22 Unrodded Axial Power Distribution at 8,000 MWD/MTU of the First Cycle

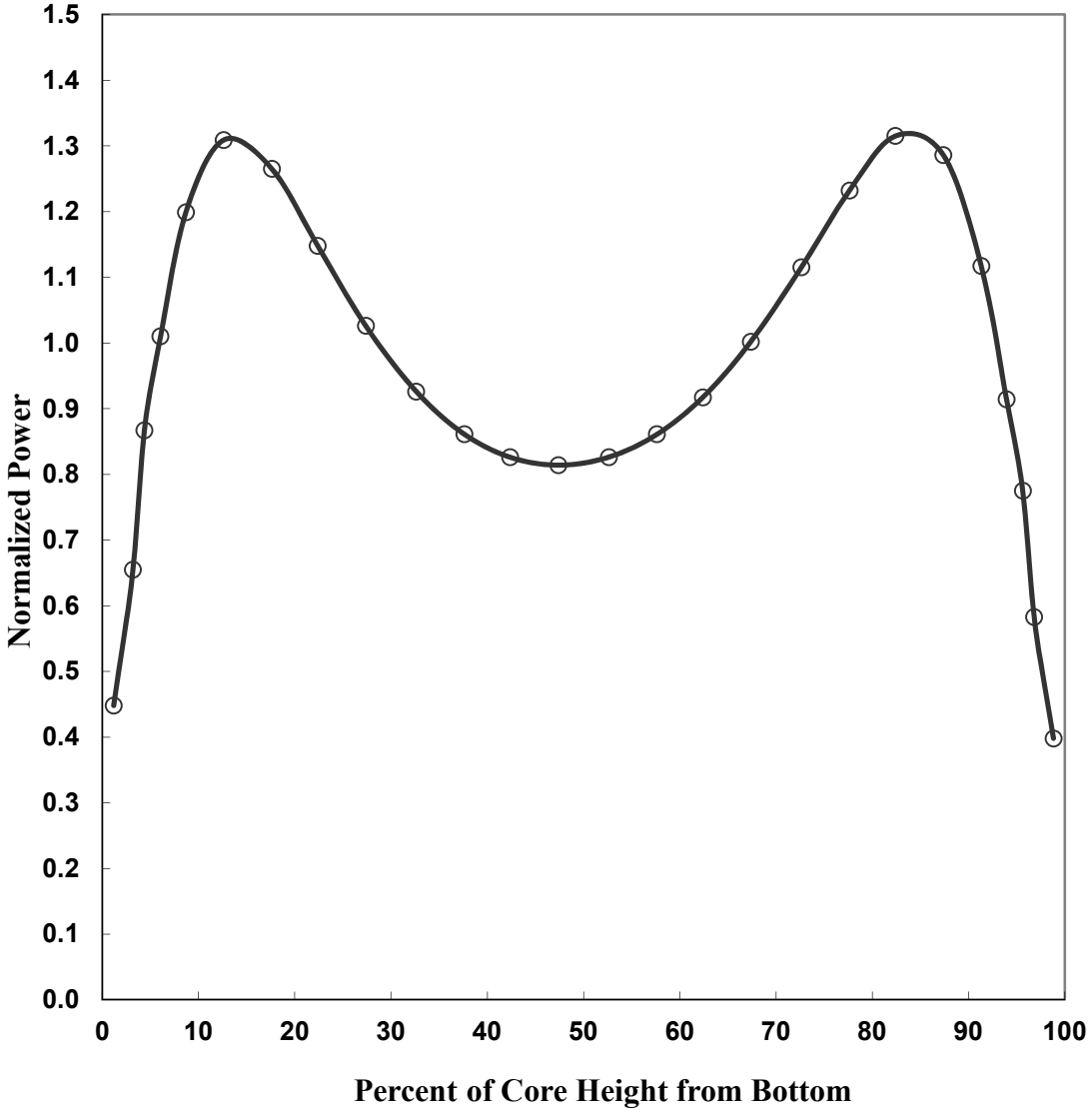

Figure 4.3-23 Unrodded Axial Power Distribution at 14,000 MWD/MTU of the First Cycle

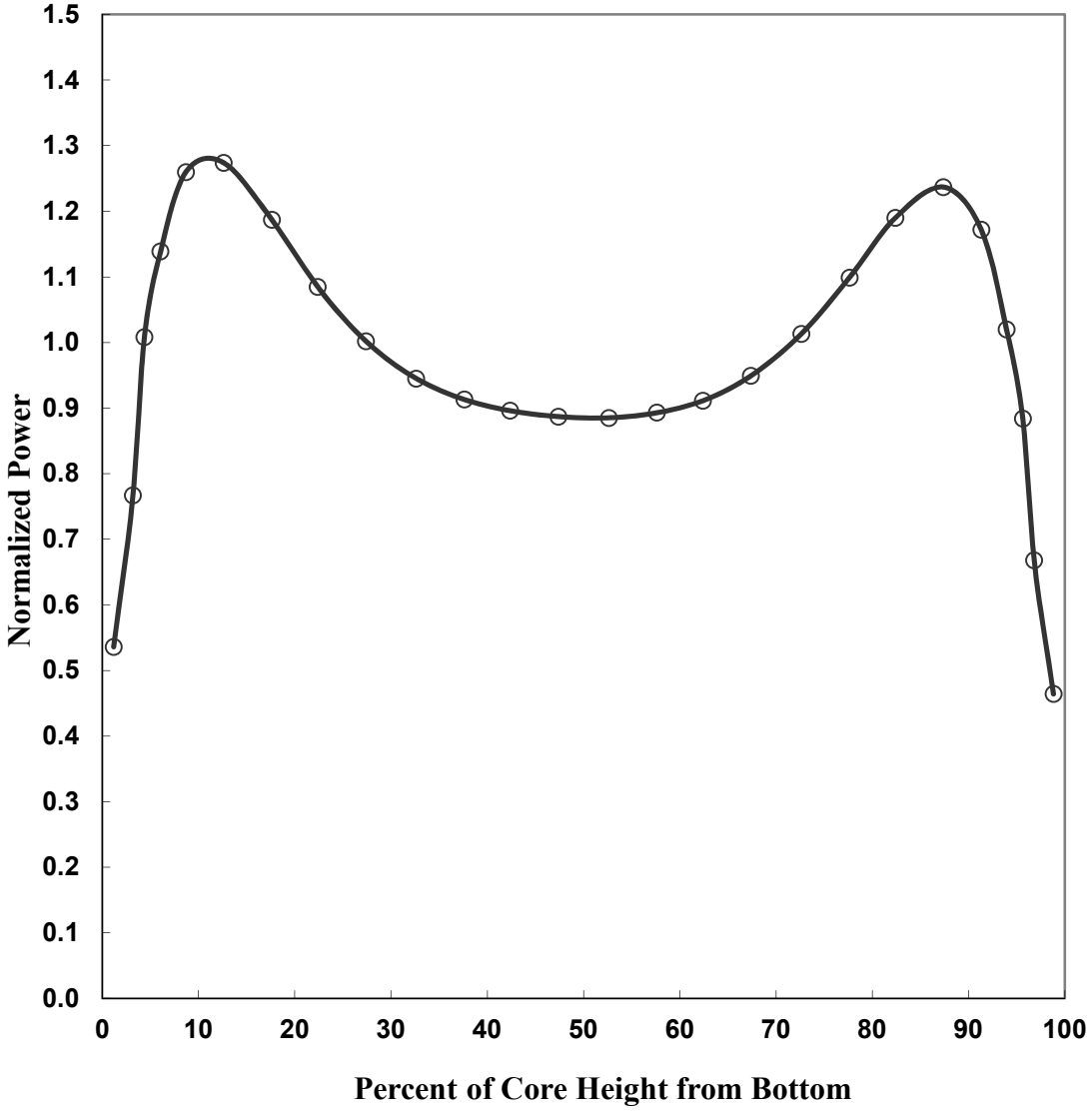

Figure 4.3-24 Unrodded Axial Power Distribution at 17,571 MWD/MTU of the First Cycle

FORMAT IS

FUEL TYPE	BOX NO.
BOX RPD	
MAX PIN	

	MAXIMUM VALUE	IN BOX
BOX RPD	1.29	64
MAX PIN	1.52	57

					J1 1 0.35 0.74	J2 2 0.53 0.92	K0 3 0.82 1.21	H1 4 0.49 0.74
			H0 5 0.32 0.68	K0 6 0.87 1.26	J2 7 0.79 1.00	K1 8 1.09 1.37	J0 9 1.15 1.37	K2 10 1.09 1.36
		H1 11 0.30 0.58	K1 12 0.85 1.23	J0 13 1.10 1.25	K2 14 1.15 1.37	H1 15 1.02 1.14	K2 16 1.24 1.44	H2 17 0.97 1.10
	H0 18 0.33 0.75	K1 19 0.84 1.22	J1 20 0.95 1.08	K2 21 1.16 1.37	J2 22 1.09 1.19	K2 23 1.26 1.46	J2 24 1.16 1.27	K2 25 1.29 1.51
	K0 26 0.87 1.28	J0 27 1.11 1.35	K2 28 1.17 1.39	H2 29 0.93 1.07	K2 30 1.22 1.40	J2 31 1.14 1.28	J1 32 1.27 1.45	J2 33 1.24 1.37
J1 34 0.35 0.74	J2 35 0.79 1.00	K2 36 1.16 1.39	J2 37 1.10 1.18	K2 38 1.22 1.40	J2 39 1.11 1.22	J2 40 1.12 1.30	K2 41 1.28 1.52	J2 42 1.17 1.32
J2 43 0.53 0.92	K1 44 1.09 1.38	H1 45 1.03 1.14	K2 46 1.26 1.46	J2 47 1.14 1.28	J2 48 1.12 1.30	K2 49 1.20 1.41	H0 50 0.96 1.15	K2 51 1.19 1.41
K0 52 0.82 1.21	J0 53 1.15 1.38	K2 54 1.24 1.45	J2 55 1.16 1.27	J1 56 1.28 1.45	K2 57 1.28 1.52	H0 58 0.96 1.15	K1 59 1.21 1.39	J2 60 1.01 1.20
H1 61 0.49 0.74	K2 62 1.09 1.36	H2 63 0.97 1.10	K2 64 1.29 1.51	J2 65 1.24 1.37	J2 66 1.17 1.32	K2 67 1.19 1.41	J2 68 1.01 1.20	H2 69 0.79 0.94

Figure 4.3-25 Planar Average Power Distribution at Beginning of Equilibrium Cycle, Unrodded

FORMAT IS

FUEL TYPE	BOX NO.	MAXIMUM VALUE	IN BOX
BOX RPD		1.34	46
MAX PIN		1.47	46

					J1 1 0.36 0.76	J2 2 0.52 0.88	K0 3 0.77 1.11	H1 4 0.48 0.72
			H0 5 0.33 0.67	K0 6 0.83 1.20	J2 7 0.78 1.01	K1 8 1.11 1.37	J0 9 1.09 1.32	K2 10 1.15 1.38
		H1 11 0.33 0.61	K1 12 0.90 1.26	J0 13 1.07 1.24	K2 14 1.24 1.43	H1 15 1.02 1.12	K2 16 1.31 1.46	H2 17 0.97 1.07
	H0 18 0.34 0.73	K1 19 0.89 1.25	J1 20 0.97 1.11	K2 21 1.29 1.46	J2 22 1.09 1.16	K2 23 1.33 1.47	J2 24 1.08 1.19	K2 25 1.32 1.44
	K0 26 0.83 1.21	J0 27 1.08 1.34	K2 28 1.29 1.47	H2 29 0.97 1.06	K2 30 1.31 1.45	J2 31 1.06 1.20	J1 32 1.13 1.33	J2 33 1.08 1.22
J1 34 0.36 0.75	J2 35 0.78 1.01	K2 36 1.25 1.46	J2 37 1.10 1.16	K2 38 1.31 1.46	J2 39 1.04 1.19	J2 40 1.04 1.19	K2 41 1.30 1.42	J2 42 1.08 1.19
J2 43 0.52 0.88	K1 44 1.11 1.38	H1 45 1.02 1.12	K2 46 1.34 1.47	J2 47 1.06 1.20	J2 48 1.04 1.19	K2 49 1.26 1.38	H0 50 0.95 1.09	K2 51 1.27 1.40
K0 52 0.77 1.11	J0 53 1.09 1.32	K2 54 1.32 1.47	J2 55 1.08 1.19	J1 56 1.13 1.33	K2 57 1.30 1.43	H0 58 0.95 1.09	K1 59 1.25 1.36	J2 60 0.99 1.15
H1 61 0.48 0.72	K2 62 1.15 1.38	H2 63 0.97 1.07	K2 64 1.32 1.44	J2 65 1.08 1.22	J2 66 1.08 1.19	K2 67 1.27 1.40	J2 68 0.99 1.15	H2 69 0.78 0.89

Figure 4.3-26 Planar Average Power Distribution at Middle of Equilibrium Cycle, Unrodded

FORMAT IS

FUEL TYPE	BOX NO.
BOX RPD	
MAX PIN	

	MAXIMUM VALUE	IN BOX
BOX RPD	1.32	21
MAX PIN	1.44	28

					J1 1 0.43 0.82	J2 2 0.59 0.91	K0 3 0.83 1.15	H1 4 0.54 0.77
			H0 5 0.41 0.72	K0 6 0.89 1.23	J2 7 0.84 1.02	K1 8 1.17 1.37	J0 9 1.09 1.25	K2 10 1.21 1.37
		H1 11 0.42 0.70	K1 12 1.05 1.36	J0 13 1.10 1.24	K2 14 1.28 1.42	H1 15 1.01 1.08	K2 16 1.29 1.40	H2 17 0.95 1.04
	H0 18 0.41 0.79	K1 19 1.05 1.35	J1 20 1.03 1.11	K2 21 1.32 1.44	J2 22 1.06 1.14	K2 23 1.28 1.39	J2 24 1.01 1.11	K2 25 1.24 1.34
	K0 26 0.89 1.23	J0 27 1.10 1.27	K2 28 1.32 1.44	H2 29 0.97 1.04	K2 30 1.27 1.38	J2 31 0.99 1.09	J1 32 1.03 1.16	J2 33 0.99 1.08
J1 34 0.43 0.81	J2 35 0.84 1.02	K2 36 1.28 1.42	J2 37 1.06 1.14	K2 38 1.27 1.38	J2 39 0.98 1.09	J2 40 0.97 1.07	K2 41 1.23 1.33	J2 42 1.00 1.06
J2 43 0.59 0.91	K1 44 1.17 1.37	H1 45 1.01 1.08	K2 46 1.27 1.39	J2 47 0.98 1.09	J2 48 0.97 1.07	K2 49 1.23 1.33	H0 50 0.92 0.98	K2 51 1.24 1.35
K0 52 0.82 1.14	J0 53 1.09 1.24	K2 54 1.29 1.40	J2 55 1.01 1.10	J1 56 1.03 1.16	K2 57 1.23 1.33	H0 58 0.92 0.98	K1 59 1.22 1.33	J2 60 0.96 1.04
H1 61 0.54 0.77	K2 62 1.21 1.37	H2 63 0.95 1.04	K2 64 1.24 1.34	J2 65 0.99 1.08	J2 66 1.00 1.06	K2 67 1.24 1.35	J2 68 0.96 1.04	H2 69 0.78 0.82

Figure 4.3-27 Planar Average Power Distribution at End of Equilibrium Cycle, Unrodded

	1	2	3	4	5	6	7	8	9	10	11	12	13	14	15	16
1	1.2606	1.1927	1.2991	1.2413	1.3032	1.349	1.3593	1.356	1.3543	1.3556	1.3433	1.2959	1.2332	1.2906	1.186	1.2564
2	1.1924	1.2679	1.1509	0.2299	1.179	1.2579	1.262	1.2581	1.257	1.2593	1.2536	1.1736	0.2285	1.1439	1.2605	1.1864
3	1.2984	1.1505	1.1727	1.0614	1.1264	1.2676	1.2289	1.2144	1.2136	1.2269	1.2642	1.1224	1.0568	1.1667	1.1442	1.2913
4	1.2402	0.2298	1.0612			1.1458	1.2197	1.1978	1.1973	1.2182	1.1434			1.057	0.2286	1.2342
5	1.3018	1.1781	1.1259			1.0615	1.1735	1.1875	1.1873	1.1725	1.0598			1.1227	1.1744	1.2973
6	1.3473	1.2567	1.2668	1.1454	1.0613	0.2295	1.1163	1.2096	1.2098	1.1159	0.2293	1.0599	1.1436	1.2647	1.2546	1.345
7	1.3574	1.2607	1.228	1.2191	1.1732	1.1162	1.2148	1.1492	1.1497	1.2149	1.1159	1.1727	1.2185	1.2275	1.2605	1.3576
8	1.3539	1.2565	1.2133	1.1971	1.1871	1.2095	1.1493			1.1497	1.2098	1.1873	1.1976	1.2143	1.2583	1.3565
9	1.3533	1.256	1.2128	1.1967	1.1868	1.2094	1.1494			1.1494	1.2099	1.1878	1.1983	1.2152	1.2593	1.3575
10	1.355	1.2586	1.2261	1.2174	1.1718	1.1153	1.2143	1.1492	1.1493	1.2149	1.1165	1.1738	1.2202	1.2297	1.2631	1.3608
11	1.343	1.2531	1.2634	1.1425	1.0589	0.2291	1.115	1.209	1.2093	1.1161	0.2295	1.0616	1.1461	1.2682	1.2589	1.3506
12	1.2958	1.1731	1.1215			1.0586	1.1712	1.1861	1.1866	1.1728	1.061			1.1268	1.1799	1.305
13	1.2326	0.2285	1.0557			1.1416	1.2162	1.1954	1.196	1.2181	1.1446			1.0615	0.23	1.2434
14	1.2884	1.142	1.1648	1.0551	1.1205	1.2617	1.2243	1.2108	1.2114	1.2262	1.2652	1.1248	1.0606	1.1727	1.1522	1.3023
15	1.1814	1.2566	1.1413	0.2282	1.1712	1.2507	1.2561	1.2533	1.2536	1.258	1.2543	1.1762	0.2294	1.1508	1.2703	1.1975
16	1.2471	1.1804	1.2865	1.2301	1.2929	1.3399	1.3518	1.35	1.3497	1.3534	1.3437	1.2989	1.2386	1.2988	1.1959	1.2694

Figure 4.3-28 Assembly Pin Power Distribution, Unrodded, Eq. Xe, 50 MWD/MTU of the First Cycle (Assembly 24)

	1	2	3	4	5	6	7	8	9	10	11	12	13	14	15	16
1	1.25	1.2239	1.3025	1.3086	1.2917	1.2706	1.2556	1.2485	1.248	1.2536	1.2672	1.2868	1.3023	1.2951	1.216	1.2408
2	1.2237	1.2724	1.2755	0.9668	1.2684	1.2306	1.2077	1.1987	1.1985	1.2061	1.2277	1.2641	0.9629	1.2689	1.2647	1.2154
3	1.3023	1.2754	1.2881	1.2511	1.2335	1.2477	1.1994	1.1841	1.184	1.198	1.2451	1.2298	1.2463	1.2819	1.2683	1.2939
4	1.3084	0.9667	1.2511			1.2206	1.2249	1.1963	1.1962	1.2236	1.2182			1.2458	0.9623	1.3006
5	1.2915	1.2682	1.2334			1.2307	0.926	1.216	1.2159	0.9252	1.2285			1.2288	1.2624	1.2846
6	1.2704	1.2303	1.2475	1.2207	1.2308	1.2601	1.2321	1.2255	1.2253	1.2308	1.2579	1.2279	1.2172	1.2434	1.2256	1.2644
7	1.2549	1.2067	1.1989	1.225	0.9265	1.2326	1.2429	1.2067	1.2061	1.2413	1.2302	0.9245	1.2219	1.1959	1.2035	1.2502
8	1.2455	1.196	1.1829	1.1969	1.2177	1.2272	1.208			1.2054	1.2239	1.214	1.1939	1.1813	1.1952	1.244
9	1.2452	1.1958	1.1828	1.1968	1.2178	1.2278	1.2091			1.2066	1.2247	1.2145	1.1942	1.1816	1.1955	1.2444
10	1.2531	1.2053	1.1976	1.2239	0.926	1.2323	1.2434	1.2085	1.2079	1.2422	1.2306	0.9248	1.2219	1.1959	1.2035	1.2504
11	1.2672	1.2275	1.245	1.2184	1.229	1.2588	1.2317	1.2265	1.2264	1.2311	1.2577	1.2275	1.2168	1.243	1.2253	1.2643
12	1.2867	1.2639	1.2297			1.2284	0.9253	1.2159	1.2162	0.9252	1.2277			1.2279	1.2618	1.2841
13	1.3019	0.9627	1.2461			1.2174	1.2222	1.1945	1.1949	1.2221	1.2168			1.2445	0.962	1.2998
14	1.2944	1.2684	1.2816	1.2456	1.2287	1.2433	1.1954	1.18	1.1805	1.1955	1.2429	1.2279	1.2445	1.2802	1.267	1.2928
15	1.2152	1.2641	1.2679	0.9621	1.2622	1.2253	1.2025	1.1924	1.1929	1.2027	1.2251	1.2616	0.9619	1.2669	1.2631	1.2144
16	1.2398	1.2147	1.2933	1.3003	1.2845	1.2643	1.2496	1.241	1.2416	1.2498	1.2642	1.284	1.2995	1.2926	1.2142	1.2392

Figure 4.3-29 Assembly Pin Power Distribution, Unrodded, Eq. Xe, 17,571 MWD/MTU of the First Cycle (Assembly 29)

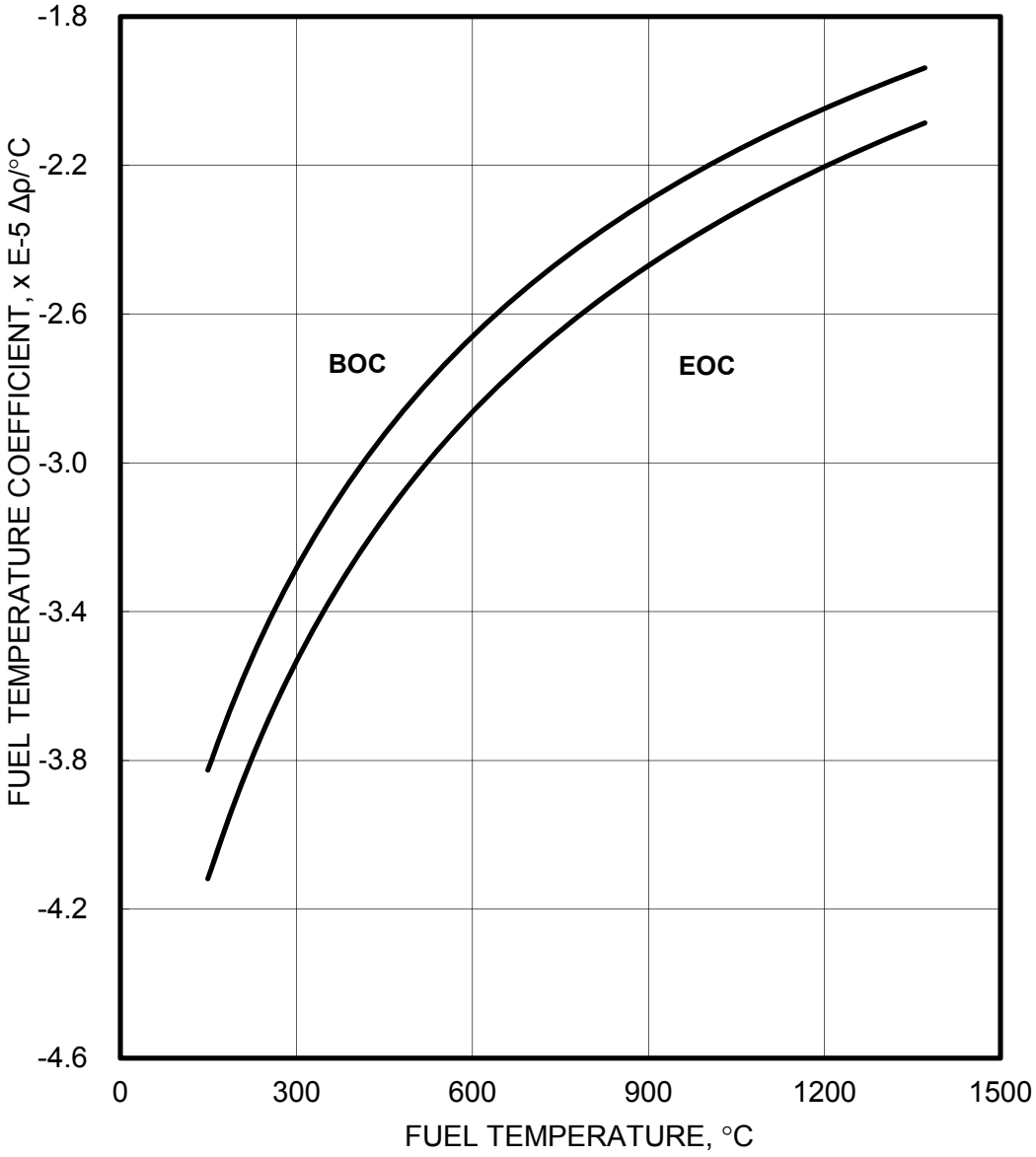

Figure 4.3-30 Fuel Temperature Coefficient vs. Effective Fuel Temperature

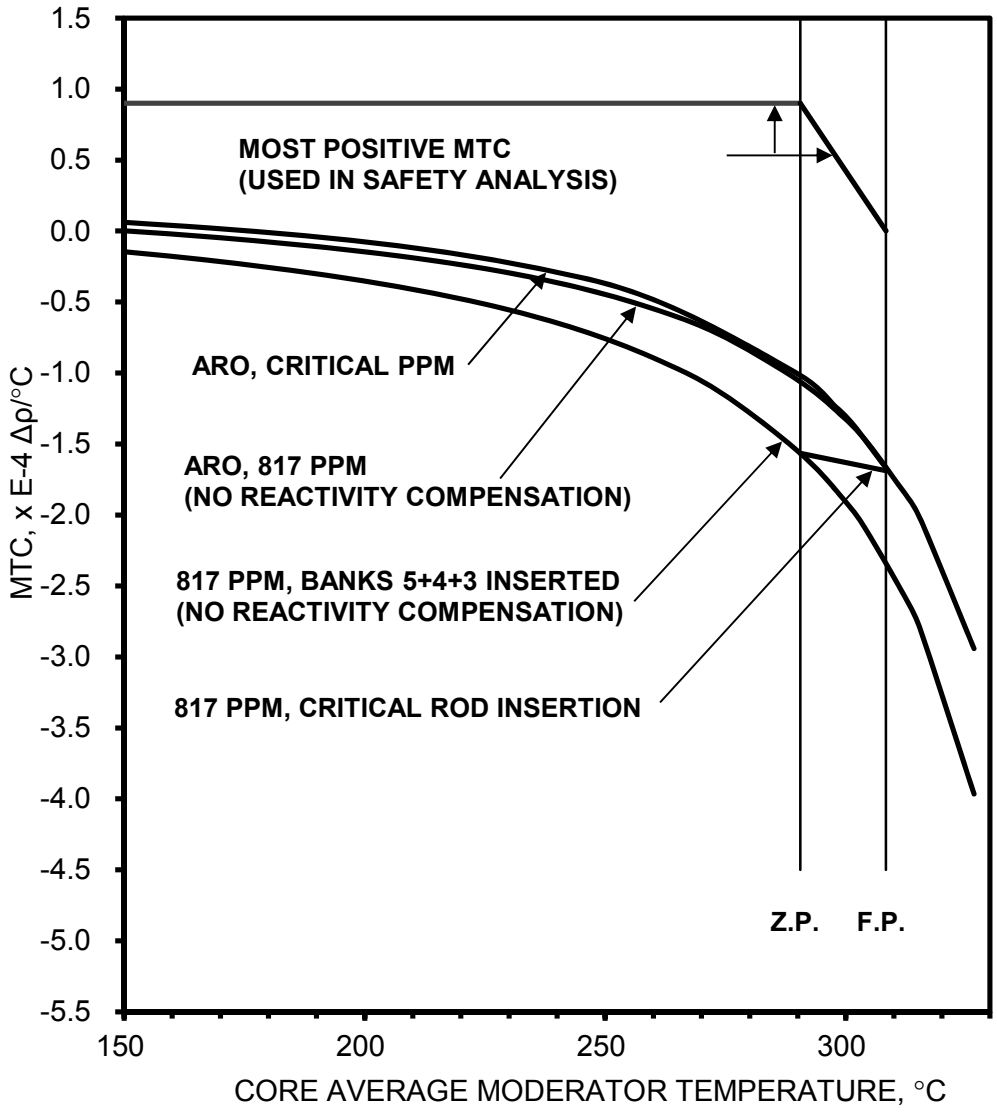

Figure 4.3-31 Moderator Temperature Coefficient vs. Moderator Temperature at BOC HFP Equilibrium Xenon and Fuel Temperature

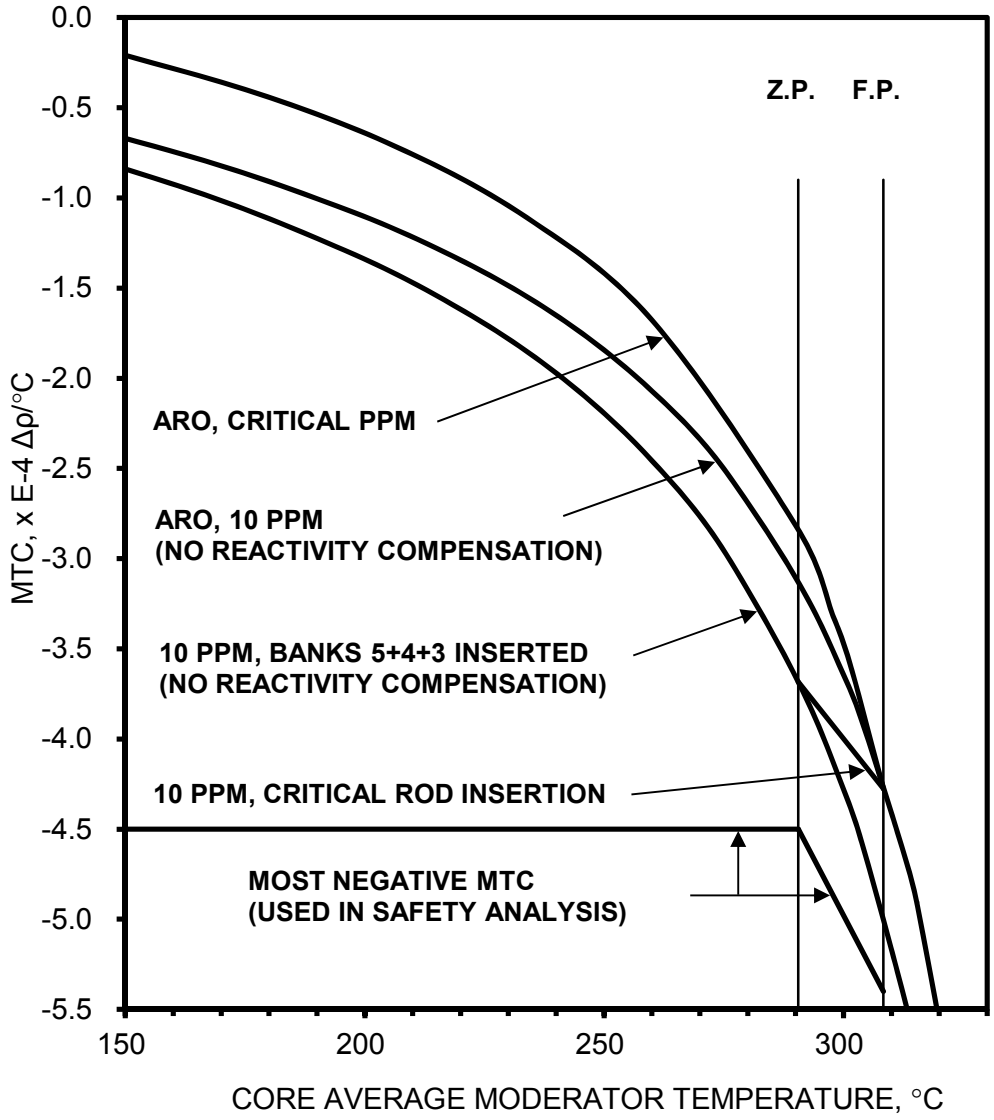

Figure 4.3-32 Moderator Temperature Coefficient vs. Moderator Temperature at EOC HFP Equilibrium Xenon and Fuel Temperature

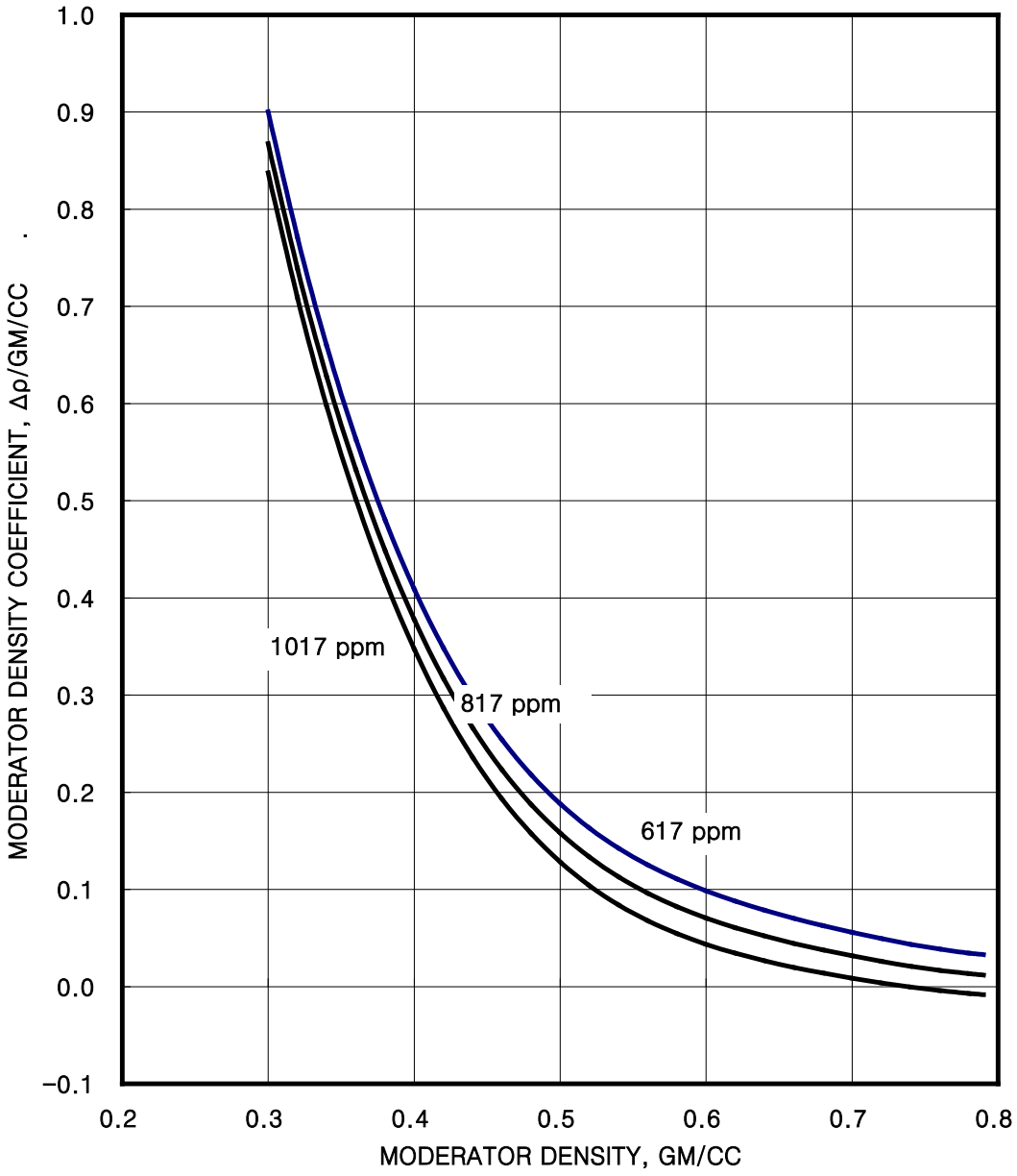

Figure 4.3-33 Moderator Density Coefficient vs. Moderator Density at BOC

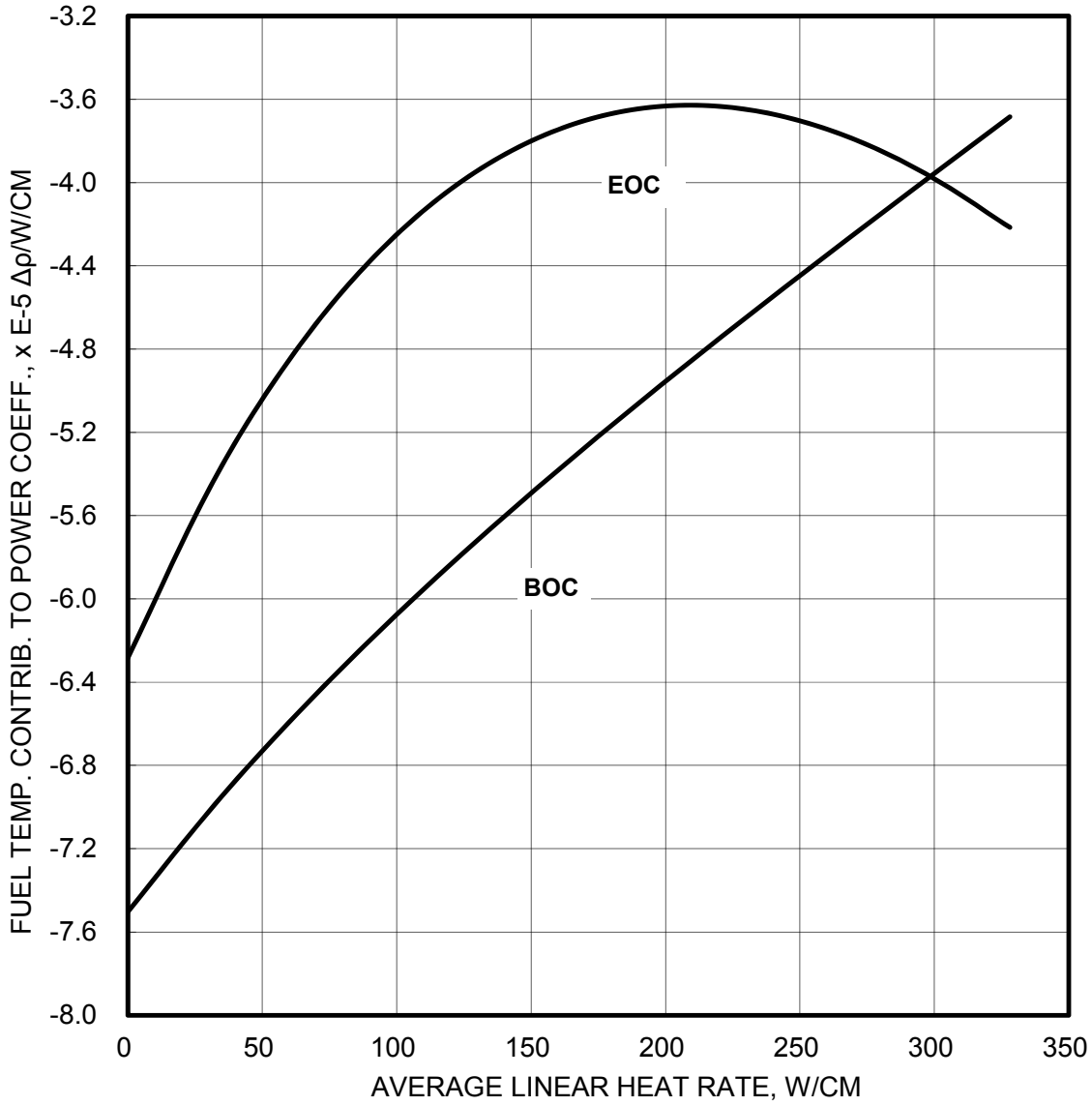

Figure 4.3-34 Fuel Temperature Contribution to Power Coefficient

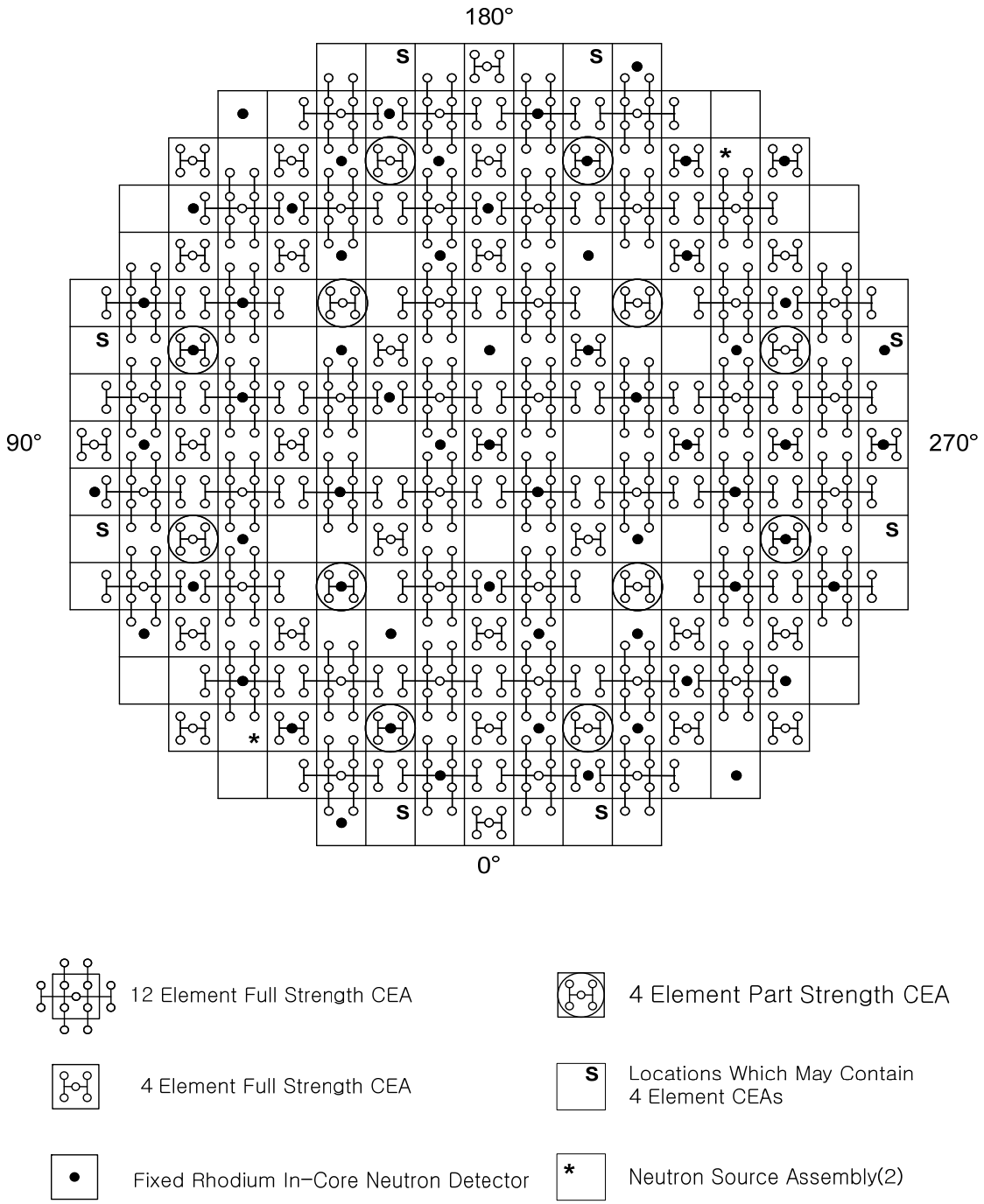

Figure 4.3-35 Control Element Assembly and Drive Location and Incore Instrument Locations

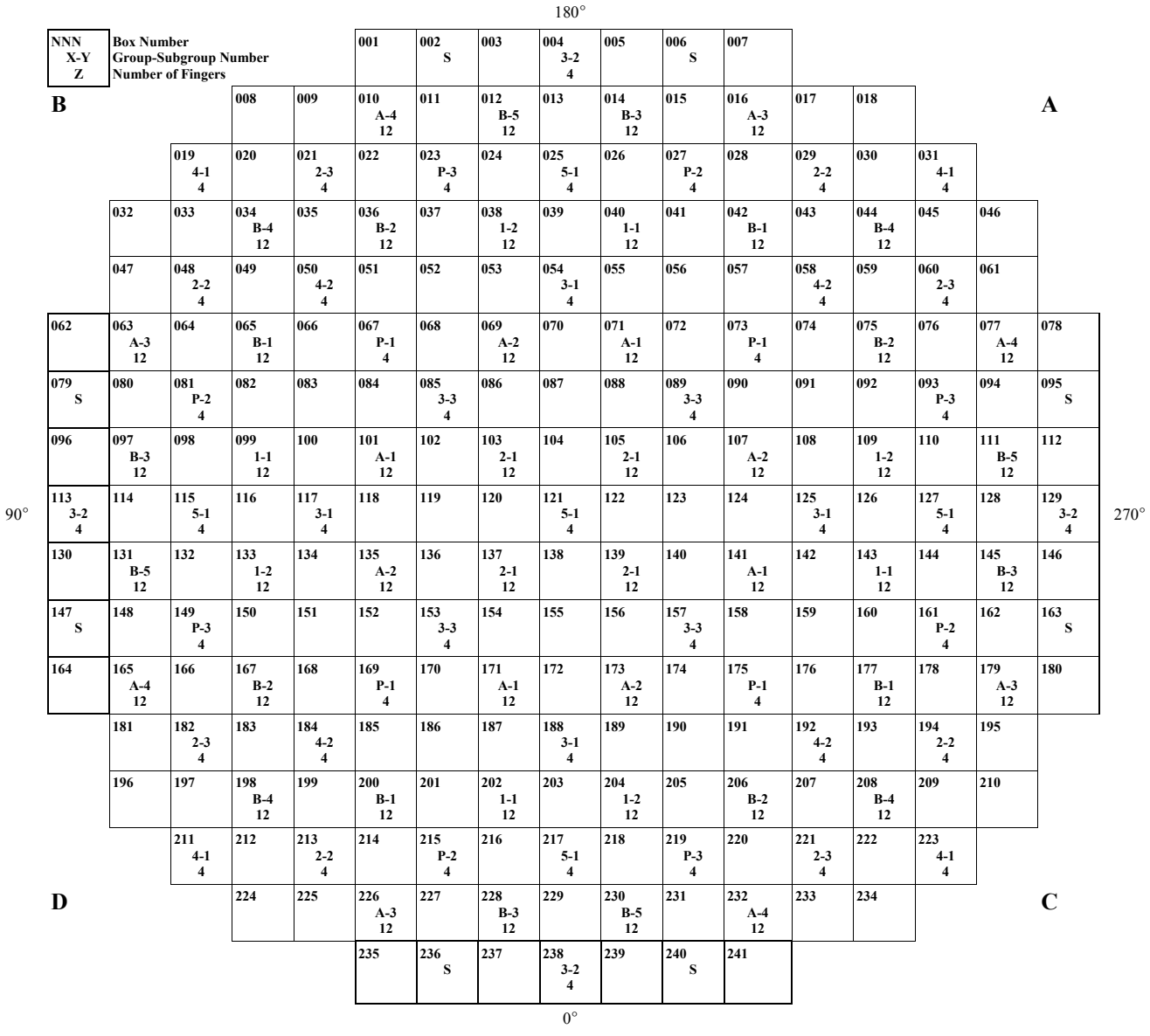

5 - Lead Regulating Bank (5)
4 - Second Regulating Bank (8)
3 - Third Regulating Bank (12)
2 - Fourth Regulating Bank (12)
1 - Last Regulating Bank (8)

B - Shutdown Bank B (20)
A - Shutdown Bank A (16)
P - PSCEA Group (12)
S - Spare CEA Location (8)

Figure 4.3-36 Control Element Assembly Group Assignment

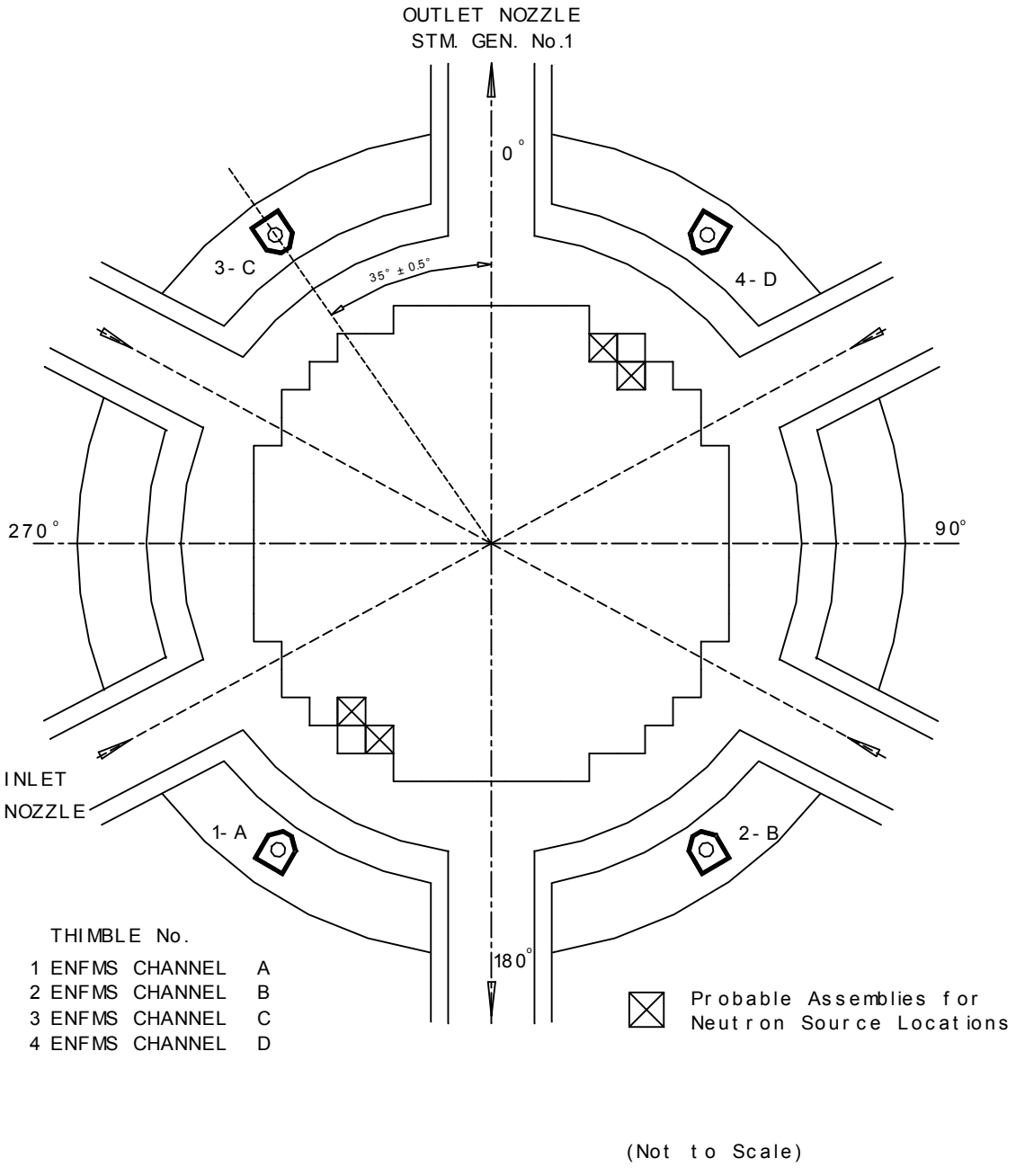

Figure 4.3-37 Ex-core Detector Location

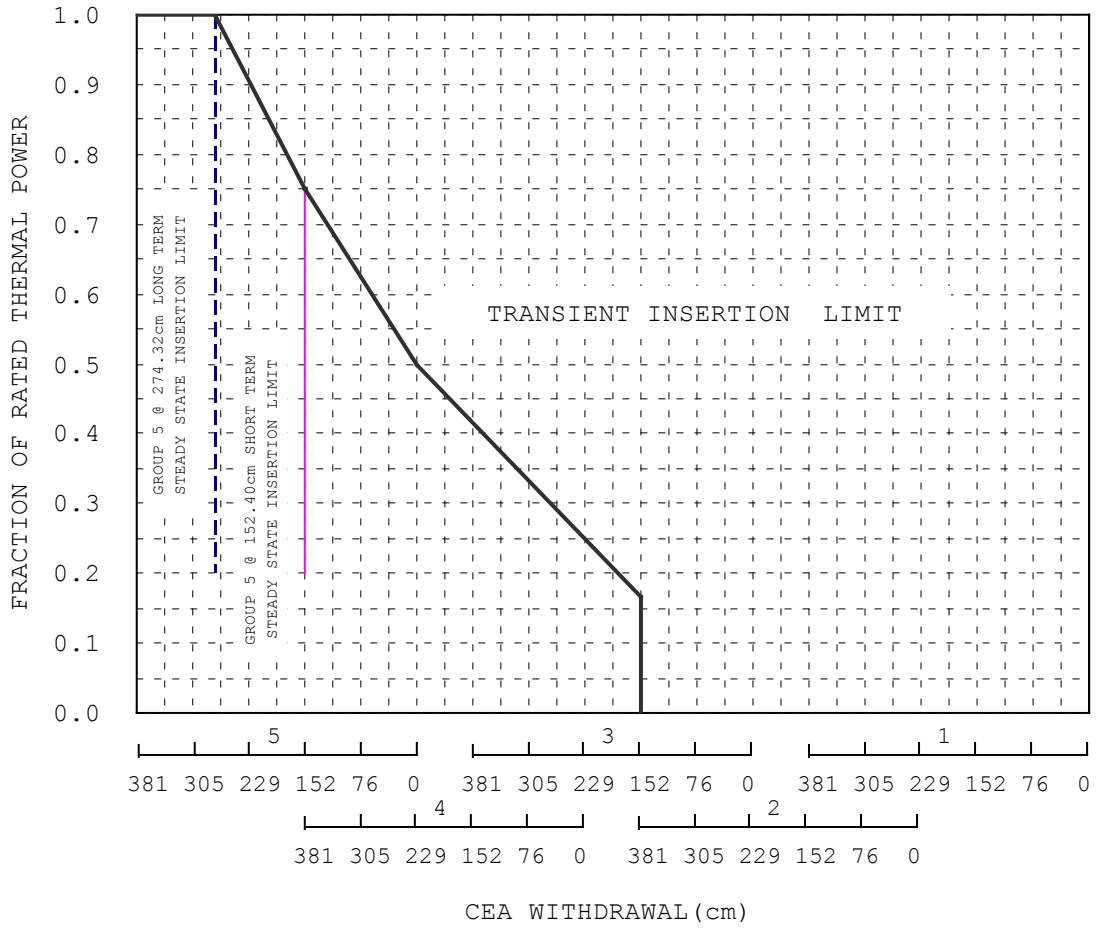

Figure 4.3-38 Typical Power Dependent CEA Insertion Limit

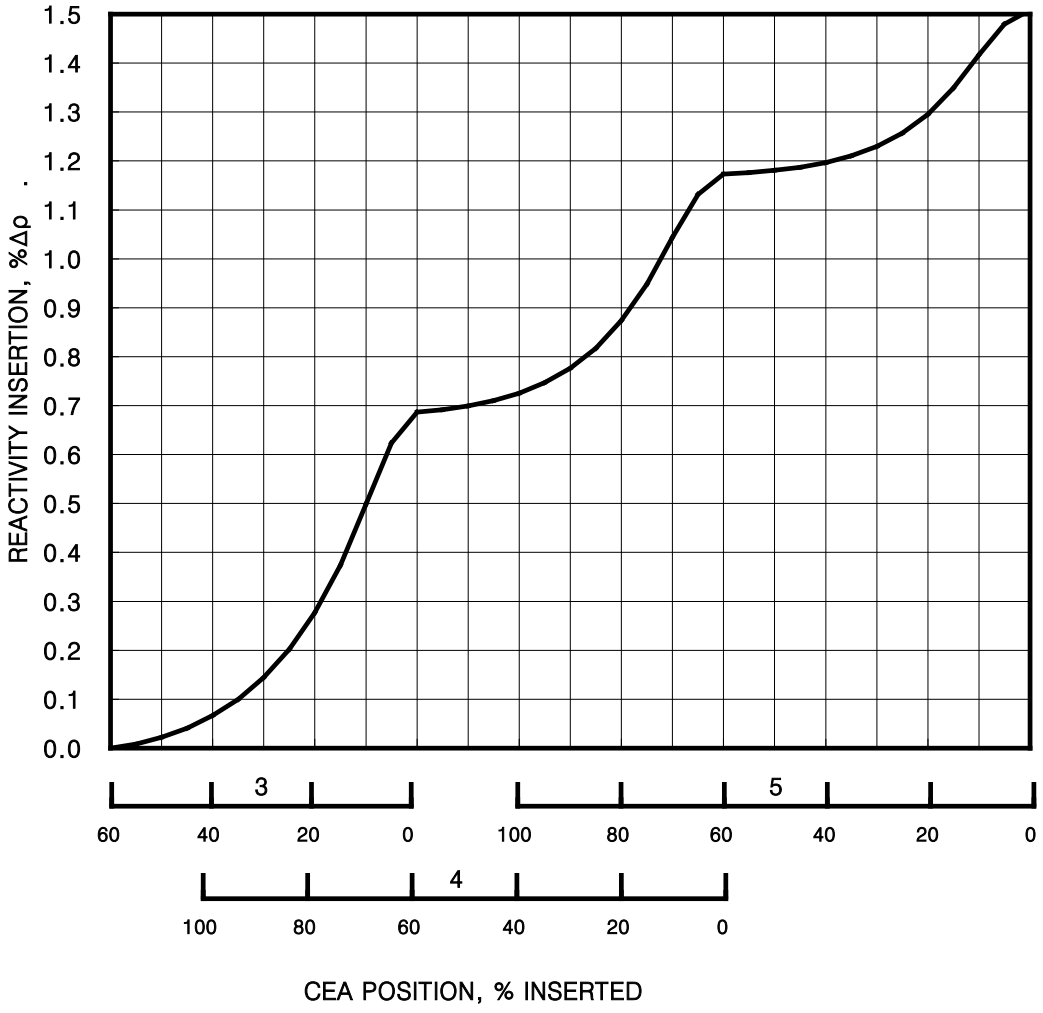

Figure 4.3-39 Typical Integral Worth vs. Withdrawal at Zero Power, EOC

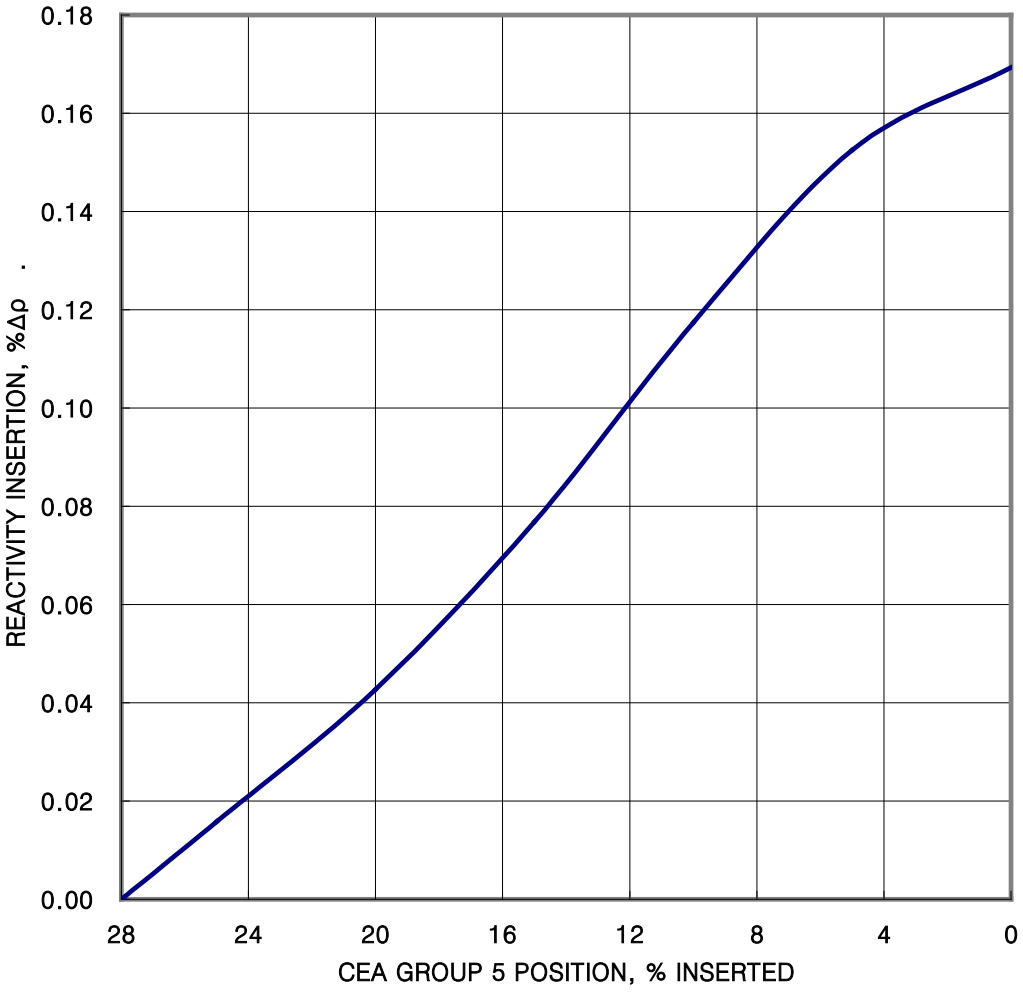

Figure 4.3-40 Typical Integral Worth vs. Withdrawal at Hot Full Power, EOC, Equilibrium Xenon Condition

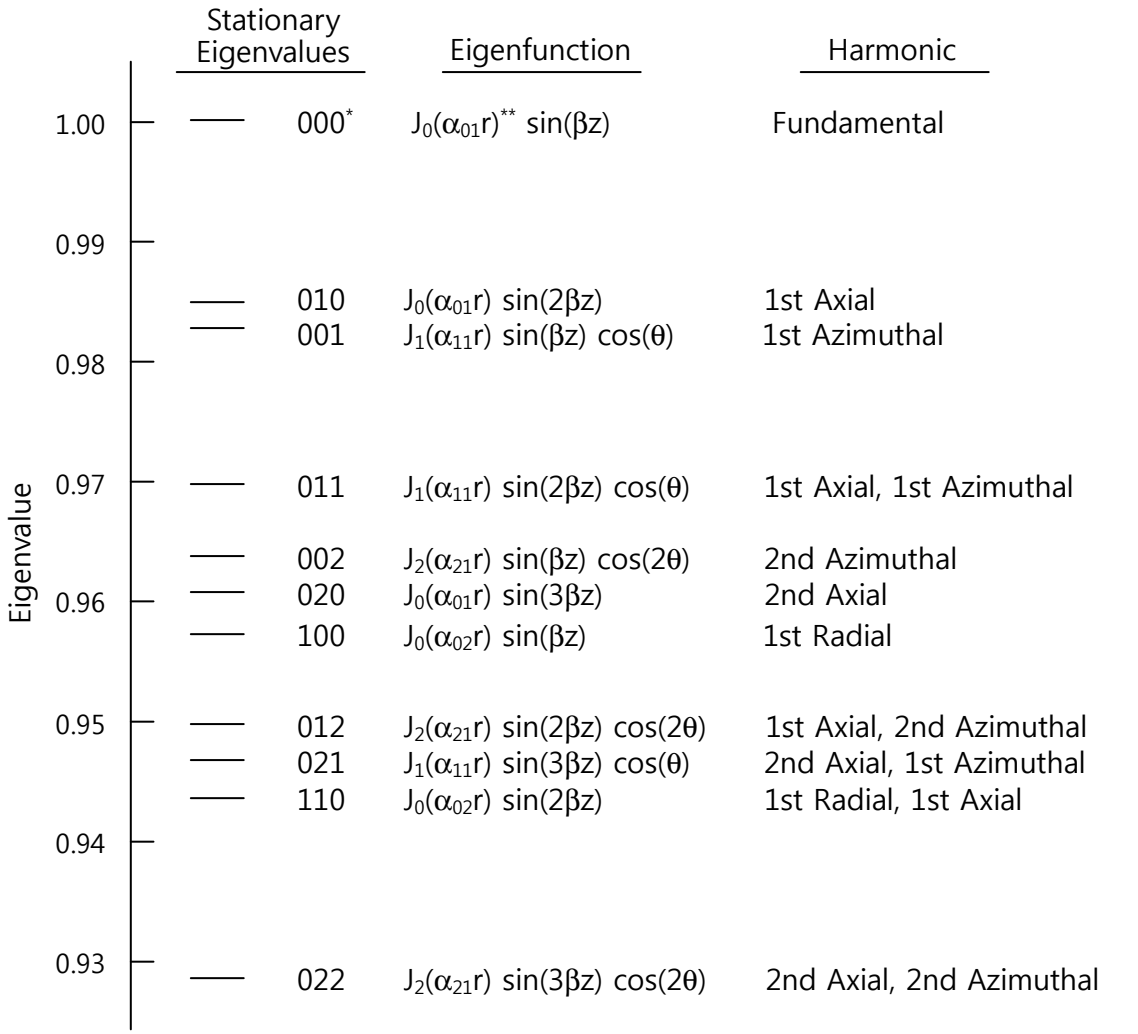

* The indices indicate radial, axial and azimuthal components of the separable modes in that order.

** α_{ij} indicates the jth zero of the ith Bessel function.

Figure 4.3-41 Reactivity Difference Between Fundamental and Excited State of a Bare Cylindrical Reactor

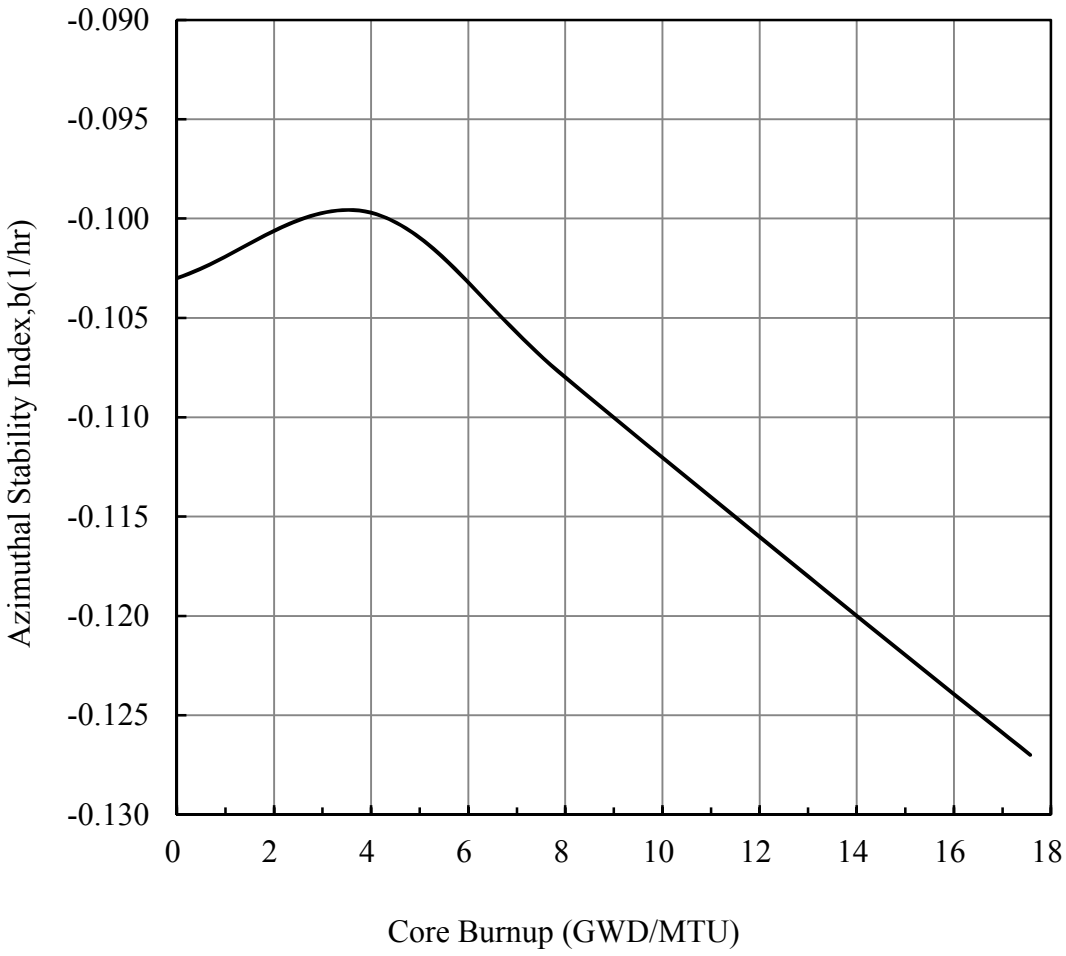

Figure 4.3-42 Expected Variation of the Azimuthal Stability Index, Hot Full Power, Unrodded

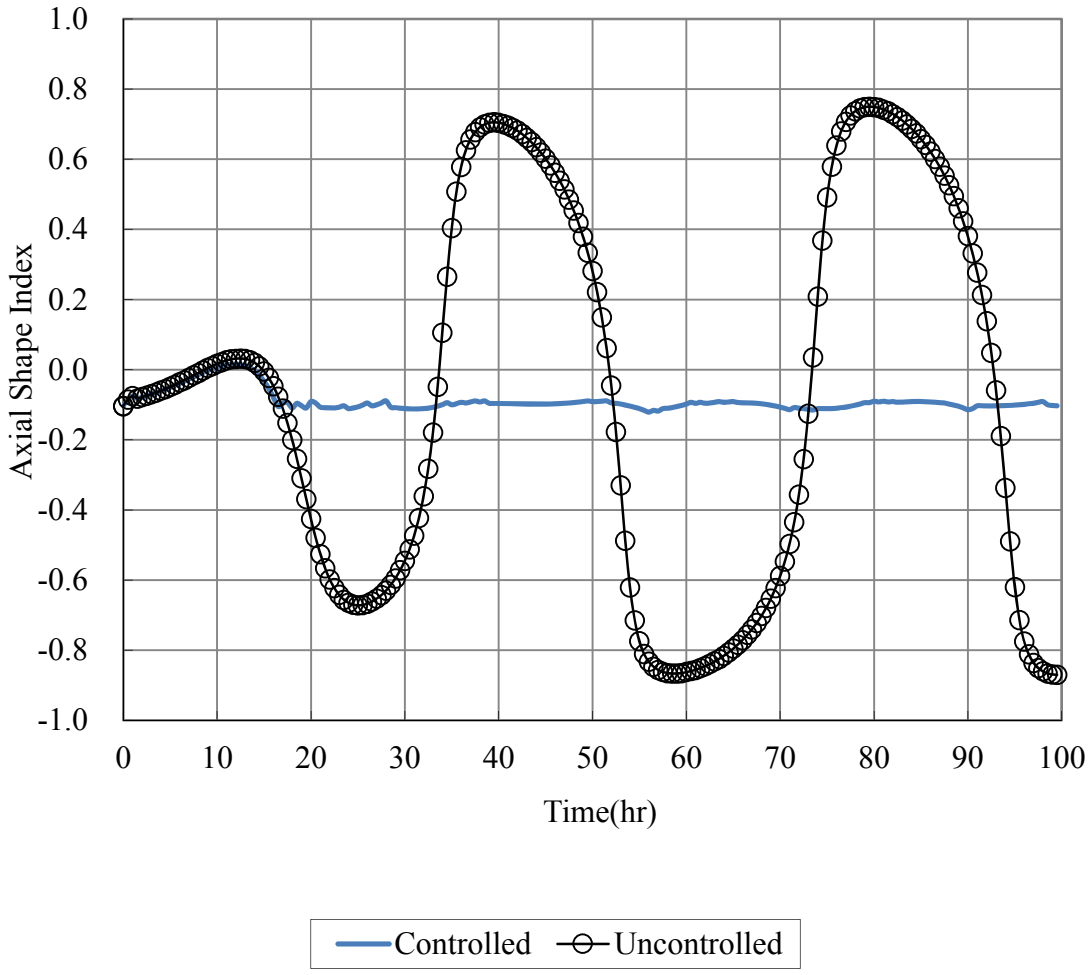

Figure 4.3-43 PSCEA Controlled and Uncontrolled Xenon Oscillation

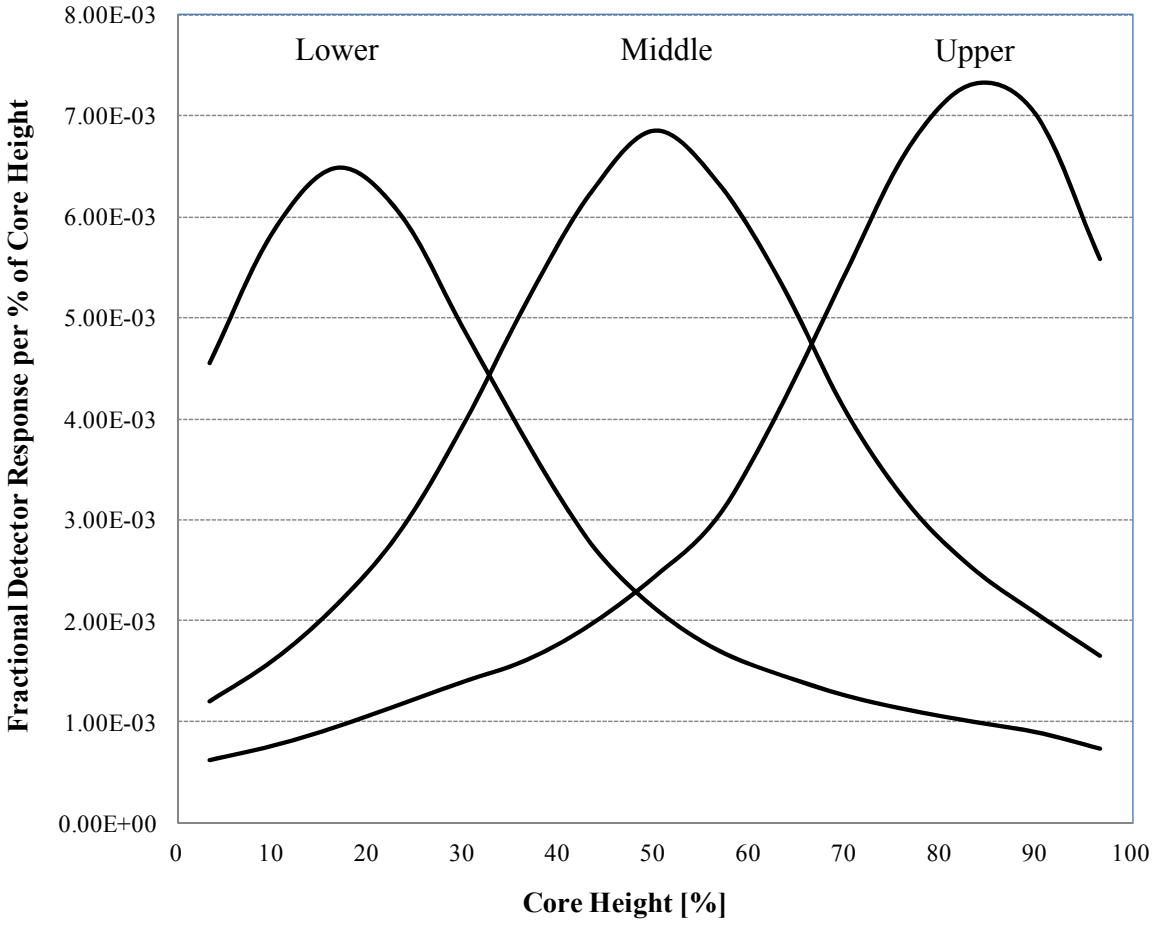

Figure 4.3-44 Typical Three Sub-Channel Annealing

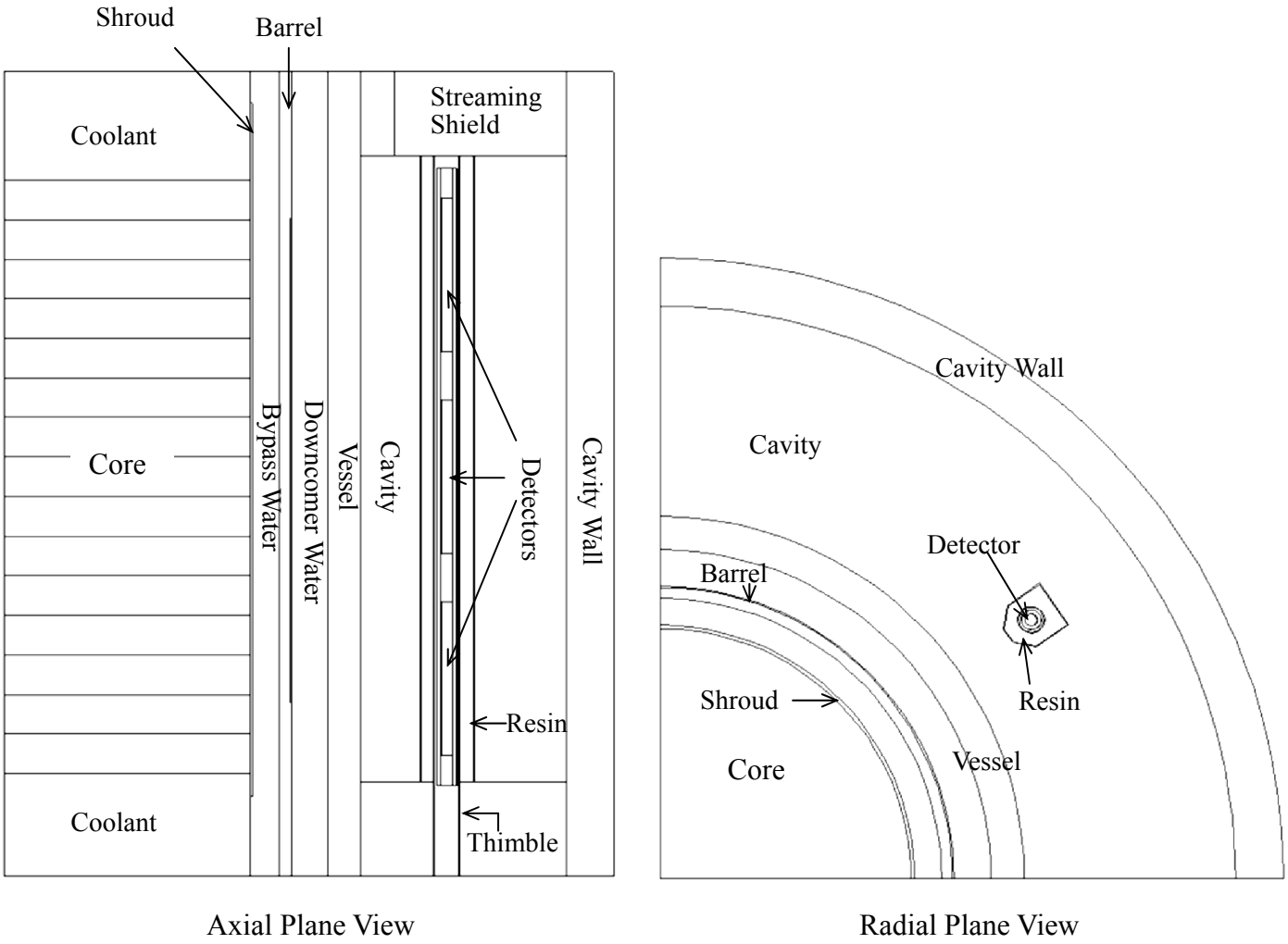

Figure 4.3-45 Geometry Layout

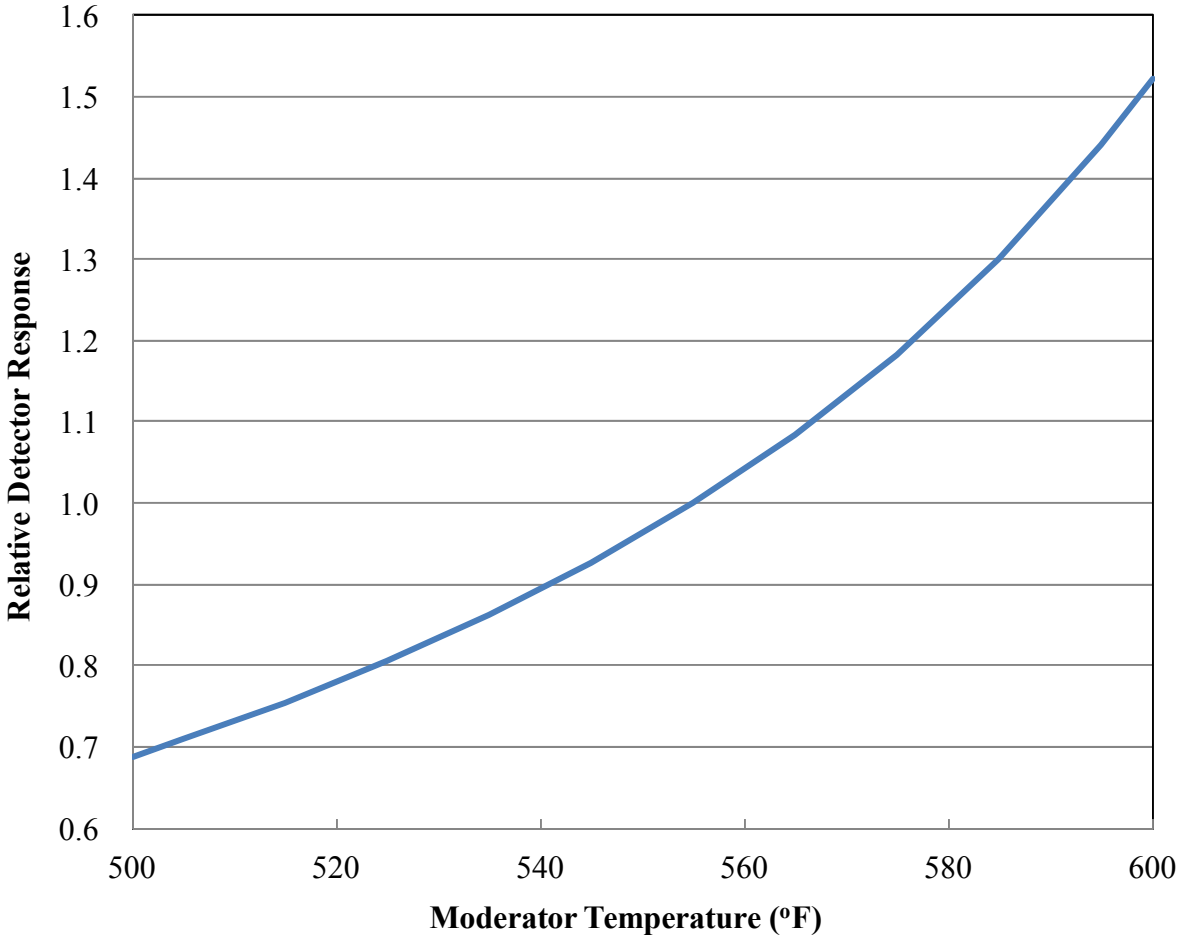

Figure 4.3-46 Typical Temperature Decalibration Effect vs. Reactor Inlet Temperature

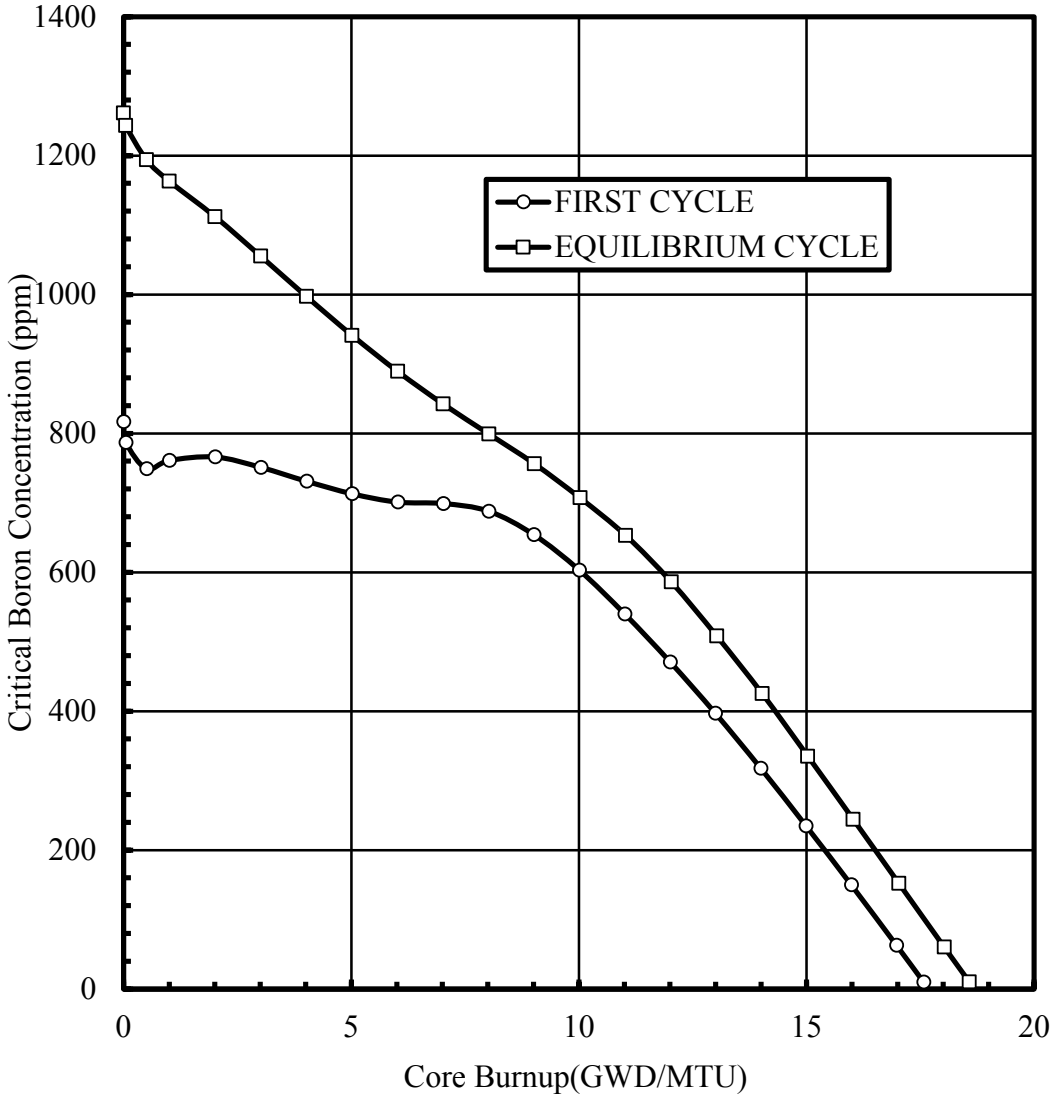

Figure 4.3-47 Critical Boron Concentration vs. Core Average Burnup Unrodded Full Power, Equilibrium Xenon

4.4 Thermal-Hydraulic Design

This section presents the steady-state thermal and hydraulic analysis of the reactor core, the analytical methods, and the experimental work done to support the analytical techniques. Evaluations of the analyses of anticipated operational occurrences (AOOs) and accidents are presented in Chapter 15. The prime objective of the thermal and hydraulic design of the reactor is to provide reasonable assurance that the core can meet steady-state and transient performance requirements without violating the design bases.

4.4.1 Design Bases

GDC 10 of 10 CFR 50 Appendix A (Reference 1) requires the reactor core and associated coolant, control, and protection systems to be designed with the appropriate margin so that the specified acceptable fuel design limits are not exceeded during any condition of normal operation, including the effects of AOOs. Because fuel cladding is one of the fission product barriers, its integrity has to be maintained during normal plant operation and AOOs to contain the fission products.

In addition, GDC 12 (Reference 1) requires the reactor core and associated coolant, control, and protection systems to be designed to provide reasonable assurance that power oscillations that can result in conditions exceeding specified acceptable fuel design limits (SAFDL) are not possible or can be reliably and readily detected and suppressed.

The following design bases are essential to achieving these objectives.

4.4.1.1 Departure from Nucleate Boiling

4.4.1.1.1 Design Basis

There is at least a 95 percent probability at a 95 percent confidence level that the hot fuel rods in the core will not undergo a departure from nucleate boiling (DNB) or critical heat flux (CHF) phenomenon during normal operation and AOOs. A departure from nucleate boiling ratio (DNBR) limit of 1.29 provides this probability and confidence, as described in Subsection 4.4.2.9.5.

4.4.1.1.2 Discussion

DNB is the onset of the transition from nucleate boiling to film boiling. Beyond DNB, steam vapor generated on a heated surface tends to form a steam layer between the heated surface and the surrounding liquid flow, and it may lead to an appreciable decrease in heat transfer.

By preventing DNB, a reasonable assurance of adequate heat transfer between the fuel rod surface and the core coolant is provided. Because the temperature difference between the fuel cladding surface and the coolant flow surrounding it is only a few degrees, additional design bases for the maximum fuel cladding temperature are not needed.

The critical condition for DNB occurrence can be characterized by surface heat flux. The DNBR, the ratio of predicted DNB heat flux to actual local heat flux, is used to express the margin to the point of DNB occurrence.

To predict DNB heat flux for the PLUS7 fuel design, the KCE-1 DNB correlation, which is described in Subsection 4.4.2.2.1, is adopted. The local coolant conditions used by the KCE-1 correlation are provided by the TORC code, as described in Subsection 4.4.2.2.1.

4.4.1.2 Fuel Temperature

4.4.1.2.1 Design Basis

During normal operation and AOOs, the fuel centerline temperature is not allowed to exceed the melting temperature accounting for degradation due to burnup and the addition of burnable absorbers.

4.4.1.2.2 Discussion

By precluding fuel pellet melting, the fuel pellet geometry is preserved and any possible adverse effects of molten fuel pellet on the cladding are eliminated, thus preventing the fuel cladding from mechanical and chemical damages.

The melting temperature of uranium dioxide pellets is 2,804 °C (5,080 °F) for unirradiated fuel and decreases by 32 °C (58 °F) per 10,000 MWD/MTU (Reference 2). The melting temperature of the gadolinia pellet is 2,579 °C (4,674 °F) at maximum content of 8 weight percent and decreases by 32 °C (58 °F) per 10,000 MWD/MTU, the same as for uranium dioxide pellets (Reference 3).

Thermal performance analyses of fuel rods are conducted by using the fuel rod design code (FATES code, References 2 and 4). Considering the uncertainties in the analysis model and fuel fabrication, fuel temperature analyses for various burnups and linear heat rates show that the fuel temperature design basis is met.

The peak linear heat rates during normal operation and AOOs are bounded by the limit of linear heat rate, which provides reasonable assurance that the fuel centerline temperatures remain below the melting temperature for the fuel rods. Because of the lower melting temperature and the lower thermal conductivity of gadolinia fuel rods, fuel temperature analysis provides a more severe result than that of uranium dioxide fuel at the same linear heat rate condition. The evaluation shows that the temperature of gadolinia fuel rods remain below the fuel melting temperature because the peak linear heat rate for gadolinia fuel rods is decreased by their reduced UO_2 enrichment content.

4.4.1.3 Coolant Flow, Velocity, and Void Fraction

4.4.1.3.1 Design Basis

The effects of coolant flow, velocity, and void fraction on the thermal margin should be considered in the thermal margin analyses.

4.4.1.3.2 Discussion

The primary coolant flow with all four pumps in operation is neither less than the design minimum nor greater than the design maximum. Some portion of the flow entering the reactor vessel is not effective for cooling the core. This portion is called the core bypass flow. The design minimum value for the core flow is obtained by subtracting the design maximum value for the core bypass flow from the design minimum primary coolant flow. For thermal margin analyses, the design minimum value for the core flow is used. The

design minimum primary coolant flow is listed in Table 4.4-1. The design maximum primary coolant flow is used in the determination of design hydraulic loads in the manner described in Subsection 4.4.2.6.3.

Although the coolant velocity, its distribution, and the coolant voids affect the thermal margin, design limits are not applied to these parameters because the parameters are not by themselves limiting. The parameters are included in the thermal margin analyses and affect the thermal margin to the design limits.

4.4.1.4 Hydraulic Instability

4.4.1.4.1 Design Basis

Hydraulic instability does not occur at any operational modes during normal operation and AOOs.

4.4.1.4.2 Discussion

If boiling flow in a reactor system is susceptible to thermal-hydraulic instabilities, it is undesirable for the following reasons:

a. Flow oscillations tend to affect the local heat transfer characteristics and may induce a boiling crisis.

b. Sustained flow oscillations may cause detrimental mechanical vibration of components.

c. Flow oscillations may cause problems in system control for core power or core power distribution.

Thermal-hydraulic instability has not been identified in pressurized water reactors (PWRs) because pressure and flow rate conditions are large enough to suppress the change of flow characteristics resulting from the void generation and serve to stabilize the system. A detailed discussion is given in Subsection 4.4.4.5.3.

4.4.1.5 Fuel Cladding and Fuel Assembly Integrity

Fuel cladding and fuel assembly integrities are maintained by complying with the above-mentioned design criteria and the fuel design bases described in Subsection 4.2.1.

4.4.2 Description of Thermal-Hydraulic Design of the Reactor Core

4.4.2.1 Summary Comparison

The thermal and hydraulic parameters for the reactor are listed in Table 4.4-1. A comparison of these parameters for System 80+ is included in this table.

4.4.2.2 Critical Heat Flux Ratios

The DNBR is defined as the ratio of the heat flux required to produce DNB at the calculated local coolant conditions to the actual local heat flux. Table 4.4-1 gives the values of minimum DNBR for the coolant conditions and engineering factors in the table, for the radial power distribution in Figures 4.4-1 and 4.4-2, and for the 1.26 peaked axial power distribution in Figure 4.4-3. The minimum DNBRs are evaluated using the following methodology.

4.4.2.2.1 DNB Correlations and Analysis

The DNBR is defined as:

$$\text{DNBR} = \frac{q''_{\text{DNB}}}{q''_{\text{local}}}$$

Where:

q''_{DNB} = DNB heat flux predicted by KCE-1 CHF correlation (Reference 5)

(= $q''_{KCE\text{-}1,U} / F_{Tong}$)

q''_{local} = actual local heat flux

F_{Tong} = non-uniform axial power distribution correction factor

The local thermal-hydraulic conditions needed to calculate DNBR are provided by TORC codes, as described in Subsection 4.4.4.5.2. TORC, with the preceding DNB correlation, is able to determine the minimum DNBR for the APR1400 core design at various conditions during normal operation and AOOs.

For the thermal-hydraulic condition beyond the range of applicability of the KCE-1 CHF correlation, the Macbeth correlation is applied to calculate DNBR as described in Subsections 15.0.2.2 and 15.1.5.3.

A comparison of the minimum DNBRs computed using a different correlation for the same power, flow, coolant temperature and pressure, and power distribution is presented in Table 4.4-2.

4.4.2.2.2 Power Distribution Factors

Rod Radial Power Factor

The rod radial power factor is the ratio of the average power per unit length produced by a particular fuel rod to the average power per unit length produced by the average-powered fuel rod in the core. The core-wide and hot assembly radial power distributions used for a typical DNB analysis are shown in Figures 4.4-1 and 4.4-2.

Axial Power Factor

The axial power factor is the ratio of the local power per unit length produced by a fuel rod to the average power per unit length produced by the same fuel rod. Figure 4.4-3 shows several axial power distributions used for this analysis.

Nuclear Power Factor

The nuclear power factor is the ratio of the maximum local power per unit length produced in the core to the average power per unit length produced by the average-powered fuel rod in the core.

Total Heat Flux Factor

The total heat flux factor is the ratio of the maximum local fuel rod heat flux to the core average fuel rod heat flux. The total heat flux factor is given in Table 4.4-1.

Augmentation Factor

The augmentation factor is defined as the ratio of the local heat flux to the unperturbed heat flux. The densification of modern fuel is insufficient to cause the formation of sufficient axial gaps. Therefore, the augmentation factor is 1.0.

4.4.2.2.3 Engineering Factors

Engineering Heat Flux Factor

The effect on local heat flux that is the result of normal manufacturing deviations from nominal design dimensions and specifications is accounted for by the engineering heat flux factor. The engineering heat flux factor given in Table 4.4-1 is applied to the rod with the minimum DNBR and increases the heat flux when calculating DNBR.

Engineering Factor on LHR

The effect of deviations from nominal fuel rod design enrichment, dimensions, and specifications on fuel temperature is accounted for by the engineering factor on LHR.

Engineering Enthalpy Rise Factor

The engineering enthalpy rise factor accounts for the effects of nominal manufacturing deviations in fuel fabrication from design dimensions and specifications on the enthalpy rise in the subchannel adjacent to the rod with the minimum DNBR. The engineering enthalpy rise factor given in Table 4.4-1 increases the enthalpy rise in the adjoining subchannels.

4.4.2.3 Linear Heat Rate

The core average and maximum fuel rod linear heat rates (LHRs) are given in Table 4.4-1. The maximum fuel rod LHR is determined by multiplying the core average fuel rod LHR by the product of the nuclear power factor, the engineering linear heat rate factor, and the ratio of the hot to the average fuel rod energy deposition fractions.

4.4.2.4 Void Fraction Distribution

The core average void fraction and the maximum void fraction are calculated using the Maurer method (Reference 6). The void fractions are values for the reactor operating conditions and engineering factors given in Table 4.4-1, for the radial power distribution in Figures 4.4-1 and 4.4-2, and for the 1.26 peaked axial power distribution in Figure 4.4-3. The average exit void fractions and qualities in different regions of the core are shown in Figure 4.4-4. The axial distribution of void fraction and quality in that subchannel is shown in Figure 4.4-5.

4.4.2.5 Core Coolant Flow Distribution

The flow holes are designed on the lower support structure bottom plate and the flow skirt to function as an orifice that stabilizes the flow and contributes to the uniform flow distribution at the core inlet. A regionalized core inlet flow distribution for a 4-pump operation based on the System 80 reactor flow test data is used. Descriptions of the System 80 reactor flow test and the regionalized distribution are given in Subsection 4.4.4.2.1 and Reference 20. The core inlet flow distribution is input to the TORC thermal margin analysis code, as described in Subsection 4.4.4.5.2.

4.4.2.6 Core Pressure Drops and Hydraulic Loads

4.4.2.6.1 Reactor Vessel Flow Distribution

The design minimum coolant flow entering the four reactor vessel inlet nozzles is given in Table 4.4-1. The main coolant flow path in the reactor vessel is down the annulus between the reactor vessel and the core support barrel, through the flow skirt, up through the core support region and the reactor core, through the fuel alignment plate, and out through the

two reactor vessel outlet nozzles. A portion of the flow leaves the main flow path as shown schematically in Figure 4.4-6. This flow is called the core bypass flow. Part of the bypass flow is used to cool the reactor internals in the areas not in the main coolant flow path and to cool the CEAs. Table 4.4-3 lists the bypass flow paths and the percentage of the total vessel flow that enters and leaves these paths.

The thermal margin analyses conservatively use the design maximum bypass flow, 3.0 percent of the total vessel flow.

4.4.2.6.2 Reactor Vessel and Core Pressure Drops

The irrecoverable pressure losses from the inlet to the outlet nozzles are calculated using the classical fluid mechanistic relationship and information from the System 80 reactor flow tests. These pressure losses have been verified by results from the flow test on the complete System 80 reactor flow model in Reference 20.

Pressure losses at 100 percent power, the design minimum primary coolant flow, and an operating pressure of 158.2 kg/cm^{2}A (2,250 psia) are listed in Table 4.4-4 together with the coolant temperature used to calculate each pressure loss. The calculated pressure losses include both flow path geometry and Reynolds number effects.

4.4.2.6.3 Hydraulic Loads on Internal Components

The major steady-state hydraulic loads that act on the reactor internals at the core loading steady-state operation are listed in Table 4.4-5. These loads are determined from analytical methods and from the results of reactor flow model and component test programs, described in Subsections 4.4.4.2.1 and 4.4.4.2.2, respectively. The design hydraulic loads consist of the static drag, impingement loads and the dynamic loads as a result of pump induced pressure pulsations, vortex shedding, and turbulence.

The hydraulic loads are initially evaluated on a best-estimate basis with a flow rate equal to the design maximum flow. The uncertainties in the input, such as flow rates, force coefficients, and dimensional tolerances, are added to the best-estimate loads. The design hydraulic loads conservatively account for pressure losses due to core crud.

In evaluating the design hydraulic loads, consideration is given to the particular pump operating configuration and coolant temperature condition that maximizes the hydraulic load for a given internal component.

The hydraulic loads in Table 4.4-5 are based on the design maximum primary coolant flow and a coolant temperature of 260 °C (500 °F).

Hydraulic loads for postulated accident conditions are described in Subsection 3.9.2.5.

4.4.2.7 Correlations and Physical Data

4.4.2.7.1 Heat Transfer Coefficient

The correlations used to determine cladding temperatures for non-boiling forced convection and nucleate boiling are described in this subsection. The surface temperature of the cladding is dependent on the axial and radial power distributions, temperature of the coolant, and surface heat transfer coefficient.

The surface heat transfer coefficient for non-boiling forced convection is obtained from the Dittus-Boelter correlation (Reference 7), where fluid properties are evaluated at the bulk condition.

$$h_{db} = \frac{0.023\ k}{De} (N_R)^{0.8} (N_{Pr})^{0.4}$$

Where:

h_{db} = heat transfer coefficient, Btu/hr-ft^2 °F

k = thermal conductivity, Btu/hr-ft °F

De = equivalent diameter = 4A/Pw, ft

N_R = Reynolds number

N_{Pr} = Prandtl number

A = cross-sectional area of flow subchannel, ft^2

Pw = wetted perimeter of flow subchannel, ft

The temperature drop across the surface film is calculated from:

$$\Delta T_{film} = q''/h_{db}$$

Where:

q" = fuel rod surface heat flux, Btu/hr-ft^2

Nucleate boiling may occur on the clad surface. In the nucleate boiling regime, the surface temperature of the cladding is determined from the Jens-Lottes correlation (Reference 8):

$$T_{wall} = T_{sat} + 60\,(q'' \times 10^{-6})^{0.25}\,[\exp(-P/900)]$$

Where:

P = pressure, psia

q" = fuel rod surface heat flux, Btu/hr-ft^2

T_{sat} = saturation temperature, °F

Nucleate boiling is assumed if T_{wall} is less than the sum of coolant temperature plus ΔT_{film}. The cladding surface temperature is calculated by summing the temperature of the coolant at the particular location and the temperature drop across the surface film; if nucleate boiling is occurring, it is calculated directly from the Jens-Lottes correlation.

4.4.2.7.2 Pressure Drops

Irrecoverable pressure losses through the core result from friction and geometric changes. The pressure losses through the top and bottom nozzles were initially calculated and then verified by testing (Subsection 4.4.4.2.2). The correlations used to determine frictional and geometric losses in the core are presented in Subsection 4.4.4.2.3.

4.4.2.7.3 Void Fraction Correlations

There are three separate void regions to be considered in flow boiling. Region 1 is the highly subcooled region in which a single layer of bubbles develops on a heated surface and remains attached to the surface. Region 2 is a transition region, changing from highly

subcooled boiling to bulk boiling where the steam bubbles detach from the heated surface. Region 3 is the bulk boiling region.

The void fraction in regions 1 and 2 is predicted using the Maurer Method (Reference 6). The calculation of the void fraction in the bulk boiling region is addressed in Subsection 4.4.4.2.3.

4.4.2.8 Thermal Effects of Operational Transients

Design basis limits on DNBR and fuel temperature are established so that thermally induced fuel damage will not occur during steady-state operation and AOOs. The core operating limits supervisory system (COLSS) provides information to aid the operator in maintaining proper steady-state conditions. The reactor protection system (RPS) provides reasonable assurance that design limits are not violated. If the operating power reaches a limiting value, an alarm is sounded. These limits are maintained by limiting conditions for operation (LCO) to provide sufficient margin in the event the most limiting AOO coincides with the operating power at the DNBR/LHR limit at steady-state as described in Section 7.2 and the applicable Technical Specification. The COLSS is an analytical approximation to the thermal margin design methods described in Subsection 4.4.4.5.2.

4.4.2.9 Uncertainties in Estimates

4.4.2.9.1 Pressure Drop Uncertainties

The reactor vessel pressure losses in Table 4.4-4 are the best-estimate values calculated for the design minimum flow with the classical fluid mechanistic relationship. The correlation uncertainties for the loss coefficients and the dimensional uncertainties on the reactor vessel and internals are accounted for when determining maximum and minimum vessel hydraulic resistance. The uncertainties at the two standard deviation level are estimated to be equivalent to approximately ±10 percent of the best-estimate vessel pressure loss.

4.4.2.9.2 Hydraulic Load Uncertainties

When determining the design hydraulic loads for normal operation, the uncertainties in items such as flow rate, force and pressure coefficients, and dimensional tolerances are evaluated at the two standard deviation level.

4.4.2.9.3 Fuel and Clad Temperature Uncertainty

Uncertainty in the ability to predict the maximum fuel temperature is a function of gap conductance, thermal conductivity, peak LHR, and heat generation distribution. Uncertainties in gap conductance and thermal conductivity are taken into account in the analytical model. Uncertainties in the peak LHR are accounted for by including the uncertainty in estimating the total nuclear peak. Uncertainties in fuel pellet density, enrichment, pellet diameter, and clad diameter are expressed by the engineering factor on LHR (Subsection 4.4.2.2.3). Uncertainty in predicting the cladding temperature at the location of maximum heat flux is the uncertainty in the film temperature drop, which is minimal where nucleate boiling occurs.

4.4.2.9.4 DNBR Calculation Uncertainties

The uncertainty considered in the calculation of minimum DNBR is as follows:

a. Uncertainty in the input to build the core analysis model

    1) Uncertainty in core geometry, by manufacturing variations within tolerances, is considered by the engineering factors in the DNBR analyses.

    2) Uncertainties in the power distribution factors are applied in the COLSS and RPS.

    3) Uncertainties in the core flow distribution are included in the design method for TORC analyses. The core inlet flow distribution is obtained from the reactor flow model testing described in Subsection 4.4.4.2.1.

4) The Blasius single-phase friction factor equation for smooth rods is given and shown to be valid in Subsection 4.4.4.2.3. The spacer grid loss coefficient is obtained from pressure drop data presented in Subsection 4.4.4.2.3.

5) The value of minimum DNBR is insensitive to crossflow resistance and momentum parameters (Reference 9).

6) The inverse Peclet number is input to the TORC code and is used to determine the effect of turbulent interchange on the enthalpy rise in adjacent subchannels as described in Subsection 4.4.4.1.

7) The same fuel rod energy deposition fraction is used for the hot rod as for the average rod. The hotter the rod, the lower the actual value of energy deposition fraction with respect to that for the average rod. A lower energy deposition fraction reduces the hot rod heat flux and increases its DNBR. Therefore, the use of the average rod energy deposition fraction for the hot rod is conservative.

b. Uncertainty in the analytical model

The ability of the TORC code to accurately predict the subchannel local conditions in rod bundles is described in Reference 9. The ability of the code to accurately predict the core-wide coolant conditions is described in Reference 11. An allowance for TORC code uncertainty is included in the SCU analysis, as presented in Subsection 4.4.2.9.5.

c. Uncertainty in the DNB correlation

The uncertainty in the DNB correlation is determined by a statistical analysis of DNB test data.

4.4.2.9.5 Statistical Combination of Uncertainty

Use of a 1.29 DNBR limit with a best-estimate design CETOP model provides assurance, with at least 95 percent probability and 95 percent confidence, that the hot rod will not

undergo a DNB. The 1.29 DNBR limit includes explicit allowances for system parameter uncertainties, CHF correlation uncertainty, rod bow, and penalties imposed by the NRC for the TORC code uncertainty.

Several conservatisms are included in the SCU methodology (Reference 12). The significant conservatisms include:

a. A combination of the system parameter probability distribution functions at the 95 percent confidence level to yield a resultant minimum DNBR at 95 percent confidence

b. Use of conservative system parameter probability distribution functions

c. Application of the new DNBR limit derivation to both four-pump and three-pump operations

d. Use of the range of state parameters used to generate the response surface

e. Application of the code uncertainty penalty imposed by the NRC

4.4.2.10 Flux Tilt Considerations

An allowance for degradation in the power distribution in the X-Y plane is provided in the protection limit setpoints.

The flux tilt is continually monitored during operation. The thermal margin calculations used in designing the reactor core are performed using the TORC and CETOP codes. Any asymmetry or tilt in the power distribution is analyzed by providing the corresponding power distribution in the TORC and CETOP input.

4.4.3 Description of Thermal-Hydraulic Design of the Reactor Coolant System

A summary description of the reactor coolant system (RCS) is given in Section 5.1.

4.4.3.1 Plant Configuration Data

An isometric view of the RCS is given in Figure 4.4-8. Dimensions are shown on the general arrangement drawings, Figures 5.1.3-1 and 5.1.3-2. The valves in the RCS are shown in Figures 5.1.2-1, 5.1.2-2, and 5.1.2-3. Table 4.4-6 lists pipe fittings that form part of the RCS.

Table 4.4-7 lists the design minimum flow through each flow path in the RCS. Table 4.4-8 provides the volume, minimum flow area, flow path length, height and liquid level of each volume, and bottom elevation for each component within the RCS.

Components of the safety injection system (SIS) are located to meet the criteria for net positive suction head (NPSH) presented in Section 6.3. Lengths and sizes of the SIS lines are determined so that they do not violate the flow rate assumed in the safety analyses described in Chapter 15. Total head losses throughout the injection lines are determined so that they do not exceed the head losses deduced from the flow rate.

Table 5.1.1-1 provides steady-state pressure, temperature, and flow distributions throughout the RCS.

4.4.3.2 Operating Restrictions on Pumps

The minimum RCS pressure at any given temperature is limited to the required NPSH for the reactor coolant pumps (RCPs) during plant heatup and cooldown. To provide reasonable assurance that the pump NPSH requirements are met under all possible operating conditions, an operating curve is used that gives permissible RCS pressure as a function of temperature.

4.4.3.3 Temperature-Power Operating Map

A typical temperature-power operating map (temperature control program) is provided in Subsection 5.4.10.2.3.

Power operation with inoperative pumps is not allowed in the APR1400. The adequacy of natural circulation for decay heat removal after reactor shutdown is described in Subsection 5.4.7.3.1.

4.4.3.4 Load Following Characteristics

Reactivity during load following is controlled by maneuvering of the CEAs and boron concentration in the RCS. When load changes are initiated, the reactor regulating system (RRS) senses a change in the turbine power and positions CEAs to attain the programmed average coolant temperature. RCS boron concentration can also be adjusted to attain the appropriate coolant temperature. The feedwater system uses a controller that senses changes in steam flow, feedwater flow, and water level and acts to maintain steam generator level at the desired point. The pressurizer pressure and level control systems respond to deviations from preselected setpoints caused by the expansion or contraction of the reactor coolant and actuate the spray or heaters and the charging or letdown systems as necessary to maintain pressurizer pressure and level. The steam pressure increase of the steam generator due to load rejection or rapid load reduction can be controlled by opening the turbine bypass valves as necessary to maintain steam pressure within a certain setpoint.

4.4.3.5 Thermal and Hydraulic Characteristics Summary Table

Principal thermal and hydraulic characteristics of the RCS components are listed in Table 4.4-9.

4.4.4 Evaluation

4.4.4.1 Critical Heat Flux

The margin to CHF or DNB is expressed in terms of the DNBR. The KCE-1 correlation (Reference 5) was used with the TORC and CETOP computer codes (References 9 and 13) to determine DNBR values for normal operation and AOOs. The KCE-1 correlation was developed in conjunction with the TORC code for DNB margin predictions for the 16 × 16 PLUS7 fuel assemblies with R-type split mixing vane spacer grids. The correlation is based on data from tests conducted for PLUS7 fuel development at the Columbia University chemical engineering research laboratories. The tests used electrically heated

6 × 6 array rod bundles simulating a corresponding portion of a 16 × 16 PLUS7 fuel assembly with R-type split mixing vane spacer grids.

Local coolant conditions at the DNB location were determined by using the TORC code in a manner consistent with the use of the code for reactor thermal margin calculations.

Turbulent interchannel mixing is used to predict DNB and local coolant conditions. The effect of turbulent interchange on enthalpy rise in the subchannels of 16 × 16 PLUS7 fuel assemblies with the R-type split mixing vane spacer grids is calculated in the TORC code by the following equation:

$$\widehat{Pe} = \frac{W'}{\overline{G}\,\overline{D}_e}$$

Where:

$\widehat{Pe}$ = inverse Peclet number

W' = turbulent interchange between adjacent subchannels, lbm/hr-ft

$\overline{G}$ = average mass velocity of the adjacent subchannels, lbm/hr-ft^2

$\overline{D}_e$ = average equivalent diameter of the adjacent subchannels, ft

The inverse Peclet number is mainly affected by the spacer grid span. It increases when the spacer grid span decreases. The inverse Peclet number of 0.0101 for the 16 × 16 PLUS7 fuel with 39.93 cm (15.72 in) mixing vane grid span was determined via the technical justification based on the similarity of geometric parameters with other Westinghouse fuel designs for which this value has been previously addressed (Reference 10). As described in Reference 10, Westinghouse used the inverse Peclet number of 0.0101 (equivalent to TDC of 0.038) for the fuel with 66.04 cm (26 in) mixing vane grid span.

4.4.4.2 Reactor Hydraulics

4.4.4.2.1 Reactor Flow Tests

The hydraulic design of the APR1400 reactor vessel and internals is supported by flow test programs with geometrically scaled models performed for System 80 and Yonggwang Nuclear Power Plant Units 3 and 4 (YGN 3&4).

Model components are geometrically similar to reactor components of System 80 except for the core. Individual fuel assemblies are represented by an array of square tubes. Axial distributions of orifice plates and crossflow holes in the tubes are sized to simulate the axial and lateral flow hydraulic resistance of the reactor core. Details of the System 80 reactor flow test and test results are presented in Reference 20. The APR1400 reactor design is similar with System 80 in size and flow area. These test results are applicable to the APR1400.

Hydraulic design parameters derived from the reactor flow test results are as follows:

a. Core inlet flow and core-exit pressure distributions

   The four-pump core inlet flow and core-exit pressure distributions used in the TORC analysis are based on the results from the 3/16-scale flow test of the System 80 reactor and internals. For the four-pump core inlet flow distribution, a regionalized distribution that was revised from the measured distribution considering the lower plenum geometry is used.

   Flow test data are used to define the core inlet flow and exit pressure distributions for transients involving the shutdown of one pump. The data were obtained from the 3/16-scale System 80 reactor flow tests and from tests on the YGN 3&4 reactor. The data for a three-pump operating condition are described in Reference 20.

b. Pressure drops in the reactor vessel

   Reactor vessel pressure drop predictions except for the core region were verified by flow test results. Where appropriate, corrections are made to flow test results to

account for differences in the Reynolds number and relative surface roughness between model and reactor. Reactor vessel pressure drop predictions for the core region are based on data from 16 × 16 fuel assembly components tests, discussed in Subsection 4.4.4.2.2. The APR1400 reactor vessel pressure drop predictions based on those test results, with some adjustment for the difference in operating conditions, are given in Table 4.4-4.

c. Hydraulic loads on reactor internal components

Design hydraulic loads on reactor internal components for normal operating conditions are based on analytical methods that use the data from flow test and component test described in Subsection 4.4.4.2.2. The measured data in flow test related to derivation of design hydraulic loads include incremental pressure drops, surface static pressure distributions, wall pressure differentials, and fluid velocity distributions.

4.4.4.2.2 Components Testing

The test on 16 × 16 PLUS7 fuel assembly components was performed to obtain information on fuel rod fretting, fuel assembly uplift, and pressure drop (*[Reference 14]**). The first subject is addressed in Section 4.2. The second subject is addressed below.

As part of the assessment of fuel assembly margin to uplift in the reactor, measurements are made of the flow rate required to produce fuel assembly liftoff. To obtain the desired information, the point of fuel assembly liftoff is determined from the accelerometer signals. Data reduction involves the calculation of an uplift coefficient describing the hydraulic uplift force acting on the assembly. The coefficient is defined as follows:

$$K_{up} = (2g_cWo) / (\rho V^2 A)$$

Where:

Wo = wet weight of assembly, lbf

V = flow velocity in assembly at the point of liftoff, ft/sec

A = envelope area of assembly, ft^2

ρ = density of water, lbm/ft^3

g_c = gravitational constant, $(ft\text{-}lbm)/(lbf\text{-}sec^2)$

A plot of the K_{up} data shows that they can be fitted by the relation:

$$K_{up} = \alpha N_R^{-\beta}$$

where α and β are peculiar to the particular component test being run. The standard error of estimate is typically 4 percent, including replication and instrument error. The uplift coefficient and its associated uncertainty are used in the analysis of the uplift forces on the fuel assemblies in the reactor. The force is determined for the most adverse assembly location for startup and normal operating conditions.

Pressure measurements are also made during the component test to verify the accuracy of the calculated loss coefficients for various fuel assembly components. Direct reduction of the pressure drop data yields the loss coefficients for the top and bottom nozzle regions, while the spacer grid loss coefficient is evaluated by subtracting a calculated fuel rod friction loss from the measured pressure drop across the fuel rod region.

The design value for the 16 × 16 PLUS7 spacer grid with the R-type split mixing vane is based on experimental results (*[Reference 14]**).

4.4.4.2.3 Core Pressure Drop Correlations

The total pressure drop along the fuel rod region of the core is calculated as the sum of the individual losses resulting from friction, acceleration of the fluid, the change in elevation of the fluid, and spacer grids. In the following paragraphs, the correlations used are summarized and the validity of the scheme is demonstrated with a comparison of measured and predicted pressure drops for single-phase and two-phase flow in rod bundles with guide tube.

For isothermal, single-phase flow, the pressure drop due to friction for flow along the bare rods is based on the equivalent diameter of the bare rod assembly and the Blasius friction factor:

$$f = 0.184\ N_R^{-0.2}$$

The pressure drop associated with the spacer grids is computed using a grid loss coefficient (K_{SG}) given by a correlation that has the following form:

$$K_{SG} = D_1 + D_2 \times N_R^{D_3} \pm \text{standard error of estimate}$$

The constants, D_n, are determined from pressure drop data obtained for a wide range of Reynolds numbers (N_R) for isothermal flow through a guide tube rod bundle fitted with the R-type split mixing vane spacer grids. The data come from the component hydraulic test program on a 16 × 16 fuel assembly design (Subsection 4.4.4.2.2). The standard error of estimate associated with the loss coefficient relation includes regression and instrument error.

To calculate pressure drop either for heating without boiling or for subcooled boiling, the friction factor given above for isothermal flow is modified through the use of the multipliers given by Pyle (Reference 15). The multipliers were considered on the effects of subcooled voids on the acceleration and elevation components of the pressure drop as well as the effect on the friction losses.

The effect of bulk boiling on the friction pressure drop is computed using a curve fit to the Martinelli-Nelson data (Reference 16) above 140 kg/cm^{2}A (2,000 psia) or the Martinelli-Nelson correlation with the modification given by Pyle below 140 kg/cm^{2}A (2,000 psia). The acceleration component of the pressure drop for bulk boiling conditions is computed for the case of two-phase flow where there may be a non-unity slip ratio. The computation method is described in Reference 17. The elevation and spacer grid pressure drops for bulk boiling are computed as for single-phase flow except that the bulk coolant density is used, where:

$$\bar{\rho} = \alpha\rho_V + (1-\alpha)\rho_l$$

Where:

α = bulk boiling void fraction

ρ_v = density of saturated vapor, lbm/ft^3

ρ_l = density of saturated liquid, lbm/ft^3

The bulk boiling void fraction used in computing the elevation, acceleration, and spacer grid losses is calculated by assuming a slip ratio of unity if the pressure is greater than 130 kg/cm^{2}A (1,850 psia) or by using the Martinelli-Nelson void fraction correlation with the modifications presented by Pyle if the pressure is below 130 kg/cm^{2}A (1,850 psia). To verify that the scheme described above accurately predicts pressure drop for single-phase and two-phase flow through the 16 × 16 assembly geometry, comparisons have been made of measured pressure drop and the pressure drop predicted by TORC for the rod bundles used in the DNB test program at Columbia University. CENPD-161 (Reference 9) shows some typical results for a 21-rod bundle of the 16 × 16 fuel assembly geometry (5 × 5 array with four rods replaced by a control rod guide tube) and the validity of the methods.

4.4.4.2.4 Effect of Partial or Total Isolation of a Loop

Operation with partial or total isolation of a loop is not taken into account in the APR1400 design.

4.4.4.3 Influence of Power Distribution

From the analysis of many three-dimensional power distributions, the important parameters that determine the thermal margin in the core are the maximum rod power and its axial power distribution (Reference 11). The maximum LHR at a given power is determined directly from the core average fuel rod LHR and the nuclear power factor.

4.4.4.4 Core Thermal Response

Steady-state core parameters are summarized in Table 4.4-1 for normal four-pump operation. Figure 4.4-7 shows the sensitivity of the minimum DNBR to small changes in pressure, inlet temperature, and flow from the conditions specified in Table 4.4-1.

The response of the core to AOOs is addressed in Chapter 15. COLSS and RPS provide reasonable assurance that the design bases in Subsection 4.4.1 are not violated for any steady-state operating condition of inlet temperature, pressure, flow, power and core power distribution, and for the AOOs described in Chapter 15 including anticipated transient without scram (ATWS).

The lower power and shutdown operation is considered, in which shutdown procedures including mid-loop operation and thermal-hydraulic characteristics of each operation mode are important. And probabilistic risk assessment for the operation is addressed in Subsection 19.1.6. Anticipated transients initiated at this operation, such as inadvertent boron dilution during Modes 4 and 5 and Mode 6, are discussed in Subsection 15.4.6.

4.4.4.5 Analytical Methods

4.4.4.5.1 Reactor Coolant System Flow Determination

The design minimum flow rate of the RCS is determined as the required mass flow to meet the design limits in Subsection 4.4.1 during steady-state operation and AOOs. This design minimum flow is specified in Table 4.4-1. The design maximum flow rate is determined as the mass flow rate at which the design hydraulic loads on the reactor and internals are evaluated.

The RCPs are sized to produce a flow rate not less than the design minimum flow rate and not higher than the design maximum flow rate including the flow measurement uncertainty at any normal operating conditions.

Upon completion of the manufacturing and testing of the pumps, the characteristic pump head or performance curves are established. The expected maximum, best-estimate, and minimum RCS flow rates are determined as follows:

a. Best-estimate expected flow

   The best estimate of the expected RCS flow is determined by equating the head loss through the reactor coolant flow path to the head rise supplied by the RCPs.

b. Maximum expected flow

   The maximum expected flow is determined in a manner analogous to the best estimate of the expected flow except that statistical techniques are used. A pump performance curve probability distribution for each pump is calculated by statistically combining measurement uncertainties in flow and head. The

uncertainties are based on performance and acceptance testing at the pump vendor's facility. The system head loss uncertainty distributions are evaluated by statistically combining the uncertainties in the correlations for loss coefficients and normal manufacturing tolerances about nominal dimensions. The expected flow rate probability distribution is determined from the statistical combination of the respective pump curve probability distributions and the probability distributions for the system resistances.

The probability distribution for the expected flow rate is in turn used to define the maximum and minimum expected flow rates. The maximum expected flow rate is defined by the upper limit on the expected flow rate probability distribution, above which the actual flow rate has only a 5 percent probability of existing. The maximum expected flow rate is equal to or less than the design maximum flow.

c. Minimum expected flow

The minimum expected flow is also determined from the expected flow rate probability distribution. The minimum expected flow rate is defined as the lower limit of the expected flow rate probability distribution, below which the actual flow rate has only a 5 percent chance of existing. This minimum expected flow rate is equal to or greater than the design minimum flow.

Upon installation of the pumps in the RCS, the operating flow is determined by one or more of the following flow measurement techniques:

a. Pump casing differential pressure method, using a correlation between pump casing differential pressure and flow rate

b. Calorimetric method (a heat balance performed on the secondary coolant)

c. Other non-intrusive flow measurement methods such as ultrasonic flow meters

The uncertainties included in determining the operating flow rate are associated with the measurement techniques used above. The best-estimate expected flow, including

uncertainties, is greater than the design minimum flow and less than the design maximum flow.

Any significant crud buildup is detected by monitoring of the RCS flow. However, a significant buildup of crud is not anticipated because the water chemistry is controlled by operation of the chemical and volume control system (CVCS).

4.4.4.5.2 Thermal Margin Analysis

Thermal margin analysis of the reactor core is performed using the TORC code, which is an open-channel analytical method based on the COBRA-IIIC code (Reference 18). A complete description of the TORC code and application of the code for detailed core thermal margin analyses is contained in Reference 9.

The CETOP code, derived from the same theoretical bases as TORC, is streamlined for use in the thermal margin analysis. A complete description of CETOP is provided in Reference 13. The codes and their use are described below.

The application of the TORC code for detailed core thermal margin calculations typically involves the following three stages:

a. The first stage consists of calculating coolant conditions throughout the core on a coarse-mesh basis. The core is modeled so that the smallest unit represented by a flow channel is a single fuel assembly.

b. In the second stage, typically the hot assembly and adjoining fuel assemblies are modeled with a coarse mesh. The hot assembly is typically divided into four partial assembly regions. One of these regions is centered on the subchannels adjacent to the rod having the minimum DNBR.

c. The third stage involves a fine-mesh modeling of the partial assembly region, which centers on the subchannels adjacent to the rod having the minimum DNBR. All flow channels used in this stage are hydraulically open to their neighbors.

This procedure is used to analyze in detail any three-dimensional power distribution superimposed on an explicit core inlet flow distribution. The detailed core thermal margin calculations are used primarily to support the simplified design core thermal margin calculation code, CETOP, described below.

The CETOP code, a variant of the TORC code, is used as a design code for the APR1400 thermal margin analyses. CETOP has the same theoretical bases as TORC, but has been improved to reduce execution time.

The CETOP code uses the transport coefficients to obtain accurate determination of diversion crossflow and turbulent mixing between adjoining channels with a less detailed calculation model. Furthermore, a predictor-corrector method is used to solve the conservation equations, replacing the iterative method used in the TORC code, and thereby reduce execution time. The conservatism of CETOP relative to TORC is documented in benchmarking analyses that demonstrate that CETOP yields accurate or conservative DNBR results relative to TORC.

4.4.4.5.3 Hydraulic Instability Analysis

Flow instabilities leading to flow excursions or oscillations have been observed in some boiling flow systems containing one or more closed, heated channels. Flow instability phenomena are a concern primarily because they may lead to a reduction in the DNB heat flux relative to that observed during a steady-flow condition. However, flow instabilities are not expected to reduce thermal margin in PWRs during normal operation or AOOs. This conclusion is based on available literature, experimental evidence, and the results of core flow stability analyses (References 19 and 21).

Flow instabilities that have been observed have occurred almost exclusively in closed-channel systems operating at low pressures relative to PWR operating pressures. Operating limits due to the occurrence of critical heat flux (CHF) are encountered before the flow stability threshold is reached. The analysis result for Westinghouse PWRs showed that flow is stable throughout the range of reactor power levels examined (Reference 21).

4.4.5 Testing and Verification

4.4.5.1 RCS Flow Measurement

RCS flow measurement tests are performed as part of the startup program. The tests verify that the measured RCS flow exceeds the design minimum flow rates used in the safety analysis, but is less than the design maximum flow rate. Also, the tests verify that the measured RCS flow coastdown is conservative with respect to the coastdown used in the safety analysis. The test program is described in Subsection 14.2.12.2.3.

4.4.5.2 Component and Fuel Inspections

Inspections performed on manufactured fuel are described in Subsection 4.2.4. Fabrication measurements critical to thermal and hydraulic analysis are obtained to verify that the engineering factors in the design analyses (Subsection 4.4.2.2.3) are met.

4.4.6 Instrumentation Requirements

4.4.6.1 Thermal Power

The DNBR-related core condition and linear heat rate are limited by core protection calculator system, which is part of reactor protection system. The system is described in Section 7.2.

Various reactor trip functions are provided to limit core power and adverse thermal hydraulic conditions. These trips are variable overpower trip, high logarithmic power level trip, high local power density trip, and low departure from nucleate boiling ratio trip.

To determine the core thermal-hydraulic condition, CEA position, ex-core neutron flux, and reactor coolant flow are measured. These measurements are addressed in Subsection 7.2.1.

4.4.6.2 Power Distribution

There are 61 in-core instrumentation (ICI) assemblies with five self-powered rhodium detectors in each assembly. The ICI assemblies are strategically distributed about the

reactor core, and the five detectors are axially distributed along the length of the core. This permits representative three-dimensional flux mapping of the core. Also, ICI assemblies include core-exit thermocouples.

The ICI system performs the following functions:

a. Determine the gross power distribution in the core during different power conditions

b. Provide data to estimate fuel burnup in each fuel assembly

c. Provide data for evaluation of thermal margins in the core

The ex-core neutron flux monitoring system (ENFMS) provides a means to measure reactor power level by monitoring the neutron flux leakage from the reactor vessel. The system continuously monitors neutron flux from the startup level to 200 percent full power and provides signal outputs for reactor protection and control. The ENFMS consists of four redundant safety channels and two independent startup and control channels.

More detailed descriptions of the ICI system and ENFMS are given in Subsection 7.7.1.

4.4.6.3 Other Monitoring Systems

Inadequate core cooling is monitored by inadequate core cooling monitoring system (ICCMS). The ICCMS instrumentation package consists of the following:

a. Hot and cold leg temperatures

b. Pressurizer pressure instruments

c. Core-exit thermocouples (CETs)

d. Heated junction thermocouple (HJTC) probe assembly for indication of reactor vessel water level

Detail of the ICCMS is described in Subsection 7.5.1.

A loose part in the primary coolant system can be indicative of degraded reactor safety resulting from failure or weakening of safety related components. A loose part can also pose a serious threat of partial flow blockage with attendant DNB, which in turn results in failures of fuel cladding. A loose part also increases the potential for control rod jamming and for accumulation of radioactive crud in the primary system, making early detection of loose metallic parts important.

The loose parts monitoring system (LPMS) provides a means for detecting and evaluating metallic loose parts through analysis of transient acoustic impact signals, which are caused by the presence of loose part impacts against the inner wall of a reactor vessel or pipe. A more detailed description of the LPMS is given in Subsection 7.7.1.

The internal vibration monitoring system (IVMS) is provided to monitor the vibration of the reactor internals, specifically the fuel assemblies and the core support barrel. The IVMS monitors the time-varying ex-core neutron flux signals that indicate changes in neutron absorption path lengths. The changes are caused by the vibration of the reactor internals.

4.4.7 Combined License Information

No COL information is required with regard to Section 4.4.

4.4.8 References

1. United States Nuclear Regulatory Commission, General Design Criteria for Nuclear Power Plants, NRC Regulations Title 10, Code of Federal Regulations, 10 CFR 50, Appendix A, December 23, 2011.

2. Combustion Engineering, Inc., “C-E Fuel Evaluation Model Topical Report,” CENPD-139-P-A (proprietary), July 1974.

3. Combustion Engineering, Inc., “C-E Methodology for Core Designs Containing Gadolinia-Urania Burnable Absorbers,” CENPD-275-P Revision 1-P-A, May 1988.

4 Combustion Engineering, Inc., "Improvements to Fuel Evaluation Model," CEN-161(B)-P Supplement 1-P-A, January 1992.

5. Korea Hydro & Nuclear Power Co., Ltd., "KCE-1 Critical Heat Flux Correlation for PLUS7 Thermal Design," APR1400-F-C-TR-12002-P (proprietary), Rev. 0 and APR1400-F-C-TR-12002-NP (non-proprietary), Rev. 0, November 2012.

6. G.W. Maurer, "A Method of Predicting Steady State Boiling Vapor Fractions in Reactor Coolant Channels," Bettis Technical Review, WAPD-BT-19, Reactor Technology, June 1960.

7. F. W. Dittus and L. M. K. Boelter, "Heat Transfer in Automobile Radiators of the Tubular Type," University of California Publication, Engineer, Vol. 2, No. 13, pp. 443–461, 1930.

8. W. H. Jens and P. A. Lottes, "Analysis of Heat Transfer, Burnout, Pressure Drop, and Density Data for High Pressure Water," ANL-4627, May 1, 1951.

9. Combustion Engineering, Inc., "TORC Code: A Computer Code for Determining the Thermal Margin of a Reactor Core," CENPD-161-P-A (proprietary), April 1986.

10. Westinghouse Electric Company LLC, "TDC (Thermal Diffusion Coefficient) for KAFD Fuel," CN-KAFD-01-1, 2001.

11. Combustion Engineering, Inc., "TORC Code Verification and Simplified Modeling Methods," CENPD-206-P-A (proprietary), June 1981.

12. Combustion Engineering, Inc., "Modified Statistical Combination of Uncertainties," CEN-356(V)-P-A, Revision 1-P-A (proprietary), May 1988.

13. Combustion Engineering, Inc., "CETOP-D Code Structure and Modelling Methods for Arkansas Nuclear One Unit 2," CEN 214(A)-NP (non-proprietary), July 1982.

14. *[Korea Hydro & Nuclear Power Co., Ltd., "PLUS7 Fuel Design for the APR1400," APR1400-F-M-TR-13001-P (proprietary), Rev. 0 and APR1400-F-M-TR-13001-NP (non-proprietary), Rev. 0, August 2013.]**

15. R. S. Pyle, "A Program for the Thermal Analysis of a Pressurized Water Nuclear Reactor During Steady-State Operation, STDY-3," WAPD-TM-213, June 1960.

16. R. C. Martinelli and D. B. Nelson, “Prediction of Pressure Drop During Forced Circulation Boiling of Water,” ASME Transactions, August 1948.

17. O.J. Mendler et al., “Natural Circulation Tests with Water at 800 to 2000 psia under Non-Boiling, Local Boiling, and Bulk Boiling Conditions,” Journal of Heat Transfer, August 1961.

18. D.S. Rowe, “COBRA-IIIC: A Digital Computer Program for Steady-State and Transient Thermal-Hydraulic Analysis of Rod Bundle Nuclear Fuel Elements,” BNWL-1695, March 1973.

19. J.A. Boure, A.E. Bergles, and L.S. Tong, “Review of Two-Phase Flow Instability,” ASME Paper 71-HT-42, August 1971.

20. KEPCO E&C, “APR1400 Core Inlet Flow and Outlet Pressure Distributions Based on Flow Model Test,” KEPCO E&C/ND/TR/12-020, December 2012.

21. Letter to J.F. Stolz, U.S. NRC, from D. H. Williams, Arkansas Power & Light Co., January 16, 1978, and enclosure, “Assessment of Core Flow Stability for C-E PWRs,” CEN-64(A), July 1977.

Table 4.4-1 (1 of 2)

Thermal and Hydraulic Parameters

Reactor Parameter	System 80+	APR1400
Core average characteristics at full power		
Total core heat output, MWt	3,914	3,983
Total core heat output, 10^6 kcal/hr (MBtu/hr)	3,367 (13,360)	3,425 (13,590)
Average fuel rod energy deposition fraction	0.975	0.975
Hot fuel rod energy deposition fraction	0.975	0.975
Primary system pressure, kg/cm^{2}A (psia)	158.2 (2,250)	158.2 (2,250)
Reactor inlet coolant temperature, °C (°F)	291.1(556)	290.6(555)
Reactor outlet coolant temperature, °C (°F)	323.9 (615)	323.9 (615)
Core-exit average coolant temperature, °C (°F)	325.0 (617)	325.0 (617)
Average core enthalpy rise, kcal/kg (Btu/lbm)	46.1 (83.0)	46.7 (84.1)
Design minimum primary coolant flow rate, L/min (gpm)	1,683,000 (444,650)	1,689,000 (446,300)
Design maximum core bypass flow, % of primary	3.0	3.0
Design minimum core flow rate, L/min (gpm)	1,633,000 (431,300)	1,639,000 (432,900)
Hydraulic diameter of nominal subchannel, cm (in)	1.196 (0.471)	1.264 (0.498)
Core flow area, m^2 (ft^2)	5.65 (60.8)	5.83 (62.7)
Core average mass velocity, 10^6 kg/h-m^2 (10^6 lbm/hr-ft^2)	12.94 (2.65)	12.60 (2.58)
Core average coolant velocity, m/s (ft/s)	5.10 (16.7)	4.94 (16.2)
Core average fuel rod heat flux, kcal/h-m^2 (Btu/hr-ft^2)	497,200 (183,300)	517,361 (190,735)
Total heat transfer area, m^2 (ft^2)	6,592 (70,960)	6,454 (69,470)
Average fuel rod LHR, W/cm (kW/ft)	175.9 (5.36)	179.2 (5.46)
Power density, kW/L	98.4	100.5
No. of active fuel rods	56,876	56,876

Table 4.4-1 (2 of 2)

Reactor Parameter	System 80+	APR1400
Power Distribution Factors		
Rod radial power factor	1.55	1.55
Nuclear power factor	2.28	2.28
Total heat flux factor	2.35	2.35
Engineering Factors		
Engineering heat flux factor	1.03	1.03
Engineering enthalpy rise factor	1.03	1.03
Engineering factor on LHR	1.03	1.03
Characteristics of Rod and Channel with Minimum DNBR		
Maximum fuel rod heat flux, kcal/hr-m^2 (Btu/h-ft^2)	1,164,000 (429,100)	1,215,000 (448,000)
Maximum fuel rod LHR, W/cm (kW/ft)	413.4 (12.6)	420.8 (12.8)
UO_2 maximum steady-state temperature, °C (°F)	1,748 (3,179)	1,712 (3,114)
Outlet temperature, °C (°F)	340.0 (644)	340.6 (645)
Outlet enthalpy, kcal/kg (Btu/lbm)	380 (648)	381 (686)
Minimum DNBR at nominal conditions (CHF correlation)	2.00 (CE-1)	2.44 (KCE-1)

Table 4.4-2

Comparison of the Departure from Nucleate Boiling Ratios
Computed with Different Correlations

Correlation	DNBRs for Nominal Reactor Conditions		DNBRs for Reactor Conditions Giving a 1.29 KCE-1 Minimum DNBR	
	Matrix Subchannel	Subchannel Next to Guide Tube	Matrix Subchannel	Subchannel Next to Guide Tube
KCE-1	2.56	2.48	1.29	1.30
CE-1	2.33	1.99	1.03	0.91

Table 4.4-3

Reactor Coolant Bypass Flows

Bypass Path	Percentage of Total Vessel Flow, Design Maximum Value (Best Estimated Value)
Outlet nozzle clearances	1.4 (1.1)
Alignment keyways	0.5 (0.4)
Core shroud annulus	0.4 (0.3)
Guide tubes	0.7 (0.6)
Total Bypass	3.0 (2.4)

Table 4.4-4

Reactor Vessel Best-Estimate Pressure Losses and Coolant Temperatures

Component	Pressure Loss kg/cm^2 (psi)	Temperature °C (°F)
Inlet nozzle and 90° turn	0.54 (7.7)	290.6 (555)
Downcomer, lower plenum, and support structure	1.05 (15.0)	290.6 (555)
Fuel assembly	1.40 (19.9)	307.2 (585)
Fuel assembly outlet to outlet nozzle	1.20 (17.1)	323.9 (615)
Total pressure loss	4.19 (59.7)	N/A (1)

(1) N/A = not applicable

Table 4.4-5 (1 of 2)

Steady State Hydraulic Loads
on Vessel Internals and Fuel Assemblies

Load Values at 260 °C (500 °F), Core Loading			
Component	Load Description		Load Value
1. Core support barrel	Radial differential pressure directed inward		8.5 kg/cm^2 D (121.3 psid)
	Uplift load		6.3×10^5 kg (1.39×10^6 lbf)
	Lateral load		1.5×10^5 kg (0.32×10^6 lbf)
2. Upper guide structure	Uplift load		3.3×10^5 kg (0.74×10^6 lbf)
	Lateral load	Differential pressure	7.7×10^4 kg (0.17×10^6 lbf)
		Drag load	9.2×10^4 kg (0.20×10^6 lbf)
	Uplift load on fuel alignment plate		166,470 kg (367,000 lbf)
	Downward load on upper guide structure support plate		13,245 kg (29,200 lbf)
	Lateral drag load on control element guide tube, maximum/tube		944 kg (2,082 lbf)
3. Flow skirt	Radial differential pressure directed inward	Maximum	4.34 kg/cm^2 D (61.7 psid)
		Average	1.98 kg/cm^2 D (28.2 psid)
	Axial load directed downward	Maximum	4,235 kg/m (2,846 lbf/ft)
		Average	1,934 kg/m (1,300 lbf/ft)
4. Lower support structure bottom plate	Uplift load	Bottom plate	36,778 kg (81,080 lbf)
		Raised bottom plate	11,281 kg (24,871 lbf)
	Lateral load		4,266 kg (9,404 lbf)

Table 4.4-5 (2 of 2)

Load Values at 260 °C (500 °F), Core Loading			
Component	Load Description		Load Value
5. Instrumentation nozzle assembly	Lateral drag load on ICI nozzle and support column		1.34 kg/cm^2 D (19.0 psid)
	Uplift load	ICI support plate	583 kg (1,285 lbf)
		Support columns	870 kg (1,918 lbf)
6. Fuel assembly	Uplift load		1,207 kg (2,660 lbf)
7. Core shroud	Radial differential pressure directed outward	Bottom of the shroud	2.76 kg/cm^2 D (39.2 psid)
		Top of shroud	0.0 kg/cm^2 D (0.0 psid)

Table 4.4-6

RCS Pipe Fittings

Elbows	Size, cm (in)	Radius, cm (in)	Quantity
35°	106.68 (42)	160.02 (63)	2
50°	76.2 (30)	114.3 (45)	4
90°	76.2 (30)	114.3 (45)	8
44°10′	76.2 (30)	114.3 (45)	4

Table 4.4-7

RCS Design Minimum Flows

Flow Path	Flow (kg/hr) / (lbm/hr)
Total minimum RCS flow	75.6×10^6 / 166.6×10^6
Core bypass flow (design maximum)	2.3×10^6 / 5.0×10^6
Core flow	73.3×10^6 / 161.6×10^6
Hot leg flow	37.8×10^6 / 83.3×10^6
Cold leg flow	18.9×10^6 / 41.7×10^6

Table 4.4-8

Reactor Coolant System Geometry

Component	Flow Path Length m (ft)	Top Elevation [1] m (ft)	Bottom Elevation [1] m (ft)	Minimum Flow Area m^2 (ft^2)	Volume m^3 (ft^3)
Hot leg (ea)	4.3 (14.10)	0.73 (2.39)	–0.53 (–1.75)	0.89 (9.62)	3.89 (137.26)
Suction leg (ea)	7.73 (25.36)	0.40 (1.30)	–3.04 (– 9.98)	0.46 (4.91)	3.61 (127.66)
Discharge leg (ea)	5.88 (19.30)	0.39 (1.27)	–0.39 (–1.27)	0.46 (4.91)	2.75 (97.18)
Pressurizer					
Liquid level (full power)	—	13.33 (43.74)	—	4.65 (50.07)	31.43 (1,110)
Surge line	22.45 (73.64)	6.08 (19.94)	0.54 (1.76)	0.05 (0.56)	1.17 (41.19)
Steam generator					
Inlet plenum	1.44 (4.74)	2.05 (6.71)	–0.16 (–0.51)	1.77 (19.07)	12.31 (434.56)
Outlet plenum	1.44 (4.74)	2.05 (6.71)	–0.16 (–0.51)	0.9 (9.74)	12.31 (434.56)
Tubes	20.7 (67.91)	11.54 (37.89)	2.05 (6.71)	0.0002 [2] (0.002)	60.80 (2,147.0)
Reactor vessel					
Inlet nozzle (ea)	1.13 (3.7)	0.45 (1.47)	–0.45 (–1.47)	0.46 (4.9)	0.59 (20.75)
Downcomer	6.07 (19.9)	3.57 (11.6)	–6.89 (–22.6)	3.14 (33.75)	33.13 (1,170.00)
Lower plenum	1.68 (5.5)	–6.28 (–20.6)	–7.89 (–25.9)	3.02 (32.5)	12.3 (434.5)
Active core	3.81 (12.5)	–1.55 (–5.1)	–5.36 (–17.6)	5.65 (60.8)	23.1 (815.7)
Outlet plenum	1.74 (5.7)	0.58 (1.9)	–0.83 (–2.7)	2.47 (26.6)	12.51 (441.7)
Top head	0.98 (3.2)	6.07(19.9)	3.87 (12.7)	0.72 (7.8)	13.26 (468.2)
Outlet nozzle (ea)	1.22 (4.0)	0.57 (1.87)	–0.57 (–1.87)	0.89 (9.6)	1.21 (42.75)
DVI nozzle (ea)	0.53 (1.73)	2.21 (7.25)	1.99 (6.54)	0.04(0.44)	0.03 (0.93)

(1) Reactor vessel nozzle centerline is the reference elevation. It has an elevation of 0.0 m (0.0 ft).

(2) Flow path area per tube

Table 4.4-9 (1 of 3)

Reactor Coolant System Component
Thermal and Hydraulic Data

Component	Data
Reactor Vessel	
Rated core thermal power, MWt	3,983
Design pressure, kg/cm^{2}A (psia)	175.8 (2,500)
Operating pressure, kg/cm^{2}A (psia)	158.2 (2,250)
Coolant outlet temperature, °C (°F)	323.9 (615)
Coolant inlet temperature, °C (°F)	290.6 (555)
Coolant outlet state	Subcooled
Total coolant flow, 10^6 kg/hr (10^6 lb/hr)	75.6 (166.6)
Average coolant enthalpy	
Inlet, kcal/kg (Btu/lb)	1.287×10^3 (553.4)
Outlet, kcal/kg (Btu/lb)	1.477×10^3 (635)
Average coolant density	
Inlet, kg/m^3 (lb/ft^3)	744.9 (46.5)
Outlet, kg/m^3 (lb/ft^3)	669.6 (41.8)
Steam Generators	
Number of units	2
Primary side (or tube side)	
Design pressure/temperature, kg/cm^{2}A/°C (psia/°F)	175.8/343.3 (2,500/650)
Operating pressure, kg/cm^{2}A (psia)	158.2 (2,250)
Inlet temperature,°C (°F)	323.9 (615)
Outlet temperature, °C (°F)	290.6 (555)
Secondary side (or shell side)	
Design pressure/temperature, kg/cm^{2}A/°C (psia/°F)	84.4/298.9 (1,200/570)
Full load steam pressure/temperature, kg/cm^{2}A/°C (psia/°F)	70.3/285 (1,000/545)
Zero load steam pressure, kg/cm^{2}A (psia)	77.3 (1,100)

Table 4.4-9 (2 of 3)

Component	Data
Steam Generators (cont.)	
Secondary side (or shell side) (cont.)	
Total steam flow per gen., kg/hr (lb/hr)	4.070×10^6 (8.975×10^6)
Full load steam quality, % (minimum)	99.75
Feedwater temperature, full power, °C (°F)	232.2 (450)
Pressurizer	
Design pressure, kg/cm^{2}A (psia)	175.8 (2,500)
Design temperature, °C (°F)	371.1 (700)
Operating pressure, kg/cm^{2}A (psia)	158.2 (2,250)
Operating temperature, °C (°F)	345 (653)
Internal volume, m^3 (ft^3)	68 (2,400)
Heaters	
Type and rating of heaters, kW	Immersion/50
Installed heater capacity, kW	2400
Reactor Coolant Pumps	
Number of units	4
Type	Vert.-Centrifugal
Rated flow, m^3/hr (gpm)	27,618.4 (121,600)
Design pressure/temperature, kg/cm^{2}A/ °C (psia/ °F)	175.8/343.3 (2,500/650)
Operating pressure, kg/cm^{2}A (psia)	158.2 (2,250)
Type drive	Squirrel cage induction motor
Total dynamic head, m (ft)	109.7 (360)
Rating and power requirements, kW (hp)	7,457 (10,000)
Pump speed, rpm	1,190
RCP heat input to RCS, MWt	24.6

Table 4.4-9 (3 of 3)

Component	Data
Reactor Coolant Piping	
Flow per loop, 10^6 kg/hr (10^6 lb/hr)	
Hot leg	37.78 (83.3)
Cold leg	18.89 (41.65)
Pipe size (inside dia.), m (in)	
Hot leg	1.07 (42)
Cold leg	
Suction leg	0.76 (30)
Discharge leg	0.76 (30)
Pipe design press./temp., kg/cm^{2}A/°C (psia/°F)	175.8/343.3 (2,500/650)
Pipe operating press./temp., kg/cm^{2}A/°C (psia/°F)	
Hot leg	158.2/323.9 (2,250/615)
Cold leg	158.2/290.6 (2,250/555)

ASSY AVG. ROD RADIAL POWER FACTOR **ASSY MAX. ROD RADIAL POWER FACTOR**					0.61 1.01	0.76 1.06	0.83 1.12	0.81 1.07
			0.65 1.04	0.88 1.14	0.98 1.17	1.09 1.22	1.12 1.24	1.19 1.30
		0.74 1.11	1.08 1.27	1.10 1.23	0.95 1.02	1.20 1.30	0.97 1.05	1.15 1.24
	0.65 1.04	1.08 1.27	1.15 1.24	0.97 1.05	1.14 1.22	0.96 1.03	1.12 1.20	0.94 1.01
	0.88 1.14	1.10 1.22	0.97 1.05	1.22 1.31	0.97 1.04	1.19 1.28	0.95 1.02	1.11 1.18
0.61 1.01	0.98 1.17	0.95 1.03	1.14 1.22	0.97 1.04	1.15 1.22	0.97 1.04	1.13 1.21	0.95 1.02
0.76 1.06	1.09 1.22	1.20 1.29	0.96 1.03	1.19 1.27	0.97 1.03	1.21 1.29	0.97 1.03	1.19 1.27
0.83 1.13	1.12 1.24	0.97 1.05	1.12 1.20	0.95 1.02	1.13 1.21	0.97 1.03	1.13 1.21	0.93 1.01
0.81 1.08	1.19 1.30	1.15 1.25	0.94 1.01	1.11 1.18	0.95 1.02	1.19 1.27	0.93 1.01	0.90 0.95

Figure 4.4-1 Core Wide Planar Power Distribution for Sample DNB Analysis

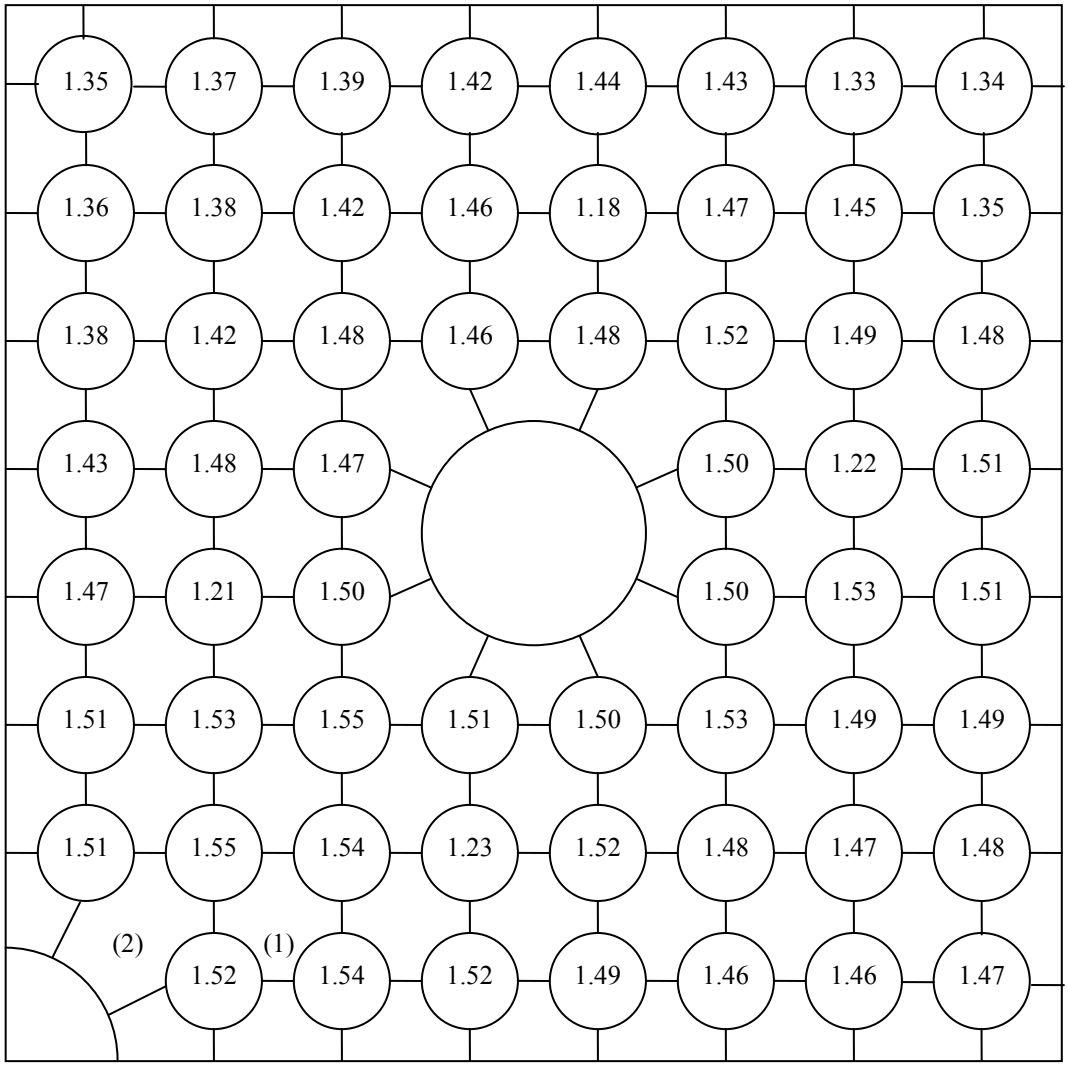

(1) : Matrix Subchannel

(2) : Subchannel next to guide tube

Figure 4.4-2 Rod Radial Power Factors in Hot Assembly Quadrant for Sample DNB Analysis

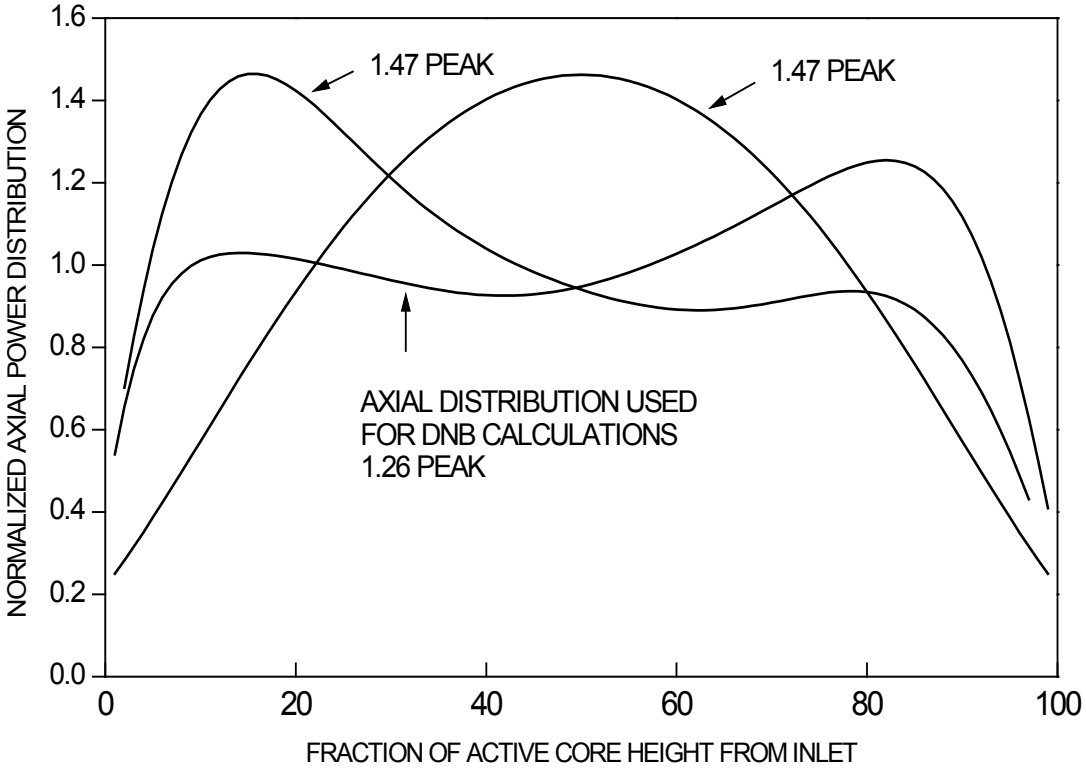

Figure 4.4- 3 Typical Axial Power Distribution

EXIT VOID FRACTION **EXIT EQUILIBRIUM QUALITY FRACTION**					0.00 -0.23	0.00 -0.20	0.00 -0.18	0.00 -0.19
			0.00 -0.23	0.00 -0.18	0.00 -0.15	0.00 -0.12	0.00 -0.03	0.00 -0.10
		0.00 -0.21	0.00 -0.13	0.00 -0.13	0.00 -0.16	0.00 -0.11	0.00 -0.15	0.00 -0.12
	0.00 -0.23	0.00 -0.13	0.00 -0.11	0.00 -0.15	0.00 -0.12	0.00 -0.15	0.00 -0.12	0.00 -0.16
	0.00 -0.17	0.00 -0.13	0.00 -0.15	0.00 -0.10	0.00 -0.15	0.00 -0.11	0.00 -0.16	0.00 -0.12
0.00 -0.23	0.00 -0.15	0.00 -0.16	0.00 -0.12	0.00 -0.15	0.00 -0.12	0.00 -0.15	0.00 -0.12	0.00 -0.16
0.00 -0.20	0.00 -0.13	0.00 -0.11	0.00 -0.15	0.00 -0.11	0.00 -0.15	0.00 -0.10	0.00 -0.15	0.00 -0.11
0.00 -0.18	0.00 -0.12	0.00 -0.15	0.00 -0.12	0.00 -0.16	0.00 -0.12	0.00 -0.15	0.00 -0.12	0.00 -0.16
0.00 -0.19	0.00 -0.11	0.00 -0.11	0.00 -0.16	0.00 -0.12	0.00 -0.16	0.00 -0.11	0.00 -0.16	0.00 -0.17

Figure 4.4-4 Average Void Fractions and Qualities in Core Region

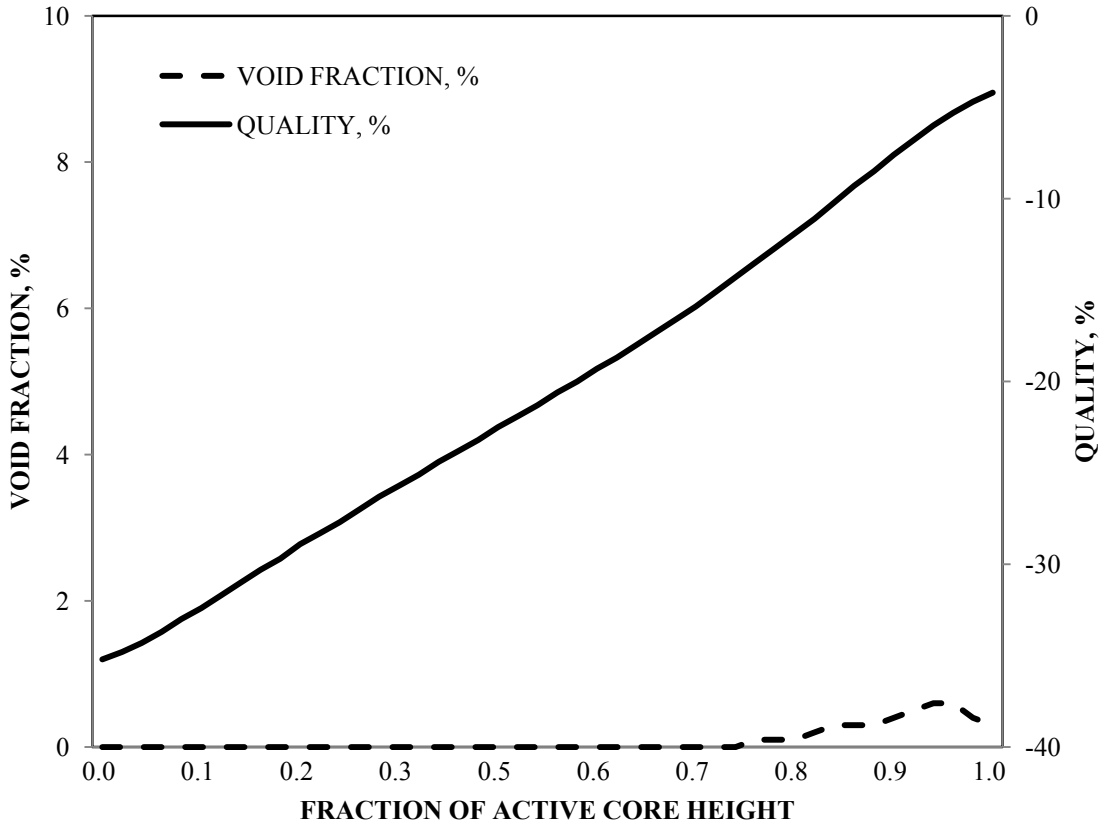

Figure 4.4-5 Axial Distribution of Void Fraction and Quality in the Subchannel Adjacent to the Rod with Minimum DNBR

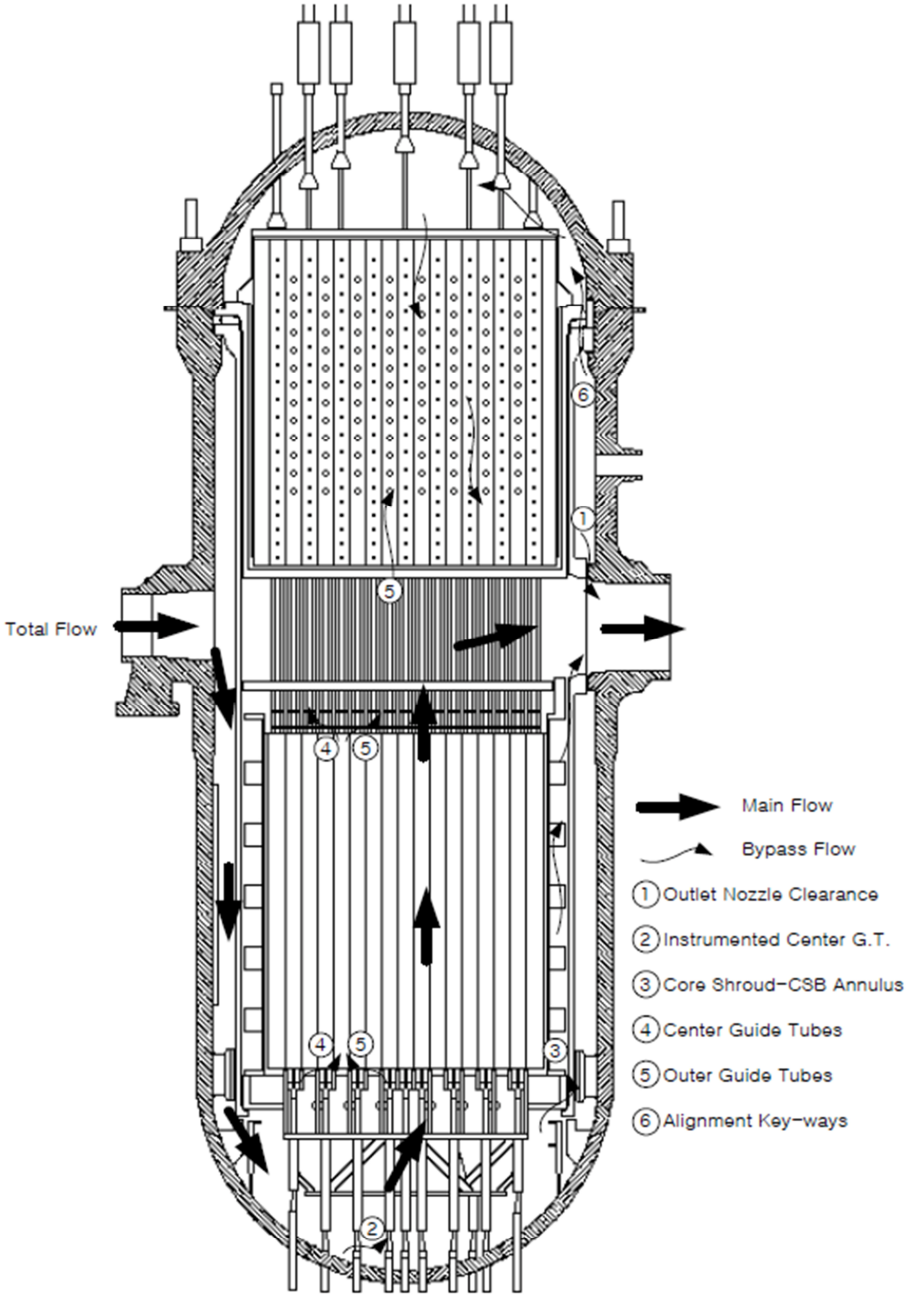

Figure 4.4-6 Reactor Flow Paths

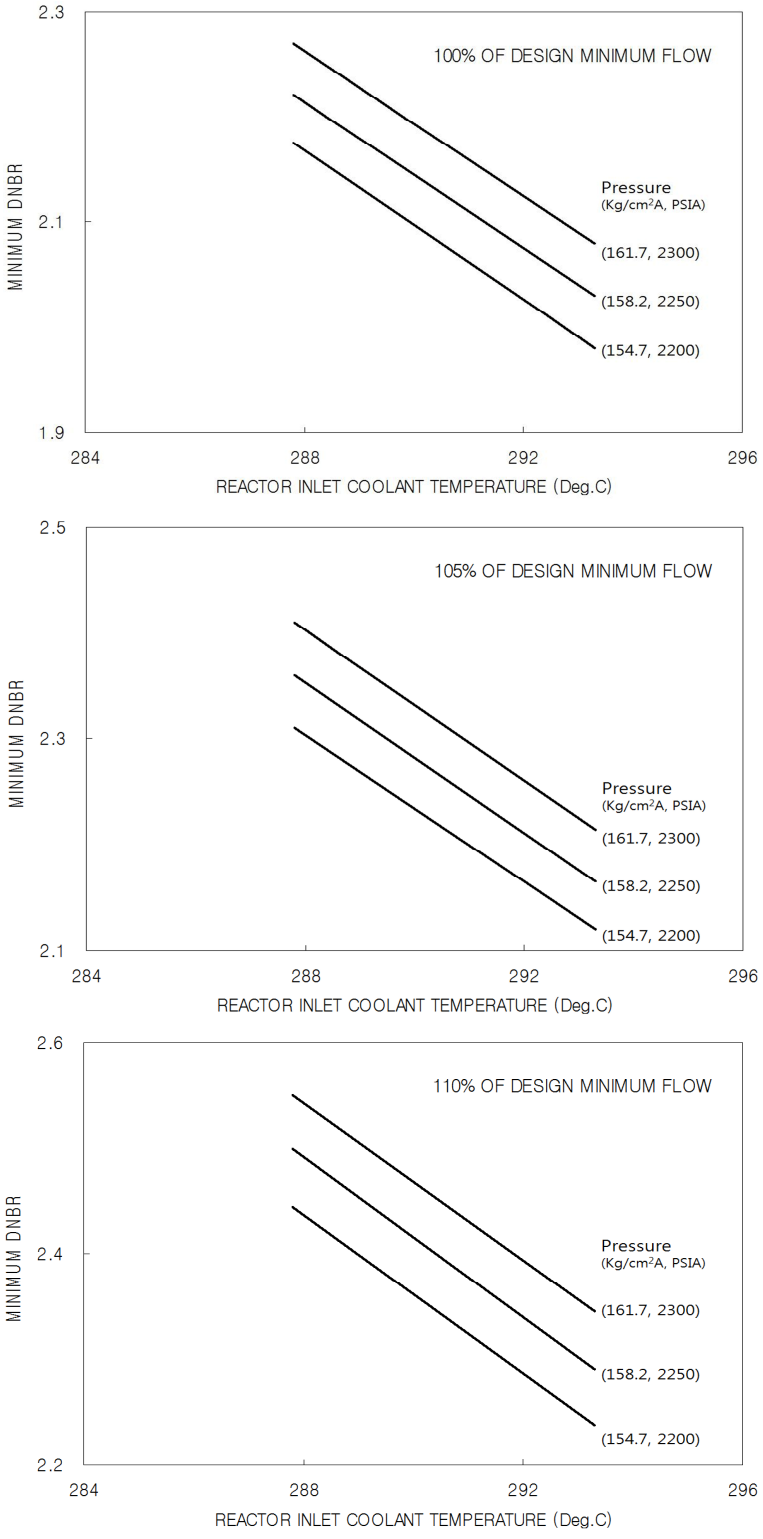

Figure 4.4-7 Sensitivity of Minimum DNBR to Small Changes in Reactor Coolant Conditions

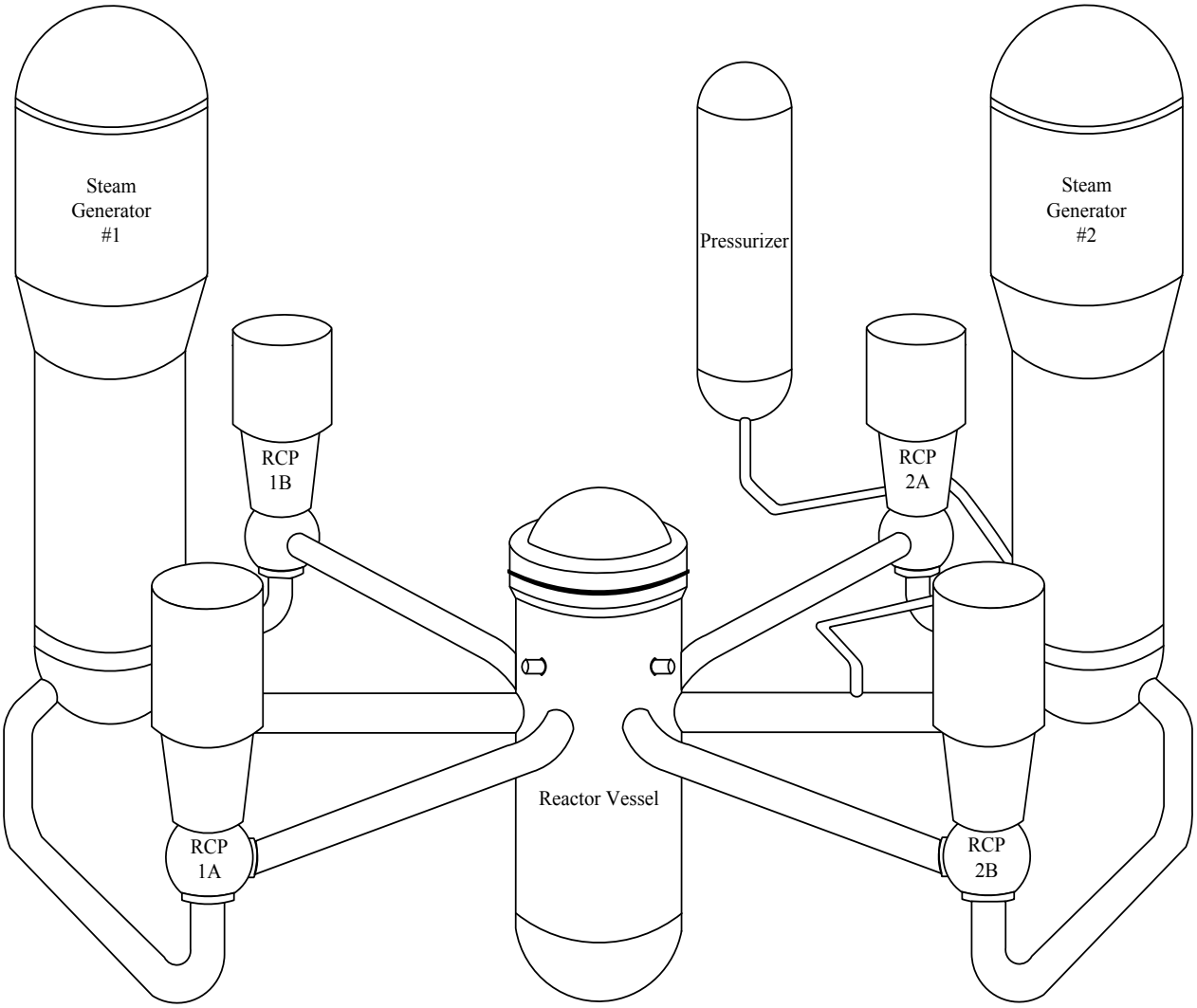

Figure 4.4-8 View of Isometric RCS

4.5 Reactor Materials

All of the materials used in the control rod drive system and the reactor internals and core support structures are compatible with the reactor coolant and have demonstrated satisfactory performance in existing operating reactor plants. Reactor coolant chemistry is addressed in Subsection 5.2.3.2.1.

4.5.1 Control Rod Drive System Structural Materials

This section describes the control rod drive system (the control element drive mechanism) structural materials and addresses relevant requirements of General Design Criteria 1 (GDC-1), GDC 14, and GDC 26 of 10 CFR 50, Appendix A (Reference 1), and also the requirements of 10 CFR 50.55a (Reference 2).

4.5.1.1 Material Specifications

a. The parts and materials used in the control element drive mechanism (CEDM) reactor coolant pressure boundary components are as follows:

1) Motor housing assembly

a) SA-182, F 347/F 348 (austenitic stainless steel)

b) ASME Code Case N-4-12 (modified Type 403 martensitic stainless steel), and the additional requirements of SA-182, tempered at 605 °C (1,125 °F) for a minimum of 4 hours

c) SB-166 (Alloy 690, thermally treated)

2) Upper pressure housing

a) SA-213, Type 316

b) SA-479, Type 316

The preceding materials are listed in ASME Section III (Reference 3) and comply with ASME Sections II and IX (References 4 and 5). Code Case N-4-12 is endorsed in NRC RG 1.84 (Reference 6). The functions of the above-listed components are addressed in Subsection 3.9.4.

b. The parts and materials in contact with the reactor coolant used in the CEDM motor assembly components are as follows:

1) Latch guide tubes

ASTM A 269, Type 316 (austenitic stainless steel)

Chrome oxide (plasma spray treatment)

2) Latch magnet and center spacer

ASTM A 276, Type 410 (martensitic stainless steel)

3) Lift magnet and latch spacer

ASTM A 276, Type 410 (martensitic stainless steel)

4) Latch housing and insert assembly

ASTM A 276, Type 316 (austenitic stainless steel)

SAE AMS 2460 (chrome plating)

ASTM A 276, Type 440C (martensitic stainless steel)

5) Spacer

ASTM A 240, Type 304 (austenitic stainless steel)

6) Alignment tab

ASTM A 276, Type 440C (martensitic stainless steel)

7) Spring

AMS 5698, Alloy X-750 (nickel-base alloy)

8) Pin

Stellite No. 6B (cobalt-base alloy) or functionally equivalent material

9) Dowel pin

Type 300 Series (austenitic stainless steel)

10) Adjusting nut

ASTM A 276, Type 321 (austenitic stainless steel)

11) Lower Lift Stop

ASTM A 276, Type 410T (martensitic stainless steel)

12) Latch and link

Haynes No. 36 (cobalt-base alloy) or functionally equivalent material

13) Locking cup and screws

Type 300 Series (austenitic stainless steel)

The functions of the CEDM motor assembly components are addressed in Subsection 3.9.4.

c. The materials in contact with the reactor coolant used in the extension shafts are as follows:

1) Shafts, operating rod tube, and plunger

   ASTM A 276, Type 304 (austenitic stainless steel)

   ASTM A 269, Type 304 (austenitic stainless steel)

   ASTM A 276, Type 410 Condition A (martensitic stainless steel)

2) Gripper

   ASTM B 446, Alloy 625 (nickel-chromium-molybdenum-columbium alloy)

3) Spring

   AMS 5699, Alloy X-750 (nickel-base alloy)

4) Pin

   Type 300 Series (austenitic stainless steel)

The functions of the extension shaft components are addressed in Subsection 3.9.4.

d. The weld rod filler materials used with the preceding components are Stainless Steel Type 308; Stainless Steel Type 316; and Alloy 52, 52M, and/or 152.

A CEDM using the materials listed above was tested to exceed lifetime requirement, as described in Subsection 3.9.4. Operating experience that shows the successful performance of the materials also exists for the APR1400 CEDMs because they are essentially identical to the Palo Verde, YGN 3&4, YGN 5&6, UCN 3&4, UCN 5&6, SKN 1&2, and SWN 1 CEDMs, which are all in operation. The experience has demonstrated that the CEDM operates without malfunction.

The CEDM structural material identified in Subsection 4.5.1.1 that has a yield strength greater than 620 MPa (90 ksi) is ASTM A 276, Type 440C, martensitic stainless steel. Its usage is limited to the steel ball in the vent valve on the top of the CEDMs, bearing inserts,

and alignment tab in the motor assembly. The steel ball is used as a seal and is not a primary load-bearing member of the pressure boundary. The inserts and alignment tab, which are Type 440C (used for surface hardness), operate under low stress and are not part of the safety release mechanism in the motor assembly. This material was tested and satisfied the lifetime requirements. Also, Type 440C is presently used in operating reactors such as Calvert Cliffs; St. Lucie Unit 1; Yonggwang Units 3, 4, 5, and 6; and Ulchin Units 3, 4, 5, and 6 and has performed satisfactorily.

Mechanical properties of materials that are not used in the RCPB and not included in either Section II, Part D of the ASME Code or NRC RG 1.84 are not described because they are not used to verify the integrity of the control element drive mechanisms.

4.5.1.2 Austenitic Stainless Steel Components

Control of the use of sensitized austenitic stainless steel is consistent with the recommendations of NRC RG 1.44 (Reference 7). Only those procedures and/or practices demonstrated not to produce a sensitized structure are used in the fabrication of CEDM structural components. Fabrication and processing of austenitic stainless steel are applicable to the CEDM stainless steel as addressed in Subsection 5.2.3.4.

The austenitic stainless steel, primary pressure-retaining welds in the CEDM structural components are consistent with the recommendations of NRC RG 1.31 (Reference 8) to preclude microfissuring.

The adequate controls for abrasive work and cleaning on austenitic stainless steel surfaces are required for prevent cold work and contamination that promotes stress corrosion cracking. The final surfaces meet the requirements specified in NRC RG 1.37 (Reference 9) and ASME NQA-1 (Reference 10).

Strain-hardened Type 300 austenitic stainless steel bolting or pin materials , if t used, are controlled to have a 0.2 percent offset yield strength that is no greater than 620 MPa (90 ksi) to reduce the probability of stress corrosion cracking.

4.5.1.3 Other Materials

Springs are made of Alloy X-750. They conform to AMS 5698 or 5699 and are drawn from hot-finished wire or rod that has been previously ground or has had surface preparation to remove scale, seams, or other injurious surface imperfections. The wire is heat treated at about 1,149 °C (2,100 °F) before being reduced to size. The springs fabricated from these materials have no failure experience in Korea.

Alloy 625 materials are used for grippers. They conform to ASTM B446 and are cold drawn and stress relieved at approximately 482 °C to 538 °C (900 °F to 1,000 °F) for 1 hour.

Cobalt alloy (Stellite No. 6B), which is used for pins, is ordered in the vacuum-annealed condition. For the latch and link, the cast form of cobalt alloy (Haynes No. 36) is used.

Bearing inserts, alignment tab, and steel ball are made of martensitic stainless steel, which conforms to ASTM A279, Type 440C. The martensitic stainless steel that is supplied has been quenched and subzero-cooled after quenching.

The materials used in the CEDM that are not included in ASME Section III, Appendix I, Division 1 are identified in Subsections 4.5.1.1 b and c.

Thermally treated Alloy 690 (690TT), and Alloys 52/52M and 152 weld metals are used for the APR1400 DC design, which have shown excellent performance against PWSCC in field operations and laboratory experiments. Alloy 600 and Alloys 82/182 are not used. Resistance to PWSCC of Alloy 690, 52/52M, and 152 in pressurized water reactors is described in EPRI report MRP-111, “Resistance to Primary Water Stress Corrosion Cracking of Alloys 690, 52, and 152 in Pressurized Water Reactors.” There are no reports of the cracking of Alloy 690, and the welds are up-to-date (as of April 2012). Non-metallic materials are not used in the CEDMs.

4.5.1.4 Cleaning and Cleanliness Control

The procedure and practices followed for cleaning and contamination protection of the CEDM structural components are in compliance with the recommendations of NRC RG 1.37, including ASME NQA-1.

Contamination of Type 300 series austenitic stainless steel by compounds that can alter the physical or metallurgical structure and/or the properties of the material are avoided during all stages of fabrication. Painting of Type 300 series stainless steels is prohibited. Grinding is accomplished with resin or rubber-bonded aluminum oxide or silicon carbide wheels that have previously been used on Type 300 series stainless steel alloys only.

Discussions of the fabrication and processing of austenitic stainless steel provided in Subsection 5.2.3.4.2 are applicable to the cleaning and cleanliness control of the CEDMs.

The shipment and storage of CEDM structural components are in compliance with the requirements of ASME NQA-1, Part II, Subpart 2.2, to avoid deleterious effects from shock, vibration, physical damage, water vapor, salt spray, condensation, or weather during shipping, handling, and storage.

4.5.2 Reactor Internals and Core Support Materials

This section describes the reactor internals and core support materials, the relevant requirements of GDC 1 of 10 CFR 50, Appendix A, and the requirements of 10 CFR 50.55a (Reference 2).

4.5.2.1 Material Specifications

Reactor internals and core support materials satisfy the requirements of ASME Section III NG-2000. Code Case N-60-5 is acceptable per NRC RG 1.84. The materials used in the fabrication of the reactor internals and core support structures are primarily Type 304 stainless steel. The flow skirt is fabricated from thermally treated Alloy 690. Welded connections are used where feasible; however, in locations where mechanical connections are required, structural fasteners are used that are designed to remain captured in the event of a single failure. Structural fastener material is typically Type 316 austenitic stainless

steel. Hardfacing of Stellite material is used at wear points. Strain-hardened austenitic Type 300 stainless steel bolting or pin materials, if used, are controlled to have a 0.2 percent offset yield strength that is no greater than 620 MPa (90 ksi) to reduce the probability of stress corrosion cracking.

The following is a list of the major components of the reactor internals and core support structures together with their material specifications:

a. Core support barrel assembly

1) Type 304 austenitic stainless steel to the following specifications:

SA-182, SA-240, SA-479, and SA-965

2) Precipitation-hardened stainless steel to the following specification:

SA-638, Grade 660

3) S21800 stainless steel to the following specification:

SA-479

4) Type 348 stainless steel to the following specification:

SA-182

b. Upper guide structure assembly

1) Type 304 austenitic stainless steel to the following specification:

SA-182, SA-240, SA-213, SA-479, SA-965, A511 (ASME Code Case N-60-5)

2) Type 347 austenitic stainless steel to the following specification:

SA-479, SA-312

3) Precipitation-hardened stainless steel to the following specifications:

SA-453, Grade 660; SA-638, Grade 660

4) S21800 stainless steel to the following specification:

SA-479

5) SA-193, Grade B8M; SA-194, Grade 8M

c. Core shroud assembly

1) Type 304 austenitic stainless steel to the following specification:

SA-479, SA-240

2) Type 348 stainless steel to the following specification:

SA-479, SA-182

3) Precipitation-hardened stainless steel to the following specification:

SA-453, Grade 660

d. Holddown ring

1) SA-182, Grade F6NM

e. Bolt and pin material

SA-453 and SA-638, Grade 660 material is used for bolt and pin applications. This alloy is heat treated in accordance with the ASME specification by precipitation hardening to have a minimum yield strength of 585 MPa (85 ksi). The corrosion properties of the alloy are similar to those of the Type 300 series

austenitic stainless steels. The alloy has an austenitic structure in all conditions of fabrication and heat treatment.

f. Chrome plating and hardfacing

Chrome plating or hardfacing is used on the reactor internals and core support structures or portions of the structures where required by function. Chrome plating complies with SAE AMS 2460. The hardfacing material is Haynes Alloy-25 or an alternate material that has been demonstrated to be functionally equivalent.

g. Special-purpose material

1) SA-479, S21800 is used for special applications where anti-galling properties are desired.

h. Weld materials

The weld rod filler materials used with the above-listed components are Stainless Steel Type 308L and Type 347.

All the materials used in the reactor internals and core support structures have performed satisfactorily in operating reactors such as Palisades; Fort Calhoun; Yonggwang Units 3, 4, 5, and 6; and Ulchin Units 3, 4, 5, and 6.

4.5.2.2 Controls on Welding

Welds used on reactor internals and core support structures are fabricated in accordance with ASME Section III NG-4000 and meet the acceptance standards delineated in ASME Section III NG-5000. The control of welding is performed in accordance with ASME Section III and Section IX. Consistency with the recommendations of NRC RGs 1.31 and 1.44 is described in Subsection 4.5.2.4.

4.5.2.3 Nondestructive Examination

For the reactor internal and core support structure materials, nondestructive examination (NDE) examinations are performed in accordance with the requirements of ASME Section III NG. For other materials that are not defined as ASME Section III NG, NDE examinations are performed in accordance with the applied material specification.

4.5.2.4 Fabrication and Processing of Austenitic Stainless Steel Components

The recommendations of NRC RG 1.44 are applied to control the use of sensitized austenitic stainless steel. Only those procedures and/or practices demonstrated not to produce a sensitized structure are used in the fabrication of reactor internals and core support structures.

Austenitic stainless steels used in the reactor internals and core support structures are addressed in Subsection 5.2.3.4.

All raw austenitic stainless steel material, both wrought and cast, used in the fabrication of the reactor internals and core support is supplied in the solution-annealed condition, as specified in the applicable ASTM or ASME material specification (i.e., 1,040 °C to 1,120 °C [1,900 °F to 2,050 °F]) for 0.5 to 1 hour per 2.54 cm (1 in) of thickness and rapidly cooled to below 370 °C (700 °F). The time at temperature is determined by the size and the type of component.

Solution heat treatment is not performed on completed or partially fabricated components. Rather, the extent of chromium carbide precipitation is controlled during all stages of fabrication.

Compliance with the recommendations of NRC RG 1.31 for the reactor internals and core support materials is addressed in Subsection 5.2.3.4.4.

Compliance with the recommendations of NRC RG 1.71 (Reference 11) for welder qualification for areas of limited accessibility is addressed in Subsection 5.2.3.3.

Compliance with the recommendations of NRC RG 1.37 for quality assurance requirements for cleaning of fluid systems and associated components of water-cooled nuclear power plants is addressed in Subsection 5.2.3.4.

4.5.2.5 Other Materials

The precipitation-hardened stainless steel used in the reactor internals and core support structures is SA-453 Grade 660 or SA-638 Grade 660. These materials are solution treated to type 1 or 2 condition at 900 °C ± 15 °C (1,650 °F ± 25 °F) for 2 hours minimum, oil or water quenched, final precipitation hardened at 705 °C to 760 °C (1,300 °F to 1,400 °F) for 16 hours, and air cooled or furnace cooled.

SA-479 S21800 are supplied in annealed conditions.

SA-182 F6NM material, which is used for the holddown ring, is heat-treated as follows: Solution heat treated at 1,010 °C (1,850 °F) and air cooled

Thermally treated Alloy 690 (690TT), and Alloys 52/52M and 152 weld metals are used for the APR1400 DC design, which have shown excellent performance against PWSCC in field operations and laboratory experiments. Alloy 600 and Alloys 82/182 are not used. Resistance to PWSCC of Alloy 690, 52/52M, and 152 in pressurized water reactors is discussed in EPRI report MRP-111, "Resistance to Primary Water Stress Corrosion Cracking of Alloys 690, 52, and 152 in Pressurized Water Reactors." There are no reports of cracking of Alloy 690, and the welds up-to-date (as of April 2012).

4.5.3 Combined License Information

No COL information is required with regard to Section 4.5.

4.5.4 References

1. NRC Regulations Title 10, "General Design Criteria for Nuclear Power Plants," Code of Federal Regulations, 10 CFR 50, Appendix A.

2. NRC Regulations Title 10, "Codes and Standards," Code of Federal Regulations, 10 CFR 50.55a.

3. ASME Boiler and Pressure Vessel Code Section III, “Rules for Construction of Nuclear Power Plant Components,” 2007 Edition with 2008 Addenda.

4. ASME Boiler and Pressure Vessel Code Section II, “Materials,” 2007 Edition with 2008 Addenda.

5. ASME Boiler and Pressure Vessel Code Section IX, “Welding and Brazing Qualifications,” 2007 Edition with 2008 Addenda.

6. NRC RG 1.84, “Design, Fabrication and Materials Code Case Acceptability ASME Section III Division 1,” Revision 35, October 2010.

7. NRC RG 1.44, “Control of the Use of Sensitized Stainless Steel,” Revision 1, March 2011.

8. NRC RG 1.31, “Control of Ferrite Content in Stainless Steel Weld Metal,” Revision 3, April 1978.

9. NRC RG 1.37, “Quality Assurance Requirements for Cleaning of Fluid Systems and Associated Components of Water-cooled Nuclear Power Plants,” Revision 1, March 2007.

10. ASME Boiler and Pressure Vessel Code NQA-1,“Quality Assurance Requirements for Nuclear Facility Applications,” 2008 Edition with 2009 Addenda.

11. NRC RG 1.71, “Welder Qualification for Areas of Limited Accessibility,” Revision 1, March 2007.

4.6 Functional Design of Reactivity Control System

The APR1400 includes the following reactivity control systems: control element drive mechanisms (CEDMs), safety injection system (SIS), and chemical and volume control system (CVCS). Applicable information, evaluations, and testing of the CEDMs are provided in Subsections 4.6.1, 4.6.2, and 4.6.3, respectively. The combined performance of the CEDMs and other reactivity control systems is described in Subsections 4.6.4 and 4.6.5.

4.6.1 Information for the Control Rod Drive System

The control rod drive system (CRDS) includes the CEDM and the digital rod control system (DRCS), which actuates the CEDMs to insert or withdraw the control element assemblies (CEAs). Component diagrams, description, and characteristics of the CEDMs are presented in Subsection 3.9.4. The functions and description of the DRCS are addressed in Subsection 7.7.1.

The CEA is inserted in the core by gravity when the electrical power is shut off from the CEDM coils. The electrical power to the CEDM coils is shut off by the trip circuit breakers that receive the reactor trip signal. Hydraulic systems are not used in the control of the CEDM.

The instrumentation and controls for reactor trip and reactor control are addressed in Sections 7.2 and 7.7, respectively. The cooling system for the CEDM is addressed in Subsection 9.4.6.1.

4.6.2 Evaluation of the Control Rod Drive System

The safety function of the CRDS is to drop CEAs into the reactor core when motive power is removed from the CEDM power bus. The active interface between the RPS and the CEDMs is at the trip circuit breakers in the reactor trip switchgear (RTSG).

4.6.2.1 Single Failure

Upon an initiation of a reactor trip signal, the RTSG removes the input motive power from the DRCS, which causes all CEAs to be inserted into the core by gravity. Therefore, a

failure of the DRCS does not prevent the reactor trip function from occurring. This is verified by a failure modes and effects analysis (FMEA) of the DRCS. No single failure in the RPS (including the RTSG) can prevent the removal of electrical motive power from the CEDMs.

For the trip function, the CEDMs are essentially passive devices. When power is removed from the CEDM coils, the armature springs automatically disengage the latches from the CEDM driveshafts, allowing insertion of the CEAs by gravity. The CEDMs operate independently of one another when a reactor trip occurs. Therefore, if one CEDM fails to trip, it would not affect the ability of any other CEDM to trip. In the event of a failure of a CEDM, the shutdown capability is retained because sufficient shutdown margin is always maintained in the reactor. Therefore, no single failure can prevent the CEDMs from providing sufficient scram reactivity to achieve a reactor shutdown.

4.6.2.2 Isolation of the CEDMs from Other Equipment

The isolation of the RPS from nonessential elements to provide reasonable assurance of a reactor trip function is addressed in Section 7.2. Control of the CEDM is performed by the DRCS. The interface between the CEDMs and the DRCS is at the DRCS power switches, which provide the isolation of the high-voltage motive power from the low-voltage logic control signal. The interface between the CEDMs and the CEAs involves no nonessential elements.

4.6.2.3 Protection from Common-Cause Failure

Protection of essential systems from the consequences of postulated pipe breaks and associated missiles is provided by physical separation, pipe whip restraints, protective structures and compartments, watertight barriers, isolation capability, or other suitable means, as addressed in Section 3.6.

4.6.3 Testing and Verification of the Control Rod Drive System

The testing and verification of the CEDM is addressed in Subsection 3.9.4.4. The initial startup test is addressed in Chapter 14, which includes hydrostatic test and verifies the reactor trip function and the proper operation of the CEDMs.

4.6.4 Information for Combined Performance of the Reactivity Control Systems

Table 4.6-1 lists all the design bases events analyzed in Chapter 15 that take credit for two or more reactivity control systems for preventing or mitigating each event. The related reactivity systems are also included in the table.

4.6.5 Evaluation of Combined Performance of the Reactivity Control Systems

The CEDMs and SIS are separate systems (Section 1.2) and totally diverse in design and operation. Because the CEDMs and the SIS are protected from missiles, pipe breaks, and their effects (as delineated in Section 3.6), there are no credible potential common-mode failures that could result in the failure of both the CEDMs and the SIS. Therefore, sufficient reactivity insertion to achieve a reactor shutdown is maintained.

As delineated in Subsection 4.6.4 and Chapter 15, only a limited number of postulated events assume the availability of two reactivity control systems to prevent or mitigate the accident. The evaluations for steam line break (SLB) and CEA ejection, which assume the combined actuation of the CRDS and the SIS, are addressed in Chapter 15. These analyses demonstrate that the CRDS and SIS reliably control reactivity changes to cool the core under postulated accidents in accordance with GDC 27.

As addressed in Subsection 9.3.4.1, the CVCS is a non-safety-related system and is not required to perform any accident mitigation or safe shutdown function. However, the CVCS is designed for a high degree of redundancy and reliability.

4.6.6 Combined License Information

No COL information is required with regard to Section 4.6.

4.6.7 References

There are no references in Section 4.6.

Table 4.6-1

Design Basis Events

Event	CEDMs	SIS	CVCS
Feedwater line break	A (1)	A	B (2)
Steam line break	A	A	B
LOCA	A	A	B
Letdown line break	A	A	B
Steam generator tube rupture	A	A	B
CEA ejection	A	A	B
Boron dilution	A	B	B
Uncontrolled CEA withdrawal	A	B	B
CEA drop	A	B	B
Inadvertent opening of an atmosphere dump valve or main steam safety valve	A	B	B
Loss of normal feedwater flow or loss of condenser vacuum	A	B	B
Reactor coolant pump shaft seizure, shaft break, or total loss of reactor coolant flow	A	B	B
Pressurizer level control system malfunction	A	B	C (3)

(1) A = Use expected and required for mitigating the event or reactivity control

(2) B = Use expected and not required for mitigating the event or reactivity control

(3) C = Use not expected and not required for mitigating the event or reactivity control